Design and Evaluation of a Biocompatible Bioluminescence Unit: Applications in Optogenetics and Beyond

Arash Azarnoush

Thesis submitted to the University of Ottawa in partial fulfillment of the requirements for the degree of PhD in Electrical and Computer Engineering

Faculty of Engineering
University of Ottawa

uOttawa

Abstract

Achieving non-invasive, deep tissue illumination is a significant challenge with applications in fields such as biophotonics and bio-optical communication. The high scattering and absorption coefficients of biological tissues limit light penetration and impose practical constraints on various applications such as optogenetics and bio-optical interfaces. Traditional methods that utilize external light sources or implanted optical fibers are limited by invasiveness and biocompatibility issues. To address these constraints, this research proposes developing a wireless, bioluminescent illumination unit powered by piezoelectric nanogenerators. The expected outcome of this system is to provide a minimally invasive method for deep tissue illumination.

This approach not only enhances in vivo optogenetic applications but also holds potential for bio-optical communications, which offer advantages over electrical methods, including higher spatiotemporal resolution and minimal invasiveness. The integration of bioluminescence with ultrasonic stimulation offers a non-invasive, controllable light source for targeted neural stimulation in optogenetics and other bio-optical applications.

This research will focus on designing the proposed illumination unit and characterizing the bioluminescent response to ultrasonic stimulation by thoroughly modelling the underlying biological processes. Additionally, it will analyze light-tissue interactions to quantify the resulting fluence distribution within biological tissue. By proposing the design of a wireless bioluminescent systems, this study aims to open new pathways for medical diagnostics and therapeutic interventions using optogenetics. Furthermore, the findings of this research could contribute to the design and analysis of wireless optical transceivers for bio-optical interfaces, potentially advancing the field of optical biocommunication for various applications.

List of Publications

A. Azarnoush, O. A. Dambri, E. Üstün Karatop, D. Makrakis, and S. Cherkaoui, "Simulation and performance evaluation of a bio-inspired nanogenerator for medical applications," *IEEE Transactions on Biomedical Engineering*, vol. 70, no. 9, pp. 1–8, 2023, ISSN: 0018-9294. DOI: 10.1109/TBME.2023.3260200.

A. Azarnoush, O. A. Dambri, E. U. Karatop, D. Makrakis, and A. S. Hafid, "Design and modeling of a bio-inspired aequorin-based light-emitting unit: Applications in optogenetics and beyond," *IEEE Transactions on Biomedical Engineering*, vol. 72, no. 10, pp. 2925–2936, Oct. 2025, ISSN: 0018-9294, 1558-2531. DOI: 10.1109/tbme.2025.3556793.

O. A. Dambri, A. Azarnoush, D. Makrakis, G. Levesque, M. Witter, and A. S. Hafid, "Design and implementation of a simulation framework for a bio–neural dust system," *Modelling*, vol. 6, no. 1, 2025, ISSN: 2673-3951. DOI: 10.3390/modelling6010008.

A. Azarnoush, D. Makrakis, P. T. Mathiopoulos, and S. Hadjiefthymiades, "Predictive modeling of calcium-sensitive aequorin mutants for bioluminescent optogenetics," Dec. 2025, Manuscript submitted.

A. Azarnoush and D. Makrakis, "Radiative transport modeling of aequorin-based bioluminescence in biological tissue," In preparation.

Acknowledgements

This PhD was both challenging and deeply fulfilling. Its interdisciplinary nature repeatedly brought me into unfamiliar territory, calling for curiosity, patience, and a willingness to learn across boundaries. Despite the hard parts, it became the most intellectually satisfying stage of my education, reaffirming how central learning and curiosity are to my sense of fulfillment.

I am profoundly grateful to my supervisor, Professor Dimitrios Makrakis, for the intellectual freedom and honesty that shaped not only this work but also how I think. His feedback taught me to question my assumptions more carefully and to separate criticism of my work from criticism of myself. This environment encouraged independence, healthy skepticism, and patience—qualities that I will carry with me beyond this thesis.

I would also like to thank my research group and department for providing a stimulating and supportive environment. In particular, I am deeply grateful to Dr. Oussama A. Dambri, whose guidance was invaluable throughout this interdisciplinary journey. His background in biology, combined with his technical expertise and conceptual insight, helped me approach unfamiliar areas with confidence.

My deepest thanks go to my family. I am grateful to my father, Majid, who played a fundamental role in shaping my research mentality by nurturing my curiosity and teaching me patience. I thank my mother, Azin, for her constant emotional support and calm reassurance. I am also thankful to my brother, Aeen, whose belief in me and willingness to listen often provided comfort and perspective. Conversations with my family consistently renewed my energy and reminded me of what truly matters.

I am especially grateful to my companion during this period, Negin. Her emotional support, stability, and motivation were essential, particularly during challenging transitions. Her presence made this journey lighter and more grounded.

I would also like to thank my friends Ahmad and Navid. Their encouragement and perspective were invaluable. They reminded me of who I am outside the PhD and helped me keep balance throughout this process.

Finally, I acknowledge the personal growth this journey required. This PhD taught me to be patient with uncertainty, more at ease with not knowing, and more humble in the face of complexity.

Contents

List of Figures

List of Tables

List of Abbreviations

E.mol^{-1} Einstein per Mole 24

μLEDs Microscale Light-Emitting Diodes 5–8, 13, 14, 107

ATP Adenosine Triphosphat 21, 22, 110

BLI Bioluminescence Imaging 24

BMI Brain-Machine Interfaces 9, 10

BRET Bioluminescence Resonance Energy Transfer 30, 31

ChR2 Channelrhodopsin-2 viii, 36, 38–40

CICR Calcium-Induced Calcium Release 107, 108, 112–114, 119, 158, 159, 196, 199, 212, 216

CitA Citrine–*Aequorin* 31

CLZ Coelenterazine 26, 28–30, 32, 113

CMOS Complementary Metal-Oxide-Semiconductor 7, 13, 14

CNC Cellulose Nanocrystals 90

DBS Deep Brain Stimulation 32, 33

DOM Discrete Ordinates Methods 83, 135

FEA Finite Element Analysis 109, 115–117

FP Fluorescent Protein 30, 31

FRET Förster Resonance Energy Transfer 24, 62

FWHM Full Width at Half Maximum 139

GA Green Fluorescent Protein–*Aequorin* 31

GEVIs Genetically Encoded Voltage Indicators 9

GFP Green Fluorescent Protein 24, 31

GPCR G-Protein-Coupled Receptors 33

HEI High-Energy Intermediate 23

IUPAC International Union of Pure and Applied Chemistry 73

LCAO Linear Combination of Atomic Orbitals 57

LED Light-Emitting Diode 4, 8, 10, 11, 13, 122

LS Least Squares 124–128

LSRE Least Squares with Relative Error 124, 126, 127, 131

LTNR Log-Transformed Nonlinear Regression 126–128, 131

MAPE Mean Absolute Percentage Error 129, 131

MOs Molecular Orbitals 57

NR Nonlinear Regression 126, 128

PDMS Polydimethylsiloxane 113

PENG Piezoelectric Nanogenerator 86, 87, 90–92, 107, 109, 111, 114, 115, 217

PVDF Polyvinylidene Fluoride 88, 90

RASM Radiation in Absorbing–Scattering Media 134, 138

RMSRE Root Mean Squared Relative Error 129, 131

RTE Radiative Transport Equation 80–84, 133, 134, 136, 138, 139, 141–146, 148, 173, 175–183, 185, 191, 192, 194, 203, 204, 213

RYR2 Ryanodine Receptors 2 108, 109, 112

SERCA Sarcoplasmic/Endoplasmic Reticulum Ca^{2+}-ATPase 107–110, 113, 119

SR Sarcoplasmic Reticulum ix, 107–114, 118, 120–122, 143, 155–159, 161, 162, 164, 169, 170, 172, 175, 197–199, 201, 203, 212, 215, 216

tdTA tandem-dimer-Tomato–*Aequorin* 31

tdTomato tandem-dimer Tomato 31

TI Transversely Isotropic 93, 94

VGCCs Voltage Gated Calcium Channels 108–112

WiOptND Wireless Optogenetics Nanonetworking Devices 14, 107

WT Wild Type 130, 131, 169

List of Symbols

This list includes the primary symbols used throughout the thesis. Unless otherwise stated at first use, symbols carry the meanings given here. Additional symbols introduced locally are defined in the text.

Geometry and kinematics

$\mathbf{r}$ Position vector.

Optical medium and wave parameters

λ Wavelength.

c Speed of light in vacuum.

n Refractive index.

v Speed of light in the medium, $v = c/n$.

Tissue optical properties and transport

μ_a Absorption coefficient.

μ_s Scattering coefficient.

μ_s' Reduced scattering coefficient, $\mu_s' = \mu_s(1 - g)$.

μ_t Extinction coefficient, $\mu_t = \mu_a + \mu_s$.

μ_t' Reduced interaction coefficient, $\mu_t' = \mu_a + \mu_s'$.

g Anisotropy factor, $g = \langle \cos\theta \rangle$.

l_t Mean free path, $l_t = 1/\mu_t$.

l'_t Transport mean free path, $l'_t = 1/\mu'_t$.

Radiometry and photon quantities

ν Frequency.

A Area of a flat surface.

$d\Omega$ Differential solid angle element.

$E(\lambda)$ Photon energy, $E(\lambda) = hc/\lambda$.

E_e Irradiance, $E_e = dP_e/dA$.

E_o Fluence rate, $E_o = dH_o/dt = dP_e/dS_{\text{sphere}}$.

h Planck constant.

H_o Fluence, $H_o = dQ_e/dS_{\text{sphere}}$.

P_e Radiant power (radiant flux).

Q_e Radiant energy.

q_p Photon flux (photons per unit time).

S_{sphere} Cross-sectional area of the small sphere used in fluence definitions.

Light transport models (RTE / diffusion)

$\hat{\mathbf{\Omega}}$ Unit propagation direction.

∇ Del operator.

$\Phi(\mathbf{r}, t)$ Fluence rate field (diffusion state variable).

$\Phi^{(0)}(r)$ Steady-state ballistic fluence rate.

$\Phi^{(c)}(r)$ Steady-state collided fluence rate.

a Radius of the spherical emitting source.

D Diffusion coefficient, $D = \frac{1}{3(\mu_a + \mu'_s)}$.

$L(\mathbf{r}, \hat{\mathbf{\Omega}}, t)$ Radiance at position $\mathbf{r}$, direction $\hat{\mathbf{\Omega}}$, time t.

$L^{(0)}(\mathbf{r}, \hat{\mathbf{\Omega}}, t)$ Uncollided (ballistic) radiance at position $\mathbf{r}$, direction $\hat{\mathbf{\Omega}}$, time t.

$L^{(c)}(\mathbf{r}, \hat{\mathbf{\Omega}}, t)$ Collided radiance at position $\mathbf{r}$, direction $\hat{\mathbf{\Omega}}$, time t.

P_0 Total emitted power, $P_0 = \frac{4\pi}{3} a^3 q$.

q Volumetric power density of the source [$\mathrm{W\,mm^{-3}}$].

$S(\mathbf{r}, \hat{\mathbf{\Omega}}, t)$ RTE source term (volumetric radiance injection/emission).

$S(\mathbf{r}, t)$ Source term in the diffusion equation.

Piezoelectricity

$[\boldsymbol{\varepsilon}^T]$ Permittivity matrix (constant-stress).

$[\mathbf{d}]$ Piezoelectric coefficient matrix.

$[\mathbf{s}^E]$ Elastic compliance matrix (constant electric field).

$\mathbf{D}$ Electric flux density vector (piezoelectric context).

$\mathbf{E}$ Electric field vector (piezoelectric context).

$\mathbf{S}$ Strain vector (Voigt notation).

$\mathbf{T}$ Stress vector (Voigt notation).

Aequorin model and simulation parameters

$[Aq]$ Aequorin concentration ($\mathrm{mol\,L^{-1}}$).

$[Ca^{2+}]$ Calcium concentration (state variable in the circuit model).

ϕ_{SR} Fraction of nanobubble volume allocated to the SR compartment.

$I_{\max}$ Maximum photon output under saturating calcium conditions.

K_R Aequorin calcium-response parameter.

K_{TR} Aequorin calcium-response parameter.

N_A Avogadro's number (mol^{-1}).

n_H Exponent (Hill-like) parameter in the Aequorin response model.

N_{Aq} Total number of Aequorin molecules in the nanobubble.

P Aequorin variant parameter set, $P = \{K_R, K_{TR}, n_H\}$.

r_B Nanobubble radius.

V_{bubble} Nanobubble volume.

$V_{\text{myocyte,ref}}$ Reference myocyte volume.

$V_{\text{SR,eng}}$ Engineered SR volume.

$V_{\text{SR,ref}}$ Reference SR volume.

1

Introduction

1.1 Context and Importance of the Study

Ion movement across cellular membranes is essential for generating electrical signals and regulating cellular responses [1]. Several types of ion channels, such as leakage channels, ligand-gated channels, and voltage-gated channels, facilitate this process, while ion pumps

like the Na^+/K^+-ATPase actively maintain electrochemical gradients. Understanding and artificially manipulating ion fluxes has become a critical tool for studying cellular processes, particularly in fields like neuromodulation and optogenetics [2].

These approaches enable the modelling of pathological conditions, offering deeper insights into their underlying mechanisms assisting to develop appropriate treatments [3]. Moreover, precise control over ion fluxes affects signal transduction pathways, gene expression, and metabolic activities, providing a robust tool for modulating cellular behaviour and advancing therapeutic interventions [4].

In the nervous system, manipulating ion fluxes (referred to as neuromodulation) not only serves as a powerful method to better understand the complexities of neuronal function and communication but also supports various therapeutic interventions [5]. This technique forms the basis for mapping neural circuits, studying synaptic plasticity, and investigating the cellular foundations of neurological disorders [5]. By modulating ion fluxes in neurons, we can examine how alterations in ion channel function contribute to diseases such as Parkinson's, Alzheimer's, and multiple sclerosis and pave the way for developing novel therapeutic strategies.

Various mechanisms, including electrical [6], pharmacological [7], and optical approaches [8], are employed for neuromodulation, each offering distinct advantages and limitations. Electrical neuromodulation works through the direct application of electrical currents, producing immediate effects with high spatial and temporal precision [6]. This method enables precise modulation in localized brain regions at different depths [6]. It is widely used due

to its rapid onset and well-established clinical applications, particularly in treatments such as deep brain stimulation for movement disorders like Parkinson's disease [9]. However, electrical stimulation lacks cell-type specificity and cannot differentiate between genetically diverse cell populations in close proximity [10]. Moreover, it is often invasive and may cause neurons to become less responsive over time [11].

Pharmacological neuromodulation relies on drugs that interact with endogenous receptors, such as G-protein-coupled receptors, to influence intracellular processes [12]. This method offers cell-type specificity by targeting particular receptors, enzymes, or ion channels. Nonetheless, it often lacks precise spatiotemporal control, as drugs can diffuse into surrounding tissues or the body more broadly [13]. Additionally, the slower onset of drug effects, potential systemic side effects, difficulties in dose regulation, and desensitization with prolonged use are significant limitations [13]. Maintaining effective drug concentrations at the target site also presents a challenge [13].

Optical neuromodulation, commonly associated with optogenetics, relies on the expression of genetically encoded light-sensitive ion channels, known as opsins, on cell membranes to manipulate neuronal activity [10]. By incorporating these opsins, cells become responsive to optical stimulation, operating on the same principle that governs visual transduction in animals. Depending on the properties of the deployed opsins, neural activity can either be excited or inhibited in response to optical stimulation [10]. The targeted expression of opsins in specific cells through genetic engineering allows optogenetics to be applied in a highly cell-specific manner. Additionally, optogenetics offers high precision in both spatial and temporal dimensions [10]. These properties have made optogenetics an invalu-

able tool for both unraveling the complexities of the nervous system [14] and advancing various therapeutic applications [15]. Beyond the nervous system, optogenetic approaches have also been applied in diverse fields, including cardiology and metabolic regulation. For instance, optogenetics enables precise cardiac pacing in cardiomyocytes and can modulate therapeutic protein synthesis in diabetic treatment models through light-controlled gene expression [16].

In optogenetics, one of the primary practical challenges is delivering light to target cells within biological tissue. This difficulty stems from the light absorption properties of biological components, such as hemoglobin and melanin, which absorb visible light strongly [17]. These molecules exhibit absorption coefficients peaking around $10^3\,\mathrm{cm}^{-1}$ in the blue wavelength range, which is about six to seven orders of magnitude higher than water's absorption coefficient (between 10^{-4} and $10^{-3}\,\mathrm{cm}^{-1}$) in the same wavelength range (see Figure 1.1)[18]. As a result, the penetration depth of visible light into biological tissue is limited, making it challenging to illuminate cells located deeper within the tissue. Due to this limitation, the use of external light sources for optogenetic applications is generally restricted to in vitro settings or to cases where target cells are near the surface of the tissue. In contrast, external illumination is often impractical for in vivo applications, where deeper tissue illumination is required.

In response to these limitations, various approaches have been developed. A simple, yet widely used method is the use of optical waveguides coupled with external light sources, such as lasers or Light-Emitting Diode (LED)s, for deep tissue optogenetics [19]. While this technique addresses the light penetration issue, it is highly invasive, as it requires

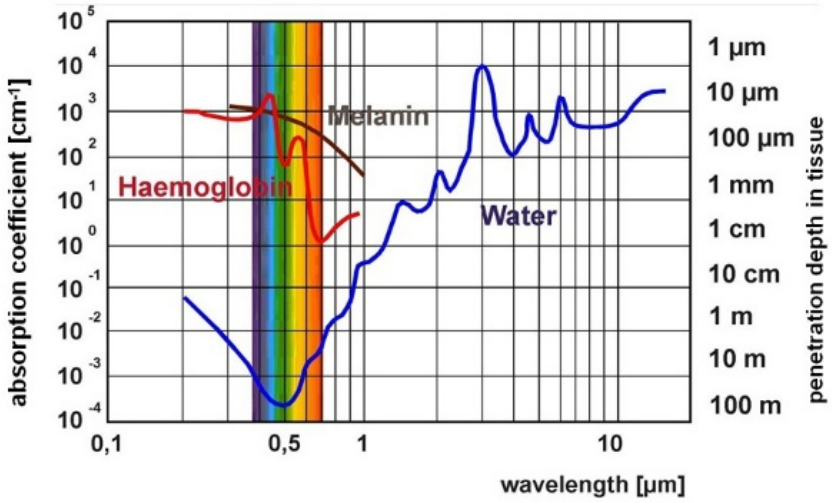

Figure 1.1: Absorption and penetration depth in water and other biological tissue constituents for different wavelengths. Figure is adapted from [18].

implanting the optical waveguide directly into the biological tissue. This procedure can cause significant tissue damage, potentially disrupting normal neuronal function and altering neuronal circuit behaviour [20]. Furthermore, there is a risk of fiber breakage within the cannula, which complicates long-term studies and can lead to further tissue damage [20]. The tethered equipment and connections in these setups can also severely restrict the mobility of the test subject and limit their natural behaviour, which limits the practicality of behavioural studies.

More recently, Microscale Light-Emitting Diodes (μLEDs) have been introduced for optogenetic illumination [21]. These tiny devices, with dimensions comparable to individual neurons, enable precise and localized light delivery without the need for implanting optical waveguides and tethering optical equipment [22]. The compact size of μLEDs and the elim-

ination of the need for external tethered light sources allow for less invasive implantation and enable more natural movement in test subjects.

However, μLEDs come with their own challenges. One of the primary issues is the mechanical mismatch between the rigid materials used in μLEDs arrays, such as silicon, and the soft, delicate neural tissues they interact with [23]. This mismatch can lead to tissue damage, inflammation, and adverse immune responses, particularly in long-term implants where micromotions worsen these problems [24].

Additionally, powering the μLEDs efficiently remains a challenge, particularly when aiming for fully implantable, wireless systems. Several approaches have been explored, each with its own advantages and limitations. In some designs, the use of electrochemical energy storage, such as batteries, has been proposed [25]. Lithium-ion batteries, in particular, providing stable electrical power through chemical reactions between their electrodes and electrolyte [26]. However, the energy capacity of a battery is directly tied to its physical volume [26]. As a result, these designs either depend on external hardware and electrical connections to the implanted devices or require periodic battery replacement. Both approaches are invasive and compromise biocompatibility.

Some other systems are designed based on electromagnetic power transfer, specifically through magnetic induction [27]. This method is commonly employed biomedical devices due to its ability to wirelessly provide energy without the need for implanted batteries. In these systems, energy is transferred between a transmitter coil located outside the body and a receiver coil integrated into the device [28]. This approach offers several bene-

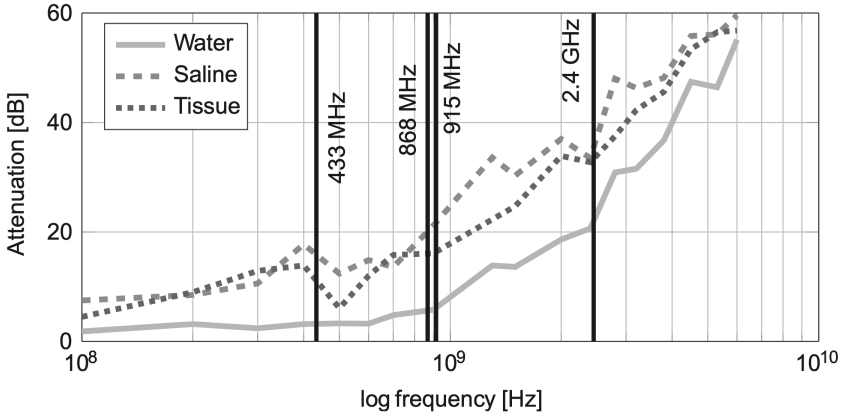

Figure 1.2: Attenuation of electromagnetic waves in pure water, a 0.9% saline solution, and human tissue over the frequency band from 100 MHz to 6 GHz. Figure is adapted from [30].

fits to optogenetic experiments, including continuous power delivery without the need for invasive battery replacements and enabling the operation of optogenetic systems without significantly restricting the mobility of animal models. However, concerns about the biocompatibility of these designs persist, particularly due to the use of conductive coils and Complementary Metal-Oxide-Semiconductor (CMOS) technology. Additionally, the inherent trade-offs in using electromagnetic waves in miniaturized devices present further challenges; Higher frequencies, necessary for smaller devices, lead to increased energy losses in biological tissues (see Figure 1.2) [29], [30]. This creates a fundamental limitation on the degree of miniaturization, as the energy losses must be controlled to prevent overheating and ensure tissue safety.

Ultrasonic wireless power transfer has also been proposed as a means of delivering energy to μLEDs-based optogenetic implants [31]. In these systems, piezoelectric materials convert ultrasonic vibrations into electrical energy. Using ultrasonic waves is particularly

advantageous in biological tissues due to their relatively low absorption rates, especially at frequencies in the 0.1–10 MHz range [32]. Therefore, piezoelectric energy harvesting shows great potential for powering small-scale, implantable optogenetic systems.

However, ultrasonic μLEDs-based optogenetic implants present their own challenges. Reflection losses at the interfaces between the piezoelectric transducer and biological tissues can reduce power transfer efficiency. Moreover, the requirement for precise alignment and focusing of the ultrasonic waves adds complexity to the system design. Additionally, since current designs utilize non-organic piezoelectric materials and LEDs, concerns regarding the biocompatibility of these systems persist.

With the variety of strategies available for light delivery in optogenetics, the field continues to be an area of active research, particularly for in vivo optogenetic applications. Key challenges include the invasiveness of implanting procedures, the biocompatibility of devices for chronic use, and the depth of tissue illumination that can be achieved. Furthermore, maintaining high temporal and spatial precision while ensuring freedom of movement in freely moving animals is a challenge. However, technological constraints often necessitate trade-offs, where addressing one limitation may worsen another. Developing a fully biocompatible, wireless method for deep tissue illumination remains a major engineering challenge, especially in studies of neural activity in freely moving subjects. Successfully overcoming this obstacle could represent a transformative advancement in the field of optogenetics, enhancing our understanding of complex neural dynamics and paving the way for novel therapeutic approaches.

The challenges of delivering or generating light within biological tissues are not limited to optogenetics and are increasingly relevant to advancements in bio-optical communications. Optical techniques hold promise as communication methods within biological systems, particularly for the development of Brain-Machine Interfaces (BMI) [33]. Compared to electrical BMI, bio-optical communication offers minimal invasiveness and higher spatiotemporal resolution. Furthermore, optical methods enable communication with a larger population of neurons simultaneously [33].

Moreover, the development of techniques such as Genetically Encoded Voltage Indicators (GEVIs) has expanded the use of bio-optical communication beyond simple activation-based applications to the monitoring of neural activity [34]. GEVIs enable the observation of electrical activity within neural circuits without requiring direct physical contact [34].

There is also growing evidence that biophotons are generated within brain tissue and other organs [35], [36], [37], [38]. Biophotons are photons naturally emitted by biological cells and studies suggest that neurons may use these photons for various communication and restoration functions [39], [40]. Research on the optical properties of neural tissues, particularly myelinated axons, further reveals that these structures can act as natural optical waveguides [41]. With specific refractive index profiles, myelinated axons can guide photons with minimal signal loss, functioning similarly to engineered optical fibers [42], [43]. This intrinsic optical capability and the presence of biophotons highlights promising potential for bio-optical communication systems that could be integrated with the body's own light-based signaling mechanisms.

These optical characteristics make bio-optical communication an ideal candidate for next-generation bio-communication applications, including BMI as well as applications in nano-networks in chips and bio-chips. In this context, advances in developing wireless, non-invasive and biocompatible optical illumination systems, capable of operating within various biological and bio-engineered environments, represent a significant step forward for bio-optical communications. This development will lay a foundation for innovative applications based on optical communication, enabling functionality within biological tissue as well as within micro- and nano-scale bio-engineered systems.

1.2 State-of-the-Art Techniques for Light Delivery in Optogenetics

In several in vitro experiments involving optogenetic applications, light is externally generated using either lasers or LEDs [44]. Lasers are used for their excellent spatial and temporal resolution which enables precise targeting of specific cells or regions [45]. They also allow for fine-tuning of their spectra to match the activation wavelengths of different opsins. However, lasers are costly and challenging to miniaturize [46], which limits their practicality in certain experimental setups, particularly those requiring portable or implantable solutions.

Alternatively, LEDs offer a more cost-effective and compact option [47]. Despite these advantages, LEDs have some drawbacks. They emit less coherent light compared to lasers

[47], which can result in reduced spatial resolution and less precise targeting. Additionally, the divergent nature of LED light makes it more challenging to be sent through optical fibers and other light-guiding systems when they are used as external light sources [48].

In organ-level studies or in vivo applications, the low penetration of light makes direct illumination ineffective [49]. Two-photon laser excitation is one of the alternatives that has been utilized to improve light penetration into biological tissues [50]. This method is used for deep tissue illumination, based on the principle discussed in section 1.1, where biological tissues exhibit lower scattering and absorption at longer wavelengths [51] (see Figure 1.1).

In two-photon excitation, two photons are absorbed nearly simultaneously for exciting a molecule from its ground state to a higher energy state (Figure 1.3). Unlike one-photon excitation, where a single photon with wavelength λ is absorbed, two-photon excitation requires absorption of two photons (λ_1 and λ_2), each providing a fraction of the the energy of a single-photon equivalent ($\lambda_1 + \lambda_2 = 2\lambda$) [52]. Because these two photons have longer wavelengths, they experience lower scattering and absorption coefficients in biological tissue, allowing them to penetrate deeper. However, as the absorption should happen almost simultaneously, the excitation likelihood in two-photon excitation is significantly lower than in one-photon excitation and depends on the square of the light intensity due to its nonlinear nature [52]. Two-photon excitation requires considerably higher light intensities than one-photon excitation, a characteristic that might suggest it is unsuitable for tissue illumination due to the risk of potential tissue damage. While this limitation has been mitigated by using extremely high-powered pulses of very short duration [53]

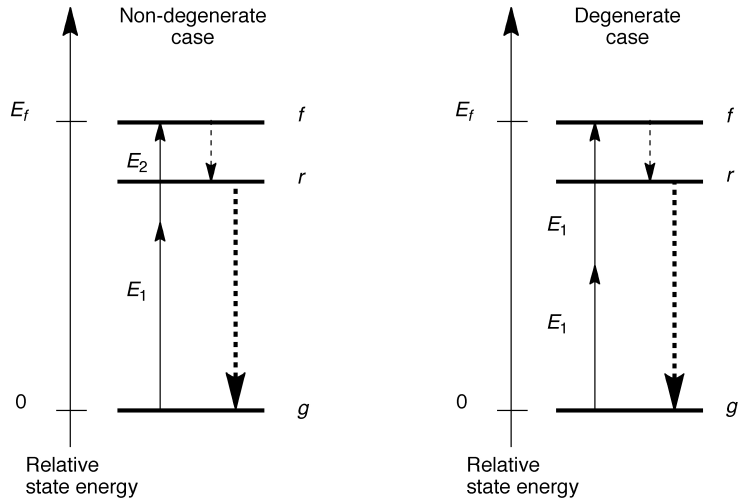

Figure 1.3: A schematic energy level diagram shows the excitation of a molecule from the ground state, g, to an excited state, f, located at energy E_f above the g state by the absorption of two photons (vertical solid arrows). The photons can have the same energy, E_1 (degenerate case, $E_f = 2E_1$), or different energies, E_1 and E_2 (nondegenerate case, $E_f = E_1 + E_2$). After excitation, the system quickly relaxes to state r, the lowest vibronic level of the lowest-energy excited state, by internal conversion or vibrational relaxation (dashed arrow). The system finally returns to the ground state by radiative or nonradiative pathways (bold dashed arrow). Figure is adapted from [53].

and two photon excitation can provide higher illumination depth in biological tissue, it requires complex and costly optical technology. Additionally, challenges related to the need for external connections and restriction of the movement of the test subject remain unresolved.

Under these circumstances, waveguides or optical fibers have been used as methods for delivering light for in vivo experiments [54], [55]. However, as discussed earlier, two major concerns with this method are the biocompatibility of the implants and the physical constraints imposed by these connections, which restrict the study of freely moving subjects

and limit experimental flexibility.

To address these issues, researchers have focused on developing flexible and biocompatible waveguides as alternatives to traditional silica fibers. Various biodegradable polymer-based optical waveguides have been created in different formats, such as polymer-based fibers [56], bioabsorbable polymer optical waveguides [57], and hydrogels [58]. Specifically, hydrogel waveguides have been engineered using materials like polyethylene glycol [59], agarose [60], and gelatin [61]. These materials can improve biocompatibility of some optogenetic settings. However, the restrictions imposed by physical connections still exist.

These limitations have driven the search for alternative methods that are better suited for in vivo optogenetic applications. One such approach involves the development of miniaturized implantable photonic devices. Various illumination systems have been proposed for optogenetics, based on implantable μLEDs [62], [63], [64], [65], [66]. Although these systems differ in design, they typically share certain features, such as conductive coils that capture electromagnetic energy from the environment to power the LEDs. Despite their potential, there are concerns about the biocompatibility of using conductive coils and CMOS technology within the human body.

Additionally, a significant challenge in miniaturizing these devices is related to the electromagnetic energy harvesting process. Current devices vary in size depending on the design, ranging from $10\,\text{mm} \times 5\,\text{mm} \times 0.2\,\text{mm}$ (Length $\times$ Width $\times$ Thickness) [62], to $5\,\text{mm} \times 5\,\text{mm} \times 4\,\text{mm}$ [64], and $13\,\text{mm} \times 10\,\text{mm} \times 0.8\,\text{mm}$ [63]. However, as discussed earlier, smaller device sizes require higher frequencies to harvest sufficient energy, which

leads to increased temperature in the surrounding tissue [58]. Therefore, even if fabrication challenges are addressed, further miniaturization of these implants remains fundamentally limited by these thermal constraints.

To address the challenges of using electromagnetic waves through biological tissues to generate electrical energy, the use of ultrasonic energy harvesting has been proposed as an alternative [67]. In this approach, ultrasonic energy is converted into optical energy to activate the opsins. A neurostimulation platform based on this concept, known as the Wireless Optogenetics Nanonetworking Devices (WiOptND), has been developed [68]. This system utilizes piezoelectric nanowires and μLEDs to produce light in response to ultrasound waves.

Despite the innovative nature of these devices, their size remains significantly larger than that of individual neurons. This, complicates efforts to stimulate neurons with single-neuron precision or to target specific brain regions accurately. Additionally, there are substantial concerns regarding the biocompatibility of employing CMOS circuits in vivo, which further complicates their application in neurological experiments.

1.3 Research Objectives

Bioluminescence which is the emission of light by living organisms offers a compelling route toward biocompatible illumination in biophotonic systems. While bioluminescent reporters are widely used for sensing and imaging, comparatively fewer studies treat bioluminescence

as a controllable light source that can be externally triggered and engineered for predictable optical output.

A recent study [69] explored aequorin-based bioluminescence as part of a wired optical transceiver concept, motivating the possibility of leveraging calcium-triggered photon emission for bio-optical interfacing. However, the detailed dynamic response of such systems (from stimulation to calcium release to photon emission) has not been quantitatively characterized in a unified model.

Accordingly, this thesis investigates a wireless, ultrasound-powered, aequorin-based bioluminescent illumination mote intended for deep-tissue optogenetic and bio-optical applications. The central objective is to develop and evaluate a system-level modelling framework that links ultrasonic excitation and energy harvesting to calcium dynamics and the resulting bioluminescent output, and to translate this source behaviour into tissue-level illumination metrics.

To achieve this goal, the work is organized around the following objectives and contributions:

- Biocompatible Wireless Stimulation

  The optical transceiver proposed in [69] is designed using nanowires. With the ultimate goal of developing a wireless, biocompatible illumination unit for optogenetic applications, this study aims to integrate a biocompatible wireless stimulation method into the design. The following key questions will be addressed:

1. What biocompatible energy harvesting mechanism is suitable for use in our design?
2. How can this energy harvesting mechanism be modeled, and what are the input-output relationships of the proposed alternative energy harvesting method?
3. Under what stimulation conditions (e.g., pulse duration and acoustic intensity) can the mote harvest sufficient energy to activate the biochemical pathway required for light generation?
4. How can the wireless stimulation stage be integrated within the modelling framework that couples energy harvesting and the bioluminescence reaction?

- Behaviour of The Bioluminescence Unit

  While the concept of an aequorin-based illumination unit was previously proposed in [70], several key aspects remain unexplored. Specifically, the biological mechanisms underlying aequorin-based light emission, along with the detailed optical response of such systems, have not been fully characterized. This research aims to address these gaps by focusing on the following:

  1. What are the characteristics of the generated light in terms of time response and light intensity?
  2. How do changes in the physical properties of the illumination unit (such as the dimensions, size, and composition of internal components) affect the characteristics of the emitted light?

3. How can the proposed aequorin-based illumination system be scaled up or down to suit different biological environments or varying sizes of tissues?
4. How does the choice of aequorin variant influence output magnitude and tunability?

- Light-Tissue Interaction

  For the proposed system to be used in practical applications, such as optogenetics or other bio-optical interfaces, the emitted light must reach its intended target within the biological tissue. Accordingly, this thesis examines light transport from the bioluminescent mote in representative tissue media and addresses the following questions:

  1. What modelling framework is appropriate for describing light propagation in biological tissue at the length scales of interest?
  2. What is the spatial distribution of the emitted light as it propagates through biological tissue?
  3. How does tissue type affect light attenuation and the resulting fluence distribution?
  4. How do the predicted fluence levels at a target location compare with reported activation ranges for light-responsive receivers (e.g., opsins), under representative source–target separations?

5. How does the predicted illumination field differ between a single emitting mote and a multi-mote configuration in terms of delivered fluence and spatial uniformity at the target?

2

Background and Literature Review

In this section, we will explore foundational concepts related to bioluminescence, optogenetics, and the challenges associated with light delivery in optogenetic applications. Additionally, we will discuss piezoelectric biomaterials, which are utilized in the energy harvesting component of the proposed bioluminescence unit.

2.1 Bioluminescence

Bioluminescence, a natural phenomenon in which organisms produce light through chemical reactions, has intrigued scientists for centuries. This unique capacity is found across a wide variety of species, including marine organisms like jellyfish, squid, and anglerfish, as well as terrestrial creatures such as fireflies and even certain fungi and bacteria [71].

The color of light emitted through bioluminescence varies among different organisms, with specific hues linked to environmental adaptation and survival strategies (Figure 2.1). Marine organisms generally emit light in the blue-green spectrum (440-520 nm), while terrestrial organisms like fireflies typically produce yellow-green light (520-590 nm). There are exceptions, such as certain deep-sea species that emit red light [72]. The specific color of bioluminescent light is primarily determined by the chemical structure of the luciferase enzyme and luciferin substrate involved in the light-producing reaction [73].

On land, yellow-green bioluminescence is more common, particularly in organisms like fireflies. This color range is highly visible in the night environment, making it effective for communication, especially during mating rituals where visual signaling is crucial. The emission of yellow-green light by fireflies serves as a key factor in mate selection, enhancing reproductive success [75].

In marine environments, blue and green light is most common because these wavelengths travel further underwater, providing organisms with an evolutionary advantage for long-distance communication and predator evasion [76]. This adaptation helps marine

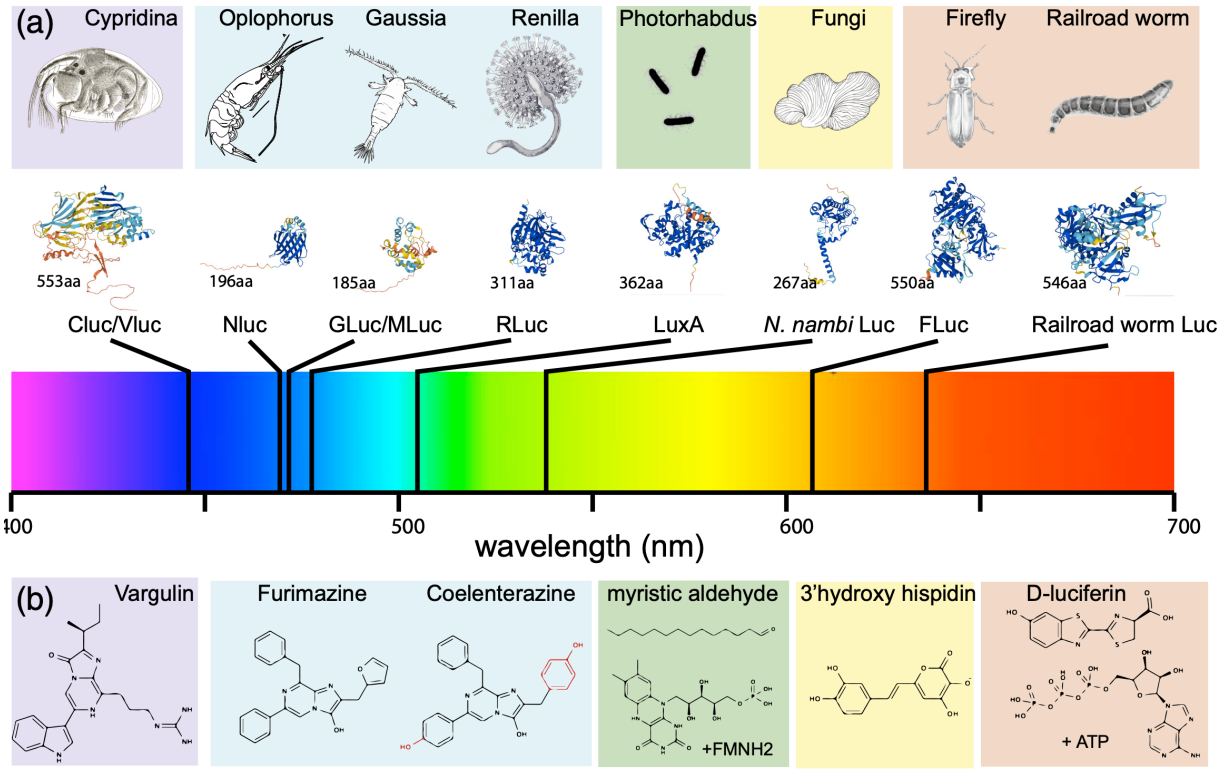

Figure 2.1: Overview of most common luciferases and their cofactors used in neuroscience applications. (a) Diversity of bioluminescent organisms and their luciferases. The shading indicates the class of cofactors and their derivatives employed: purple = vargulin, blue = coelenterazine, green = FMNH2/aldehyde, yellow = hispidine, and orange = D-luciferin. The catalytic subunits of the luciferase have been modeled in AlphaFold2 and are scaled approximately to their relative size. The number of aminoacids is indicated in each structure, and their peak emission wavelength is visualized below as a vertical black line within the visible spectrum. The display is not exhaustive and various chemical modifications exist for CTZs, D-luciferins, and others. Some luciferins require secondary substrates for their activity (FMNH2, reduced Flavin-mononucleotide; Adenosine Triphosphat (ATP), adenosine triphosphate), others require calcium as cofactor (e.g., aequorin, not shown), and most if not all require oxygen for their reaction. (b) Chemical structures of some representative luciferin substrates used by the luciferases mentioned in panel. Figure is adapted from [74].

species effectively signal and interact over greater distances in the dark ocean depths. Conversely, some deep-sea organisms emit red light, allowing them to communicate or detect prey without alerting other marine life, thereby gaining an advantage in the predator-prey dynamic [77].

In addition to roles in communication and camouflage, bioluminescence has been proposed to function as a defensive strategy through the so-called burglar alarm hypothesis. This hypothesis suggests that when a bioluminescent organism is attacked or disturbed by a predator, it emits light to attract higher-level predators, thereby increasing the likelihood that the original predator will be detected or attacked [78]. In this way, light emission indirectly benefits the prey organism by reducing predation pressure. This mechanism has been observed in various marine organisms, including dinoflagellates, which produce bright flashes when mechanically stimulated, potentially exposing grazing predators to their own predators [79]. Although not universally applicable across all bioluminescent species, the burglar alarm hypothesis remains a widely cited explanation for the ecological function of bioluminescence in predator-prey dynamics.

Bioluminescence results from a chemiluminescent reaction in which enzymatic processes generate an excited-state product that emits light as it relaxes to the ground state. In most described systems, light production involves oxidation of a small-molecule substrate, often referred to generically as a *luciferin* (despite substantial structural diversity across taxa) by molecular oxygen in a reaction catalyzed by a luciferase. The specific biochemical requirements vary across organisms; for example, some reactions are ATP-dependent, whereas in photoprotein-based systems the substrate can be pre-bound in a stable protein complex

and emission is triggered by ions such as Ca^{2+} [72], [73].

The bioluminescence reaction can be broken down into the following stages. Initially, luciferin reacts with oxygen to form a High-Energy Intermediate (HEI), typically a peroxide with a weak bond. This intermediate molecule undergoes decomposition, leading to the production of oxyluciferin in an excited state. As the oxyluciferin returns to its ground state, it releases energy by emitting photons. The wavelength of this light corresponds to the energy difference between the excited and ground states of the oxyluciferin. The structure of this molecule dictates the potential range of emitted colors. For example, in firefly bioluminescence, oxyluciferin can exist in different forms, such as the monoanion (C1) and dianion (C2), that emit red (615 nm) and yellow-green (560 nm) light, respectively [73].

The luciferase enzyme can also plays a role in modulating the color of the emitted light. It can influence the active site of the light-emitting molecule and modulate its structure and electronic state at the moment of emission. In other words, the luciferase can modify the emission spectrum through changes in active-site configuration during the reaction. For example, the same synthetic luciferin analogue (adenylate of D-5,5-dimethylluciferin) can emit photons with different wavelenghts depending on the luciferase catalyzing the reaction [73].

In addition to enzyme influences, some organisms modify the color of bioluminescent emission through energy transfer mechanisms. This is especially common among marine species, where the blue light generated by the luciferin-luciferase reaction is transferred

to a nearby fluorescent protein via Förster Resonance Energy Transfer (FRET). In these organisms, the fluorescent protein, such as Green Fluorescent Protein (GFP), absorbs the energy and re-emits it at a longer wavelength, typically as green light. This mechanism accounts for the green bioluminescence observed in jellyfish like Aequorea victoria, even though its photoprotein, aequorin, initially emits blue light [73]. Similarly, certain fish employ red fluorescent proteins to convert blue luminescence into red [72].

The efficiency of bioluminescence is measured by the bioluminescence quantum yield, expressed in terms of Einstein per Mole ($E.mol^{-1}$), which quantifies the number of photons produced per mole of luciferin. In an ideal situation, each luciferin molecule would produce one photon, yielding a quantum efficiency of 1 $E.mol^{-1}$. However, actual yields are typically considerably lower [80].

Bioluminescence has found a wide range of applications beyond its natural occurrence in ecosystems. It is frequently utilized as a tool for monitoring cellular and molecular processes [73]. Inserting genes responsible for bioluminescence into other organisms through genetic engineering can facilitate tracking the expression and activity of other genes within an organism [81]. This technique has been applied in various fields. In cancer research, Bioluminescence Imaging (BLI) offers a non-invasive method to visualize and quantify molecular and cellular processes and has enhanced our understanding of tumor growth, metastasis, and treatment response dynamics [82]. In developmental biology it aids in studying gene expression patterns during organismal development [83]. Furthermore, bioluminescence has practical applications in environmental monitoring. Bioluminescent bacteria, for example, are employed to assess water quality. In this technique, biolumines-

cent organisms emit light under normal conditions, but a decrease in light emission can indicate the presence of toxic substances in the water [84].

Among the luciferase systems currently used for bioluminescence imaging, firefly luciferase- and NanoLuc-based platforms are widely regarded as important benchmarks. Firefly luciferase from *Photinus pyralis*, used with D-luciferin, has long served as a standard reporter for in vivo bioluminescence imaging because of its robust performance and extensive validation in preclinical models [85], [86]. More recently, NanoLuc, an engineered luciferase derived from *Oplophorus gracilirostris*, has become widely used because of its small size, ATP independence, and high photon output; however, its native blue emission is less favorable for deep-tissue imaging due to stronger absorption and scattering in biological tissues [86], [87], [88]. To improve deep-tissue performance, engineered firefly luciferase systems such as Akaluc used with AkaLumine have been developed to produce red-shifted to near-infrared emission and substantially higher sensitivity in deep tissues, including the brain, compared with the conventional D-luciferin/firefly luciferase system [85], [89]. In parallel, NanoLuc-based constructs and substrates have also been optimized for in vivo applications, including brain imaging, for example through red-shifted BRET reporters such as Antares and improved furimazine analogs such as cephalofurimazine [88], [90]. Together, these systems illustrate that the current state of the art in bioluminescence imaging is driven largely by engineering of both luciferases and luciferins to improve brightness, spectral properties, substrate bioavailability, and tissue penetration.

2.1.1 Bioluminescence of Jellyfish

The bioluminescence reaction of jellyfish has some unique properties. At the core of jellyfish bioluminescence is a molecule called Coelenterazine (CLZ), which belongs to the imidazopyrazinone class. When CLZ reacts with oxygen, it forms a peroxide. This reaction is similar to that found in firefly bioluminescence, but with a key distinction: in jellyfish, the resulting peroxide forms a stable complex (or adduct) with the enzyme apoaequorin. This complex molecule is known as aequorin photoprotein.

Aequorin photoprotein contains three EF-hand calcium-binding domains, specifically EF-hands I, III, and IV. Upon the binding of calcium ions to these domains, the molecule undergoes a conformational change that leads to the opening of the imidazolone ring of the CLZ peroxide. This opening leads to the formation of a 1,2-dioxetanone intermediate. This unstable intermediate decomposes, releases carbon dioxide and generates oxyluciferin (named coelenteramide) in an excited state. As the molecule returns to its ground state, energy is emitted in the form of light [91]. This process is depicted in Figure 2.2.

Unlike many other bioluminescence systems that rely on a direct reaction between luciferin and luciferase, the jellyfish mechanism involves a luciferin-protein complex that reacts with calcium ions. As a result, the amount of light emitted is directly proportional to the amount of aequorin present. This represents a significant distinction from luciferin-luciferase systems where light emission depends on the luciferin substrate rather than the enzyme [73].

On this basis, aequorin's bioluminescence is being used as a tool in the study of calcium

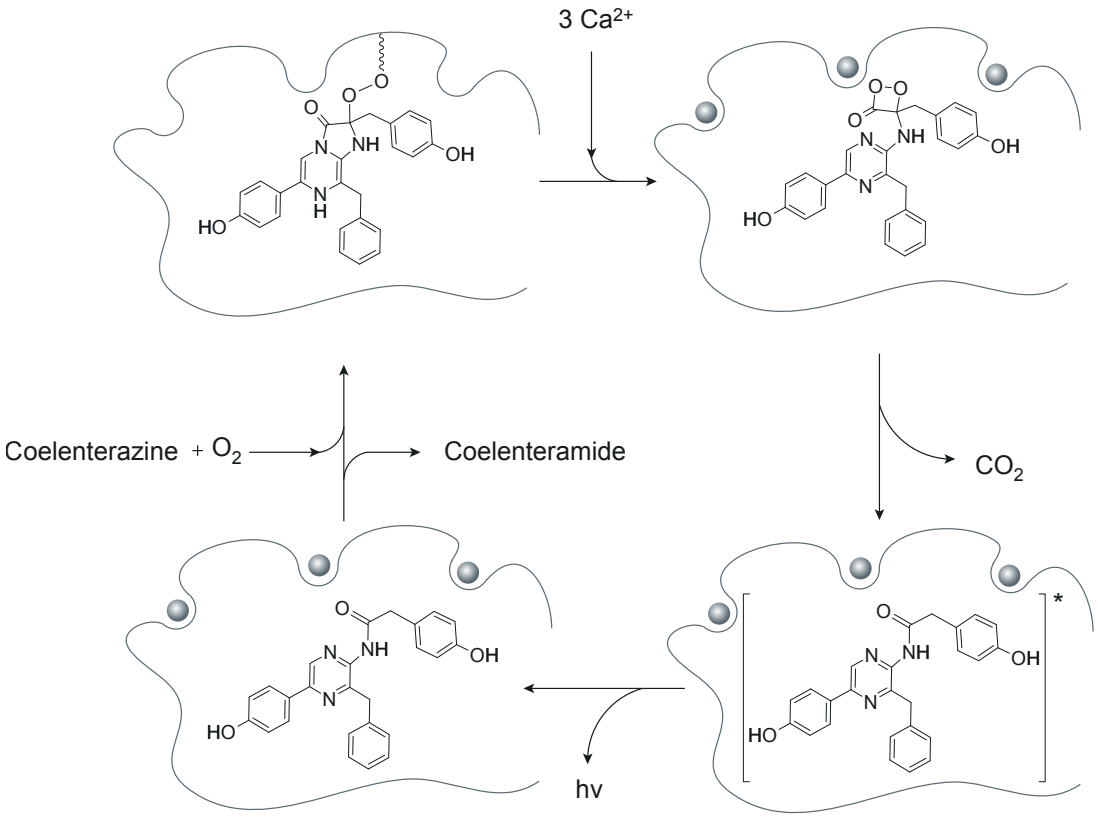

Figure 2.2: Calcium-based bioluminescence of Aequorin. Top left: Coelenterazine (CLZ) is bound within apoaequorin (outlined structure). Top right: Upon binding of calcium ions (gray spheres), the protein undergoes a conformational change that leads to the formation of a high-energy intermediate. Bottom right: This intermediate decomposes, releasing CO_2 and producing coelenteramide in an excited state. Bottom left: As coelenteramide returns to the ground state, a photon is emitted.

signaling within various cellular compartments [92]. By genetically engineering aequorin to target specific intracellular locations, this photoprotein is used to measure calcium concentrations in different regions of the cells. Upon binding calcium ions, aequorin emits light, which is then measured using specialized equipment like luminescence readers. This allows for real-time monitoring of calcium dynamics, providing insights into cellular processes like muscle contraction, neurotransmitter release, and apoptosis. For instance, in mammalian cells, aequorin-based probes have been used to track subcellular calcium fluctuations during signal transduction events [93].

2.1.2 Modifications of aequorin Bioluminescence

Aequorin's bioluminescence reaction as discussed in section 2.1.1 can be modified using various strategies. These modifications generally fall into three categories: mutagenesis of the calcium-binding sites of the apoaequorin protein, the use of CLZ analogs, and the fusion of fluorescent proteins to aequorin.

In apoaequorin mutagenesis, one or more amino acids are substituted to modify the light emission reaction (Figure 2.3). Mutations within or near the EF-hand calcium-binding motifs are introduced to alter calcium-binding affinity [94]. Additionally, Aequorin contains a 600 Å hydrophobic cavity where the CLZ chromophore is stabilized by 21 hydrophobic residues. Substitutions in this CLZ-binding pocket are primarily aimed at spectral tuning, such as shifting the emission wavelength [95]. These modifications enable modulation of the bioluminescence reaction by altering calcium-binding affinity, interdomain interactions

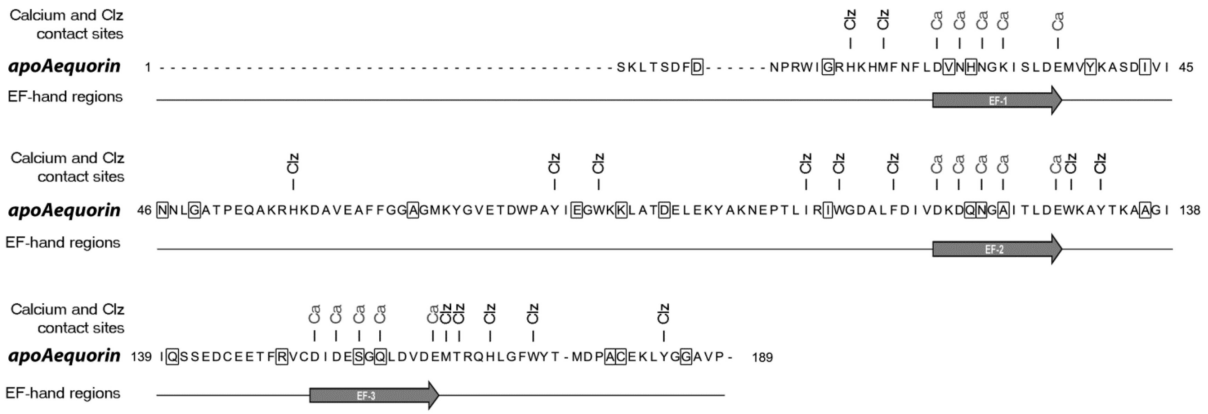

Figure 2.3: Apoaequorin amino acid sequence highlighting the mutated sites screened for enhanced Ca^{2+} sensitivity. The apoaequorin sequence from *Aequorea victoria* (*PDB code: 1EJ3*) is 189 amino acids long. Random, non-conservative substitution was performed on boxed amino acids in order to alter aequorin Ca^{2+} affinity. Amino acids involved in CLZ and Ca^{2+} (Ca) binding are indicated. Figure is adapted from [94].

(particularly between EF-hands II and III), and the coupling between calcium-binding and coelenterazine-binding domains.

While many mutants exhibit negligible changes in calcium sensitivity compared to wild-type aequorin, some others significantly enhance this sensitivity. For example, [94] reports that mutations such as Q159D [1], Q159T, S157D, N121D, A123D, and A179T have been shown to increase the protein's responsiveness to calcium and are often classified as "AequorinXS" variants. Conversely, some mutations, such as Y38S and A69M, result in diminished luminescence output. Building on the enhanced luminescence observed in single mutants, combinations of these mutations have also been investigated. For example,

[1]These mutations are denoted using the standard nomenclature of the original amino acid, residue number, and substituted amino acid (e.g., Q159D indicates the substitution of glutamine with aspartic acid at position 159).

double mutants incorporating Q159D or Q159T with N121D exhibited even greater Ca^{2+} sensitivity and increased light emission rates [94].

In addition to modifying the calcium-binding domains, the bioluminescent properties of aequorin can be tuned by replacing CLZ with structural analogs [95]. The emission profile, particularly the peak wavelength, depends on the electronic structure of CLZ, which drives the bioluminescent reaction. This spectrum is influenced by electron conjugation across its aromatic rings. Within the active site of aequorin, CLZ is stabilized by hydrogen bonds, π–π interactions, and hydrophobic contacts that help fix the orientation of its ring systems [95]. Modifying the CLZ molecule can affect its non-covalent interactions within the binding pocket and influences its conformation and flexibility. When native CLZ is used to reconstitute apoaequorin, the resulting wild-type aequorin emits blue light with a peak wavelength around 470 nm. To modulate the bioluminescent properties, several structural analogs of CLZ have been developed and used. For example:

- CLZ-f is a modified analog of CLZ, in which a fluorine atom replaces a hydroxyl group on the phenol ring. When aequorin is reconstituted with CLZ-f, the bioluminescence reaction exhibits increased calcium sensitivity [96].
- CLZ-hcp is a synthetic analog of CLZ, in which the imidazo-pyrazinone core is chemically modified at the phenolic position. CLZ-hcp is known for increased calcium sensitivity and shifts the emission maximum to 445 nm [97].

A third modification method for aequorin bioluminescence involves fusion of a Fluorescent Protein (FP) to the photoprotein. This approach takes advantage of Bioluminescence

Resonance Energy Transfer (BRET), in which radiationless energy transfer occurs from the excited oxyluciferin intermediate to the FP [98]. The fluorescent protein then emits light at its characteristic wavelength, resulting in a red-shifted emission relative to native aequorin's blue bioluminescence. In addition to spectral tuning, fusion constructs may also enhance protein stability and Ca^{2+} sensitivity.

Several aequorin–FP fusions have been reported:

- Green Fluorescent Protein–*Aequorin* (GA) is a fusion construct with GFP. GA shows increased sensitivity to submicromolar Ca^{2+} concentrations compared to aequorin alone and functions as both a fluorescent marker and a Ca^{2+} sensor, emitting green light via BRET [96].

- tandem-dimer-Tomato–*Aequorin* (tdTA) , also referred to as Redquorin, is a fusion with the red FP tandem-dimer Tomato (tdTomato). This construct shifts emission into the red spectral region [99].

- Citrine–*Aequorin* (CitA) is a fusion with Citrine, a yellow FP, resulting in yellow-shifted bioluminescence [99].

Such modifications allow the bioluminescent properties of aequorin to be engineered for various applications, including enhanced calcium sensitivity and spectral tuning. In practice, these strategies are often used in combination to meet specific requirements. For example, among double mutants incorporating EF-hand domain modifications, QD+AT[2]

[2]Double mutants are typically named by combining the abbreviations of the individual mutations (e.g., QD+AT for Q159D+A179T).

and QT+AD when paired with specific CLZ-f showed high Ca^{2+} sensitivity, with EC_{50}[3] values of 216 nM and 279 nM, respectively, which are significantly lower than the 659 nM observed for the wild type [100].

2.2 Optogenetics

The emergence of optogenetics dates back to the early 2000s, when a published study [101] described how a light-sensitive microbial protein called opsin can be used to control neurons by light. As a combination between optical technologies, genetic targeting and molecular biology, optogenetics holds the potential to revolutionize our understanding of neural circuits[45]. Besides neurology, optogenetics has recently been used in several fields, including cardiology [49], immunology [102], and urology [103]. Recent advancements in genetic engineering for opsin development as well as new optical techniques have offered new possibilities for the use of optogenetics in diagnostic and therapeutic procedures.

For instance, one study [8] introduced an innovative all-optical technique capable of simultaneously manipulating and monitoring multiple neurons. This approach combines two-photon optogenetic activation with calcium imaging, allowing for highly precise targeting and high-resolution tracking of neural activity. Notably, this method enables researchers to investigate the same neuronal populations across different behavioural states and to selectively target neural ensembles based on their specific functions. Also, a research study [104] employed frequency-specific optogenetic Deep Brain Stimulation (DBS)

[3] EC_{50} refers to the concentration of Ca^{2+} required to elicit 50% of the maximal luminescent response.

of the subthalamic nucleus to enhance motor function in Parkinsonian models. The study demonstrated that high-frequency optogenetic stimulation could replicate the therapeutic effects of conventional electrical DBS in alleviating symptoms. This examples underscores the valuable role of optogenetics in both studying and potentially treating neurological disorders.

2.2.1 Opsins

In optogenetics, the ability to optically manipulate neuronal activity relies on the presence of a particular photosensitive ion channel called opsin on the neuron's membrane. Opsins are capable of triggering various cellular responses, such as inducing action potentials, inhibiting neural activity, or modifying intracellular signaling pathways, in millisecond temporal precision [105], [106].

Opsins are broadly classified into two main types: microbial opsins (Type I) and vertebrate opsins (Type II). Type I opsins, which function as ion channels or pumps, are present in various microorganisms, including bacteria and algae. These proteins help the microorganisms navigate their environment by regulating ion concentrations and controlling the movement of cellular appendages [101], [108]. Type II opsins, found in animal cells, typically serve in vision and the regulation of circadian rhythms. They function as G-Protein-Coupled Receptors (GPCR), initiating slower signaling cascades upon light activation [10], [105].

While opsins are naturally present in photoreceptor cells, similar mechanisms can be

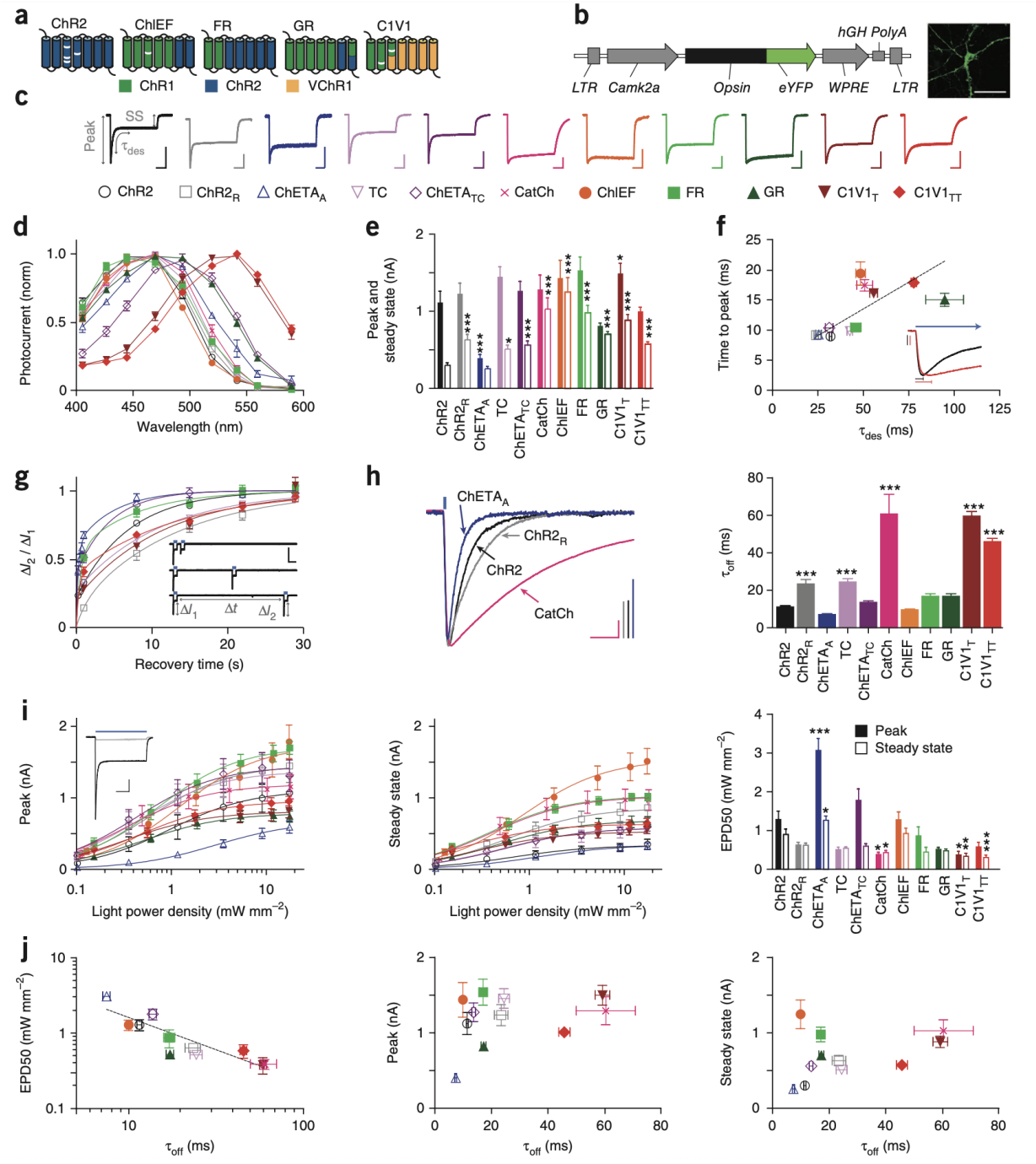

Figure 2.4: Properties of depolarizing optogenetic tools (continues on next page).

(a) Depolarizing tool classes. White bars indicate mutations. (b) Construct design and representative image for *in vitro* characterization. Scale bar, 50 μm. (c) Normalized representative photocurrents. Scale bars, 400 pA, 200 ms. Horizontal scale bar applies to all traces. Color and shape legend applies throughout the figure. (d) Action spectra ($n = 5$–11). (e) Peak (filled bars) and steady-state (hollow bars) photocurrents to 1 s light ($n = 8$–27). (f) Time to peak ($n = 8$–27) versus τ_{des} ($n = 8$–50). Traces show normalized representative ChR2 (black) and C1V1$_{\text{TT}}$ (red) onset photocurrents. Vertical scale bars represent 200 pA, bars indicate time to peak, and blue arrow indicates ongoing light pulse. (g) Recovery from desensitization ($n = 5$–20). Vertical and horizontal scale bars represent 1 nA and 2 s. (h) Normalized representative traces and summary plots of τ_{off} ($n = 8$–53). Scale bars, 200 pA and 25 ms. (i) Peak and steady-state photocurrents across light intensities. Inset, representative ChR2 photocurrents at low (light gray) versus high (dark gray) light intensity. Scale bars, 250 pA and 250 ms. EPD50 for peak (filled bars) and steady state (hollow bars) ($n = 5$–15). (j) τ_{off} versus EPD50 and peak and steady-state photocurrents. All population data are plotted as mean ± s.e.m. $^{*}P < 0.05$, $^{**}P < 0.01$ and $^{***}P < 0.001$. Unless otherwise indicated, C1V1$_{\text{T}}$ and C1V1$_{\text{TT}}$ were activated with 560-nm light, and all other tools were activated with 470-nm light at ∼5 mW mm^{-2}. Figure is adapted from [107].

utilized in other neurons that have been genetically modified to express opsins. This capacity to manipulate ion flow in response to light is a fundamental aspect of the field of optogenetics [49]. Numerous practical factors must be considered when designing an optogenetic experiment. For instance, choosing the appropriate type of opsin involves understanding the direction of ionic current, the specific ions involved, the tool's temporal precision and kinetics, the magnitude of the evoked photocurrent, and its spectral properties. Figure 2.4 provides an overview of the characteristics of several commonly used depolarizing opsins, demonstrating their functional differences and suitability for various experimental applications.

Commonly used in optogenetics, rhodopsins are a class of Type II opsins. They serve as the opsins of rod cells in the retina and are light-sensitive receptor proteins that trigger

visual phototransduction. Rhodopsins are capable of either depolarizing or hyperpolarizing cell membranes, leading to cellular excitation or inhibition. For example, depolarizing opsins like ChR2 induce depolarization when exposed to blue light, with a peak activation wavelength between 470 and 490 nanometers. By opening non-selective cation channels, these opsins cause a net influx of positive ions, resulting in action potential generation. In contrast, hyperpolarizing opsins such as halorhodopsin induce hyperpolarization when activated by light, primarily responding to green light with a peak activation spectrum of 570–590 nm. These opsins transport ions like protons or chloride ions, leading to membrane hyperpolarization and a subsequent decrease in neuronal activity [49].

Generally, opsins are made up of seven transmembrane helices, which create a pocket that houses a retinal chromophore (Figure 2.5A to C). When light interacts with this chromophore, it undergoes photoisomerization, transitioning from its 11-cis configuration to an all-trans configuration. This transformation induces a conformational change in the opsin protein resulting in the opening of the ion channel and allowing particular ions to pass through (Figure 2.5 D).

2.2.2 Photocycles and Modelling of ChR2

ChR2 is commonly used in optogenetics experiments because it offers a good balance of fast activation, reliable depolarization, and ease of use across various experimental setups. Its well-characterized properties, broad compatibility with different cell types, and fast kinetics make it ideal for precise control of neuronal activity. Although different opsins exhibit

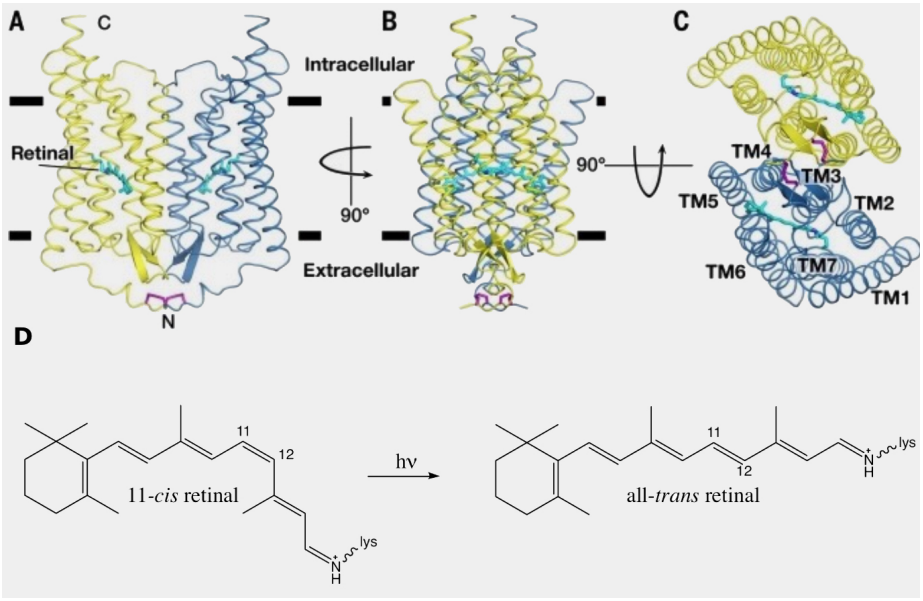

Figure 2.5: (A to C) Overall structure presentation of the ChR2 dimer. (D) 11-*cis* to *all-trans* isomerization in animal rhodopsins. (A to C) are adapted from [109] and (D) is adapted from [110].

varying kinetics, their photocurrents can generally be modeled using similar frameworks. In this section we focus on the modelling of ChR2, outlining the methods and dynamics that govern its photocycle.

There are several approaches for modelling the behaviour of ChR2, ranging from the simpler three-state model [111] to the more detailed four-state [112] and six-state models[113]. The three-state model provides a foundational understanding with two closed states and one open state, though it lacks the granularity needed to capture intermediate transitions. The four-state model, which includes two open and two closed states, offers a more precise representation of ChR2 kinetics, effectively capturing both fast and slow channel dynamics. The six-state model further refines this by incorporating additional intermediate states, providing the most comprehensive kinetic description, although with increased complexity. Here, we provide a brief overview of the four-state model to explore its mechanisms as stated in [112].

This model includes two open states (O_1 and O_2) and two closed states (C_1 and C_2), as shown in Figure 2.6. In this model, states C_1 and O_1 are dark-adapted closed and open states, while states C_2 and O_2 are light-adapted closed and open states. Upon absorbing light, ChR2s move from the closed state C_1 to the open state O_1 at an activation rate α_1. After a short period, some channels shift from the highly conductive O_1 state to the less conductive O_2 state at a rate e_{12}. Transitions from open states to closed states can occur

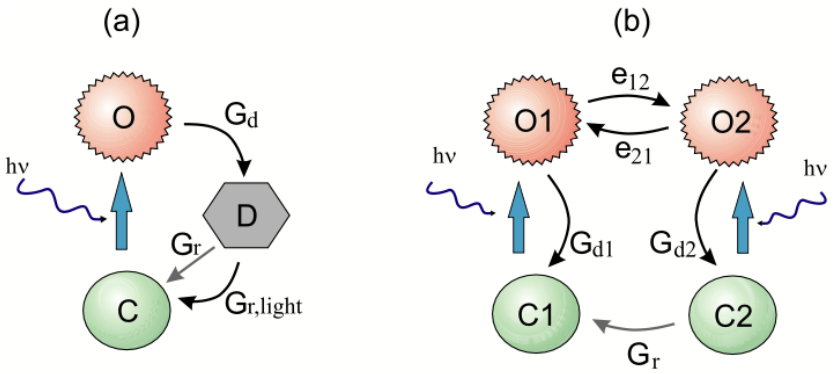

Figure 2.6: Two models of ChR2 photocycle which can qualitatively reproduce the photocurrents in ChR2 transfected neurons. (a) The three-state model: C—closed/ground, O—open and D—closed/desensitized states. (b) Four-state model, with two closed C1 and C2 and two open states O1 and O2. The transition rate constants are described in the text. Figure is adapted from [112].

as follows:

$$O_1 \to C_1 \quad (\text{rate } G_{d1}),$$

$$O_2 \to C_2 \quad (\text{rate } G_{d2}).$$

We define $P_{O_1}(t)$, $P_{O_2}(t)$, $P_{C_1}(t)$, and $P_{C_2}(t)$ as the probabilities of the molecule being in states O_1, O_2, C_1, and C_2, respectively, at time t. Therefore, the state transitions are

described by the following system of differential equations:

$$\frac{dP_{O_1}(t)}{dt} = \alpha_1 P_{C_1}(t) - (G_{d1} + e_{12})P_{O_1}(t) + e_{21}P_{O_2}(t), \tag{2.1}$$

$$\frac{dP_{O_2}(t)}{dt} = \alpha_2 P_{C_2}(t) + e_{12}P_{O_1}(t) - (G_{d2} + e_{21})P_{O_2}(t), \tag{2.2}$$

$$\frac{dP_{C_2}(t)}{dt} = G_{d2}P_{O_2}(t) - (\alpha_2 + G_r)P_{C_2}(t). \tag{2.3}$$

2.2.3 Photocurrent Dynamics in ChR2

The photocurrent observed in ChR2-expressing cells results from ion flow through the two open states, O_1 and O_2. The total current can be expressed as:

$$I(t) = V \times N_{ChR2} \times \left(g_1 P_{O1}(t) + g_2 P_{O1}(t)\right), \tag{2.4}$$

where N_{ChR2} is the total number of ChR2 channels, g_1 and g_2 represent the conductances of the channels in the O_1 and O_2 states respectively, and V is the membrane voltage.

During light stimulation, ChR2 channels transition from C_1 to O_1, causing a rapid rise in current. Over time, as more molecules move to the less conductive O_2 state, the current declines and reaches a steady plateau. This biphasic current response is characterized by an initial peak followed by a sustained lower plateau (Figure 2.7).

Once the light is turned off, the current decays biexponentially as the channels return

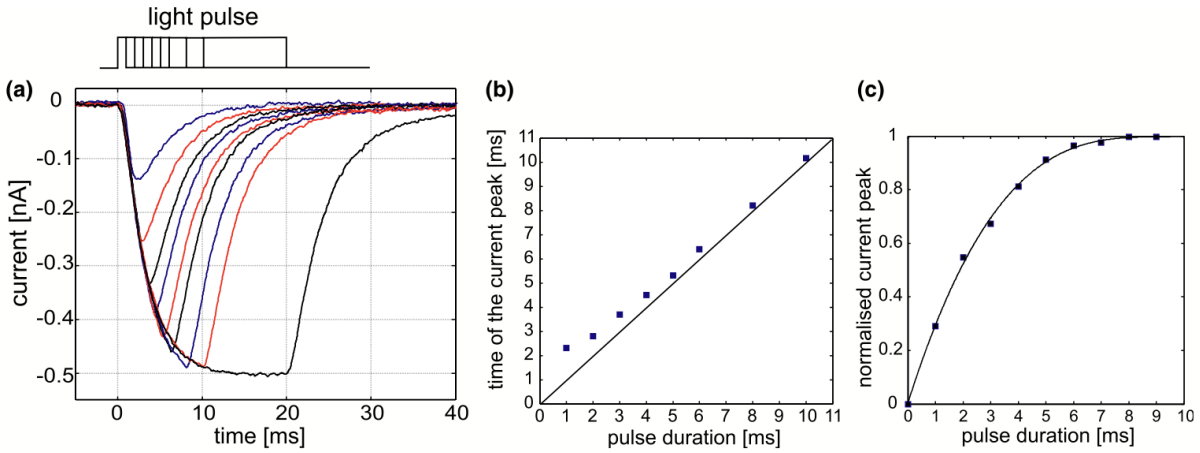

Figure 2.7: (a) Photocurrents in ChR2-expressing hippocampal cells for short light pulses (1, 2, 3, 4, 5, 6, 8, 10 and 20 ms). Light intensity is approximately 1 mW mm^{-2}. (b) Time to peak photocurrent and (c) normalized values for the peak current *vs* photostimulus duration. Figure is adapted from [112].

to the closed states. This decay is modeled by:

$$I_{\text{off}}(t) = A_{\text{fast}} e^{-t/\tau_1} + A_{\text{slow}} e^{-t/\tau_2}, \tag{2.5}$$

where A_{fast} and A_{slow} are the amplitudes of the fast and slow decay components, and τ_1 and τ_2 are their respective time constants.

2.3 Piezoelectricity

Piezoelectricity refers to the coupling between mechanical and electrical quantities within certain materials. It is fundamentally characterized as a linear interaction, where mechan-

ical and electrical responses are directly related. Materials that exhibit this behaviour are classified as piezoelectric materials [114].

The phenomenon exhibits two distinct modes of energy conversion [114]:

1. **Direct Piezoelectric Effect:** Mechanical input is converted into electrical output. When a mechanical load deforms the material, it induces a macroscopic change in electric polarization. This change produces measurable electrical charges or voltages proportional to the applied deformation.

2. **Inverse Piezoelectric Effect:** Electrical input is converted into mechanical output. An applied electric voltage across the electrodes causes the material to deform mechanically.

The underlying physical mechanism of the piezoelectric effect lies in the internal structure of the material. In its original, undeformed state, the material remains electrically neutral, because the center of positive charges (CQ^+) coincides geometrically with the center of negative charges (CQ^-). When a mechanical load is applied, the resulting deformation shifts these charge centers relative to one another. As CQ^+ and CQ^- no longer coincide, a net dipole moment is established, which are characterized by the electric polarization (P). The magnitude of this polarization increases with the geometric separation between the charge centers. This mechanism is commonly referred to as displacement polarization [114].

In the inverse piezoelectric effect, the process is reversed. An applied electric voltage

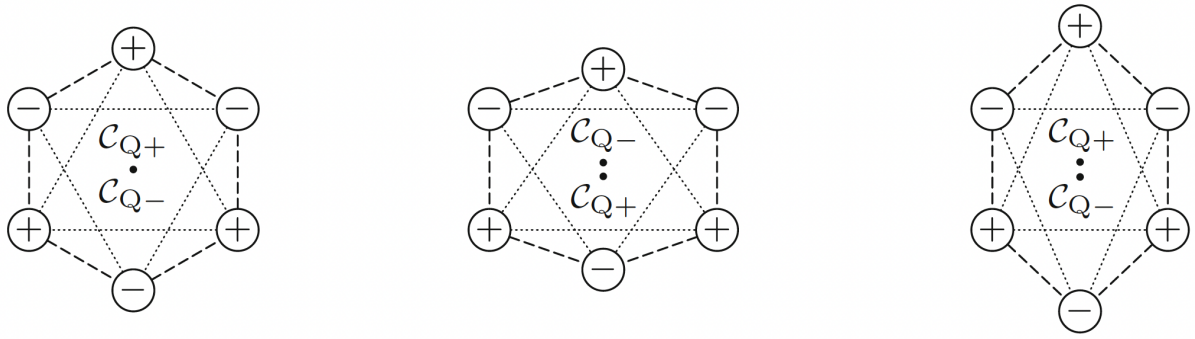

Figure 2.8: Simplified relative positions of the center of positive charges (CQ^+) and the center of negative charges (CQ^-) in a crystal under piezoelectric loading. Left: Original state of the crystal without mechanical loading. Middle: Longitudinal mode. Right: transverse mode of the direct piezoelectric effect under applied mechanical forces. Electric polarization is directed from (CQ^-) to (CQ^+). Figure is adapted from [114]

induces charges on the electrodes, creating an internal electric field. To restore electrostatic equilibrium, the material develops an internal dipole moment. This requires a relative shift between CQ^+ and CQ^-, which in turn leads to a mechanical deformation of the material.

Piezoelectric properties are observed in materials that possess a crystal structure or regions with crystal-like structural order. The occurrence of piezoelectricity depends on the absence of a center of symmetry within the unit cell. Out of the 32 crystallographic point groups, 21 are noncentrosymmetric, and among these, 20 exhibit piezoelectric behaviour. These piezoelectric point groups are distributed across seven crystal systems: triclinic, monoclinic, orthorhombic, tetragonal, rhombohedral, hexagonal, and cubic [115].

2.3.1 Mathematical Formulation of Piezoelectric Materials' Behaviour

The piezoelectric phenomenon can be described using the first law of thermodynamics, which relates changes in internal energy to both external work and thermal energy [116]. In a closed system, this relationship is given by:

$$dU = d\mathcal{W} + dQ = d\mathcal{W}_{\text{electrical}} + d\mathcal{W}_{\text{mechanical}} + dQ, \tag{2.6}$$

where dU denotes changes in internal energy, $d\mathcal{W}$ represents external work done on the system, and dQ indicates changes in thermal energy. To analyze the piezoelectric system, we define state variables such as T_{ij} and S_{ij} (mechanical stress [4] and strain [5]), E_m and D_m (electric field intensity and electrical flux density), and θ and η (temperature and entropy per unit volume, respectively). The change in internal energy can be expressed as:

$$dU = E_m dD_m + T_{ij} dS_{ij} + \theta d\eta, \tag{2.7}$$

where dD_m, dS_{ij}, and $d\eta$ represent changes in the extensive state variables D_m, S_{ij}, and η, respectively. To explore the system under specified intensive variables (E_m, T_{ij}, θ), Gibbs

[4] Mechanical stress (T) is the internal force experienced by a material per unit area due to an applied external force: $T = F/A$ where F is the applied force and A is the cross-sectional area over which the force is applied.

[5] Mechanical strain (S) is the measure of deformation representing the displacement between particles in the material body relative to a reference length: $S = \Delta L/L_0$ where ΔL is the change in length and L_0 is the original length.

free energy G is utilized, defined as:

$$G = U - E_m D_m - T_{ij} S_{ij} - \theta\eta. \tag{2.8}$$

At thermodynamic equilibrium, the Gibbs free energy is minimized, and the derivative dG is zero:

$$dG = -D_m dE_m - S_{ij} dT_{ij} - \eta d\theta = 0. \tag{2.9}$$

The extensive state variables D_m, S_{ij}, and η can be determined by fixing intensive state variables:

$$D_m = -\frac{\partial G}{\partial E_m}\Big|_{T,\theta}, \quad S_{ij} = -\frac{\partial G}{\partial T_{ij}}\Big|_{E,\theta}, \quad \eta = -\frac{\partial G}{\partial \theta}\Big|_{T,E}. \tag{2.10}$$

Assuming isothermal conditions ($d\theta = 0$) and using the Taylor series expansion, higher-order terms are ignored due to their negligible influence, resulting in linearized changes of extensive state variables:

$$dD_m = \frac{\partial D_m}{\partial E_n}\Big|_T dE_n + \frac{\partial D_m}{\partial T_{kl}}\Big|_E dT_{kl}, \tag{2.11}$$

$$dS_{ij} = \frac{\partial S_{ij}}{\partial E_n}\Big|_T dE_n + \frac{\partial S_{ij}}{\partial T_{kl}}\Big|_E dT_{kl}. \tag{2.12}$$

In equation 2.11, the first term on the right side represents the Dielectric Material Law and the second term represents the Direct Piezoelectric Effect. Equation 2.12 demonstrates the Inverse Piezoelectric Effect with the first term in the right-hand side, and Hooke's law with the second term [114].

By renaming the constants and assuming initial conditions of zero for the state variables, the linearized constitutive equations under isothermal conditions are derived:

$$D_m = \varepsilon_{mn}^T E_n + d_{mkl} T_{kl}, \tag{2.13}$$

$$S_{ij} = d_{ijn} E_n + s_{ijkl}^E T_{kl}, \tag{2.14}$$

where ε_{mn}^T is the second-rank tensor for electric permittivity, d_{mkl} and d_{ijn} are third-rank tensors for piezoelectric coefficients, and s_{ijkl}^E is the fourth-rank tensor for elastic compliance. These tensors quantify the interactions between electrical and mechanical states in piezoelectric materials.

The tensor equations 2.13 and 2.14 can be simplified and represented in a matrix form, considering the symmetry properties and the number of independent variables. This approach gives the d-form Voigt notation for the constitutive equations of piezoelectric materials, expressed as:

$$\mathbf{D} = \left[\boldsymbol{\varepsilon}^T\right] \mathbf{E} + [\mathbf{d}]\, \mathbf{T} \tag{2.15}$$

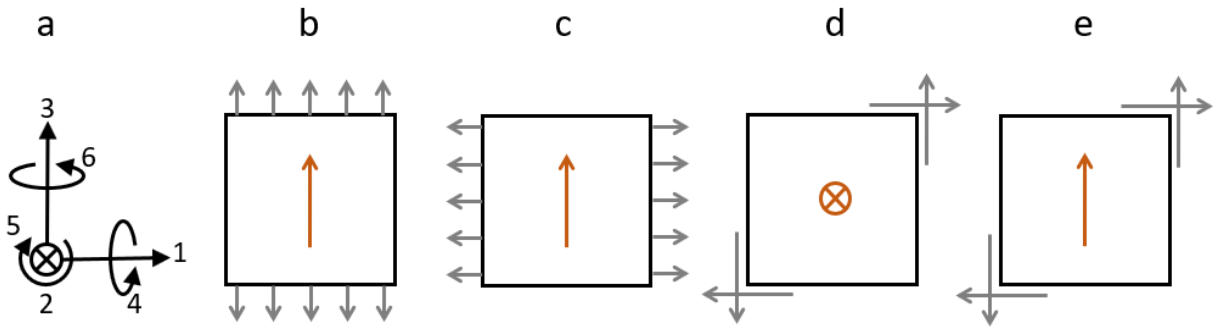

Figure 2.9: (a) demonstration of Cartesian directions and shear directions in piezoelectric material. (b) to (e) different modes of piezoelectricity: Longitudinal (b), Transverse(c), Longitudinal shear (d) and transverse shear (e). The gray arrows show the direction of mechanical strain, and the orange arrows show the direction of electrical polarization. In diagram (d), the cross symbol indicates a direction perpendicular to the page, pointing inward (into the page).

$$\mathbf{S} = [\mathbf{d}]^{\mathsf{T}} \mathbf{E} + \left[\mathbf{s}^{E}\right] \mathbf{T} \tag{2.16}$$

Here, the vector $\mathbf{D} = [D_1, D_2, D_3]^{\mathsf{T}}$ represents the electric flux density, measured in units of Cm^{-2}. The vector $\mathbf{E} = [E_1, E_2, E_3]^{\mathsf{T}}$ stands for the electric field intensity, with units of Vm^{-1}. Both vectors have three components, commonly aligned with the x, y, and z directions of a three-dimensional Cartesian coordinate system (Figure 2.9 a). The mechanical stress vector $\mathbf{T} = [T_1, T_2, T_3, T_4, T_5, T_6]^{\mathsf{T}}$, with units Nm^{-2}, and the mechanical strain vector $\mathbf{S} = [S_1, S_2, S_3, S_4, S_5, S_6]^{\mathsf{T}}$, are characterized by six components. The first three elements of these vectors typically correspond to stress or strain along the x, y, and z axes, while the last three elements represent shear effects in planes perpendicular to these axes.

The matrix $\left[\boldsymbol{\varepsilon}^{T}\right]$ is a 3×3 matrix that defines the material's electric permittivity in

Table 2.1: Piezoelectric tensors for various crystal systems and point groups. Adapted from [117].

Crystal system	**Point groups**	**Piezoelectric tensor**
Cubic	23	$\begin{pmatrix} 0 & 0 & 0 & d_{14} & 0 & 0 \\ 0 & 0 & 0 & 0 & d_{14} & 0 \\ 0 & 0 & 0 & 0 & 0 & d_{14} \end{pmatrix}$
Cubic	$\overline{4}3m$	$\begin{pmatrix} 0 & 0 & 0 & d_{14} & 0 & 0 \\ 0 & 0 & 0 & 0 & d_{14} & 0 \\ 0 & 0 & 0 & 0 & 0 & d_{14} \end{pmatrix}$
Tetragonal	$\overline{4}2m$	$\begin{pmatrix} 0 & 0 & 0 & d_{14} & 0 & 0 \\ 0 & 0 & 0 & 0 & d_{14} & 0 \\ 0 & 0 & 0 & 0 & 0 & d_{36} \end{pmatrix}$
Tetragonal	$\overline{4}$	$\begin{pmatrix} 0 & 0 & 0 & d_{14} & d_{15} & 0 \\ 0 & 0 & 0 & -d_{15} & d_{14} & 0 \\ d_{31} & -d_{31} & 0 & 0 & 0 & d_{36} \end{pmatrix}$
Hexagonal	$\overline{6}m2$	$\begin{pmatrix} 0 & 0 & 0 & 0 & 0 & -d_{22} \\ -d_{22} & d_{22} & 0 & 0 & 0 & 0 \\ 0 & 0 & 0 & 0 & 0 & 0 \end{pmatrix}$
Hexagonal	$\overline{6}$	$\begin{pmatrix} d_{11} & -d_{11} & 0 & 0 & 0 & -d_{22} \\ -d_{22} & d_{22} & 0 & 0 & 0 & -d_{11} \\ 0 & 0 & 0 & 0 & 0 & 0 \end{pmatrix}$

different directions. The element ε_{ij} within this matrix describes how electric permittivity in direction i responds when an electric field is applied in direction j. The superscript T indicates measurements taken under constant mechanical stress conditions. The piezoelectric constant matrix $[\mathbf{d}]$ is 3×6 in size and measured in units of mV^{-1} or CN^{-1}. In this matrix, element d_{ij} links the electric flux density generated in direction i to the mechanical stress applied in direction j. This matrix can describe different piezoelectric effects: longitudinal (Figure 2.9 b), where stress and electric flux are parallel; transverse, where they are perpendicular (Figure 2.9 c); and shear modes, which deal with the response to shear stresses (Figure 2.9 d-e).

The elastic compliance matrix $\left[\mathbf{s}^E\right]$, seen in equation 2.10, is a 6×6 matrix with units of m^2N^{-1}. The superscript E signifies that the compliance values are calculated under a constant electric field. This matrix's structure depends on the material's molecular properties.

These matrices often have specific zero elements and symmetries based on the crystal structure of the material. These symmetries are a key topic in crystallography [115]. for instance, Table 2.1 shows the format of piezoelectric matrix for some crystal systems [6].

[6] A crystal system is a classification scheme in crystallography that categorizes crystalline materials based on the symmetry and dimensions of their unit cells (the smallest repeating units that make up the crystal lattice).

2.4 Light, Matter, and Their Interactions

Understanding the nature of light and how it interacts with biological matter is fundamental to many biophotonics applications, including optogenetics. Biological tissues have optical properties that affect light as it travels through them. Phenomena such as absorption, scattering, reflection, and refraction dictate how light is attenuated, redirected, or modified within tissues. These interactions depend on the molecular and structural makeup of biological materials. Additionally, comprehending the interactions between light and matter is necessary for explaining the physical principles behind biological processes involving the emission of light, such as bioluminescence.

To provide the necessary foundation for this work, this section reviews the basic principles of light and its interactions with biological materials. The discussion begins by outlining the properties of light, including its dual wave-particle representation, and continues with the behaviour of light as it travels through different media. It further explores various mechanisms involved in light-tissue interactions.

2.4.1 Wave-Particle Duality of Light

The nature of light has long been the subject of scientific investigation, with ongoing debates about whether it behaves as a wave or a particle. This apparent paradox has largely been addressed by the concept of wave-particle duality, which proposes that light exhibits both wave-like and particle-like characteristics, depending on how it is observed. This

duality is a foundational principle in modern physics, providing a basis for understanding the interactions between light and matter at both macroscopic and microscopic levels. However, it is important to recognize that the descriptions of light as a wave or as a particle are simplified conceptual models. As Björn points out in [118], "The wave and the particle are both models, incomplete pictures or imaginations of the nature of light. The limitations of our senses and our brain prevent us from getting closer to reality than this, simply because it has not made sense during our evolution to get closer to reality. This limitation does not prevent us from using our models very successfully as long as we use them in a correct way".

2.4.2 Wave Representation of Light

In the wave model, light is represented as an electromagnetic wave consisting of oscillating electric and magnetic fields that propagate through space. These fields are oriented perpendicular to each other and to the direction of propagation, making light a transverse wave. A plane electromagnetic wave traveling in the z-direction can be expressed as:

$$\mathbf{E}(z,t) = E_0 \cos(\omega t - kz)\,\hat{x}, \quad \mathbf{B}(z,t) = B_0 \cos(\omega t - kz)\,\hat{y} \tag{2.17}$$

Here, $\mathbf{E}$ and $\mathbf{B}$ are the electric and magnetic field vectors, respectively; E_0 and B_0 denote their amplitudes; $\omega = 2\pi\nu$ is the angular frequency; $k = 2\pi/\lambda$ is the wave number; and $\hat{x}, \hat{y}$ represent orthogonal polarization directions transverse to the propagation direction $\hat{z}$ [119].

The wave propagates at a phase velocity v, which in a medium characterized by permittivity ε and permeability μ, is given by:

$$v = \frac{1}{\sqrt{\varepsilon\mu}} \tag{2.18}$$

In vacuum, this reduces to the speed of light:

$$c = \frac{1}{\sqrt{\varepsilon_0\mu_0}} = 299{,}792{,}456\,\mathrm{m/s}, \tag{2.19}$$

where $\varepsilon_0 = 8.854\,187\,8128 \times 10^{-12}\,\mathrm{F\,m^{-1}}$ and $\mu_0 = 4\pi \times 10^{-7}\,\mathrm{N\,A^{-2}}$ (SI units). The relationship among the speed of light c, wavelength λ, and frequency ν in vacuum is expressed as:

$$c = \lambda\nu \quad \Rightarrow \quad \lambda = \frac{c}{\nu}, \quad \nu = \frac{c}{\lambda} \tag{2.20}$$

When light enters a medium, its speed and wavelength decrease proportionally due to the medium's refractive index, while the frequency ν remains unchanged [118].

In physical optics, light is further understood as a succession of wavefronts which are surfaces of constant phase. For a point source emitting spherical waves, the wavefronts form concentric spheres centered on the source. Each wavefront corresponds to points of identical phase, typically drawn through the maxima or minima of the sinusoidal electric field. The spatial distance between two adjacent wavefronts defines the wavelength λ [120].

At distances much larger than the wavelength and the source size, spherical wavefronts can be approximated as planar. In such cases, the direction of propagation is represented by rays perpendicular to these phase fronts. This abstraction is known as ray optic or geometrical optics. While it neglects wave properties like phase and interference, it effectively describes light paths at macroscopic scales and large-scale optical effects such as reflection and refraction [120].

Theoretical treatments often begin by assuming light is monochromatic; composed of a single frequency or wavelength. Mathematically, such a wave is described by an infinitely long sinusoid in time. In practice, however, real light sources emit polychromatic radiation, consisting of continuous or discrete distributions of wavelengths. In these cases, the electric field can be expressed as a superposition of many monochromatic components [120].

2.4.3 Particle Representation of Light

While the wave model of light accounts for many propagation-related phenomena, it fails to fully describe certain interactions between light and matter, particularly those involving absorption, emission, and scattering of energy. Describing these processes require a complementary particle representation of light, where light is treated as being composed of discrete quanta called photons [119].

In the quantum view, each photon carries a specific amount of energy that depends only on its frequency ν. This relationship is described by Planck's law:

$$E = h\nu = \frac{hc}{\lambda} \tag{2.21}$$

Here, h is Planck's constant ($h \approx 6.626 \times 10^{-34}\,\mathrm{J{\cdot}s}$), ν is the frequency, λ is the wavelength, and c is the speed of light in vacuum [120]. The energy of electromagnetic radiation is therefore quantized, meaning it can only be absorbed or emitted in integer multiples of $h\nu$. This implies that the smallest possible packet of light energy corresponds to the energy of a single photon.

In practical terms, the total energy E of a light pulse containing N photons having wavelength $\lambda = 1/\nu$ is given by:

$$E = Nh\nu, \tag{2.22}$$

This quantization underpins all light absorption and emission processes in atoms and molecules, where transitions occur between discrete energy levels. Crucially, these interactions are binary: a photon must deliver exactly the energy $h\nu$ needed to promote an electron to a higher energy level. If the photon energy does not match the transition energy, it is not absorbed [120].

Photons also posses momentum, despite having no rest mass. The momentum p of a photon is derived from its wave properties and is given by:

$$p = \frac{h}{\lambda} = \frac{h\nu}{c} \tag{2.23}$$

This momentum is significant in phenomena involving changes in light direction, such as scattering or refraction, resulting in corresponding momentum changes [120].

Although a photon's energy is directly tied to its frequency, it is fundamentally impossible to determine the exact frequency, wavelength, or energy of a single photon with absolute precision. This indeterminacy reflects the probabilistic nature of quantum systems and places fundamental limits on the characterization of a single photon's wave-like attributes [118].

2.4.4 Introduction to the Nature of Matter

The modern understanding of matter is rooted in a set of revolutionary discoveries from the early 20^{th} century, which fundamentally altered classical conceptions of the atomic and subatomic world. Matter, once believed to be indivisible at the atomic scale, is now recognized as a quantum mechanical system with both particle-like and wave-like properties. These dual characteristics form the basis of quantum theory and are essential for describing phenomena that cannot be accounted for by classical physics alone [119].

The particle nature of matter is described by classical Newtonian mechanics, where particles exhibit properties such as mass, velocity, momentum, and kinetic energy. The momentum is given by $p = mv$, and the kinetic energy is:

$$E_k = \frac{1}{2}mv^2 \tag{2.24}$$

At the subatomic level, particles such as electrons exhibit wave-like behaviour, as described by the de Broglie hypothesis [121]:

$$\lambda = \frac{h}{mu} \tag{2.25}$$

Here, λ is the wavelength, h is Planck's constant, and mu is the momentum of the particle. The wave nature of matter introduces constraints that are absent in classical mechanics. The internal energy of atoms is quantized and arises from the discrete energy levels available to electrons bound by the electrostatic attraction to the nucleus. These energy levels are solutions to the time-independent Schrödinger equation, which defines the allowed states an electron can occupy around a nucleus. Each solution is associated with a wave function, known as an orbital, representing the spatial distribution and probability of finding an electron in a given region [119].

Each orbital is characterized by a set of quantum numbers: the principal quantum number n, which denotes the energy level; the angular momentum quantum number l, which determines the shape of the orbital; the magnetic quantum number m_l, which describes the orientation of the orbital in space; and the spin quantum number m_s, which reflects the intrinsic spin state of the electron. Together, these quantum numbers define the permissible electronic configurations of atoms [119].

For multi-electron atoms, the solutions become more complex due to electron-electron repulsion. Orbital filling follows three fundamental principles: the Aufbau principle, where electrons occupy orbitals starting from the lowest energy levels; the Pauli exclusion princi-

ple, which allows a maximum of two electrons per orbital with opposite spins; and Hund's rule, which states that degenerate orbitals are singly occupied before any pairing occurs [119].

In molecules, the situation becomes more complex due to the presence of multiple nuclei. The total molecular wave function depends on both electronic and nuclear coordinates. The Born–Oppenheimer approximation simplifies the problem by decoupling electronic and nuclear motions, allowing the electronic Schrödinger equation to be solved at fixed nuclear positions. This leads to quantized electronic states and associated Molecular Orbitals (MOs) [119]. MOs arise from the Linear Combination of Atomic Orbitals (LCAO), yielding bonding and antibonding orbitals depending on whether the overlap of wave functions is constructive or destructive. These orbitals are filled based on the same principles as atomic orbitals, and their configuration determines the electronic properties of the molecule [119].

Beyond electronic transitions, molecules also exhibit vibrational degrees of freedom, corresponding to the oscillatory motion of nuclei about their equilibrium positions. These vibrations are quantized, with energy levels described by:

$$E_v = \left(v + \frac{1}{2}\right) h\nu \tag{2.26}$$

Here, v is the vibrational quantum number, h is Planck's constant, and ν is the vibrational frequency. The non-zero energy of the $v = 0$ state reflects the quantum mechanical nature of molecular vibrations. Unlike the classical oscillator, a quantum harmonic oscillator cannot possess zero energy, because confinement of the nuclei near the equilibrium

geometry necessarily implies a finite uncertainty in momentum. Consequently, the ground vibrational state has a minimum energy of $\frac{1}{2}h\nu$, referred to as the zero-point energy. The vibrational frequency is inversely proportional to the reduced mass of the nuclei and directly proportional to the square root of the bond's force constant (bond strength) [119].

In polyatomic molecules, the number of possible vibrational modes depends on molecular geometry and is given by $3N-5$ for linear molecules and $3N-6$ for nonlinear molecules, where N is the number of atoms [119].

Moreover, molecules can undergo rotational transitions, which result from quantized changes in their angular momentum as they rotate about their center of mass. In diatomic molecules, only one axis of rotation contributes, while in polyatomic molecules, up to three mutually perpendicular axes may be active. These rotational levels are also quantized and depend on the moment of inertia and the symmetry properties of the molecule.

In addition to vibrational and rotational states, molecules, especially biomolecules, can adopt various conformational states, such as folded, twisted, or extended geometries. These conformers possess distinct potential energies and can dynamically interconvert.

2.4.5 Interaction of Light and Biological Matter

The interaction between light and matter is governed by fundamental quantum mechanical and electromagnetic principles. As previously discussed, both light and matter exhibit dual wave–particle properties; thus, their interaction inherently involves exchanges of energy and momentum mediated by electromagnetic fields.

As previously described, light propagates as electromagnetic waves consisting of oscillating electric and magnetic fields, and is quantized into discrete energy packets called photons. Each photon carries energy proportional to its frequency. Biological molecules such as proteins, nucleic acids, and chromophores exhibit quantized energy states derived from electronic, vibrational, rotational, and conformational transitions.

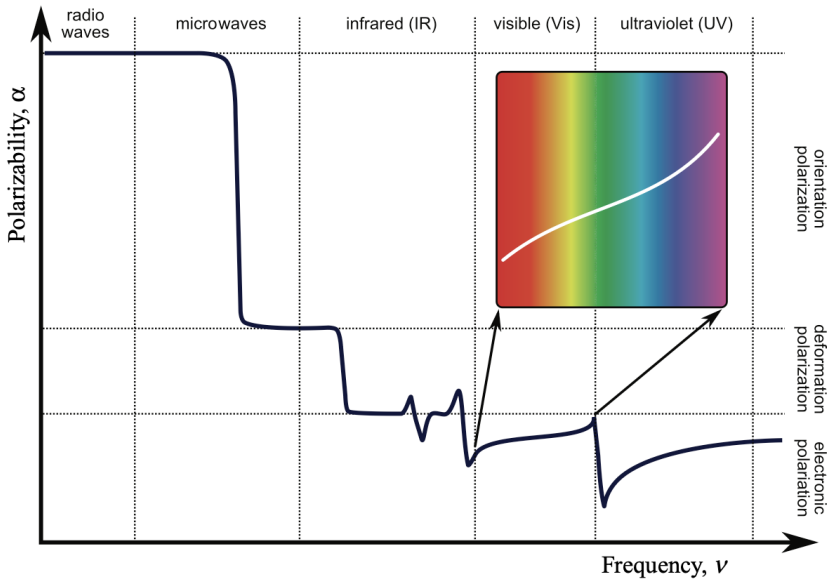

Figure 2.10: Changes of the polarizability α with frequency. Figure is adapted from [122].

The interaction between electromagnetic radiation and biological matter primarily occurs through electric dipole interactions. A permanent dipole arises from an intrinsic charge separation within a molecule, with dipole moment $\boldsymbol{\mu} = q\mathbf{r}$, where q is the magnitude of the charge and $\mathbf{r}$ is the separation vector.

In the presence of an external electric field, the molecular electron cloud can be dis-

torted, producing an additional *induced* dipole moment $\boldsymbol{\mu}_{\text{ind}}$; thus the total dipole moment can be written as $\boldsymbol{\mu}_{\text{tot}} = \boldsymbol{\mu}_0 + \boldsymbol{\mu}_{\text{ind}}$. For sufficiently weak fields (linear response),

$$\boldsymbol{\mu}_{\text{ind}} = \boldsymbol{\alpha} \cdot \mathbf{E}, \tag{2.27}$$

where $\boldsymbol{\alpha}$ is the polarizability tensor and $\mathbf{E}$ is the incident electric field.

The frequency-dependent polarizability of molecules determines their response to electromagnetic radiation across various spectral regions (Figure 2.10). Orientation polarization (dipole reorientation) dominates at microwave frequencies (around 10^{10} Hz), deformation polarization at infrared frequencies (around 10^{13} Hz), and electronic polarization at ultraviolet and higher frequencies (above 10^{15} Hz).[7]

The nature of interactions between photons and biological molecules depends on photon energy relative to the quantized energy states of the target molecules. These interactions induce photophysical and photochemical processes, each with specific energy transitions and characteristic timescales (Figure 2.11). The principal outcomes include:

- **Absorption:** Photons with energies matching molecular energy gaps are absorbed, exciting molecules to higher electronic, vibrational, or rotational states. This process typically occurs on femtosecond (10^{-15} s) timescales.

[7]Here, *orientation polarization* refers to the partial alignment (reorientation) of *permanent* molecular dipoles with an applied field; *deformation* (or ionic/vibrational) polarization refers to field-driven relative displacement of bound charges/nuclei within molecules, often associated with vibrational modes; and *electronic polarization* refers to distortion of the electron cloud relative to the nuclei.

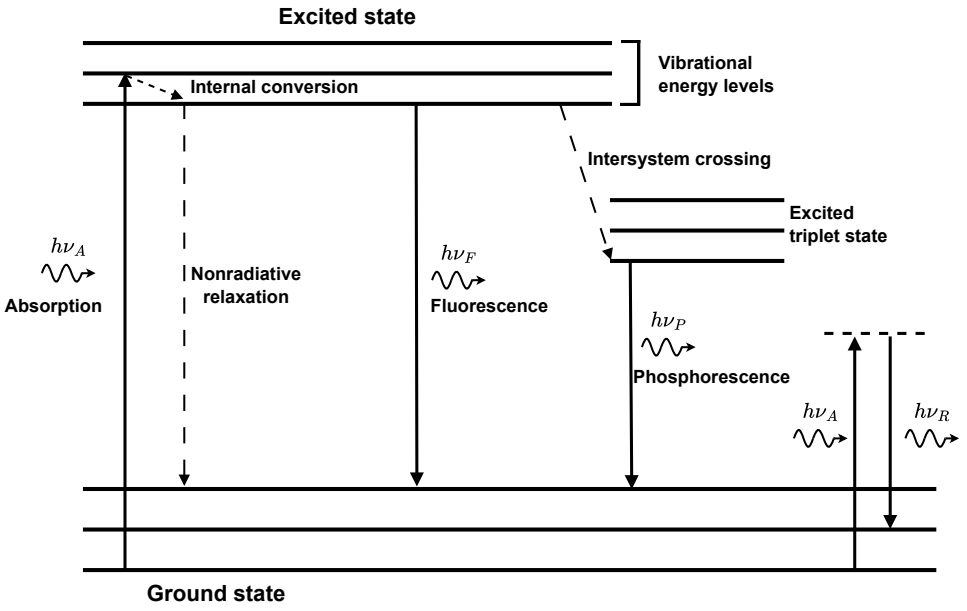

Figure 2.11: Jablonski energy diagram showing excitation and various possible relaxation mechanisms. Each $h\nu$ denotes the photon energy, where subscripts A, F, P, and R denote absorption, fluorescence, phosphorescence, and Raman scattering, respectively.

- **Spontaneous Emission:** Excited molecules emit photons as they return to lower energy states.
  - *Fluorescence:* Occurs on nanosecond (10^{-9} s) timescales.
  - *Phosphorescence:* Involves intersystem crossing to a triplet state and may occur over milliseconds or longer.
- **Stimulated Emission:** In stimulated emission, an incident photon that is resonant with an allowed molecular transition, induces an excited molecule to emit a second photon into the same optical mode. The emitted photon has energy

$$E = h\nu = \Delta E, \tag{2.28}$$

  where ΔE is the energy gap between the upper and lower molecular states.
- **Scattering:**
  - *Elastic (Mie and Rayleigh) Scattering:* Photon direction changes without energy loss; occurs nearly instantaneously.
  - *Inelastic (Raman) Scattering:* Photons exchange energy with molecular vibrational states, resulting in shifted frequencies. Raman scattering occurs on femtosecond timescales.
- **Energy Transfer:** Non-radiative transfer of excitation energy to nearby molecules.
  - *FRET:* Distance- and orientation-dependent transfer within nanoseconds.

  - *Dexter Energy Transfer:* Involves electron exchange; relevant over very short distances.

- **Photochemical Reactions:** Photon-induced chemical transformations, such as bond cleavage, isomerization, or redox reactions, relevant to biological processes like photosynthesis and DNA photodamage. These reactions can span femtoseconds to milliseconds depending on the mechanism.

The following sections will examine some of the aforementioned processes in greater detail, with particular emphasis on their origin in biological matter.

2.4.6 Physical Basis of Absorption

At the molecular level, absorption is mediated by the interaction between the electric field of the incident light and the molecule's electric dipole moment. Upon photon absorption, the electronic distribution within the molecule shifts, often resulting in a relative displacement of negative charge. This redistribution leads to a change in the dipole moment between the ground and excited electronic states, which is described by the transition dipole moment $\mathbf{M}$. The transition dipole moment is defined as the vector difference between the dipole moments of the excited ($\mathbf{D}_E$) and ground ($\mathbf{D}_G$) states [118]:

$$\mathbf{M} = \mathbf{D}_E - \mathbf{D}_G. \tag{2.29}$$

The magnitude of **M** can be inferred from experimental absorption spectra. The oscillator strength, which is the square of the transition dipole moment, can be estimated by integrating the molar absorption coefficient $\varepsilon(\nu)$ over the frequency ν of the absorption band. This is expressed as [118]:

$$|\mathbf{M}|^2 \approx 1.0222 \times 10^{-62}\, n \int [\varepsilon(\nu)/\nu]\, d\nu \quad \mathrm{C}^2\mathrm{m}^2, \tag{2.30}$$

where n is the refractive index of the surrounding medium.

The probability of photon absorption is proportional to the square of the magnitude of the transition dipole moment and the cosine squared of the angle α between **M** and the electric field vector **E**:

$$\text{Probability of absorption} \propto |\mathbf{M}|^2 \cos^2 \alpha \tag{2.31}$$

This angular dependence forms the basis of linear dichroism, a phenomenon in which the orientation of biomolecules relative to the polarization direction of incident light significantly influences absorption. This effect is particularly pronounced in anisotropic environments such as living cells [118].

In bulk biological materials, absorption is quantified by the absorption coefficient μ_a, which defines the probability per unit path length that a photon will be absorbed. In tissues, $\mu_a \approx 0.1\,\mathrm{cm}^{-1}$ is a typical value but varies with tissue composition [120]. The reciprocal of μ_α is referred to as the mean absorption length, representing the average

distance light travels in the medium before being absorbed

The Beer–Lambert law describes how irradiance from a collimated, monochromatic light decays exponentially as light penetrates an absorbing (non-scattering) medium:

$$\frac{dI(x)}{dx} = -\mu_a I(x) \quad \Rightarrow \quad I(x) = I_0 e^{-\mu_a x}, \tag{2.32}$$

where x is an axis parallel to the direction of the light propagation, $I(x)$ is irradiance, and I_0 is the irradiance at $x = 0$. The transmittance is defined as:

$$T(x) = \frac{I(x)}{I_0} = e^{-\mu_a x}, \tag{2.33}$$

representing the probability that a photon travels distance x without being absorbed.

In biological tissues, absorption primarily arises from specific chromophores, including Hemoglobin, Melanin, Water, Flavins, porphyrins, and other pigments. Each chromophore exhibits a unique, wavelength-dependent absorption spectrum.

2.4.7 Scattering of Light in Biological Matter

Scattering is the process by which the trajectory of light is redirected due to its interaction with particles or inhomogeneities in a medium. In biological tissues, such interactions occur when light encounters cellular and subcellular structures, including membranes, organelles, and macromolecular assemblies. The physics of scattering is governed by the

relative size of scattering centers compared to the incident wavelength, and by the refractive index mismatch between the scatterers and the surrounding medium [118]. Three principal theoretical frameworks can be used to describe light scattering:

- **Mie theory:** Mie theory describes the scattering of a plane monochromatic wave by a spherical particle of arbitrary size. It is derived from Maxwell's equations and assumes that the particle is composed of a homogeneous and isotropic material. In biomedical optics, Mie theory is widely used to model light scattering in tissues. Typically, treating the incident light as a plane wave is a valid approximation when the wavefront is much broader than both the wavelength and particle diameter. The theory enables calculation of scattering efficiency Q_s (see Equation 2.35) and the anisotropy factor g (see Equation 2.39). A distinguishing characteristic of Mie scattering is its lack of strong wavelength dependence. Although different wavelengths are scattered and refracted differently, the effects tend to cancel out, leading to wavelength-independent behaviour. Mie theory applies to all particle sizes and reduces to Rayleigh theory in the limit where the particle is much smaller than the wavelength [118], [123].

- **Rayleigh scattering:** A limiting case of Mie theory for particles much smaller than the wavelength ($r \ll \lambda$), with scattering intensity scaling as λ^{-4} [122]. Rayleigh scattering results from interactions of light with small particles such as molecules or atoms. There are no interfaces where traditional reflection or refraction occur, but the oscillating electric field of the light can induce dipole moments in the scatterers.

Most substances exhibit strong Rayleigh scattering in the ultraviolet region because their absorption bands often lie in that range. This results in strong wavelength dependence, with scattering intensity increasing sharply for shorter wavelengths. For instance, blue light is scattered more than red light, explaining the color of the sky. Unlike Mie scattering, Rayleigh scattering does not change the direction of the electric field of the incident light [118].

- **Raman scattering:** Unlike Mie and Rayleigh scattering, which conserve photon energy (elastic light scattering), Raman scattering involves an energy exchange between the photon and the scattering particle (inelastic light scattering). In Raman scattering, either the photon gives up part of its energy (Stokes scattering) or gains energy from the molecule (anti-Stokes scattering), corresponding to vibrational transitions in the molecular structure. The resulting frequency shift in the scattered photon encodes molecular vibrational information, making Raman scattering a powerful technique for biochemical analysis. Although generally weak and not significant for most photobiological phenomena, Raman scattering is extremely useful in spectroscopic studies [118].

In biological media, light typically undergoes multiple scattering events. The spatial arrangement of scatterers determines the applicable regime [120]:

- **Multiple scattering:** Occurs in densely packed tissues where scatterers are closely spaced. Scattering events are coupled, meaning that one event affects the subsequent

ones, and more complex radiative transport models are required. In this case, single-scattering theory does not apply.

- **Single scattering:** Applies when scatterers are sparsely distributed, such that the mean distance between them is much greater than both their physical size and the wavelength of light. Scattering events can then be considered independent, and single-scattering theory is valid.

It is important to distinguish between a single coupled-scattering event involving multiple particles and successive independent-scattering events, each involving only one particle [120]. For loosely packed scattering media, the scattering coefficient μ_s is defined as the probability per unit length that a photon is scattered in a medium. In biological tissue, it has a representative value of $\mu_s \approx 100\,\mathrm{cm}^{-1}$ [120]. The reciprocal of this corresponds to a mean free path of approximately $0.01\,\mathrm{cm}$ (or $100\,\mu\mathrm{m}$), which is the average distance a photon travels before being scattered.

For a medium containing many scatterers distributed randomly in space, the scattering coefficient is given by:

$$\mu_s = N_s \sigma_s, \tag{2.34}$$

where N_s is the number density of scatterers and σ_s is the scattering cross section [123]. The scattering cross section is related to the geometric cross-sectional area σ_g by

$$\sigma_s = Q_s \sigma_g, \tag{2.35}$$

where Q_s is the scattering efficiency [123]. The probability that a photon does not scatter after traveling a distance x, also known as the ballistic transmittance $T(x)$, is described by the Beer–Lambert law [123]:

$$T(x) = e^{-\mu_s x}. \tag{2.36}$$

The combined effects of scattering and absorption in tissue are described by the extinction (or total interaction) coefficient μ_t:

$$\mu_t = \mu_a + \mu_s, \tag{2.37}$$

and the reciprocal of μ_t represents the mean free path between any two interaction events, regardless of whether the event is absorption or scattering [123]:

$$l_t = \frac{1}{\mu_t}. \tag{2.38}$$

Moreover, biological tissues tend to scatter light in a strongly forward-directed manner. Each scattering event typically causes only a small deflection from the photon's original path. To account for this behaviour, the reduced (or transport) scattering coefficient, μ_s', is introduced and defined as [124]:

$$\mu_s' = \mu_s(1 - g), \tag{2.39}$$

where $g = \langle \cos\theta \rangle$ is the anisotropy factor, representing the average cosine of the scattering angle θ. In soft biological tissues, g is often close to 0.9 [124], indicating strong forward scattering. The reduced scattering coefficient adjusts for this anisotropy and gives a more useful measure of how much the scattering actually changes the direction of photon travel.

When absorption is included alongside reduced scattering, the reduced (or transport) interaction coefficient μ_t' is used:

$$\mu_t' = \mu_a + \mu_s', \tag{2.40}$$

where μ_a is the absorption coefficient. This quantity represents the overall attenuation of directional light due to both absorption and the cumulative angular redistribution from scattering. Reduced (or transport) mean free path l_t' is defined as reciprocal of reduced interaction coefficient:

$$l_t' = \frac{1}{\mu_t'}. \tag{2.41}$$

These reduced coefficients are especially useful when working with diffusion-based models (see subsection 2.4.11) or in cases where the goal is to describe the spatial spread of energy fluence, rather than the directional radiance (see subsection 2.4.9 for the definitions).

2.4.8 Quantification of Light

A common but misleading simplification in both scientific communication and experimental practice is the treatment of light intensity as a scalar quantity. As discussed in subsection 2.4.4, the quantification of light is inherently multidimensional, involving a range of parameters that collectively represent its complex physical nature. This complexity is particularly significant in fields such as biophotonics, where light interacts with anisotropic, heterogeneous, and dynamic systems. In such contexts, careful consideration of these multidimensional aspects is essential for accurate light quantification.

The first misconception arises from the colloquial use of the term intensity. In precise radiometric terms, intensity may refer to distinct quantities such as irradiance, radiant intensity, or radiance, each defined under specific geometric and contextual conditions [122]. Accordingly, no single scalar value can adequately represent the characteristics of a light field.

To capture the complexity of light measurement, five fundamental dimensions must be considered:

- **Temporal Considerations** It is essential to distinguish between instantaneous and time-integrated quantities, for example, between power and energy, or fluence rate and fluence. This distinction is especially important when comparing pulsed and continuous light sources, as well as in interpreting biological responses such as photosynthesis or phototropism [119].

- **Spectral Composition** Light, often mistakenly treated as a uniform continuum, is actually composed of different wavelengths, each of which interacts differently with biological materials. Accurate quantification therefore requires measuring energy or photon flux across the relevant spectral range.

- **Directionality** Light is not evenly distributed in space; its angular distribution, whether collimated (e.g., from a laser), diffuse, or isotropic, affects both how it interacts with materials and how it can be measured.

- **Polarization** Polarization refers to the orientation of the light wave's electric field vector and, although often neglected in radiometric contexts, can influence optical interactions in anisotropic or birefringent media. Light can be polarized linearly, circularly, or elliptically [125].

- **Coherence** Coherence refers to the degree of phase correlation between light waves in time and space. Coherent sources, such as lasers, support interference and diffraction-based techniques, while incoherent sources—like sunlight or LEDs—exhibit random phase relationships [120]

Although polarization and coherence are relevant in certain areas of biophotonics and optical engineering, they fall outside the scope of this thesis and are mentioned here for completeness only.

2.4.9 Radiometric Quantities

This section defines and contextualizes the primary radiometric quantities, including those used in this work, following International Union of Pure and Applied Chemistry (IUPAC)'s recommendations in the Glossary of Terms Used in Photochemistry [126]:

Radiant Energy

Radiant energy, denoted Q_e, is the total electromagnetic energy (including all wavelenghts) emitted, transferred, or received in a defined period of time. It represents the integral of power over time:

$$Q_e = \int P_e(t)\, dt, \tag{2.42}$$

where $P_e(t)$ is the instantaneous Radiant Power (Radiant Energy Flux, Radiant Flux) at time t with units of watts (W). The SI[8] unit of radiant energy is the joule (J).

Fluence, Radiant (Energy) Fluence, Radiant Exposure

Fluence (H_o or F_o) quantifies the total radiant energy incident on a small sphere divided by the cross-sectional area of the sphere, from all directions over a time period:

$$H_o = \frac{dQ_e}{dS}, \tag{2.43}$$

where S is the area of cross-section. The SI unit is J·m^{-2}. This measure is especially

[8]International System of Units.

relevant in pulsed systems or time-integrated dose calculations in photobiology and photochemistry.

Fluence Rate, Radiant (Energy) Fluence Rate, Spherical Irradiance

The fluence rate, E_o, is the time derivative of fluence:

$$E_o = \frac{dH_o}{dt} = \frac{dP_e}{dS}, \tag{2.44}$$

and is expressed in $\mathrm{W{\cdot}m^{-2}}$. Here H_o denotes the fluence, P_e is the radiant power and S is the cross-sectional area of a small spherical volume over which the radiant energy is incident. In this work, the fluence rate is denoted by the Greek letter Φ.

Irradiance (Radiant Flux Density)

Irradiance E_e with SI units of $\mathrm{W{\cdot}m^{-2}}$ is defined as the radiant power incident on a flat surface, from all upward directions, per unit area:

$$E_e = \frac{dP_e}{dA}, \tag{2.45}$$

with A representing the area of the flat surface.

Radiance

Radiance $L_{e,\Omega}$ describes the radiant power per unit of projected area per unit of solid angle. Consider a differential surface element dA with outward normal vector $\hat{\mathbf{n}}$. Radiation

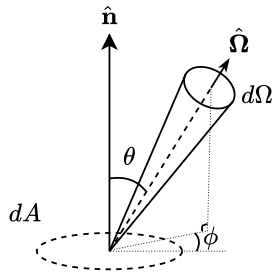

Figure 2.12: Geometry of the definition of radiance.

traveling within a narrow cone of directions subtending solid angle $d\Omega$ about direction $\hat{\mathbf{\Omega}}$ makes an angle θ with the surface normal $\hat{\mathbf{n}}$ (see Figure 2.12). In this context, the radiance $L_{e,\Omega}$ is defined as the power per unit area per unit solid angle, given by:

$$L_{e,\Omega} = \frac{d^2 P_e}{dA \cos\theta \, d\Omega}. \tag{2.46}$$

and it quantifies the distribution of radiant power emerging from or passing through a surface element in a specified direction. The factor $\cos\theta$ accounts for the projected area perpendicular to the direction of propagation. The SI unit of radiance is watts per square meter per steradian ($\mathrm{W{\cdot}m^{-2}{\cdot}sr^{-1}}$).

In this reference, integrating the radiance L over the entire sphere of solid angle 4π steradians yields the fluence rate (or spherical irradiance):

$$E_o = \int_{4\pi} L(\Omega) d\Omega = \int_0^{2\pi} \int_0^{\pi} L(\theta, \phi) \sin\theta \; d\theta d\phi. \tag{2.47}$$

In Equation 2.47, the rightmost expression represents the integral in spherical coordinates, where θ is the polar angle and ϕ is the azimuthal angle (see Figure 2.12).

For collimated light, the expression simplifies and the radiance is defined as the radiant power that passes through a small surface element in a specific direction, divided by the area of that surface projected perpendicular to the direction of the beam:

$$L = \frac{dP_e}{dA \cos\theta}, \tag{2.48}$$

where θ is the angle between the direction of the radiation and the normal to the surface.

Radiance may be connected to electromagnetic energy transport through the time-averaged Poynting vector $\langle \mathbf{S} \rangle$. For a surface element dA with unit normal $\hat{\mathbf{n}}$, the differential radiant power associated with directions within $d\Omega$ about $\hat{\mathbf{\Omega}}$ is

$$dP_e = L(\hat{\mathbf{\Omega}})\,(\hat{\mathbf{\Omega}} \cdot \hat{\mathbf{n}})\,dA\,d\Omega. \tag{2.49}$$

Defining the radiative flux vector by

$$\mathbf{F} = \int_{4\pi} L(\hat{\mathbf{\Omega}})\,\hat{\mathbf{\Omega}}\,d\Omega, \tag{2.50}$$

the net power crossing the surface is $dP_e = \mathbf{F} \cdot \hat{\mathbf{n}}\,dA$. Thus, under the assumptions of radiative transfer or geometrical optics, $\mathbf{F}$ is the radiometric analogue of the cycle-averaged Poynting vector.

Spectral Quantities

Radiometric quantities may be defined spectrally, i.e., per unit wavelength or frequency. For instance, the spectral radiant energy $Q_{e,\lambda}$ is defined as:

$$Q_{e,\lambda} = \frac{dQ_e}{d\lambda}, \tag{2.51}$$

with SI units of $\mathrm{J\,nm^{-1}}$, representing the radiant energy per unit wavelength interval. Also, the spectral radiant power $P_{e,\lambda}$ is given by:

$$P_{e,\lambda} = \frac{dP_e}{d\lambda}, \tag{2.52}$$

with SI units of $\mathrm{W\,nm^{-1}}$, describing the radiant power per unit wavelength interval. Similarly, spectral fluence is denoted by $H_{o,\lambda}$ with SI units of $\mathrm{J\,m^{-2}\,nm^{-1}}$, and the spectral radiance is represented by $L_{e,\lambda,\Omega}$ with SI units of $\mathrm{W\,m^{-2}\,sr^{-1}\,nm^{-1}}$. Also, the spectral fluence rate is shown by $E_{o,\lambda}$ and the spectral irradiance is denoted by $E_{e,\lambda}$, both with SI units of $\mathrm{W{\cdot}m^{-2}{\cdot}nm^{-1}}$.

2.4.10 Photonic Quantities

The radiometric quantities like radiant energy (Q_e), radiant power (P_e), irradiance (E_e), and radiance ($L_{e,\Omega}$) (which are expressed in SI units such as joules (J), watts (W), or derived units like $\mathrm{W \cdot m^{-2}}$ and $\mathrm{W \cdot m^{-2} \cdot sr^{-1}}$), correspond to photonic quantities like photon

number (N_p), photon flux (q_p), photon irradiance (E_p), and photon radiance (L_p). These photonic quantities are expressed in terms of the number of photons per unit time, area, or solid angle. The fundamental relationship connecting these radiometric and photonic measures is the energy of a single photon, defined by:

$$E = h\nu = \frac{hc}{\lambda}, \tag{2.53}$$

where h is the Planck constant, ν is the frequency, c is the speed of light, and λ is the wavelength of the radiation.

For monochromatic radiation at a specific frequency (ν) or wavelength (λ), the radiant energy (Q_e) is related to the total number of photons (N_p) by:

$$N_p = \frac{Q_e}{h\nu} = \frac{Q_e\lambda}{hc}. \tag{2.54}$$

For polychromatic radiation with a wavelength range from λ_1 to λ_2, a spectral radiometric quantity at a given wavelength ($G_{e,\lambda}$), is related to the corresponding spectral photonic quantity ($G_{p,\lambda}$) by:

$$G_{e,\lambda} = E(\lambda)G_{p,\lambda} = \frac{hc}{\lambda}G_{p,\lambda}. \tag{2.55}$$

To calculate a total photonic quantity (G_p) from a spectral radiometric quantity ($G_{e,\lambda}$), the following integral is used:

$$G_p = \int_{\lambda_1}^{\lambda_2} G_{p,\lambda}(\lambda)\, d\lambda = \frac{1}{hc} \int_{\lambda_1}^{\lambda_2} G_{e,\lambda}(\lambda)\lambda\, d\lambda. \tag{2.56}$$

For example, the total photon flux (q_p) (defined as the number of photons per time interval with SI unit is s^{-1}) can be calculated from the spectral radiant power ($P_{e,\lambda}$) as follows:

$$q_p = \frac{1}{hc} \int_{\lambda_1}^{\lambda_2} P_{e,\lambda}(\lambda)\lambda\, d\lambda. \tag{2.57}$$

Conversely, to calculate a total radiometric quantity (G_e) from a spectral photonic quantity ($G_{p,\lambda}$), the relationship is:

$$G_e = \int_{\lambda_1}^{\lambda_2} G_{e,\lambda}(\lambda)\, d\lambda = hc \int_{\lambda_1}^{\lambda_2} G_{p,\lambda}(\lambda)\frac{1}{\lambda}\, d\lambda. \tag{2.58}$$

For instance, the total irradiance (E_e) can be calculated from the spectral photon irradiance ($E_{p,\lambda}$) as:

$$E_e = hc \int_{\lambda_1}^{\lambda_2} E_{p,\lambda}(\lambda)\frac{1}{\lambda}\, d\lambda. \tag{2.59}$$

2.4.11 Mathematical Models for Light Propagation in Biological Tissues

Biological tissues are optically heterogeneous, consisting of components with varying refractive indices and structural scales. These components include chromophores, intracellular

organelles, cells, and elements of the extracellular matrix (Figure 2.13). This complexity influences how light is absorbed, scattered, and propagated. As a result, models of light transport must be carefully selected and tailored to the specific spatial, temporal, and application-specific requirements.

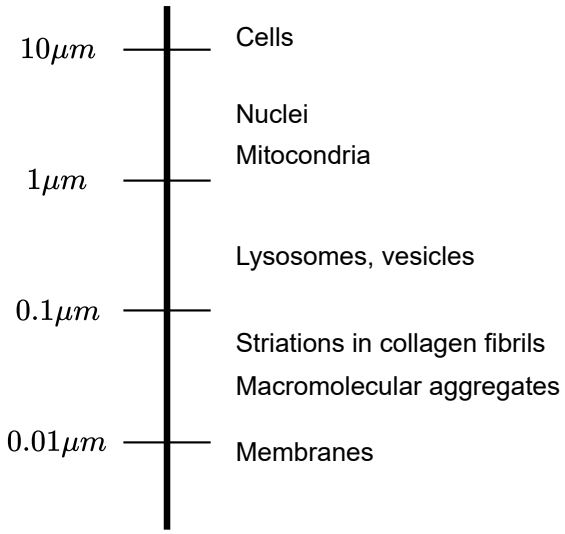

Figure 2.13: Biological structures of various sizes. Figure is adapted from [123].

Depending on the spectral properties of the light and the scale of observation, light propagation in biological tissues can be described by one of three primary theoretical frameworks. At the most fundamental level, Maxwell's equations provide a full electromagnetic wave-based description, capturing all wave phenomena including interference and polarization. At the mesoscopic scale, the Radiative Transport Equation (RTE) offers a statistical approach that accounts for absorption and scattering but neglects wave effects.

In highly scattering media, the diffusion approximation, a simplified form of the RTE, can be used due to its computational efficiency and practical applicability.

Maxwell's Equations

At the most fundamental level, propagation of light, as an electromagnetic wave is governed by Maxwell's equations. A set of coupled partial differential equations that describe the time-dependent behaviour of electric and magnetic fields in a medium is provided below [127]:

$$\nabla \cdot \mathbf{E} = \frac{\rho}{\varepsilon}, \quad \nabla \cdot \mathbf{B} = 0, \quad \nabla \times \mathbf{E} = -\frac{\partial \mathbf{B}}{\partial t}, \quad \nabla \times \mathbf{B} = \mu \mathbf{J} + \mu\varepsilon \frac{\partial \mathbf{E}}{\partial t}. \tag{2.60}$$

Here, $\mathbf{E}$ is the electric field (V/m), $\mathbf{B}$ is the magnetic flux density (T), ρ is the electric charge density (C/m^3), $\mathbf{J}$ is the electric current density (A/m^2), ε is the permittivity of the medium (F/m), and μ is the permeability of the medium (H/m).

These equations provide a comprehensive physical model of electromagnetic wave phenomena, capturing effects such as interference, diffraction, birefringence, and polarization. Maxwell's framework is particularly useful in modelling light interactions at or below the wavelength scale, where wave-based effects dominate.

Maxwell's equations can be used to model light propagation in biological tissues with high precision. In practice, however, solving Maxwell's equations for biological light transport presents several challenges. First, the computational cost is significant and accurate solutions require extremely fine spatial and temporal discretization, which in large

or heterogeneous biological domains can become prohibitively expensive. Second, material parameters such as the spatial distribution of electric permittivity (ε) and magnetic permeability (μ) are often poorly characterized in biological tissues, particularly at the microscopic scale.

Despite the computational and practical challenges, Maxwell-based models remain essential in specific scenarios where wave-level accuracy is required. These include subwavelength or near-field structures, where phenomena such as near-field effects, diffraction, and strong scattering dominate; polarization- and coherence-sensitive phenomena. Full-wave modelling is also appropriate when modelling structures on the order of the wavelength (e.g., vesicles, microtubules, or nanoparticles), or in domains limited in size, such as subcellular regions.

Radiative Transport Equation (RTE)

At mesoscopic scales, where scattering and absorption events remain significant but wave phenomena such as interference and polarization can be neglected, the RTE provides a physically robust framework for modelling light propagation. Unlike Maxwell's equations, the RTE ignores phase information, which is appropriate in biological tissues after light has experienced several scattering events and coherence is effectively lost.

The RTE models radiance $L(\mathbf{r}, \hat{\mathbf{\Omega}}, t)$ at location $\mathbf{r}$, in direction $\hat{\mathbf{\Omega}}$, and at time t. The equation is expressed as [123], [128]:

$$\frac{1}{v}\frac{\partial L(\mathbf{r},\hat{\mathbf{\Omega}},t)}{\partial t} = -\hat{\mathbf{\Omega}}\cdot\nabla L(\mathbf{r},\hat{\mathbf{\Omega}},t) - \mu_t L(\mathbf{r},\hat{\mathbf{\Omega}},t) + \mu_s \int_{4\pi} p(\mathbf{r},\hat{\mathbf{\Omega}}'\to\hat{\mathbf{\Omega}})\, L(\mathbf{r},\hat{\mathbf{\Omega}}',t)\, d\Omega' + S(\mathbf{r},\hat{\mathbf{\Omega}},t) \tag{2.61}$$

where $v = c/n$ is the speed of light in the medium, with c the speed of light in vacuum and n the refractive index. $\hat{\mathbf{\Omega}}\cdot\nabla L(\mathbf{r},\hat{\mathbf{\Omega}},t)$ is the divergence term, describing how radiance changes spatially along direction $\hat{\mathbf{\Omega}}$, and $\mu_t = \mu_a + \mu_s$ is the total extinction coefficient [mm^{-1}], accounting for both absorption μ_a and scattering μ_s losses. Also, $p(\mathbf{r},\hat{\mathbf{\Omega}}'\to\hat{\mathbf{\Omega}})$ is the phase function representing the probability density that light traveling in direction $\hat{\mathbf{\Omega}}'$ is scattered into direction $\hat{\mathbf{\Omega}}$, and is typically dependent only on the angle between them. $\int_{4\pi}\cdots d\Omega'$ is an integral over all incoming directions on the unit sphere, representing the total in-scattered contribution from all directions. $S(\mathbf{r},\hat{\mathbf{\Omega}},t)$ is the source term representing any volumetric emission or injection of radiance [$\mathrm{W\cdot mm^{-3}\cdot sr^{-1}}$] into the medium.

RTE does not assume either scattering-dominant conditions or isotropy in the medium. This generality makes it especially well-suited for modelling light transport in tissues with moderate to high scattering, in contexts where angular or directional information is important and in situations where the assumptions underlying diffusion theory (as discussed below) fail, particularly near boundaries or in low-scattering regions.

While analytical solutions to the RTE are available only for highly simplified geometries, numerous numerical methods have been developed to solve it, including Discrete Ordinates Methods (DOM) [129], and Monte Carlo simulations [123]. Among these, Monte Carlo methods are widely used in biophotonics due to their flexibility, scalability, and ability to

accurately model complex tissue geometries and spatially varying optical properties [123].

Diffusion Approximation

After multiple scattering events in a highly scattering medium, not only is the phase coherence of light lost, but also its directionality becomes randomized. This results in an approximately isotropic radiance distribution. Under such conditions, the RTE can be simplified to a diffusion approximation. The key assumption is that scattering dominates over absorption, i.e., $\mu_s' \gg \mu_a$, where μ_s' is the reduced scattering coefficient (see Equation 2.39) [123].

By neglecting higher-order terms in the spherical harmonics expansion of the radiance (the P_1 approximation) and assuming an isotropic source, radiance can be described only in term of fluence rate $\Phi(\mathbf{r}, t)$, through time-dependent diffusion equation [123]:

$$\frac{1}{v}\frac{\partial \Phi(\mathbf{r}, t)}{\partial t} + \mu_a \Phi(\mathbf{r}, t) - \nabla \cdot [D \nabla \Phi(\mathbf{r}, t)] = S(\mathbf{r}, t), \tag{2.62}$$

where v is the speed of light in the medium, $S(\mathbf{r}, t)$ is the source term, and $D = \frac{1}{3(\mu_a + \mu_s')}$ is the diffusion coefficient.

Diffusion approximation holds under two primary conditions [123]:

1. Radiance must be nearly isotropic, which requires that photons undergo many scattering events.

2. Relative variation in the fluence rate over one reduced mean free path l_t is minimal. In other words, the change in fluence rate across a single transport mean free path

is much less than one.

These conditions are typically met in media where scattering strongly dominates over absorption, satisfying $\mu_s' \gg \mu_a$. The diffusion approximation also is more accurate when the observation point is sufficiently far from both sources and boundaries, so that the assumption of isotropic radiance is valid at the location. However, appropriate boundary conditions can be applied to improve accuracy near interfaces and source regions [123].

It is important to note that the diffusion equation does not depend on the scattering coefficient μ_s and anisotropy factor g independently, but rather on their combination μ_s'.

3

Piezoelectric Nanogenerators

Piezoelectric Nanogenerators (PENGs) are nanoscale devices that convert mechanical energy into electrical energy through the piezoelectric effect. As previously discussed, piezoelectricity enables energy conversion under mechanical stress, and PENGs apply this principle at the micro- and nanoscale. Their capacity to harvest energy from mechanical stimuli such as ultrasonic waves—has extended the role of piezoelectric materials beyond conventional sensors and actuators into wireless biomedical systems.

The increasing demand for wirelessly powered biomedical implants has brought attention to PENGs as a viable energy harvesting solution. Compared to electromagnetic transducers, piezoelectric converters typically offer higher efficiency and simpler manufacturing [130]. Moreover, ultrasonic waves provide an effective energy transmission method in biological tissues due to their low attenuation, particularly within the 0.1–10 MHz range [67]. These characteristics make PENGs well-suited for powering implantable devices such as the system proposed in this work.

Two main features underscore the suitability of PENGs for this application:

- **Wireless Triggering:** Piezoelectric materials have long been employed in electromechanical transduction, and the concept of using PENGs to convert ultrasonic energy into electricity is well established. The first nanogenerator was based on this principle and demonstrated successful energy harvesting from ultrasonic waves [131].

- **Nanoscale Advantages:** PENGs constructed from piezoelectric nanowires benefit from their high aspect ratio[1] and mechanical sensitivity. These structures are capable of producing substantial electrical output (reaching open-circuit voltages of 1.2 V to 2 V and currents of 100 nA in optimized arrays) in response to very small mechanical forces (ranging from 80 nN down to the picoNewton level) [130]. This sensitivity enables effective energy harvesting from ultrasound, which is critical for driving miniature wireless electronic systems.

[1] In the context of nanowires, aspect ratio is defined as the ratio of length to diameter (L/D). A high aspect ratio indicates a long, thin structure.

Despite their high performance, traditional piezoelectric materials such as lead zirconate titanate (PZT) or barium titanate ($BaTiO_3$) suffer from several drawbacks that limit their use in biomedical implants. Their rigidity, lack of biocompatibility, and, in some cases, toxic composition raise concerns for long-term implantation. While synthetic polymers like Polyvinylidene Fluoride (PVDF) offer greater flexibility, they are typically non-biodegradable and may release harmful by-products during synthesis or degradation [130].

To address these limitations, increasing attention has turned to natural piezoelectric biomaterials. Derived from biological sources. Their compatibility with soft tissue environments makes them highly promising for applications requiring safe and sustainable integration within the human body.

In this context, the wireless device proposed in this thesis aims to incorporate a piezoelectric biomaterial as its energy harvesting component. The next section will examine these biomaterials in greater detail.

3.1 Piezoelectric Biomaterials

Piezoelectric biomaterials can be broadly categorized into five major classes: amino acids, peptides, proteins, viruses, and polysaccharides. These materials are of particular interest for bio-integrated devices due to their inherent biocompatibility, biodegradability, and mechanical compatibility with soft tissues. This section evaluates representative materials

from each category with a focus on their longitudinal piezoelectric response, which is critical for efficient energy harvesting under external ultrasonic stimulation.

Amino acids, the fundamental units of proteins, possess intrinsic piezoelectricity arising from dipole moments between their amino (NH_2) and carboxyl (COOH) groups [132], [133]. Glycine is the most studied amino acid for piezoelectric applications and exists in three polymorphs: α, β, and γ [134]. Of these, β-glycine shows a high shear piezoelectric coefficient ($d_{16} = 178 \pm 11$ pmV^{-1}) [135]. However, it is thermodynamically unstable under ambient conditions and its response is primarily shear-based, which limits its utility in compressive or tensile applications [136]. γ-glycine, while more stable, presents longitudinal activity ($d_{33} \approx 10.4$ pmV^{-1}), but forming single crystals under neutral aqueous conditions is difficult and achieving domain alignment in flexible films remains a significant challenge [137].

Some peptides, which are short amino acid chains, also display piezoelectricity [138]. For instance, Diphenylalanine (FF) is a peptide that can self-assemble into nanostructures like microrods and nanotubes, and exhibit strong shear responses ($d_{15} \approx 80 \pm 15$ pmV^{-1}) [139]. Aligned FF microrods have achieved a longitudinal coefficient of $d_{33} = 17.9$ pmV^{-1} [139], but precise control over alignment typically requires electric poling or tailored self-assembly, adding complexity to fabrication for longitudinal-mode devices.

Larger biomolecules such as proteins and polysaccharides also exhibit piezoelectricity, although their performance varies significantly depending on molecular structure and alignment [140]. Between the proteins, Collagen is the most abundant structural in the body

which shows piezoelectric behaviour primarily from aligned peptide chains [141], [142]. However, this response is generally weak and dominated by shear, with reported d_{14} values up to -12 pmV^{-1} and effective constants often near 2 pmV^{-1}. Silk fibroin, when electrically poled, has demonstrated improved longitudinal performance with d_{33} values reaching 38 pmV^{-1}. In contrast, elastin typically exhibits low effective coefficients around 1 pmV^{-1}. The inherent complexity and molecular disorder in these proteins often limits dipole alignment and thus their practical use in axial-mode energy harvesting.

Polysaccharides such as cellulose and chitosan, are widely available and exhibit piezoelectricity due to their non-centrosymmetric crystalline domains [143]. Cellulose Nanocrystals (CNC) films have shown particularly promising results, with shear coefficients ($d_{25} = 210 \pm 5$ pmV^{-1}) [144] and longitudinal d_{33} values up to 19.3 ± 2.9 pmV^{-1} in vertically aligned films, which is comparable to synthetic polymers like PVDF. Chitosan films have similarly demonstrated $d_{33,\text{eff}}$ values of up to 18.4 pmV^{-1} in neutralized films. Although scalable fabrication is well established for polysaccharide films, their intrinsic piezoelectric response remains limited by molecular structure and alignment efficiency.

Among piezoelectric materials, the M13 bacteriophage offers an advantageous combination of structural and functional properties, making it particularly well-suited for integration into our proposed system as a PENG. The M13 virus is a filamentous phage with a length of approximately 880 nm and a diameter of 6.6 nm [145]. It is composed of a circular single-stranded DNA (ssDNA) that is 6407 nucleotides in length, encapsulated within a protein shell made up of capsid, replication, and assembly proteins [146]. The virus is synthesized using the bacterium *Escherichia coli* (*E. coli*), relying on the bacterial

pilus for its formation [145]. Its surface is composed of thousands of identical pVIII coat proteins arranged helically along its length. Each pVIII protein adopts an α-helical conformation, resulting in a dipole moment oriented from the amino to the carboxy-terminal end. This ordered nanoscale architecture effectively functions as a natural piezoelectric nanowire [146].

One of the key advantages of the M13 phage lies in its genetic tunability. The N-terminus of the pVIII protein can be altered using recombinant DNA technology by adding variable amounts of negatively charged glutamate (E) amino acids [147], [148]. The wild-type M13 has a single negative charge at the insertion site, and introducing additional negative charges enhances the virus's piezoelectric attributes [149]. For example, engineered variants such as the 4E-phage [2] and 6H-phage [3] have been developed to optimize performance. When assembled into vertically aligned nanopillar arrays via template-assisted self-assembly, engineered M13 phages have achieved out-of-plane effective coefficients up to $d_{33,\text{eff}} = 13.2$ pmV^{-1} [147]. This is significantly higher than what has been reported for non-aligned collagen films. Furthermore, the ability to fabricate aligned phage-based films at the nanoscale offers scalability and integration potential with various system designs.

These features make M13 PENGs capable of transducing mechanical energy from ultrasonic stimulation into usable electrical power. For the biocompatible, wirelessly powered nanogenerator proposed in this work, the M13 phage offers a promising material platform.

[2] 4E-phage is genetically engineered M13 phage, in which four glutamate amino-acids (E) are added to the coat protein PVIII.

[3] 6H-phage is a genetically engineered M13 phage, in which six histidine amino acids (H) are added to the coat protein PVIII.

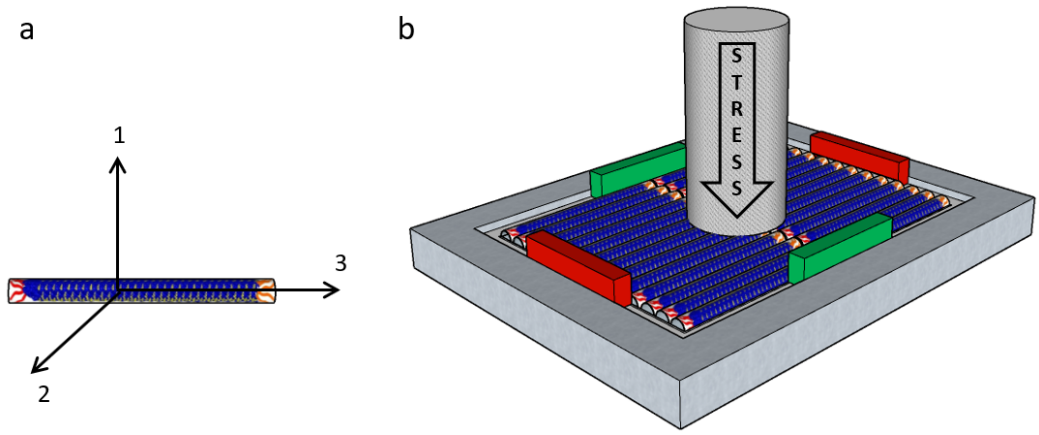

Figure 3.1: Direction presentation of M13 phage. (a) Axes numbering: dimensions 1, 2, and 3 correspond to the z , x , and y directions in the Cartesian coordinate system (b) Schematic illustration of electrode connections. The green electrodes correspond to d_{21} and the red electrodes correspond to d_{31} piezoelectric mode.

3.2 Piezoelectric properties of M13 PENGs

Several experimental studies have investigated the piezoelectric properties of M13 bacteriophages at macro scale dimensions [146]. Here, we use these experimental findings to approximate the parameters that characterize the mechanical and piezoelectric behaviour of M13 bacteriophages at the nanoscale. This, enables us to simulate the piezoelectric responses of M13 nanogenerators. We determine the compliance matrix $[\mathbf{s}^E]$, piezoelectric coefficients $[\mathbf{d}]$, and dielectric constant matrix $[\boldsymbol{\varepsilon}^T]$ as introduced in Equation 2.15 and Equation 2.16. In this study, the z-axis will be considered aligned with the length of the M13 bacteriophage and the coordinate dimensions 1, 2, and 3 corresponds to the z, x, and y directions of the Cartesian coordinate system, respectively (Figure 3.1).

The M13 bacteriophage exhibits a highly ordered filamentous structure, in which thousands of copies of the major coat protein (pVIII) are arranged helically around the viral DNA. This arrangement gives rise to a quasi-crystalline organization with repeating structural units along the longitudinal axis, which underlies the effective hexagonal symmetry and supports its classification within the C_6 symmetry group [4], and is part of the type VII Transversely Isotropic (TI) [5] materials class [149], [150]. This classification allows us to model the mechanical behaviour of the phage using the compliance matrix format as follows [151]:

$$\left[\mathbf{s}^T\right] = \begin{bmatrix} \frac{1}{E_p} & -\frac{\nu_p}{E_p} & -\frac{\nu_{zp}}{E_z} & 0 & 0 & 0 \\ -\frac{\nu_p}{E_p} & \frac{1}{E_p} & -\frac{\nu_{zp}}{E_z} & 0 & 0 & 0 \\ -\frac{\nu_{pz}}{E_p} & -\frac{\nu_{pz}}{E_p} & \frac{1}{E_z} & 0 & 0 & 0 \\ 0 & 0 & 0 & \frac{1}{2G_{zp}} & 0 & 0 \\ 0 & 0 & 0 & 0 & \frac{1}{2G_{zp}} & 0 \\ 0 & 0 & 0 & 0 & 0 & \frac{1+\nu_p}{E_p} \end{bmatrix}. \tag{3.1}$$

In this matrix, E_p and E_z refer to Young's modulus [6] in the plane of symmetry [7] and

[4]The C6 symmetry group refers to a hexagonal symmetry characterized by a sixfold rotational axis. This means the structure repeats itself every 60 degrees when rotated around this central axis.

[5]Transversely isotropic materials are a subset of anisotropic materials that exhibit isotropic properties in all directions within a plane (the transverse plane or plane of symmetry) but have different properties along an axis perpendicular to this plane (the longitudinal axis).

[6]Young's Modulus (E) is a measure of a material's stiffness, defined as the ratio of longitudinal stress to longitudinal strain within the elastic limit: $E = \sigma/\epsilon$ where σ is the stress (force per unit area) and ϵ is the strain (deformation per unit length).

[7]Plane of symmetry is a plane within the material where mechanical properties are identical in all directions

normal to it, respectively. ν_p is the Poisson's ratio [8] within the plane of symmetry. ν_{pz} represents the transverse strain in the z-direction due to longitudinal stress in the plane of symmetry. ν_{zp} represents the transverse strain in the plane due to longitudinal stress in the z -direction. G_{zp} denotes the shear modulus [9].

It is worth mentioning that specific symmetries exist in the compliance matrix of certain types of materials. For example, in TI materials the equation $\frac{\nu_{pz}}{E_p} = \frac{\nu_{zp}}{E_z}$ holds true. This equality arises because, in TI materials, the mechanical properties are isotropic within the plane but differ along the perpendicular axis. When stress is applied in one direction, it induces strains not only in that direction but also in perpendicular directions due to Poisson's effect. The symmetry of the material causes that the ratios of the Poisson's ratios to their corresponding Young's moduli are equal in reciprocal directions.

In the design of microscale systems, it is common to approximate their properties based on bulk characteristics as bulk properties are often more readily available and better understood [152]. As systems decrease in size from macro to micro, they generally become less stiff due to the increased freedom of movement of individual components, which are no longer constrained by surrounding components. Consequently, the micro-scale mechanical properties of M13 phages can be approximated from the macro-scale systems, particularly in the absence of direct experimental data. On this basis, we refer to the experimentally

[8] Poisson's Ratio (ν) describes the ratio of transverse strain to longitudinal strain when a material is stretched or compressed: $\nu = -\epsilon_{\text{transverse}}/\epsilon_{\text{longitudinal}}$. Transverse strain ($\epsilon_{\text{transverse}}$) is the deformation perpendicular to the applied stress and longitudinal strain ($\epsilon_{\text{longitudinal}}$) is the deformation in the direction of the applied stress.

[9] Shear Modulus (G) measures a material's response to shear stress, defined as $G = \tau/\gamma$, where τ is the shear stress (force applied parallel to the surface per unit area) and γ is the shear strain (angular deformation).

measured mechanical properties of the M13 phage as reported in [153]. The Young's modulus for a horizontally structured 4E-M13 phage film has been reported as 4.1 ± 0.6 GPa, while the vertically aligned structure yields a modulus of 1.6 ± 1 GPa [149]. These values provide the basis for E_p and E_z, respectively. Since experimental values for Poisson's ratio and shear modulus are not readily available, we follow the approximation used in [154], which draws on lysozyme protein crystal parameters, and we set $\nu_p = \nu_{zp} = 0.38$ [155]. Using the relation between elastic moduli E and shear modulus G as:

$$E = 2G(1 + \nu), \tag{3.2}$$

we can compute G_{zp} as 0.59 GPa for vertical loading.

Once these parameters are defined, we can construct the compliance matrix for the 4E-M13 phage given as follows:

$$[\,\mathbf{s}^T\,] = \begin{bmatrix} 0.2439 & -0.0927 & -0.2533 & 0 & 0 & 0 \\ -0.0927 & 0.2439 & -0.2533 & 0 & 0 & 0 \\ -0.0927 & -0.0927 & 0.6667 & 0 & 0 & 0 \\ 0 & 0 & 0 & 0.6494 & 0 & 0 \\ 0 & 0 & 0 & 0 & 0.6494 & 0 \\ 0 & 0 & 0 & 0 & 0 & 0.3366 \end{bmatrix} \times 10^{-9} \tag{3.3}$$

We also calculate the matrix of piezoelectric coefficients based on the results published

from experimental studies. Piezoelectric Force Microscopy (PFM) is the primary method for measuring piezoelectric coefficients in materials. Depending on both the direction of the applied force and the axis along which the deformation is measured, the resulting values correspond to different elements of the $[\mathbf{d}]$ matrix. A study by Yan et al. [148] measured the piezoelectric response in three directions for 4E-M13 phage particles, where the phages were horizontally arranged in a thin film. From their results, the reported values were: $d_{11} = 6.5 \pm 0.5\,\mathrm{pm\,V^{-1}}$, $d_{21} = 7.6 \pm 1.0\,\mathrm{pm\,V^{-1}}$, and $d_{31} = 12.1 \pm 1.0\,\mathrm{pm\,V^{-1}}$. Given the structural symmetry of the phage, we assume $d_{22} = d_{11}$, $d_{12} = d_{21}$, and $d_{31} = d_{32}$. Furthermore, the piezoelectric coefficient for vertically aligned M13 phages was reported as $13.2\,\mathrm{pm\,V^{-1}}$ by Lee et al. [147], and this value is assigned to d_{33}.

With these values, the piezoelectric coefficient matrix for an M13 phage film with a thickness of 80 nm can be expressed as:

$$[\mathbf{d}] = \begin{bmatrix} 6.5 & 7.8 & 0 & 0 & 0 & 0 \\ 7.8 & 6.5 & 0 & 0 & 0 & 0 \\ 12.1 & 12.1 & 13.2 & 0 & 0 & 0 \end{bmatrix} \times 10^{-12}\,\mathrm{V^{-1}}.$$

To determine the electric permittivity matrix, we refer to the reported relative permittivity values for M13 phage, which range from $\varepsilon_r = 2.1$ in [148] to $\varepsilon_r = 3$ in [149]. In our model, we take the average value $\varepsilon_r = 2.55$, thus the absolute permittivity can be calculated as:

$$\varepsilon = \varepsilon_r \varepsilon_0 = 22.577 \times 10^{-12}\,\mathrm{Fm}^{-1}. \tag{3.4}$$

Next, the density of the virus is also required. The M13 bacteriophage is a rod-shaped molecule with a diameter of 6.6 nm and an approximate length of 880 nm [146]. The total weight of the capsid proteins is reported to be 11 MDa [156], while the genome of the M13 phage, composed of 6400 base pairs, has a total weight of 4.16 MDa [157]. Therefore, the total mass of the M13 bacteriophage is $m_{\mathrm{total}} = 15.16\,\mathrm{MDa}$.

Given this value for the mass, we can calculate the density of the phage, assuming a cylindrical volume:

$$\rho = \frac{m}{v} = \frac{15.16\,\mathrm{MDa}}{\pi \times (3.3\,\mathrm{nm})^2 \times 880\,\mathrm{nm}} = 833.88\,\frac{\mathrm{kg}}{\mathrm{m}^3}. \tag{3.5}$$

To assess the accuracy of the computed parameters, a three-dimensional finite-element model of a vertically aligned 6H-M13 [10] layer was implemented in COMSOL Multiphysics [158] using the Piezoelectric multiphysics interface, which couples Solid Mechanics and Electrostatics. The active layer was modeled as a homogenized transversely isotropic piezoelectric continuum with in-plane dimensions of $0.5\,\mathrm{cm} \times 0.5\,\mathrm{cm}$ and a thickness of 880 nm. The constitutive matrices $[\mathbf{s}^E]$, $[\mathbf{d}]$, and $[\boldsymbol{\varepsilon}^T]$ derived above were assigned to this layer, with the 3-direction aligned with the longitudinal axis of the vertically oriented phages. The

[10] The M13-6H phage has been engineered to include a 6-histidine tag on its minor coat proteins, specifically on the pIII or pVI proteins. This modification is designed to enhance the vertical alignment of the phage particles, particularly on surfaces or within materials that rely on controlled orientation. The 6-histidine tag has a strong affinity for metal ions, such as nickel or cobalt. [147]

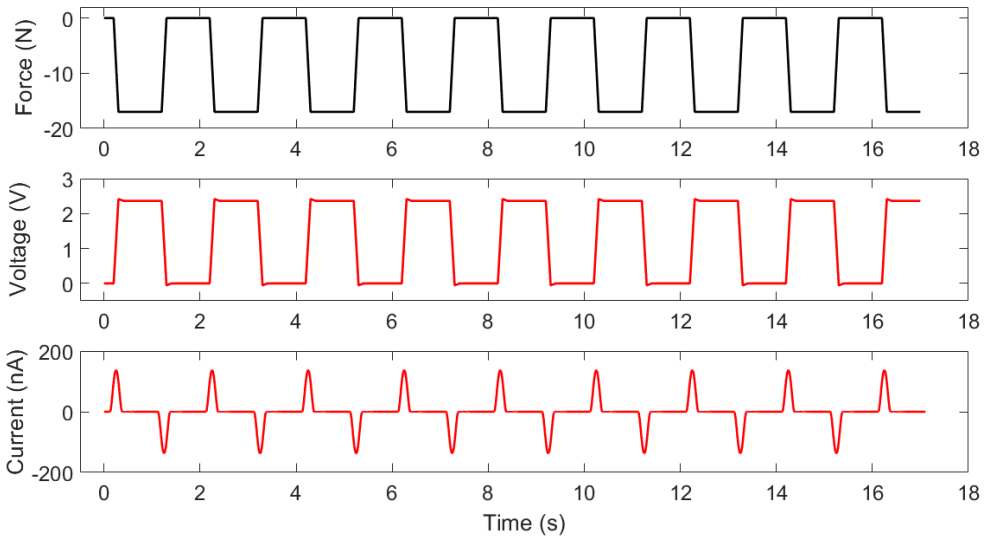

Figure 3.2: Simulation results of vertically aligned 6H-M13 phage upon vertical loading.

M13 layer was deposited on a mechanically rigid support represented by a fixed bottom boundary. Electrical contacts were applied to top and bottom surfaces, corresponding to the experimental d_{33}-type measurement geometry. Mechanically, the bottom surface was fixed, the lateral surfaces were traction-free, and a compressive load of 17 N was applied as a uniform pressure over the full top surface. Electrically, the bottom electrode was set to ground and the top electrode was defined as a Floating Potential to compute the open-circuit voltage. The short-circuit current was obtained using the corresponding terminal or circuit condition used in COMSOL. A mesh-convergence study was carried out by progressively refining the mesh, particularly through the film thickness. The simulated output was then compared with Supplementary Figure 11 of Lee et al. [147].

Additionally, peak voltage and current values were calculated for various applied load

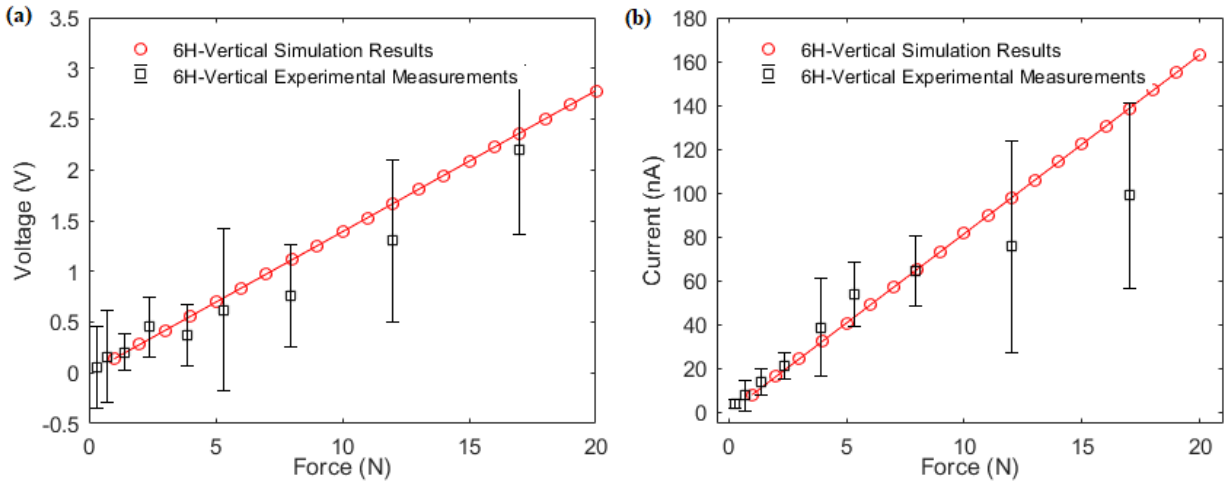

Figure 3.3: Variations in the electrical output of the 6H-M13 phage at different force values. (a) the experimental and simulated voltage values and (b) experimental and simulated current values.

levels. These simulated results were compared with the experimental data reported in [147], and the comparison outcomes are shown in Figure 3.3. The simulated results fall within the first standard deviation of the experimental data for vertical loads ranging from 1 N to 20 N. This demonstrates a strong correlation between the simulation and experimental outcomes across the specified load range.

Lastly, a 1 cm $\times$ 1 cm aligned phage film with a thickness of 300 nm was simulated to evaluate its electrical characteristics and the results were compared with the experimental data reported in [149]. Under a 34 N force, the experimentally measured open-circuit voltage ranged from 0.25 V to 0.4 V, while the short-circuit current peaked at 4 nA. In our simulations, the peak values were 0.16 V for the voltage and 3.8 nA for the current, as shown in Figure 3.4. The slight discrepancy in voltage peaks could be attributed to additional

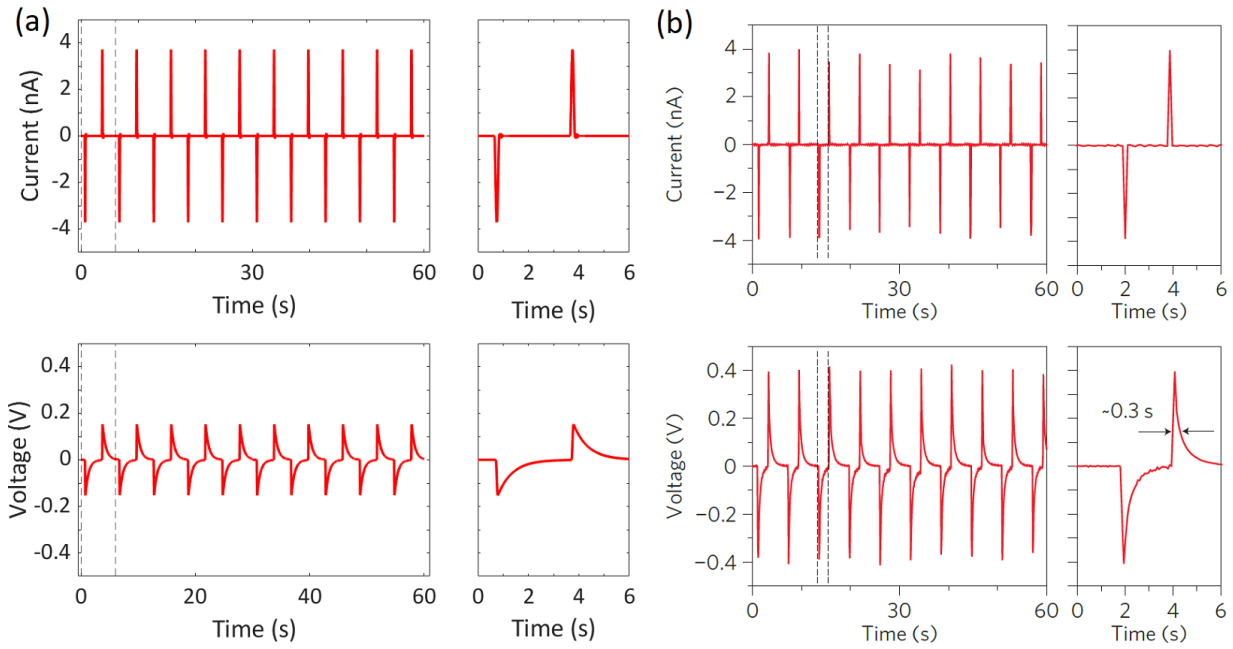

Figure 3.4: (a) Simulation results and (b) experimental measurements of nematically aligned 4E-M13 phage upon 34N loading.

factors that influence the piezoelectric response of the M13 phage, which are not captured by the linear piezoelectric model used in this study [149]. Specifically, non-linear effects such as strain-dependent piezoelectric coefficients and electro-mechanical coupling may play a role. Under higher mechanical stresses, the piezoelectric constants of materials can change, resulting in a non-linear relationship between the applied force and the generated electric field [159], [160]. This suggests that more complex factors, such as non-linear effects or variations in material properties, may need to be considered for a more precise simulation.

To investigate the piezoelectric response of the M13 phage at the nanoscale, we modeled

a single 900 nm-long, 6.6 nm-wide phage as a cylinder aligned along the z-axis (Figure 3.1a). Two distinct mechanical configurations were considered: cantilevered and fixed-ended. These configurations were chosen because they are representative of real-world conditions that the phage may encounter in practical applications. By modelling these two scenarios, we aim to understand how different boundary conditions affect the phage's piezoelectric properties. In the cantilevered configuration, one end of the virus (at $z = 0$) is mechanically fixed, while the other end (at $z = 900$) is free to move in any direction. In this setup, we assumed that electrical electrodes are connected to both ends of the phage along the z-axis, allowing the measurement of the electrical response. This configuration simulates a scenario where the virus can experience deflection due to external forces. This setup is analogous to situations in biosensors and nanomechanical devices where phages are immobilized on surfaces to detect mechanical or electrical changes [161]. In such applications, the free end of the phage can interact with target molecules, causing mechanical movements that generate electrical signals due to the piezoelectric effect.

In the fixed-ended configuration, both ends of the virus (at $z = 0$ and $z = 900\,\text{nm}$) are mechanically fixed, allowing the virus to resonate in its middle sections. This scenario is particularly relevant in the fabrication of phage-based nanofibers or thin films used in energy harvesting and tissue engineering applications [149]. In both configurations, an acoustic pressure is applied parallel to the x-axis to induce mechanical deformation.

The first important response used to study the nanogenerator is its resonance frequencies. We performed an Eigen Frequency Study to find the resonance frequencies. The first two resonance frequencies of the cantilevered configuration virus are obtained as

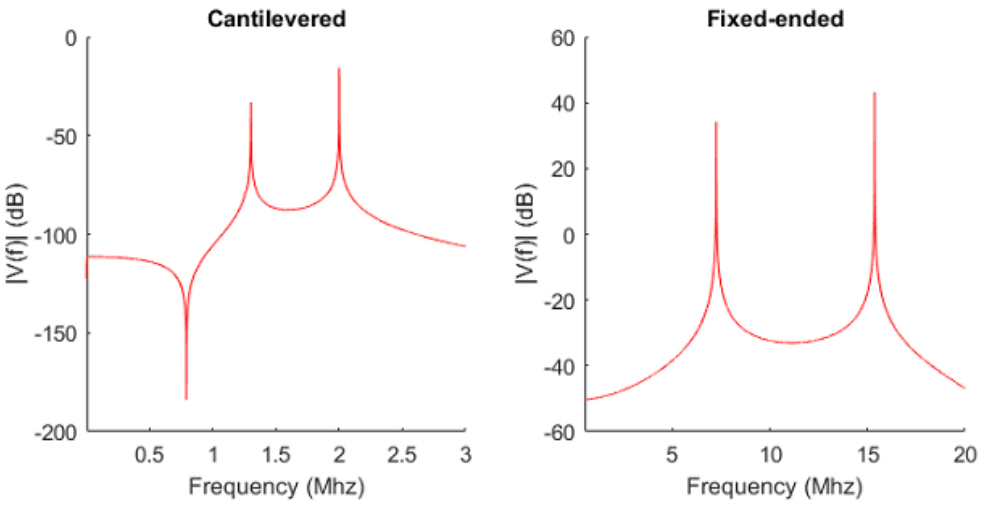

Figure 3.5: Frequency response of the amplitude of the open circuit voltage generated by the phage for cantilevered and fixed-ended condition.

$f_{rc1} = 1.2985\,\text{MHz}$ and $f_{rc2} = 1.9981\,\text{MHz}$. For the fixed-ended configurations, the first two resonances occur at $f_{rf1} = 7.2432\,\text{MHz}$ and $f_{rf2} = 15.367\,\text{MHz}$. On the other hand, we obtained the frequency response for the magnitude of the open-circuit voltage of each configuration in response to an acoustic pressure with an intensity of $10\,\text{mW}\,\text{cm}^{-2}$ applied to the phage. As expected, the peak amplitudes of the voltages are observed at the resonance frequencies (Figure 3.5).

The power transferred to the load is influenced by the impedance of the load, which depends on the difference between the internal impedance of the generator and that of the load. Figure 3.6 illustrates the voltage, current, and power transferred to a resistive load across various load values. These values correspond to an acoustic pressure intensity of $10\,\text{mW}\,\text{cm}^{-2}$, applied at f_{rc2} for the cantilevered configuration and at f_{rf2} for the fixed-

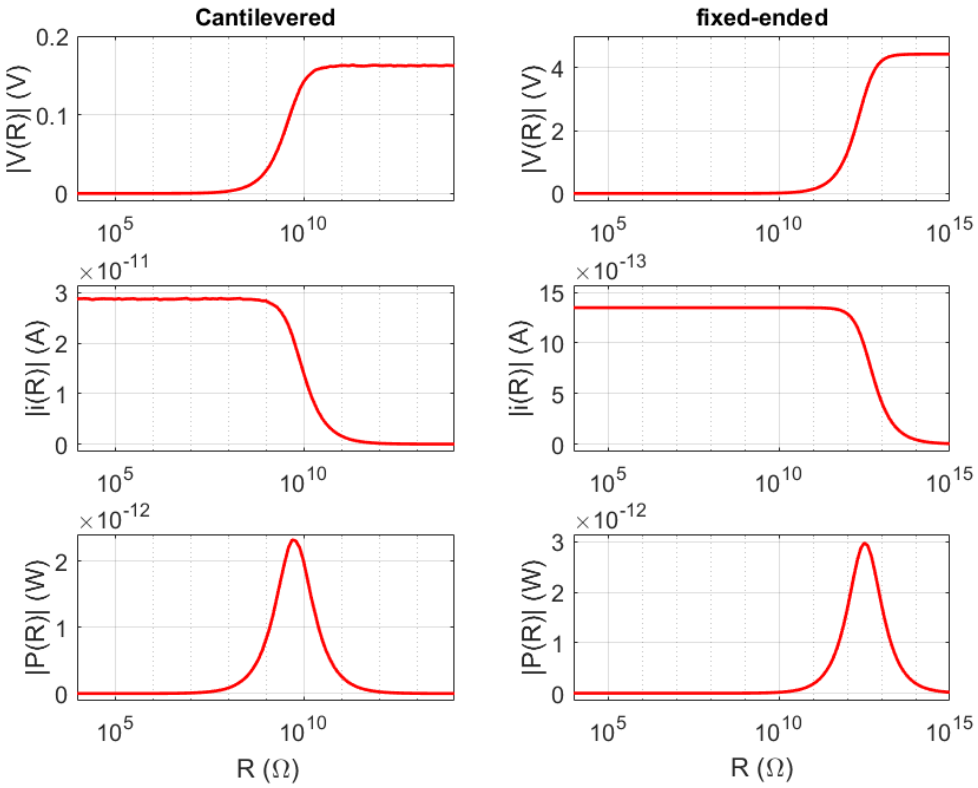

Figure 3.6: Amplitude of the voltage, current and power that is transferred to the resistive load as a function of the load value (plotted in logarithmic scale) for both mechanical configurations. The applied acoustic pressure is tuned at the second resonance frequency.

ended configuration. As expected, increasing the load value leads to an increase in the generated voltage, while the current flowing through the resistive load decreases. The maximum impedance match occurs at $R = 5.01 \times 10^9\,\Omega$ for the cantilevered configuration, and at $R = 3.16 \times 10^{12}\,\Omega$ for the fixed-ended configuration.

The electrical properties of the nanogenerator are also linked to the acoustic pressure that is applied to it. We obtained the magnitude of the generated voltage when connected

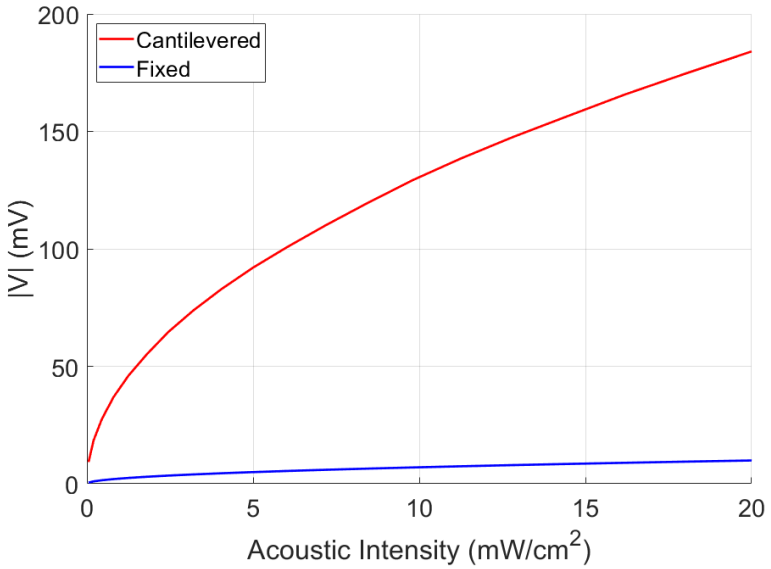

Figure 3.7: The amplitude of the generated voltage as function of the acoustic intensity when connected to a resistive load R=$5.2 \times 10^9\Omega$.

to a $5.2 \times 10^9\,\Omega$ resistive load. In this part of the simulation, the acoustic wave applied to each configuration is tuned to its first resonance frequency. As expected, Figure 3.7 shows that the electrical voltage increases as the power of the acoustic stimulation increases. For the specific resistive load of $5.2 \times 10^9\,\Omega$, the fixed-ended configuration saturates at smaller acoustic intensities, and therefore the cantilevered configuration can generate considerably higher voltages.

These simulations confirm the reliability of the extracted mechanical and piezoelectric parameters, illustrating how the electrical power generated by a single M13 virus nano-generator varies with both the frequency and intensity of the applied acoustic stimulation. Furthermore, the power transferred to the load is influenced by the load's impedance.

The presented method serves as a valuable tool for selecting the optimal configuration based on the desired electrical output, allowing for precise tuning of the frequency and amplitude of the acoustic input to meet the energy demands of specific loads. By optimizing these parameters, the performance of the nanogenerator can be tailored for various applications, enhancing its efficiency in energy harvesting and power generation.

4

Design and Modelling

This chapter presents the system design of a wireless bioluminescent mote and develops a modelling framework to characterize the resulting bioluminescence output. We begin with a system-level overview, followed by detailed descriptions and modelling of each design subunit. These modules are then integrated into an equivalent-circuit model to enable end-to-end performance analysis.

4.1 System Overview

Our design builds on the WiOptND concept [68], which uses piezoelectric structures (specifically, zinc oxide) to harvest ultrasound energy for driving μLEDs. However, our design addresses the challenges in biocompatibility and miniaturization by replacing inorganic elements with a bioluminescent pathway. In this context, a central design challenge is the need to trigger the bioluminescent reaction wirelessly. To achieve this, and building upon the discussion in section 3.2, we propose the integration of M13 bacteriophage–based PENGs with an aequorin-based bioluminescent system. This configuration creates a wireless, bio-inspired light-emitting device. The system converts ultrasonic stimulation into blue photon emission via a sequence of bio-electro-chemical processes.

During each illumination cycle, a low-MHz ultrasound stimulation mechanically deforms the engineered M13 nanogenerators. Through the piezoelectric effect, this deformation generates a localized electric field near the SR. The resulting field initiates release of Ca^{2+} ions and produces a transient Ca^{2+} pulse via the CICR process. The released Ca^{2+} bind to aequorin Photoproteins and emit blue photons (peak wavelength $\sim 470\,\text{nm}$). Finally, SERCA pumps reuptake calcium back into the SR, completing the cycle and resetting the system for subsequent ultrasound stimulation (see Figure 4.1).

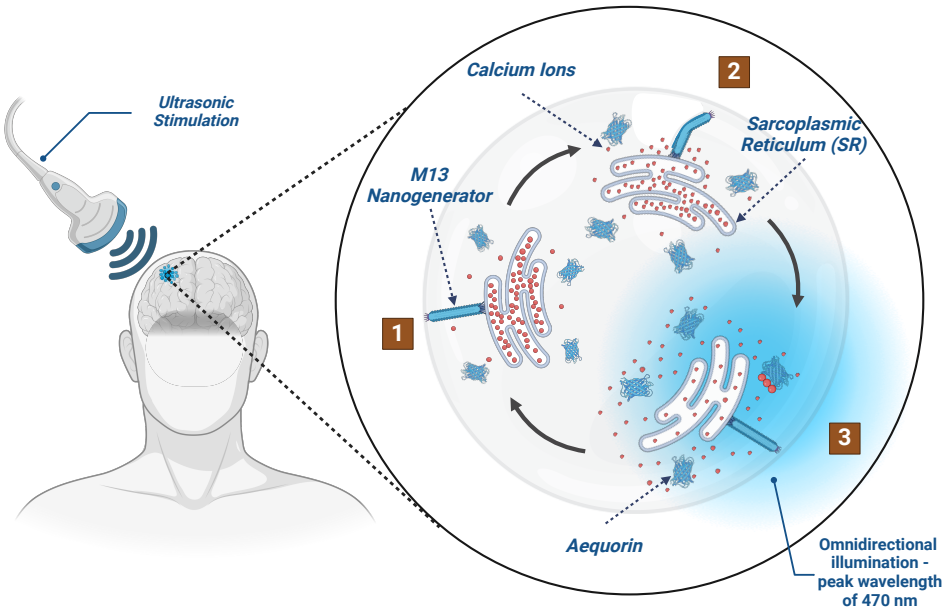

Figure 4.1: Schematic representation of the proposed bio-inspired wireless nanosystem and the biological processes in one illumination cycle. On the left: Optogenetics is depicted as a potential application of our proposed design, where the generated light from several bioluminescence units can be used to wirelessly activate opsins. On the right: 1—The resting condition is shown, with a high concentration of calcium ions inside the SR and a low concentration of calcium in the medium. 2—In response to ultrasonic stimulation, the change in the structure of the M13 piezoelectric nanogenerator is illustrated, which creates an electric field. The Voltage Gated Calcium Channels (VGCCs) are activated in response, initiating a flux of calcium ions into the medium. 3—Following the initial increase in calcium concentration in the medium, the Calcium-Induced Calcium Release (CICR) is triggered by the activation of Ryanodine Receptors 2 (RYR2) channels. With the increase in calcium concentration in the medium, the likelihood of calcium ions binding to the aequorin molecules increases, generating omnidirectional photon illumination with a peak wavelength of 470 nm. The rise in calcium concentration in the medium consequently activates the Sarcoplasmic/Endoplasmic Reticulum Ca^{2+}-ATPase (SERCA) ion pumps, which reabsorb the calcium ions into the SR, returning to step 1.

4.2 Design of the Wireless Bioluminescence Mote

Conceptually, the mote comprises three coupled subunits: (1) a power unit based on M13 bacteriophage PENGs that harvests ultrasound energy and generates electric fields; (2) a calcium-handling module based on the SR, incorporating VGCCs, RYR2, and SERCA pumps; and (3) a bioluminescence module based on aequorin photoproteins, which converts calcium transients into photon emission. The emitted light then propagates through the surrounding tissue. The following sections describe each subunit in detail, beginning with the M13-based PENGs.

4.2.1 Power Unit

Building on the discussion in section 3.1, we propose using M13-based PENGs as the power unit. This module acts as a transduction interface that converts incident ultrasound energy into a localized electric field. Energy harvesting occurs via cantilevered M13 structures placed on the SR membrane, where the resulting electric field influences nearby VGCCs.

The vibrational modes are determined by the geometry and material properties of the cantilevered M13 PENG. We therefore choose the incident ultrasound frequency to match the eigenfrequency of the desired mode and thereby excite it. Eigenfrequency analysis using Finite Element Analysis (FEA) (see section 3.2) identifies the main resonance frequency of the cantilevered M13 PENG at $f_r = 1.2985\,\mathrm{MHz}$. Accordingly, we tune the ultrasonic stimulation to f_r to maximize energy transfer. Quantitative parameters appear in section 3.2,

and the underlying piezoelectric harvesting mechanism is detailed in section 2.3.

To achieve the required spatial arrangement, we propose immobilizing M13 phages on the surface of the SR, particularly targeting VGCCs [1]. We specifically suggest using the extracellular domain of the VGCCs for binding. Subsequently, M13 phages are genetically engineered to display proteins on their coat, particularly at the pVII and pIX terminals, which are engineered to bind strongly and specifically to these target sites. By choosing VGCCs as the binding sites, the electrical field generated by the oscillation of the M13 phages can interact with the voltage sensor domains of these channels, inducing a conformational change in the VGCCs.

SR is the main component of the calcium-handling unit. In the proposed design, SR functions similarly to its role in muscle cells, serving as a storage and release site for calcium ions [163]. Inside the SR, proteins like calsequestrin and calreticulin facilitate calcium storage by binding the ions with low affinity but high capacity [164]. Despite the majority of calcium being bound to these proteins, the free calcium concentration inside the SR can reach up to 1 mM, maintained by the function of SERCA pumps. SERCA pumps transport calcium ions from the extra-SR space into the SR using energy derived from ATP hydrolysis [165]. During this process, the pump bind calcium ions from the extra-SR space, hydrolyzes ATP, and undergoes a conformational change that releases the ions inside, thereby maintaining a higher calcium concentration within the SR compared to the extra-SR medium. The rate of calcium transport is modulated by calcium concentrations

[1] This can be achieved using a targeted binding technique [162], which enables a highly selective interaction between the M13 phages and specific proteins on the SR membrane. In this approach, proteins on the SR membrane are first identified as potential target sites.

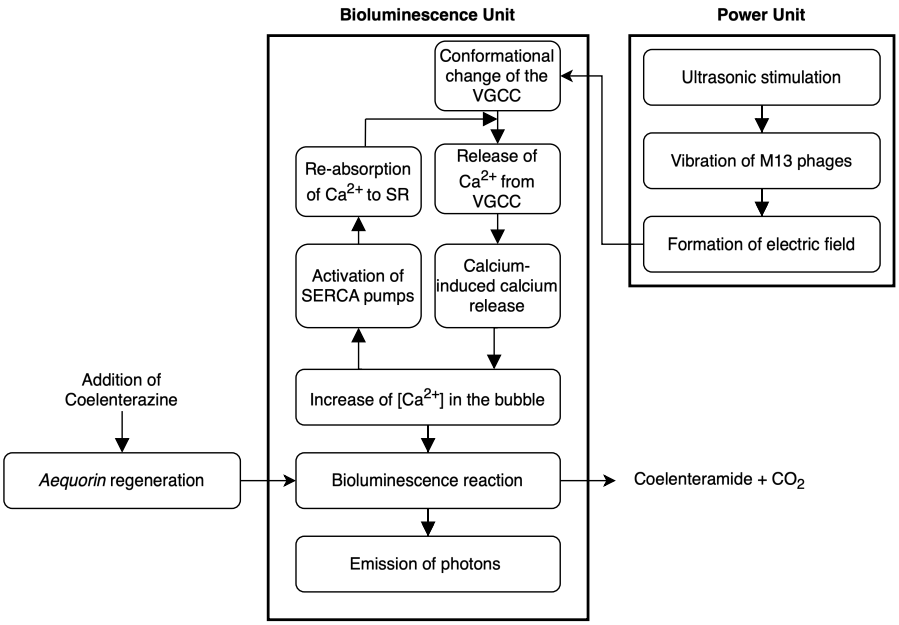

Figure 4.2: Block diagram describing the flow of executed processes in our design.

on both sides of the SR membrane; higher extra-SR calcium levels stimulate the pump's activity, while elevated calcium concentrations within the SR trigger feedback inhibition to regulate the process [166].

In the proposed system, the release of calcium ions from the SR is initiated by the activation of VGCCss on the SR membrane, triggered by the electric field generated by the power unit. While some studies suggest the natural presence of VGCCs on the SR membrane [167], we propose increasing their expression via genetic engineering [168] to ensure the initiation of the calcium ions release process. The VGCCs possess voltage sensor domains that react to the electric fields generated by M13 PENGs, triggering conformational changes in the channel that open the pores and allows calcium ion release.

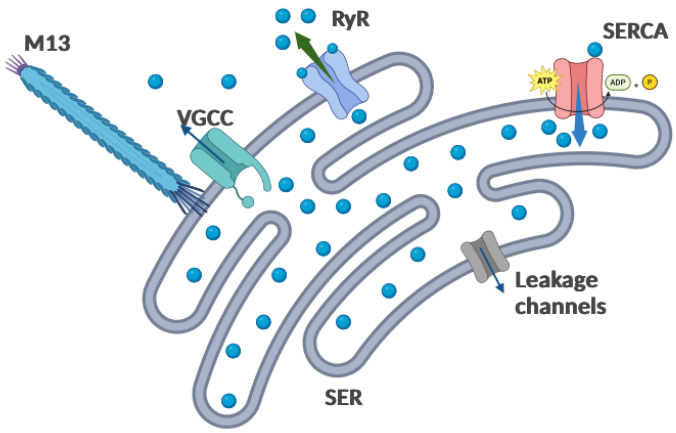

Figure 4.3: The ion channels on the SR membrane that contribute to the CICR.

Following the release of calcium ions from the SR through VGCCs and the subsequent increase in calcium concentration outside the SR, a process known as CICR is triggered, leading to the release of substantial amount of calcium ions into the surrounding environment[2]. In our design, we propose using SR isolated from cardiac muscle cells[3], where RYR2 channels are responsible for regulating CICR (Figure 4.3). These RYR2 channels possess two types of calcium-binding sites on the extra-SR side: high-affinity sites, which trigger calcium release, and low-affinity sites, which inhibit it. This results in a feedback mechanism where low external calcium concentrations activate release, while high concentrations

[2]The exact mechanisms governing CICR vary depending on tissue type, as different cells utilize specific ion channels and intracellular processes for this function. In non-excitable cells, CICR is primarily mediated by IP_3 receptors, while in excitable cells such as neurons and muscle tissues, RYR2 play the dominant role [169].

[3]The isolation of the SR from skeletal muscle is an established process supported by optimized protocols using differential centrifugation and sucrose density gradients. There is also evidence suggesting that isolated organelles can be sustained under suitable conditions [170], [171].

suppress it, creating a bell-shaped curve for calcium regulation [169].

The next stage involves the bioluminescence module. The released calcium ions diffuse through the medium and bind to aequorin photoproteins. This binding triggers the opening of the imidazolone ring in the CLZ peroxy anion, resulting in the formation of an intermediate. As this intermediate returns to its ground state, light is emitted with a peak wavelength of 469 nm. The increase in calcium concentration resulting from CICR will also stimulate the activation of SERCA pumps, ultimately leading to the reuptake of calcium ions into the SR.

For aequorin to emit light again, it must be recharged with CLZ [172]. CLZ can be supplied either through genetically modified bacteria that continuously produce it or by chemical supplementation. However, this study does not focus on the delivery method, assuming its constant presence throughout the experiments. A practical consideration of this scheme is the number of achievable stimulation cycles and the associated limiting factors, particularly in relation to the consumption of bioluminescent components. This aspect is discussed in detail in the Conclusion section.

To maintain biocompatibility and system stability, we suggest encapsulating the components within porous Polydimethylsiloxane (PDMS) nanobubbles [173]. The porous structure allows exchange with the surrounding medium, including diffusion of gaseous byproducts such as CO_2 out of the nanobubble, while still protecting the encapsulated components. Encapsulation in PDMS provides a controlled microenvironment that protects the components from external biological degradation while maintaining their functional integrity.

Literature suggests that such encapsulation can enhance the longevity and stability of biological agents [174].

Figure 4.2 is a block diagram illustrating the sequence of processes in our design. It represents the flow of operations, from ultrasonic energy harvesting to CICR, followed by light emission and calcium reuptake into the SR.

4.3 Modelling the Wireless Bioluminescence Mote

To analyze the behaviour of our proposed design, we will model its components. In this section, we will use equivalent electrical circuits to model the processes and assess their behaviour as well as the functionality of the entire system. Each component is modeled using an electrical circuit analog (see Figure 4.4). The M13 nanogenerator is represented by the equivalent circuit of piezoelectric nanogenerators. Furthermore, we propose a circuit to represent the dynamics of the SR calcium ion release and re absorption. Lastly, the bioluminescent reaction of aequorin, which is driven by Ca^{2+}, is modeled as a diode. A detailed explanation of the system's modelling approach is discussed in the subsequent sections.

4.3.1 Modelling of M13 Nanogenerators

We adopt the modelling scheme proposed in [175] to simulate the first vibrational mode of the M13 PENGs (Figure 4.4). In this scheme, each vibrational mode is represented by an

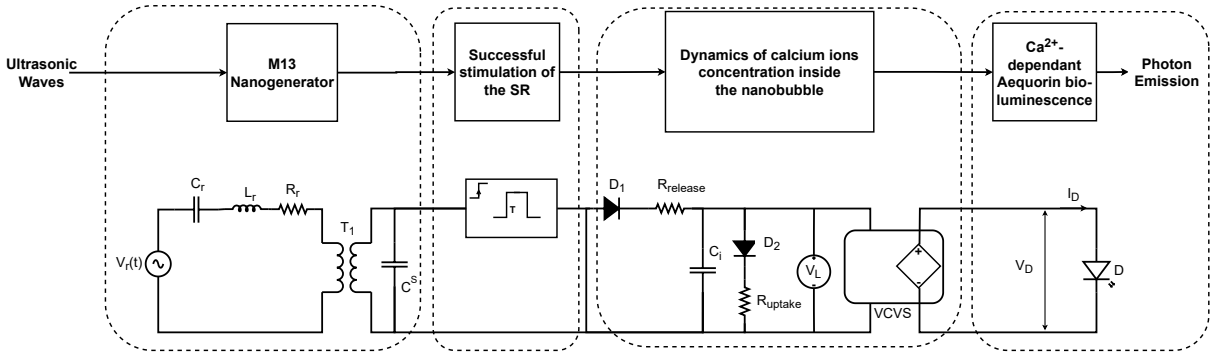

Figure 4.4: Block diagram describing the connectivity of the units forming the system and the equivalent electric circuit emulating it.

RLC equivalent circuit. Specifically, we model the primary vibrational mode, which occurs at the resonance frequency $f_r = 1.2985\,\text{MHz}$, as obtained from FEA (see section 4.2). In this model, the inductor (L_r), capacitor (C_r), and resistor (R_r) correspond to the mass, stiffness, and damping of the nanogenerator, respectively. The capacitor C^S represents the static clamped capacitance, which reflects the capacitance under constant strain conditions. An ideal transformer (T_1) models the electromechanical coupling between the mechanical and electrical domains

To simulate the PENG's performance, the values of the circuit components must first be determined. This is achieved by analyzing the admittance $Y(j\omega)$ of the nanogenerator, which defines the relationship between the applied voltage and the resulting current. FEA of the M13 nanogenerator, based on the parameters derived in section 3.2, enables calculation of the impedance at any given frequency. Furthermore, as shown in Figure 4.4, the equivalent admittance of the nanogenerator can be expressed as:

$$Y(j\omega) = j\omega \left(C^S + \frac{C_{mr}}{1 - L_{mr}C_{mr}\omega^2 + jR_{mr}C_{mr}\omega} \right), \tag{4.1}$$

where, C_{mr}, L_{mr}, and R_{mr} represent the capacitance, inductance, and resistance, respectively, transferred to the secondary side of the transformer T_1 with a voltage transformation ratio of N_{T_1}. These transferred values are related to the original components C_r, L_r, and R_r by the following relationships:

$$L_{mr} = \frac{L_r}{N_{T_1}^2}, \quad R_{mr} = \frac{R_r}{N_{T_1}^2}, \quad C_{mr} = \frac{C_r}{N_{T_1}^2}. \tag{4.2}$$

In Equation 4.1, for very small and very large values of ω, we have:

$$Y(j\omega) = \begin{cases} j\omega \left(C^S + C_{mr} \right) = j\omega \left(C^T \right) & \omega \to 0 \\ j\omega C^S & \omega \to \infty, \end{cases} \tag{4.3}$$

The capacitance C^T represents the static capacitance measured in the absence of external mechanical forces acting on the energy harvester. Using FEA and analyzing the nanogenerator's admittance at both low and high frequencies, we can determine the values of C^S, C_{mr}, and C^T. Furthermore, as the angular frequency ω approaches the resonance frequency ω_r, Equation 4.1 can be rewritten as

$$Y(j\omega) = Y_{\mathrm{d}} + Y_{\mathrm{mot}}, \tag{4.4}$$

where

$$Y_{\mathrm{d}} = j\omega C^{S}, \tag{4.5}$$

and

$$Y_{\mathrm{mot}} = \frac{j\omega C_{mr}}{1 - L_{mr}C_{mr}\omega^2 + jR_{mr}C_{mr}\omega}. \tag{4.6}$$

In these equations, Y_{d} and Y_{mot} refer to the damped admittance and motional admittance, respectively [175]. We apply FEA to determine the nanogenerator's admittance as ω approaches ω_r. The motional admittance values obtained from this analysis are then used to calculate the remaining components of the equivalent circuit, following the approach proposed in [175].

$$\begin{cases} R_{mr} = \dfrac{1}{\max[\mathrm{Re}(Y_{\mathrm{mot}})]} \\ L_{mr} = \dfrac{R_{mr}}{\omega[\min[\mathrm{Im}(Y_{\mathrm{mot}})] - \max[\mathrm{Im}(Y_{\mathrm{mot}})]]} \\ N_{T_1} = \sqrt{\dfrac{1}{L_{mr}}} \end{cases} \tag{4.7}$$

The calculated values for the equivalent circuit of the nanogenerator in our system, found using the above-mentioned procedure, are reported in Table 4.1.

Table 4.1: Parameter values for the equivalent circuit of a single virus fixed-ended M-13 nanogenerator

$\mathbf{R_r}$	$\mathbf{C_r}$	$\mathbf{L_r}$	$\mathbf{N_{T_1}}$	$\mathbf{C^S}$
$1.8M\Omega$	$3.3 \times 10^{-18}F$	$3.6 \times 10^{3}H$	0.01	$2.1 \times 10^{-17}F$

4.3.2 Modelling the Calcium Dynamics

The light emission in our proposed bioluminescence system is driven by the calcium-dependent luminescence of aequorin. Therefore, a key objective of our model is to replicate the dynamics of calcium concentration within the nanobubble, denoted as $[Ca^{2+}]_{int}(t)$. As discussed in section 4.2, the fluctuations in calcium concentration are triggered by the release and reuptake of calcium ions from the SR within the nanobubble. The mechanisms governing calcium release and uptake by SR have been well-documented in previous studies [176], [177].

To model these dynamics, we reference the calcium concentration behaviour observed in human atrial cells. This approach is chosen based on the similarities between the intracellular environment, the confined space of the nanobubble and the analogous role of SR in both systems in regulating calcium dynamics. This allows us to approximate the calcium ion concentration variations within the nanobubble by applying established models from cell biology.

Figure 4.5(a) presents experimental data on average intracellular calcium levels in human atrial myocytes following a stimulation, denoted as $[Ca^{2+}]_{ref}(t)$ in this study. According to [177], once the SR is successfully activated, the time profile of $[Ca^{2+}]_{ref}(t)$ remains

consistent, regardless of the stimulation's duration or amplitude, as long as the stimulation lasts more than 5 ms and exceeds 50 mV. This observation indicates that once the threshold for activation has been passed, the primary processes of CICR and calcium uptake via the SERCA pumps follow a predictable trajectory, regardless of the specific characteristics of the stimulation pulse.

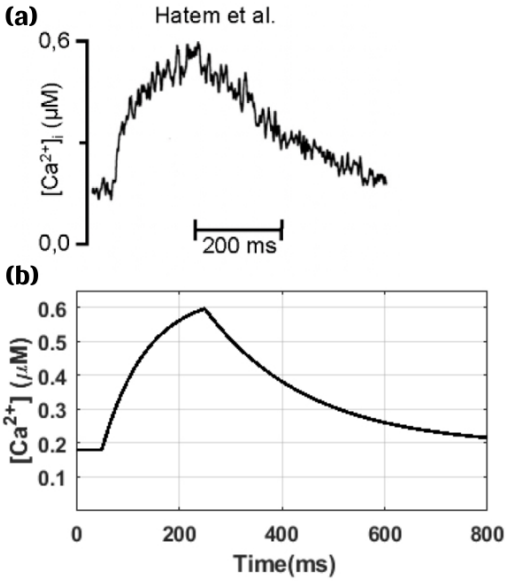

Figure 4.5: (a) Experimentally measured intracellular Ca^{2+} concentration in human atrial myocytes.(b) The transient of calcium concentration in the nanobubble measured from the voltage of the capacitor C in the circuit.

In our model, a monostable multivibrator emulates the activation of CICR. Based on experimental data from [177], the pulse duration is set at 200 ms. Additionally, a capacitor labeled C_{i} is used to represent the calcium ion concentration within the nanobubble. This is because a capacitor's charge and discharge behaviour mimics calcium ion release and

uptake. The circuit is designed with separate charging and discharging pathways to capture the distinct kinetics of calcium release and uptake. Diode D_1 allows the capacitor C_i to charges through resistor R_release. This process with a time constant $\tau_\mathrm{release} = R_\mathrm{release} \times C_\mathrm{i}$ models the SR calcium release. Conversely, the discharge occurs via resistor R_uptake, with a time constant $\tau_\mathrm{uptake} = R_\mathrm{uptake} \times C_\mathrm{i}$, which mimics the calcium uptake by the SR. The component values, specifically $R_\mathrm{release} = 1.8\,\mathrm{M\Omega}$, $R_\mathrm{uptake} = 5\,\mathrm{M\Omega}$, and $C_\mathrm{i} = 50\,\mathrm{nF}$, were chosen to align the charging and discharging dynamics with experimental data shown in Figure 4.5a. Figure 4.5b demonstrates how the voltage across C_i, denoted as $V_{C_\mathrm{i}}(t)$, tracks the measured intracellular calcium concentration in the reference myocyte cell, $[\mathrm{Ca}^{2+}]_\mathrm{ref}(t)$.

In addition to using $[Ca^{2+}]_\mathrm{ref}(t)$ as a reference, the model must also account for the effect of size differences between the engineered and natural SRs on the resulting calcium concentrations. A larger engineered SR can store more calcium ions than its natural counterpart, leading to a higher peak calcium concentration upon stimulation, as more ions are released. Conversely, a smaller engineered SR possesses a reduced calcium storage capacity, resulting in lower peak calcium concentrations over the same time frame. Because the number of ion channels scales with the SR size, we assume that the calcium release and uptake mechanisms adjust proportionally to support this increased ion exchange, thereby maintaining consistent kinetics. We define the calcium concentration within the nanobubble as $[Ca^{2+}]_\mathrm{int}(t)$, and denote the ratio of the engineered to natural SR volumes as n_1. Accordingly, we assume that $[Ca^{2+}]_\mathrm{int}(t)$ scales linearly with n_1 [4].

[4]Here, the effective SR volume refers to the total volume of all SR structures within the nanobubble. Thus, whether calcium is released from a single SR or multiple SRs, the resulting concentration depends on the aggregate SR volume, and the model implicitly accounts for this through the scaling parameter n_1.

Furthermore, because we use myocyte cells as a reference, the volume of the nanobubble compared to the volume of a myocyte also affects the calcium ion concentration in our system. If the nanobubble is smaller, the same quantity of calcium ions is released into a more confined space, which increases the peak concentration, and vice versa for larger nanobubbles. Significant deviations between the ratio of the nanobubble size and its engineered SR, and the ratio of the reference myocyte cell size and its SR, would introduce nonlinearities due to differences in diffusion properties and changes in the kinetics of ion release. However, we assume that for small deviations, these effects are minimal. Thus, we simplify the model by assuming that $[\mathrm{Ca}^{2+}]_{\mathrm{int}}(t)$ is inversely proportional to the ratio of the nanobubble volume to the cell volume, denoted as n_2.

To incorporate these size-dependent effects into our electrical model, we adjust the voltage across the capacitor C_{i}, denoted as $V_{C_{\mathrm{i}}}(t)$, to reflect the scaled calcium concentration inside the nanobubble, $[Ca^{2+}]_{\mathrm{int}}(t)$. Specifically, $V_{C_{\mathrm{i}}}(t)$ is scaled by the physical size ratios to represent changes in calcium concentration arising from variations in the engineered and natural structures. To model this relationship, we introduce a Voltage-Controlled Voltage Source (VCVS) into the equivalent circuit. The gain of the VCVS is defined as:

$$G = \frac{n_1}{n_2}, \tag{4.8}$$

where n_1 and n_2 represent the relative size ratios of the engineered SR and the nanobubble, respectively, compared to their counterparts in a reference myocyte cell.

When $G = 1$, the dimensions of both the engineered SR and the volume of the nanobub-

ble match those of the reference myocyte cell. A scenario with $G > 1$ indicates either an increase in the SR size or a decrease in the nanobubble size, leading to a higher peak calcium concentration due to greater storage capacity or a more confined release environment. Conversely, $G < 1$ corresponds to a reduction in the SR size or an increase in the nanobubble size, resulting in lower calcium storage capacity or a less confined release.

The output voltage of the VCVS, which represents the calcium concentration inside the nanobubble, $[Ca^{2+}]_{\text{int}}(t)$, is expressed as:

$$V_{\text{VCVS}}(t) = G \times V_{C_{\text{i}}}(t). \tag{4.9}$$

4.3.3 Modelling the aequorin's Calcium-Dependent Bioluminescence

With $V_{\text{VCVS}}(t)$ representing the calcium concentration inside the nanobubble, $[Ca^{2+}]_{\text{int}}(t)$, the next objective is to model the calcium-dependent bioluminescent response of aequorin. This response is represented in the equivalent circuit by a behavioral light-emission element, drawn using the LED symbol as a convenient analog component. Here, the symbol is not used to imply the intrinsic rectifying current–voltage behavior of a semiconductor diode. Instead, it serves as a compact circuit representation of a transduction element, whose input is intracellular calcium concentration and its output is photon emission rate. Accordingly, the voltage across the element corresponds to calcium concentration, while the resulting current is defined to represent the rate of photon emission.

To capture the nonlinear calcium response of aequorin, the current–voltage relation assigned to this element is not the standard diode equation, but a redefined empirical constitutive law derived from reported calcium-dependent bioluminescence data [93]. The current $I_D(t)$ through the element is therefore described by the following equation:

$$I_D(t) = \lambda \cdot I_{\max} \left(\frac{1 + K_R \cdot V_D(t)}{1 + K_{TR} + K_R \cdot V_D(t)} \right)^{n_H}. \tag{4.10}$$

Here, $V_D(t) = V_{\mathrm{VCVS}}(t)$, reflects the time-varying calcium concentration in the system. The constants K_R, K_{TR}, and n_H characterize the calcium-binding behaviour of the specific aequorin variant being modeled. $I_{\max}$ denotes the maximum photon output under saturating calcium conditions, and λ is a scaling factor representing the photon emission rate at full activation, typically set to $1\,\mathrm{s}^{-1}$ [93].

This modelling approach is parametrically flexible, allowing it to represent the calcium-dependent bioluminescence of various aequorin variants. Each variant is defined by a unique set of parameters, which determine its luminescent response to calcium. By substituting the appropriate parameter set, the same circuit can model a broad range of photoprotein behaviours.

Typically, for each variant, normalized bioluminescence measurements are experimentally obtained across a range of calcium concentrations and reported as paired values of calcium concentration and relative bioluminescence. To enable the model to represent different aequorin mutants, the response function (Equation 4.10) must be fitted to the experimental bioluminescence data to determine the parameter set $P = \{K_R, K_{TR}, n_H\}$

that best characterizes the observed luminescence profile.

To achieve this, two nonlinear fitting strategies were used and compared. Each method aims to identify the parameter vector $P = \{K_R, K_{TR}, n_H\}$ that minimizes the discrepancy between the model's response and experimentally measured normalized bioluminescence across a range of calcium concentrations. Alternative parameter-estimation approaches could be considered, including standard unweighted Least Squares (LS) minimization, robust regression schemes to reduce sensitivity to outliers, or Bayesian estimators [178]. In the present work, the available response data are typically reported as normalized luminescence values extracted from the literature, for which a detailed and consistent noise model is generally not available. Moreover, because the response spans several orders of magnitude, a suitable fitting method must mitigate the dominance of high-luminescence points while preserving sensitivity in the low-calcium regime without requiring extensive assumptions about the error distribution. For these reasons, two widely used strategies were selected for comparison: a relative error-based LS formulation implemented through weighted residuals, and a log-transformed regression approach that reduces dynamic range during parameter estimation. Although both approaches share the same underlying model function, they differ in how the fitting error is defined and minimized.

Least Squares with Relative Error (LSRE)

The first method is based on LS fitting. The experimental data are given as a set of points $\{([Ca^{2+}]_i, y_i)\}$, where $[Ca^{2+}]_i$ denotes the calcium concentration and y_i denotes the corresponding normalized bioluminescence response reported in the literature. Since the

available data are normalized optical measurements rather than absolute current values, the fitting is performed using the normalized form of Equation 4.10. Under the assumption that photon emission rate is proportional to the current I_D of the behavioral light-emission element, the multiplicative constants in Equation 4.10 are absorbed into the normalization. The resulting dimensionless model function is therefore written as

$$f([\mathrm{Ca}^{2+}]_i; P) = \left(\frac{1 + K_R \cdot [\mathrm{Ca}^{2+}]_i}{1 + K_{TR} + K_R \cdot [\mathrm{Ca}^{2+}]_i} \right)^{n_H}, \tag{4.11}$$

where $P = (K_R, K_{TR}, n_H)$ denotes the vector of model parameters. In this formulation, $f([\mathrm{Ca}^{2+}]_i; P)$ represents the predicted normalized bioluminescence response at calcium concentration $[\mathrm{Ca}^{2+}]_i$. Thus, the fitting is carried out against normalized luminescence data, while I_D remains the circuit-level analog of photon emission rate used in the equivalent-circuit model.

The standard LS objective minimizes the sum of squared residuals between the model prediction and the experimental data. However, this formulation weights all absolute residuals equally. Because the aequorin response spans several orders of magnitude as calcium concentration increases, data points at high luminescence levels tend to dominate the objective function. As a result, the fitted model may achieve good agreement in the high-calcium regime while showing poor accuracy in the low-calcium region. This behavior is illustrated in Figure 4.6(a), where the optimizer disproportionately prioritizes the upper portion of the response curve.

To address this issue, a modified objective function was adopted that minimizes the

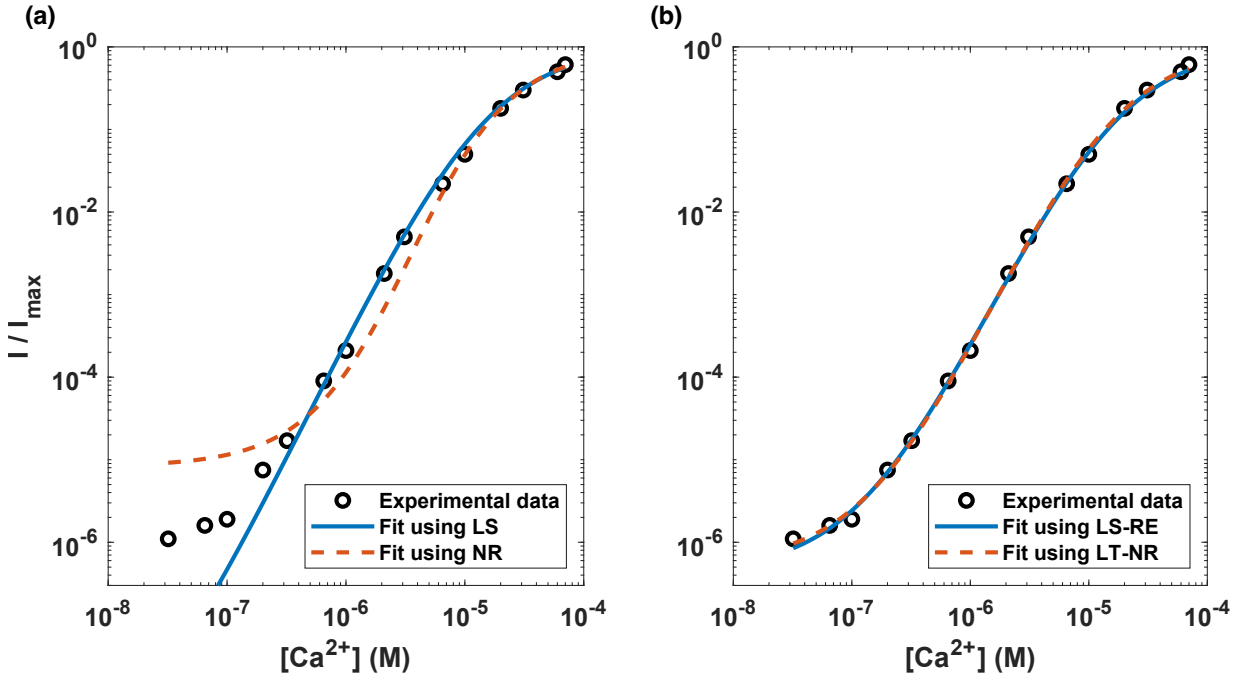

Figure 4.6: Comparison of fitting methods applied to wild type aequorin's calcium-dependent normalized bioluminescence. Experimental data are extracted from [179]. **(a)** Experimental data (black circles) are fitted using standard Least Squares (LS) (blue solid line) and Nonlinear Regression (NR) (orange dashed line). Both methods minimize absolute error, leading to poor fitting at low calcium concentrations. **(b)** Enhanced fitting methods: Least Squares with Relative Error (LSRE) (blue solid line) and Log-Transformed Nonlinear Regression (LTNR) (orange dashed line). These approaches improve fitting across the full range, especially in low-calcium regions, by reducing the dominance of high-luminescence points in the objective function.

relative error at each point rather than the absolute error. In this approach, the residual at each calcium concentration is scaled relative to the corresponding measured value y_i. The resulting weighted LS objective function is defined as:

$$\mathcal{E}_{\text{rel}}(P) = \sum_{i=1}^{N} \left(\frac{f([\text{Ca}^{2+}]_i; P) - y_i}{y_i} \right)^2 . \tag{4.12}$$

This formulation results in proportional accuracy across the full range of calcium concentrations, rather than allowing high calcium concentration data points to dominate. The relative error-based fitting denoted by LSRE was implemented using MATLAB's `lsqnonlin` function, with the residuals defined as in Equation 4.12. As shown in Figure 4.6(b), this approach significantly improved fitting in the low-calcium region.

Log-Transformed Nonlinear Regression (LTNR)

The second method approaches the fitting problem from a statistical regression perspective. In this formulation, the experimentally measured normalized bioluminescence y_i at each calcium concentration $[\mathrm{Ca}^{2+}]_i$ is modeled as the sum of a deterministic component and an additive random error term:

$$y_i = f([\mathrm{Ca}^{2+}]_i; P) + \varepsilon_i, \quad \varepsilon_i \sim \mathcal{N}(0, \sigma^2), \tag{4.13}$$

where $f([\mathrm{Ca}^{2+}]_i; P)$ is defined by Equation 4.11, and ε_i represents independent and identically distributed (i.i.d.) Gaussian noise with zero mean and identical variance across data points. The parameter set $P = \{K_R, K_{TR}, n_H\}$ is estimated by minimizing the sum of squared residuals between measured and predicted values, as in standard LS fitting:

$$\mathcal{E}_{\mathrm{REG}}(P) = \sum_{i=1}^{N} \left(y_i - f([\mathrm{Ca}^{2+}]_i; P)\right)^2. \tag{4.14}$$

This method assumes that the measurement errors have constant absolute variance (i.e. additive noise) across all calcium concentrations. However, this assumption does not hold

for calcium-dependent bioluminescence data, where signal intensity spans several orders of magnitude and the absolute measurement variability increases with the signal level. As a result, in its original form (similar to the LS approach) high-luminescence data points tend to dominate the error function (see Figure 4.6(a)). Unlike `lsqnonlin`, which allows direct customization of the residual vector, MATLAB's `nlinfit` function, used here to implement the Nonlinear Regression (NR) approach, does not support user-defined weighting schemes. To address this limitation, we defined a new regression model in log space, corresponding to multiplicative noise on the original scale:

$$\log_{10}(y_i) = \log_{10}(f([\mathrm{Ca}^{2+}]_i; P)) + \varepsilon_i'. \tag{4.15}$$

This formulation corresponds to assuming a multiplicative noise model on the original scale, i.e., $y_i = f([\mathrm{Ca}^{2+}]_i; P) \cdot 10^{\varepsilon_i'}$. This assumption is appropriate here because the measured bioluminescence spans several orders of magnitude, and the experimental uncertainty increases approximately in proportion to the signal level. In such data, expressing the model in logarithmic space prevents high-intensity points from dominating the optimization. Therefore, the logarithmic transformation reduces the dynamic range of the data, decreases the influence of high-calcium points, and improves the fitting algorithm's sensitivity to low-calcium regions. A representative fit using the LTNR approach is shown in Figure 4.6(b), illustrating the improved agreement at the lower end of the response curve.

Fitting Evaluation Metrics

To enable a quantitative evaluation of the fitting strategies, two relative error metrics were used. These metrics focus on the proportional difference between the fitted model and measured values. The first metric is the Mean Absolute Percentage Error (MAPE), defined as:

$$\text{MAPE} = \frac{100}{N} \sum_{i=1}^{N} \left| \frac{y_i - \hat{y}_i}{y_i} \right|, \tag{4.16}$$

where y_i is the measured bioluminescence value, $\hat{y}_i = f([\text{Ca}^{2+}]_i; P)$ is the model prediction, and N is the number of data points. MAPE expresses the average error as a percentage of the signal magnitude and helps assess how well the model captures the overall proportional trend in the data.

The second metric is the Root Mean Squared Relative Error (RMSRE), defined as:

$$\text{RMSRE} = \sqrt{\frac{1}{N} \sum_{i=1}^{N} \left(\frac{y_i - \hat{y}_i}{y_i} \right)^2}. \tag{4.17}$$

RMSRE serves a similar purpose but places greater emphasis on larger relative error due to the squaring operation. This makes it more sensitive to outliers. In the context of calcium-dependent bioluminescence, RMSRE helps identify poor performance in specific regions of the concentration range.

Parameter estimation of aequorin mutants

With both fitting strategies and comparison metrics defined, we next apply them to

estimate the parameter sets $P = \{K_R, K_{TR}, n_H\}$ for several aequorin mutants. Each mutant exhibits a unique calcium-dependent bioluminescence profile and requires a distinct set of parameter values to reproduce its behavior. The goal is to calibrate the model to each variant's response curve, using the available experimental data.

To validate the adaptability of the model, five specific aequorin mutants were selected for detailed analysis. While engineered mutations exhibit either increased or decreased calcium sensitivity relative to the Wild Type (WT), the selection for this study spans the range from the WT baseline to the variants with the highest reported sensitivities. This ensures that the fitting procedure is evaluated across the dynamic ranges most relevant to the target optogenetics applications, where maximizing photon emission is advantageous. It should be noted that these specific examples serve only as a representative subset. The proposed modelling framework is applicable to any aequorin mutant with experimentally characterized response data. The modular nature of the model enables adaptation to new variants by simply substituting the corresponding parameter set (K_R, K_{TR} and n_H).

To identify the most suitable parameters for each mutant, both modified fitting methods were applied to each example. Fitting quality for each mutant was evaluated using the relative error metrics introduced earlier. These metrics help determine which method provides the most reliable parameter estimates. It should be noted, however, that no single algorithm consistently outperforms the other across all mutants. Differences in the measurement errors and dynamic range of the experimentally measured bioluminescence responses affect how each fitting method responds to specific data sets.

Table 4.2: Fitting performance and estimated parameters for five aequorin mutants using both Least Squares with Relative Error (LSRE) and Log-Transformed Nonlinear Regression (LTNR) methods. For each mutant, the method with the lower fitting error, based on Mean Absolute Percentage Error (MAPE) and Root Mean Squared Relative Error (RMSRE), is highlighted in bold to indicate better fit quality.

Mutant	**LSRE**					**LTNR**				
	MAPE	RMSRE	**Estimated Parameters**			MAPE	RMSRE	**Estimated Parameters**		
			K_R	K_{TR}	n_H			K_R	K_{TR}	n_H
WT [179]	10.87	0.130	7.77e6	130	3.00	**9.52**	**0.122**	**6.22×10^6**	**91**	**3.19**
WT [94]	**14.33**	**0.156**	**8.35×10^6**	**47**	**3.00**	14.56	0.159	7.57e6	38	3.15
Q159D	16.36	0.197	3.39e8	130	1.91	**16.33**	**0.192**	**3.13×10^8**	**111**	**1.95**
Q159T	**32.18**	**0.350**	**4.14×10^7**	**170**	**2.24**	33.46	0.411	6.02e7	230	2.16
QD+AT	**11.34**	**0.149**	**9.99×10^7**	**383**	**1.50**	12.95	0.154	3.75e8	1554	1.49

The results of the fitting procedures for the five representative aequorin mutants are summarized in Table 4.2. For each mutant, both fitting methods were applied, and their respective fitting errors and estimated parameter sets are reported. In each case, the method with the lower fitting error is highlighted to indicate the better-performing approach. For example, the LTNR method produced a more accurate fit for the wild-type mutant described in [179], while the LSRE method achieved lower fitting errors for variants such as Q159T and QD+AT.

The agreement between experimental measurements and model outputs confirms that the circuit-based approach, when appropriately parameterized, can reproduce the luminescence profiles of different aequorin mutants. The same circuit element (the modified diode) can thus be reused across variants through adjustments to the parameter set $P = \{K_R, K_{TR}, n_H\}$.

Updating the model with the estimated parameters

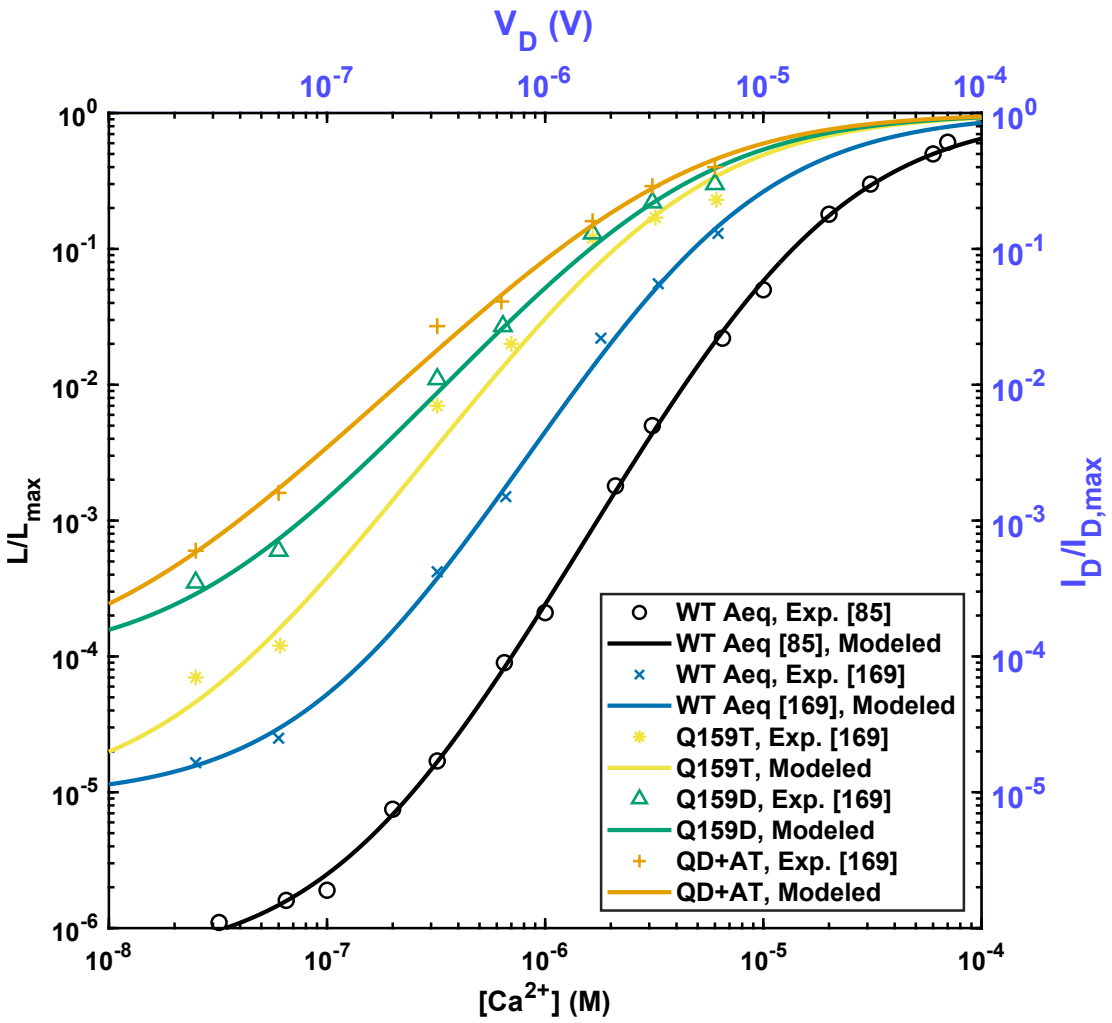

Figure 4.7: Comparison of experimental measurements and model predictions for five aequorin variants. Experimental domain (biology): Markers represent normalized calcium-dependent luminescence ($L/L_{\max}$) as a function of calcium concentration [Ca^{2+}] (bottom x-axis, left y-axis). Data were extracted from previously published studies [94], [179]. Model domain (equivalent circuit): Solid curves show predictions from the modified diode model, expressed as normalized diode current ($I_D/I_{\mathrm{D,max}}$) versus diode voltage (V_D) (top x-axis, right y-axis). Here, I_D is the current through the equivalent diode, $I_{\mathrm{max,D}}$ its maximum value, and V_D the corresponding diode voltage. For each variant, the curve shown corresponds to the fitting method (LSRE or LTNR) that produced the better agreement, based on MAPE and RMSRE (see Table 4.2).

Once the parameter sets are identified, they can be directly substituted into Equation 4.10 to define the current–voltage relationship of the diode component for each mutant. This allows the circuit model to dynamically adjust and reproduce the calcium-dependent bioluminescence behavior of the selected aequorin mutant.

For instance, Figure 4.7 shows the model's output for the five aequorin mutants. In each plot, experimental data (represented by the markers) are overlaid with the corresponding model (illustrated with the curves), computed using the optimized parameter sets within the circuit framework.

4.4 Modelling Light Propagation

To evaluate the proposed system, the next step is to analyze how the bioluminescent light propagates through the surrounding biological tissue. As discussed in Section 2.4.11, several theoretical frameworks can be used to model light propagation in biological media. These include Maxwell's equations, the RTE, and the diffusion approximation. The selection of an appropriate model depends on the optical properties of the tissue, the dominant scattering and absorption mechanisms, and the spatial and temporal scales of interest.

In our case, several factors guide the selection of an appropriate modelling framework. Aequorin exhibits a spectral emission peak at 470 nm, and the surrounding medium is biological tissue, specifically brain tissue, with a spatial domain of interest on the order of tens of micrometers, comparable to the dimensions of several neuronal cells. Modelling

light propagation at this scale using Maxwell's equations would require detailed knowledge of the local electric permittivity and magnetic permeability at subcellular resolution. Such data are not available for a heterogeneous environment like brain tissue [180]. Additionally, this domain is too large for full-wave electromagnetic modelling, which is computationally expensive and ultimately unnecessary due to the loss of phase coherence after a few scattering events (see Section 2.4.11). The diffusion approximation is similarly unsuitable as it assumes that the light is nearly isotropic. However, brain tissues exhibit strong scattering anisotropy ($g \approx 0.9$) [124], resulting in highly forward scattering (See subsection 2.4.7).

Taken together, these considerations led us to model bioluminescent light propagation through brain tissue using the time-dependent RTE (Equation 2.61) which accounts for anisotropic scattering and absorption at the mesoscopic scale, without requiring subcellular detail or assuming isotropy. This makes the RTE particularly well suited for modelling light propagation in strongly forward-scattering brain tissue over tens of micrometers. As such, interference and polarization effects are not considered, consistent with the multiple-scattering regime described in Section 2.4.11.

4.4.1 Computational Modelling of the RTE

Building on the considerations above, we next describe the numerical solution employed to model bioluminescent light propagation. Because general closed-form solutions of the RTE are not available for the geometries and optical conditions considered here, a numerical approach is required. We solved the equation using the Radiation in Absorbing–Scattering

Media (RASM)[5] interface in COMSOL Multiphysics, which discretizes the angular variable through the DOM[6] and converts the integro–differential equation into a coupled system of directional balance equations[7] [181].

The computational domain consists of a brain-tissue volume containing N_s bioluminescent sources and N_n spherical neuronal targets (Figure 4.8 illustrates a representative case with $N_s = N_n = 1$). Each bioluminescent nanobubble $i \in \{1, \ldots, N_s\}$ is modeled as a spherical source (emitter) volume

$$V_i = \left\{ \mathbf{r} \in \mathbb{R}^3 : \ \|\mathbf{r} - \mathbf{r}_{s,i}\| \leq r_{b,i} \right\}, \tag{4.18}$$

where $\mathbf{r}_{s,i}$ is the source center and $r_{b,i}$ is the source (nanobubble) radius. Emitters are incorporated into Equation 2.61 through the volumetric source term $S(\mathbf{r}, \hat{\mathbf{\Omega}}, t)$, where $\hat{\mathbf{\Omega}}$ denotes a unit propagation direction. The total source term is obtained as a superposition

[5] In COMSOL Multiphysics, the *Radiative Transfer in Participating Media* interface (often abbreviated as RTE/RASM in COMSOL documentation) provides a numerical implementation of radiative transfer in scattering/absorbing media and supports multiple angular discretizations, including the discrete ordinates method. See the COMSOL documentation for the interface description and governing equation conventions [181].

[6] The discrete ordinates method (DOM) discretizes propagation directions into a finite set of angular quadrature directions; the RTE is then solved for each direction, producing a coupled set of direction-dependent transport equations. COMSOL adopts this DOM viewpoint in its RTE interface documentation [181].

[7] In COMSOL's DOM formulation, the angular integral term is replaced by a weighted sum over discrete directions, yielding one balance equation per direction coupled through the scattering source term; COMSOL refers to these as "directional" (or direction-resolved) balance/transport equations [181].

of individual contributions,

$$S(\mathbf{r}, \hat{\mathbf{\Omega}}, t) = \sum_{i=1}^{N_s} Q_i(\mathbf{r}, \hat{\mathbf{\Omega}}, t). \tag{4.19}$$

Each emitter is treated as an isotropic volumetric source: for source i, the volumetric emission rate density $q_i(t)$ is taken to be spatially uniform within V_i and zero elsewhere, yielding

$$Q_i(\mathbf{r}, \hat{\mathbf{\Omega}}, t) = \frac{q_i(\mathbf{r}, t)}{4\pi}, \qquad q_i(\mathbf{r}, t) = \begin{cases} q_i(t), & \mathbf{r} \in V_i, \\ 0, & \mathbf{r} \notin V_i. \end{cases} \tag{4.20}$$

The source parameters $\{r_{b,i}, q_i(t)\}$ (design parameters and the resulting emission profile) are assigned individually from the bioluminescence modelling results. This formulation supports single- or multi-source configurations with distinct emission characteristics. Each unique configuration therefore requires a dedicated simulation setup to account for corresponding emission properties.

Each target neuron was modeled as a sphere representing the soma, positioned at specified distances from the sources. Soma radii were selected to reflect biologically relevant dimensions. For light transport, the soma was assigned the same optical properties as the surrounding brain tissue and was not treated as an optically distinct inclusion. This choice is justified by the modelling scale of the RTE. The coefficients μ_a, μ_s, and the phase function used in the RTE are effective-medium optical properties that already represent scattering from cellular and subcellular refractive-index heterogeneity [182], [183]. Introducing micron-scale somatic domains with separate optical coefficients would therefore

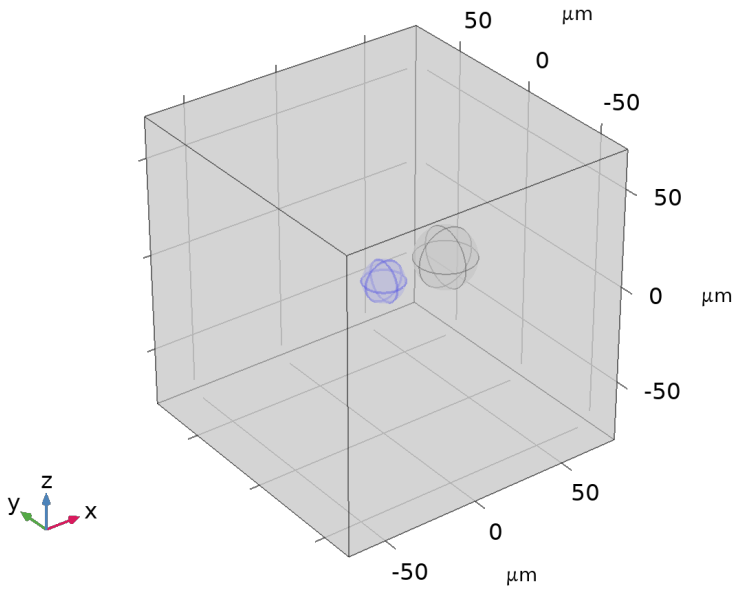

Figure 4.8: Representative geometry used in the radiative transfer simulations. The domain is modeled as a cubic volume of brain tissue with side length $L = 150$ µm. In this representative case, a single bioluminescent mote is placed at the center of the domain and modeled as a spherical *volumetric isotropic* source with radius $r_b = 10$ µm. The neuronal target is represented as a spherical soma with radius $r_{\text{tgt}} = 15$ µm, positioned along the x-axis with center at $x = -50$ µm. The medium (outside the source) is assumed homogeneous and is characterized by the emission-weighted optical properties of the brain region being modeled. While this figure shows a representative configuration, the simulation framework allows multiple bioluminescent motes with varying radii and emission profiles, as well as neuronal targets placed at arbitrary locations within the domain.

require compartment-specific μ_a, μ_s, and phase-function parameters that are not independently parameterized in conventional bulk brain optical property measurements [182], [183]. Moreover, reported refractive-index contrasts between intracellular compartments are typically small, implying that the soma does not constitute a strongly distinct inclusion at the spatial resolution of an RTE model [184], [185]. Consequently, spherical soma are introduced to define biologically meaningful sampling surfaces (specifically the somatic membrane where opsins are expressed) at which the fluence rate $\Phi(\mathbf{r}, t)$ is evaluated, while leaving light transport governed by the brain tissue optical properties.

Dendritic and axonal structures were not explicitly modeled. Although it is possible to incorporate these features to capture finer spatial detail, this would substantially increase both the computational cost and the complexity of the model. Moreover, studies have shown that dendritic illumination requires nearly twice the ChR2 density or irradiance compared to somatic illumination in order to achieve a similar activation threshold [113]. This suggests that somatic stimulation is inherently more efficient. Therefore, the somatic illumination representation offers a biologically meaningful and computationally tractable approximation within our modelling framework.

In terms of boundary conditions, the "Continuity on Interior Boundary"[8] condition was applied at internal interfaces within the COMSOL RASM module. This includes the boundaries between the bioluminescent source and the surrounding medium, as well as the

[8] "Continuity on Interior Boundary" is a COMSOL boundary-condition setting for the RTE interface that enforces continuity of the dependent radiative-transfer variables across an internal boundary when the participating-medium description is intended to be the same on both sides (i.e., no additional interface model such as Fresnel reflection/refraction is introduced). See the COMSOL RTE interface boundary-condition description [181].

boundaries between the target soma and the medium. This ensures conservation of radiative flux across internal boundaries[9]. At the outer surfaces of the cubic domain, "Opaque Surface"[10] boundary conditions were applied. These boundaries absorb all outgoing radiation, thereby preventing unphysical back-reflections and effectively simulating an open, non-reflective tissue environment surrounding the modeled volume[11].

Although aequorin emits across a spectral band, we adopt a monochromatic treatment in our modelling primarily to reduce the computational cost associated with solving the RTE. This simplification is justified because, as shown in Figure 4.9, the empirical optical properties of human brain tissue (which is our target medium) exhibit only modest variation within the 440 nm to 520 nm interval. This interval corresponds to the Full Width at Half Maximum (FWHM) [12] of aequorin's emission spectrum [95].

To account for remaining spectral variation within the emission half-width range, we computed emission-weighted (band-averaged) optical parameters by:

[9] With identical participating-medium properties on both sides of an internal boundary and continuity enforced, the numerical solution does not introduce spurious sources/sinks at that interface; equivalently, transport across the interface is treated as continuous in the participating-medium sense used by the RTE solver [181].

[10] "Opaque Surface" is a COMSOL boundary-condition setting for the RTE interface that treats the boundary as non-transmitting; outgoing radiation is removed (absorbed) rather than reflected back into the domain. It is commonly used as an absorbing (non-reflecting) outer boundary in RTE/DOM simulations to avoid artificial re-entry of radiation from the domain boundary; see COMSOL's RTE boundary-condition definitions [181].

[11] Because the computational domain is finite, an absorbing outer boundary is used so that radiation leaving the modeled volume does not re-enter due to numerical reflection at the truncation boundary; the "Opaque Surface" option implements this absorbing-truncation behavior in COMSOL's RTE interface [181].

[12] FWHM refers to the spectral interval over which the emission intensity of aequorin remains at or above one-half of its maximum value.

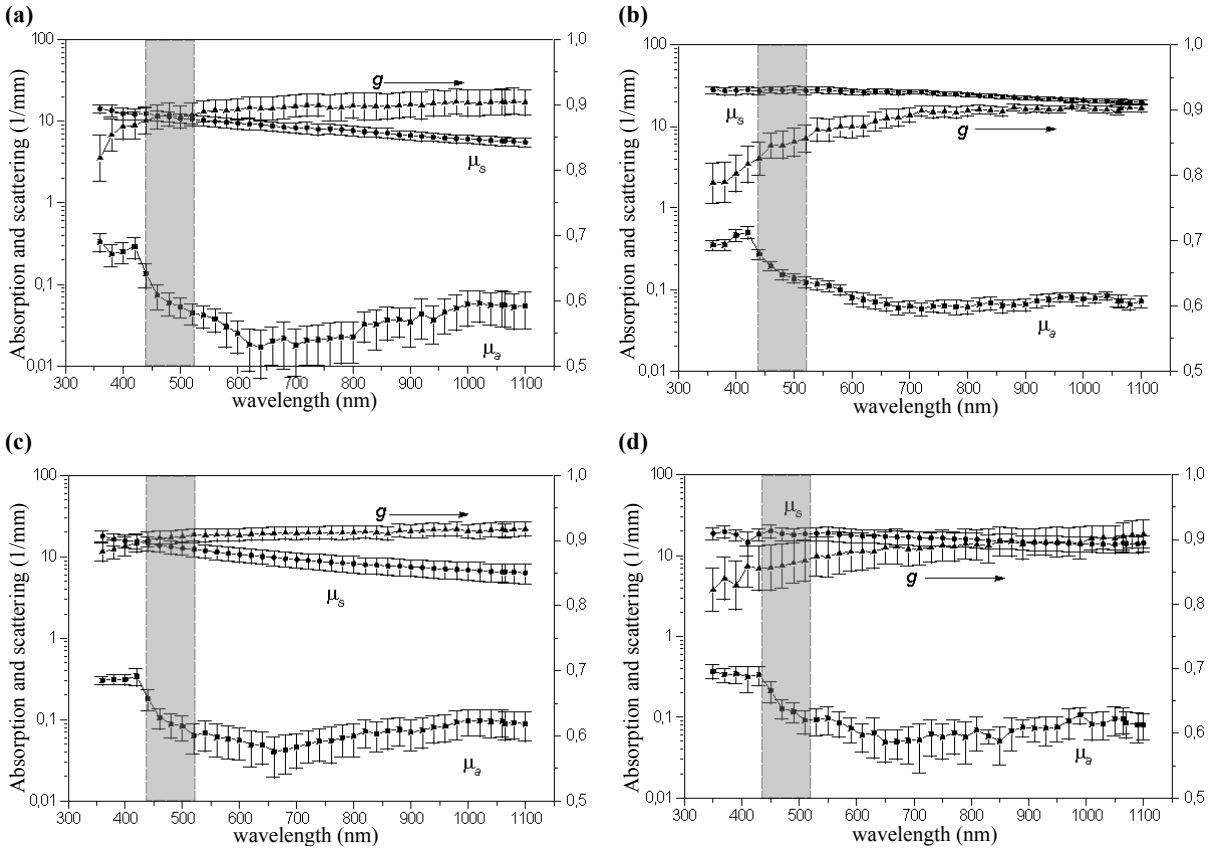

Figure 4.9: Optical properties of four human brain tissues. Average of seven samples for each tissue. Squares: absorption coefficient, circles: scattering coefficient, triangles: anisotropy factors, and bars: standard errors. Native (non-coagulated) samples are shown for (a) grey matter, (b) cerebellum, (c) pons, and (d) thalamus. Overlapping grey rectangles indicate the wavelength range around 470 nm where the aequorin illumination spectrum falls to half of its maximum. The main figure is adapted from [186], and the aequorin wavelength reference is taken from [95].

Table 4.3: Emission-weighted (band-averaged) optical parameters over 440 nm to 520 nm used in the monochromatic simulations at 470 nm. Parameters are computed over the aequorin half-maximum band (440–520 nm) using Equation 4.21 with emission weights extracted from [95].

Tissue	$\langle \mu_a \rangle_S$ [mm^{-1}]	$\langle \mu_s \rangle_S$ [mm^{-1}]	$\langle g \rangle_S$
Grey matter	0.07	10.97	0.88
Cerebellum	0.16	28.02	0.84
Pons	0.11	12.46	0.91
Thalamus	0.18	19.28	0.85

$$\langle X \rangle_S = \frac{\sum_{k=1}^{N} X(\lambda_k)\, S_k}{\sum_{k=1}^{N} S_k}, \qquad X \in \{\mu_a, \mu_s, g\},\ \lambda_k \in 440\,\text{nm to } 520\,\text{nm}. \tag{4.21}$$

Here, $X(\lambda_k)$ denotes the corresponding optical parameter of brain tissue at wavelength λ_k, and S_k is the normalized spectral emission intensity of aequorin at that wavelength. The summation extends over the set of discrete wavelengths $\{\lambda_k\}$ for which experimental optical data are available (see Figure 4.9).

We denote these emission-weighted optical parameters as $\langle \mu_a \rangle_S$, $\langle \mu_s \rangle_S$, and $\langle g \rangle_S$ and use them in the monochromatic RTE. These band-averaged optical parameters provide a compact yet spectrally informed representation of the tissue's optical response to aequorin's emission, while retaining the computational efficiency of a monochromatic treatment.

For this study, we considered four native human brain tissues, namely grey matter, cerebellum, pons, and thalamus. These regions were selected because they are among commonly targeted areas in optogenetics research, and experimentally measured opti-

cal properties are available for them in the relevant spectral range [186]. The resulting emission-weighted parameters are summarized in Table 4.3.

We assigned a refractive index to each brain tissue type considered in the simulations. Experimental optical coherence tomography studies of acute rat brain slices report refractive indices in the range $n = 1.361$–1.369 for grey matter, while white matter exhibits slightly higher values, around $n = 1.41$ [187]. These results indicate that regional differences across grey-matter–dominated structures (such as cortex, cerebellum, pons, and thalamus) fall within a narrow interval and remain close to the lower end of the measured range. Accordingly, we assigned a uniform refractive index of $n = 1.37$ to all four tissue types.

The use of a spatially uniform refractive index constitutes a simplifying assumption that is consistent with the effective-medium nature of the RTE. In this formulation, the optical coefficients μ_s and the phase function already account for scattering arising from unresolved refractive-index heterogeneity at cellular and subcellular scales [182], [183]. Introducing spatial variations in refractive index at the micron scale (e.g., between intracellular and extracellular regions or between soma and surrounding tissue) would therefore require additional interface models and compartment-specific optical parameters that are not independently parameterized in conventional bulk optical property measurements.

Moreover, reported refractive indices of brain tissue and intracellular components fall within a relatively narrow range ($n \approx 1.35$–1.38) [182], [184], [185], implying weak refractive-index contrast. At this level of contrast, Fresnel reflection and refraction effects are small

compared to volumetric scattering and absorption, which dominate light transport in tissue. Consequently, representing the medium with a uniform refractive index provides a physically consistent and computationally efficient approximation for the present RTE-based modelling framework.

For the source domain, we assigned optical properties representative of intracellular cytoplasm. This reflects the fact that photons originate within an aqueous, protein-rich environment (specifically, inside the nanobubble that contains SR, water, and ions) before entering the surrounding tissue. In the blue–green spectral region near $\lambda = 470\,\mathrm{nm}$, molecular absorption by cytosolic constituents is negligible [188]. Accordingly, we set $\mu_a \approx 0\,\mathrm{mm}^{-1}$. Scattering at these wavelengths is governed primarily by refractive-index discontinuities introduced by subcellular organelles and membranes, whereas the homogeneous cytosolic background contributes very little. To reflect this behaviour, we assigned a low scattering coefficient of $\mu_s = 0.1\,\mathrm{mm}^{-1}$ and an anisotropy factor of $g = 0.9$ [188], [189] for the medium inside the nanobubble. Also, refractometric measurements across mammalian cell types report values in the range $n \approx 1.35$–1.38, from which we adopted $n = 1.37$ [189] for the source domain in our modelling.

In the RTE-based modelling, our primary output of interest is the fluence rate, $\Phi(\mathbf{r}, t)$, expressed in units of $\mathrm{W\,mm}^{-2}$. As discussed in subsection 2.4.9, the fluence rate represents the radiant power per unit area incident from all directions at a given point within the

medium. It is computed as the angular integral of the radiance:

$$\Phi(\mathbf{r}, t) = \int_{4\pi} L(\mathbf{r}, \hat{\mathbf{\Omega}}, t)\, \mathrm{d}\Omega,$$

where $L(\mathbf{r}, \hat{\mathbf{\Omega}}, t)$ denotes the radiance in direction $\hat{\mathbf{\Omega}}$. This quantity provides a suitable and physically meaningful metric for our application, because opsin activation depends on the total incident photon flux and is independent of its direction of arrival. Accordingly, we compute $\Phi(\mathbf{r}, t)$ at selected positions within the tissue, with particular attention to the surfaces of neuronal membrane where opsins are expressed. These values are used to assess the light availability for optogenetic activation.

4.4.2 Analytical Benchmark

To evaluate the COMSOL implementation of the RTE, we introduce a reference case for which an analytical expression for the uncollided [13] (ballistic) term can be obtained. The configuration consists of a single spherical bioluminescent source of radius a, centered at the origin (Figure 4.10). The position vector is denoted by $\mathbf{r}$, with $r = |\mathbf{r}|$.

Throughout this section we use the optical parameters introduced in chapter 2, where absorption μ_a, scattering μ_s, total extinction $\mu_t = \mu_a + \mu_s$, anisotropy g, and refractive index n were defined. When multiple regions with different optical properties appear later in the analysis, we will distinguish them using descriptive subscripts (for example, "in" for

[13] The uncollided, or ballistic, component denotes radiance associated with photons that have not undergone any scattering event.

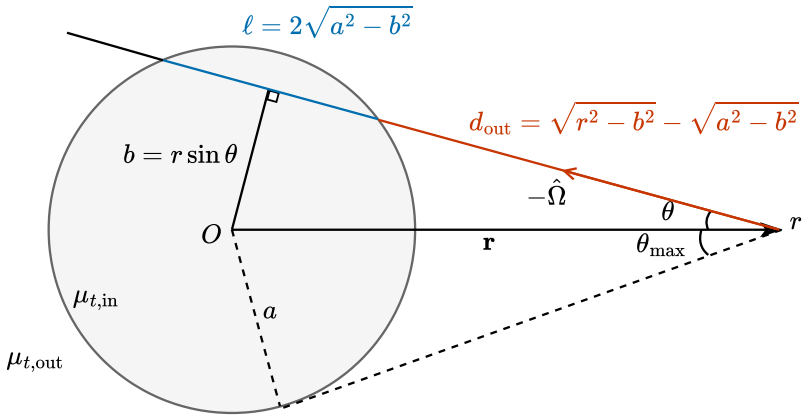

Figure 4.10: Geometry and notation for the spherical source benchmark. A backward ray traced from an observation point at radius $r \geq a$ intersects the source only when the impact parameter satisfies $b \leq a$. In such cases, the ray traverses an external segment of length d_{out} followed by an internal chord of length ℓ. The set of all such directions defines the visible solid angle that contributes to the uncollided radiance integral. The polar angle θ defines the direction of each ray relative to the radial vector $\mathbf{r}$.

parameters inside the emitting region and "out" for those in the surrounding tissue).

The medium is divided into two regions. Inside the source ($r < a$), the absorption and scattering coefficients are ($\mu_{a,\text{in}}$, $\mu_{s,\text{in}}$), and the corresponding total extinction coefficient is $\mu_{t,\text{in}} = \mu_{a,\text{in}} + \mu_{s,\text{in}}$. Outside the source ($r \geq a$), the surrounding tissue is homogeneous with coefficients ($\mu_{a,\text{out}}$, $\mu_{s,\text{out}}$) and $\mu_{t,\text{out}} = \mu_{a,\text{out}} + \mu_{s,\text{out}}$.

The source emits uniformly throughout its volume with isotropic power density q [W/mm^3], giving a total emitted power $P_0 = \frac{4\pi}{3} a^3 q$. In the analysis that follows, the radiance field is evaluated only in the external region $r \geq a$, where the medium is homogeneous and the uncollided solution of the RTE can be obtained in closed form.

Because the characteristic dimensions of the source and surrounding tissue are on the

micrometer scale, the photon transit time (femtoseconds) is negligible compared to the millisecond timescale of bioluminescent emission. The problem can therefore be treated as quasi-stationary. We thus consider the steady-state form of the RTE. From Equation 2.61, recall the time-dependent formulation:

$$\frac{1}{v}\frac{\partial L(\mathbf{r},\hat{\mathbf{\Omega}},t)}{\partial t} = -\hat{\mathbf{\Omega}}\cdot\nabla L(\mathbf{r},\hat{\mathbf{\Omega}},t) - \mu_t(\mathbf{r})L(\mathbf{r},\hat{\mathbf{\Omega}},t) + \mu_s(\mathbf{r})\int_{4\pi} p(\mathbf{r};\hat{\mathbf{\Omega}}'\to\hat{\mathbf{\Omega}})\,L(\mathbf{r},\hat{\mathbf{\Omega}}',t)\,d\Omega' + S(\mathbf{r},\hat{\mathbf{\Omega}},t). \tag{4.22}$$

In steady state, the radiance does not vary in time, so the time derivative vanishes. The transport equation then reduces to:

$$\hat{\mathbf{\Omega}}\cdot\nabla L(\mathbf{r},\hat{\mathbf{\Omega}}) + \mu_t(\mathbf{r})\,L(\mathbf{r},\hat{\mathbf{\Omega}}) = \mu_s(\mathbf{r})\int_{4\pi} p(\mathbf{r};\hat{\mathbf{\Omega}}'\to\hat{\mathbf{\Omega}})\,L(\mathbf{r},\hat{\mathbf{\Omega}}')\,d\Omega' + S(\mathbf{r},\hat{\mathbf{\Omega}}). \tag{4.23}$$

The term $\hat{\mathbf{\Omega}}\cdot\nabla L(\mathbf{r},\hat{\mathbf{\Omega}})$ represents directional streaming of radiance along $\hat{\mathbf{\Omega}}$. The quantity $\mu_t(\mathbf{r})\,L(\mathbf{r},\hat{\mathbf{\Omega}})$ accounts for losses due to absorption and scattering out of direction $\hat{\mathbf{\Omega}}$. The integral term gives the in-scattered [14] contribution from all incoming directions, weighted by the phase function p. The term $S(\mathbf{r},\hat{\mathbf{\Omega}})$ denotes any volumetric radiance emitted or injected into direction $\hat{\mathbf{\Omega}}$.

The radiance field described by the steady-state RTE contains contributions from photons that reach $\mathbf{r}$ without scattering and from photons that have undergone one or more scattering events. Owing to the linearity of the transport equation, these contributions

[14] Here, *in-scattering* term represents photons that are redirected by scattering events from other directions $\hat{\mathbf{\Omega}}'$ into the observation direction $\hat{\mathbf{\Omega}}$ at position $\mathbf{r}$, thereby increasing the radiance along $\hat{\mathbf{\Omega}}$.

may be separated by superposition. We therefore write

$$L(\mathbf{r}, \hat{\mathbf{\Omega}}) = L^{(0)}(\mathbf{r}, \hat{\mathbf{\Omega}}) + L^{(c)}(\mathbf{r}, \hat{\mathbf{\Omega}}), \tag{4.24}$$

where $L^{(0)}(\mathbf{r}, \hat{\mathbf{\Omega}})$ denotes the uncollided (ballistic) radiance and $L^{(c)}(\mathbf{r}, \hat{\mathbf{\Omega}})$ the radiance due to all photons that have scattered at least once.

Substituting this decomposition into Equation 4.23 gives:

$$\begin{aligned} &[\hat{\mathbf{\Omega}} \cdot \nabla L^{(0)}(\mathbf{r}, \hat{\mathbf{\Omega}}) + \mu_t(\mathbf{r}) L^{(0)}(\mathbf{r}, \hat{\mathbf{\Omega}})] + [\hat{\mathbf{\Omega}} \cdot \nabla L^{(c)}(\mathbf{r}, \hat{\mathbf{\Omega}}) + \mu_t(\mathbf{r}) L^{(c)}(\mathbf{r}, \hat{\mathbf{\Omega}})] \\ &= \mu_s(\mathbf{r}) \int_{4\pi} p(\mathbf{r}; \hat{\mathbf{\Omega}}' \to \hat{\mathbf{\Omega}}) \left[L^{(0)}(\mathbf{r}, \hat{\mathbf{\Omega}}') + L^{(c)}(\mathbf{r}, \hat{\mathbf{\Omega}}') \right] \mathrm{d}\Omega' + S(\mathbf{r}, \hat{\mathbf{\Omega}}) \end{aligned} \tag{4.25}$$

where the two parenthetical terms on the left describe streaming and attenuation of the uncollided and collided components, respectively. On the right-hand side, the first integral gives the contribution obtained when the uncollided radiance field is redirected into direction $\hat{\mathbf{\Omega}}$ by scattering at $\mathbf{r}$. The second integral gives the corresponding contribution from the collided radiance field, whose photons have previously scattered elsewhere in the medium and undergo an additional scattering event at $\mathbf{r}$ into direction $\hat{\mathbf{\Omega}}$.

By construction, $L^{(0)}$ represents radiance corresponding to photons that have not undergone any scattering event. Consequently, it cannot receive contributions from either of the in-scattering integrals in Equation 4.25 and must satisfy a transport equation containing only streaming, attenuation, and the source term:

$$\hat{\mathbf{\Omega}} \cdot \nabla L^{(0)}(\mathbf{r}, \hat{\mathbf{\Omega}}) + \mu_t(\mathbf{r}) L^{(0)}(\mathbf{r}, \hat{\mathbf{\Omega}}) = S(\mathbf{r}, \hat{\mathbf{\Omega}}). \tag{4.26}$$

The collided component $L^{(c)}$ then satisfies the complementary equation

$$\begin{aligned} &\hat{\mathbf{\Omega}} \cdot \nabla L^{(c)}(\mathbf{r}, \hat{\mathbf{\Omega}}) + \mu_t(\mathbf{r}) L^{(c)}(\mathbf{r}, \hat{\mathbf{\Omega}}) \\ &= \mu_s(\mathbf{r}) \int_{4\pi} p(\mathbf{r}; \hat{\mathbf{\Omega}}' \to \hat{\mathbf{\Omega}})\, L^{(0)}(\mathbf{r}, \hat{\mathbf{\Omega}}')\, d\Omega' \;+\; \mu_s(\mathbf{r}) \int_{4\pi} p(\mathbf{r}; \hat{\mathbf{\Omega}}' \to \hat{\mathbf{\Omega}})\, L^{(c)}(\mathbf{r}, \hat{\mathbf{\Omega}}')\, d\Omega', \end{aligned} \tag{4.27}$$

where the first integral gives the contribution due to the uncollided radiance being redirected into direction $\hat{\mathbf{\Omega}}$ by scattering at $\mathbf{r}$, and the second integral gives the corresponding contribution generated from the collided radiance field.

For the near-source benchmark considered in this section, we focus exclusively on the uncollided component $L^{(0)}$ of the radiance described by Equation 4.26. This choice is motivated by two main considerations. First, the governing Equation 4.26 has a closed-form solution, which enables an analytical expression suitable for comparison with numerical results. Second, in the immediate vicinity of the source, the uncollided term is expected to dominate the radiance field, as photons that have undergone one or more scattering events represent only a small fraction of the total energy at such short distances. As a result, the analytical solution provides a reliable lower bound on the full radiance, while the complete numerical solution of the RTE in COMSOL serves as the reference for the total response. In this sense, the analytical expression of the uncollided fluence rate serves as a controlled benchmark in a regime where a closed-form solution is both available and physically meaningful.

The uncollided component obeys Equation 4.26. Its solution is obtained by integrating this equation along the backward ray originating from $\mathbf{r}$ in direction $-\hat{\mathbf{\Omega}}$. Let $\xi \geq 0$ denote the path length measured along this ray, and let σ be a dummy running variable over the same path. The formal solution may be written as:

$$L^{(0)}(\mathbf{r}, \hat{\mathbf{\Omega}}) = \int_0^{\infty} S(\mathbf{r} - \xi\hat{\mathbf{\Omega}}, \hat{\mathbf{\Omega}}) \exp\left[- \int_0^{\xi} \mu_t(\mathbf{r} - \sigma\hat{\mathbf{\Omega}})\, d\sigma \right] d\xi, \tag{4.28}$$

where the inner integral represents the optical depth accumulated along the segment of the ray between the observation point and the point $\mathbf{r} - \xi\hat{\mathbf{\Omega}}$. Full derivations of this formal solution are provided in standard radiative transfer texts, e.g. [190], [191].

Equation 4.28 shows that the uncollided radiance at $\mathbf{r}$ collects contributions from all source points on the backward ray, each attenuated according to the optical depth between its emission location and $\mathbf{r}$. Only locations where the source term $S(\mathbf{r} - \xi\hat{\mathbf{\Omega}}, \hat{\mathbf{\Omega}}) \neq 0$ contribute to the integral.

We now evaluate Equation 4.28 for the spherical source geometry shown in Figure 4.10. The source is centered at the origin with radius a. The observation point lies in the exterior region, with $r = \|\mathbf{r}\| \geq a$. A backward ray in direction $-\hat{\mathbf{\Omega}}$ forms a polar angle θ with the outward radial direction $\hat{\mathbf{r}} = \mathbf{r}/r$.

It is convenient to introduce the impact parameter

$$b \equiv r \sin\theta, \tag{4.29}$$

which is the minimum distance between the ray and the origin. The backward ray intersects the spherical source if and only if $b \leq a$. Only such rays contribute to $L^{(0)}(\mathbf{r}, \hat{\mathbf{\Omega}})$, because the source term vanishes outside the sphere.

For directions with $0 \leq b \leq a$, the backward ray consists of two contiguous segments. The first is an exterior segment from the observation point to the sphere boundary, with length:

$$d_{\text{out}}(r, b) = \sqrt{r^2 - b^2} - \sqrt{a^2 - b^2}. \tag{4.30}$$

Along this segment, the source term vanishes, i.e., $S(\mathbf{r} - \xi\hat{\mathbf{\Omega}}, \hat{\mathbf{\Omega}}) = 0$, and the extinction coefficient is constant: $\mu_t = \mu_{t,\text{out}}$.

The second is an interior segment that is the chord inside the spherical source, with length

$$\ell(b) = 2\sqrt{a^2 - b^2}. \tag{4.31}$$

On this segment, the source term is isotropic and uniform, given by $S(\mathbf{r} - \xi\hat{\mathbf{\Omega}}, \hat{\mathbf{\Omega}}) = q/(4\pi)$ [$\text{W}\cdot\text{mm}^{-3}\cdot\text{sr}^{-1}$], and the extinction coefficient is given by $\mu_t = \mu_{t,\text{in}}$.

For a source point on the interior segment of the ray, the path length from the observation point can be written as $\xi = d_{\text{out}} + \xi_{\text{in}}$, where d_{out} is the distance traveled in the exterior medium and ξ_{in} is the distance traveled inside the sphere. Because μ_t is piecewise

constant along the ray, the optical-depth integral splits:

$$\begin{aligned}\int_0^{\xi} \mu_t(\mathbf{r} - \sigma\hat{\mathbf{\Omega}})\, d\sigma &= \int_0^{d_{\text{out}}} \mu_{t,\text{out}}\, d\sigma + \int_{d_{\text{out}}}^{d_{\text{out}}+\xi_{\text{in}}} \mu_{t,\text{in}}\, d\sigma \\ &= \mu_{t,\text{out}}\, d_{\text{out}} + \mu_{t,\text{in}}\, \xi_{\text{in}}.\end{aligned} \tag{4.32}$$

Thus the total attenuation factor separates into an exterior part and an interior part:

$$\exp\left[-\int_0^{\xi} \mu_t(\mathbf{r} - \sigma\hat{\mathbf{\Omega}})\, d\sigma\right] = \exp[-\mu_{t,\text{out}}\, d_{\text{out}}]\, \exp[-\mu_{t,\text{in}}\, \xi_{\text{in}}]. \tag{4.33}$$

Furthermore, the source term $S(\mathbf{r} - \xi\hat{\mathbf{\Omega}}, \hat{\mathbf{\Omega}})$ is nonzero only on the interior segment of the ray. Therefore the outer integral in (4.28) reduces to integration over the interior chord only. Introducing a local interior coordinate u, measured from the entry point on the sphere boundary along the ray, we can write any point on the chord as $\mathbf{r} - (d_{\text{out}} + u)\hat{\mathbf{\Omega}}$ with $0 \le u \le \ell(b)$. Along this segment one has $\xi = d_{\text{out}} + u$ and $d\xi = du$, so that

$$L^{(0)}(r, \theta) = \frac{q}{4\pi}\, \exp[-\mu_{t,\text{out}}\, d_{\text{out}}(r, b)] \int_0^{\ell(b)} e^{-\mu_{t,\text{in}}\, u}\, du. \tag{4.34}$$

Evaluating the remaining exponential integral gives the closed-form expression

$$L^{(0)}(r, \theta) = \frac{q}{4\pi\, \mu_{t,\text{in}}}\, \exp[-\mu_{t,\text{out}}(\sqrt{r^2 - b^2} - \sqrt{a^2 - b^2})]\, [1 - e^{-2\mu_{t,\text{in}}\sqrt{a^2-b^2}}]. \tag{4.35}$$

The uncollided fluence rate is obtained by integrating the radiance over all directions,

$$\Phi^{(0)}(r) = \int_{4\pi} L^{(0)}(r, \hat{\mathbf{\Omega}})\, d\Omega. \tag{4.36}$$

Because the geometry and source are spherically symmetric, the radiance depends only on the polar angle θ measured from the radial direction. The azimuthal angle φ (defined in the usual spherical-coordinate sense around $\hat{\mathbf{r}}$) does not appear in the geometry and the integrand is independent of it. The integration over φ therefore contributes a factor of 2π, and the solid-angle element reduces to

$$d\Omega = 2\pi \sin\theta\, d\theta. \tag{4.37}$$

Using the relation $b = r\sin\theta$, the change of variables $\theta \mapsto b$ gives

$$d\Omega = \frac{2\pi\, b\, db}{r\sqrt{r^2 - b^2}}. \tag{4.38}$$

A backward ray with impact parameter $b > a$ does not intersect the source and contributes no uncollided radiance, i.e. $L^{(0)}(r, \theta) = 0$ for $b > a$. Thus the angular integral is restricted to $0 \le b \le a$, and the fluence rate in the exterior region becomes

$$\Phi^{(0)}(r) = \frac{q}{2\,\mu_{t,\mathrm{in}}} \int_0^a \frac{b}{r\sqrt{r^2 - b^2}}\, \exp\Big[-\mu_{t,\mathrm{out}}(\sqrt{r^2 - b^2} - \sqrt{a^2 - b^2})\Big]\, [1 - e^{-2\mu_{t,\mathrm{in}}\sqrt{a^2 - b^2}}]\, db, \qquad r \ge a. \tag{4.39}$$

This expression provides the radial dependence of the steady-state ballistic fluence rate

outside the source for a uniformly emitting sphere with constant volumetric power density q. For a time-dependent illumination, the source emission is modulated by a temporal envelope $E(t)$. Under this assumption and given the negligible propagation time in the medium, the instantaneous ballistic fluence rate can be obtained by multiplying the spatial profile in Equation 4.39 by $E(t)$,

$$\Phi^{(0)}(r,t) = E(t)\,\Phi^{(0)}(r), \qquad r \geq a. \tag{4.40}$$

This time-dependent ballistic fluence rate serves as the analytical benchmark for the ballistic (uncollided) fluence rate outside the source.

5

Simulation Results

5.1 Analysis of the Mote's Behaviour

This section investigates the illumination response of the proposed wireless bioluminescent system and evaluates how variations in design parameters influence the system's behaviour. The analysis focuses on three adjustable design parameters: the aequorin concentration

[Aq], the nanobubble radius r_B, and the relative SR volume fraction ϕ_{SR}.

5.1.1 General Simulation Setup and Parameter Definitions

Simulations were conducted in MATLAB Simulink (Version 2024a), and the results are reported in terms of three primary observables: the calcium ion concentration within the nanobubble, the instantaneous illumination rate, and the total photon emission over a single stimulation cycle.

The calcium concentration, denoted as $[Ca^{2+}]$, is obtained from the voltage across capacitor C_i in the equivalent circuit (see Figure 4.4). The illumination rate is determined from the current through diode D, which follows the nonlinear emission model described in subsection 4.3.3, expressed by:

$$I_D(t) = \lambda \cdot I_{\max} \left(\frac{1 + K_R \cdot V_D(t)}{1 + K_{TR} + K_R \cdot V_D(t)} \right)^{n_H}. \tag{5.1}$$

Here, λ is a normalization factor (typically set to $1\,\mathrm{s}^{-1}$ [93]), I_D and V_D denote the current through and the voltage across the diode, respectively. K_R, K_{TR}, and n_H are variant-specific coefficients. The term $I_{\max}$ represents the maximum photon output under saturating calcium conditions and is defined as:

$$I_{\max} = N_{Aq}\,\Phi, \tag{5.2}$$

with quantum yield of aequorin's bioluminescence reaction $\phi_{\mathrm{SR}} = 0.3$ [172] and N_{Aq} repre-

senting the total number of aequorin molecules:

$$N_{Aq} = [\text{Aq}] \times N_A \times V_{\text{bubble}} = [\text{Aq}] \times N_A \times \frac{4}{3}\pi r_B^3 \times 10^3, \tag{5.3}$$

where $[\text{Aq}](mol/L)$ is the aequorin concentration, $N_A(mol^{-1})$ is Avogadro's number, and $r_B(m)$ is the nanobubble radius.

The total number of emitted photons is obtained by integrating the illumination rate over the entire simulation duration, providing a cumulative measure of photon emission from the system.

To quantify the volume of the engineered SR, we introduce the parameter ϕ_{SR}, defined as the fraction of nanobubble volume allocated to the SR compartment:

$$V_{\text{SR,eng}} = \phi_{\text{SR}} \cdot V_{\text{bubble}}. \tag{5.4}$$

Substituting this relationship into Equation 4.8 yields a geometric scaling term that depends on ϕ_{SR}:

$$G(\phi_{\text{SR}}) = \phi_{\text{SR}} \cdot \frac{V_{\text{myocyte,ref}}}{V_{\text{SR,ref}}}. \tag{5.5}$$

This formulation defines the SR volume as a fraction of the nanobubble volume, which permits controlling ϕ_{SR} to examine the effect of SR volume on calcium dynamics and illumination output. Defining the SR in relative rather than absolute terms also prevents

unrealistic configurations that would occur if the SR volume were specified independently. This constraint avoids cases in which the SR occupies an unphysically small or excessively large portion of the nanobubble.

The concentration of aequorin $[Aq]$ is determined from its solubility characteristics. Based on commercially available purified aequorin products[1], the maximum molar concentration can be estimated as:

$$[Aq]_{\max} = \frac{\text{Solubility (g/L)}}{\text{Molecular Weight (g/mol)}} = \frac{10}{21{,}700} = 0.000461\,\text{mol/L} = 461\,\mu\text{M}. \tag{5.6}$$

We introduce a dimensionless coefficient α to represent the ratio of the working concentration to this maximum limit. This approach provides flexibility to scale aequorin concentrations in different test scenarios.

5.1.2 Overview of the Test Scenarios

Figure 5.1 presents the simulated time-domain responses for four representative conditions based on the QD+AT aequorin mutant.[2] Each case reflects a distinct combination of the three design parameters, as listed in Table 5.1. Each scenario isolates the effect of one

[1] Purified aequorin products typically have a solubility of $10\,\text{mg}\,\text{mL}^{-1}$ and a molecular weight of 21.7 kDa [192].

[2] The QD+AT variant was selected for this analysis due to its higher photon yield compared to other mutants. As discussed in subsection 4.3.3, the same circuit model can be adapted for alternative variants by substituting the relevant diode parameters.

Table 5.1: Description of the Four Test Scenarios.

	[Aq] (μM)	Nanobubble Radius (μm)	$\phi(SR)$ (%)	Peak Illumination Rate(Photon/s)
Scenario #1	350	15	3	3.7×10^8
Scenario #2	350	**19.5**	3	8.1×10^8
Scenario #3	350	15	**3.9**	5.17×10^8
Scenario #4	**455**	15	3	4.81×10^8

design parameter by increasing it by 30% relative to scenario 1, while all other parameters remain constant.

In all cases, the ultrasonic stimulation duration was set to 5 ms, as shown in Figure 5.1(a). This duration initiates CICR in as described in Section 4.2. Pulses shorter than this threshold do not trigger CICR and result in calcium concentrations near baseline levels. Stimulation begins 50 ms after the start of the simulation to establish a baseline prior to activation.

5.1.3 Scenario-Specific Results

In the first scenario in Figure 5.1, the geometrical parameters of the engineered system match those of the reference myocyte cell[3].

[3]Reference myocyte cell data: cell volume 14 000 µm^3, with the SR occupying approximately 3 % of this volume [176], as described in Table 5.1. This equates to a nanobubble with a radius of 15 µm and an SR volume of 420 µm^3.

Moreover, for this scenario we set $[Aq]$ to 350 µM corresponding to $\alpha = 0.76$:

$$[Aq] = \alpha \times [Aq]_{\max} = 0.76 \times 461 = 350\,\mu\text{M}. \tag{5.7}$$

This provides flexibility to increase aequorin concentrations in the subsequent test scenarios.

The subplots (b), (c), and (d) in Figure 5.1, display the time evolution of calcium concentration, illumination rate, and cumulative photon emission, respectively.

Upon ultrasonic stimulation at $t = 50$ ms, we observe the onset of CICR in Figure 5.1(b). For scenario 1 (black curve), the calcium concentration within the bubble reaches a peak of approximately 516 nM. This transient increase in calcium concentration produces a corresponding peak illumination rate of 3.7×10^8 photons/s, as shown in Figure 5.1(c). Over the course of one second, the cumulative photon emission reaches 1.44×10^8, as illustrated in Figure 5.1(d).

In scenario 2 (orange curves in Figure 5.1), the nanobubble radius was increased to 19.5 µm. As shown by the orange curve in subplot (b), the calcium concentration profile remains unchanged compared to scenario 1. This occurs because the relative SR volume fraction, ϕ_{SR}, was kept constant at 3%. Consequently, the absolute SR volume increases proportionally with the larger bubble size, leading to a greater total number of released calcium ions. However, since these ions are distributed within a proportionally larger nanobubble, the resulting calcium concentration remains unchanged.

In contrast, the red curve in subplot (c) shows an increase in illumination rate, with

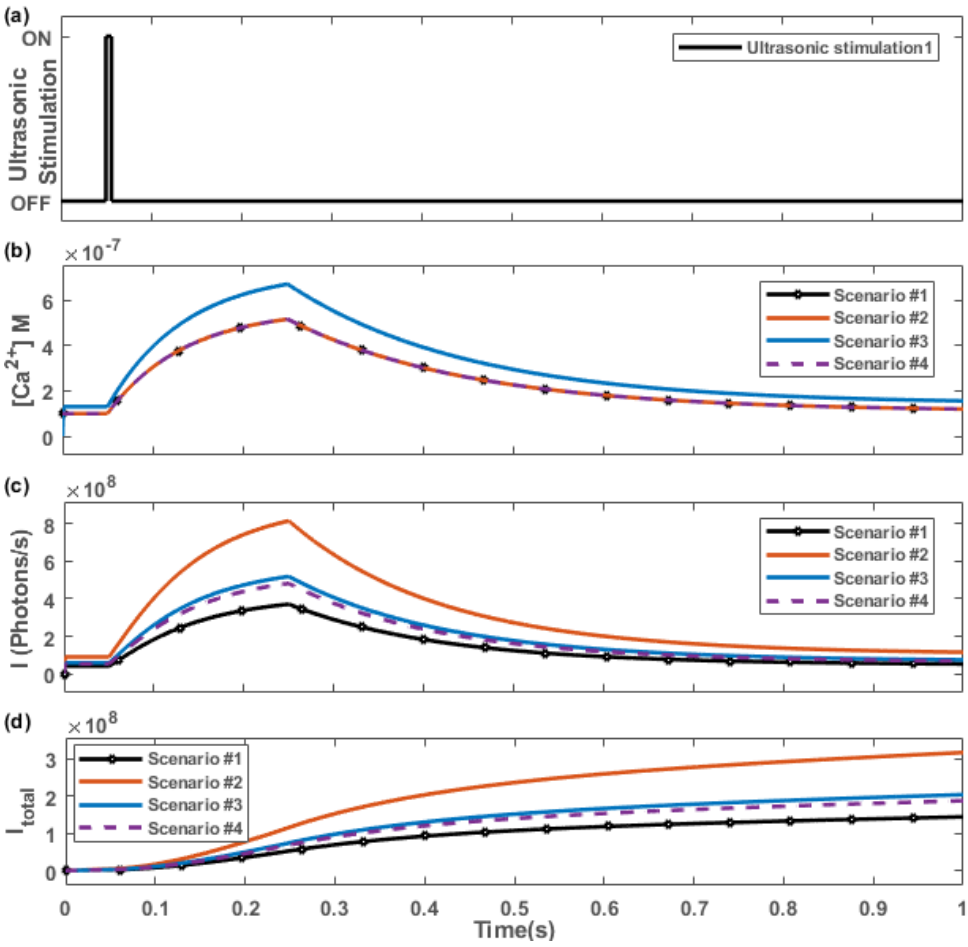

Figure 5.1: The behaviour of the system under four test scenarios. (a) Duration of ultrasonic stimulation, (b) dynamics of calcium concentration inside the bubble, (c) illumination rate and (d) the total emitted photons.

a peak of approximately 8.1×10^8 photons/s. This increase results from the greater total number of aequorin molecules present in the larger bubble. Although the aequorin concentration remains constant, the expanded volume yields a higher absolute number of aequorin molecules, which increases the likelihood of calcium binding and leads to an increased photon emission rate. As shown in subplot (d), the total number of photons emitted during the 1 s cycle reaches 3.15×10^8 in this case.

In scenario 3 (blue curves in Figure 5.1), we investigated the effect of increasing the SR fractional volume from 3% to 3.9%. Compared to scenario 1, the nanobubble radius remained fixed to isolate the influence of SR volume on system behaviour. As shown in subplot (b), the increased SR volume leads to a higher peak calcium concentration, reaching approximately 671 nM. This outcome is expected, since a larger SR stores more calcium ions and upon stimulation, releases them into the same nanobubble volume.

The elevated calcium level results in a higher illumination rate, as seen in subplot (c), where the peak reaches 5.17×10^8 photons/s. As a consequence, the total number of photons emitted during the 1 s cycle increases to 7.46×10^7, as shown in subplot (d).

Finally, scenario 4 (illustrated by the dashed purple curves in Figure 5.1) explores the effect of increasing the aequorin concentration in the system. In this case, the bubble size and SR volume are kept constant, as in scenario 1, which results in an unchanged calcium concentration. However, the higher concentration of aequorin molecules increases the probability of calcium ions binding to them, leading to a peak illumination rate of 4.81×10^8 photons/s. This increase can be attributed to a higher $I_{\max}$ value in Equation 4.10,

which reflects the greater likelihood of calcium-aequorin interactions. Thus, despite the constant calcium concentration, the increased aequorin concentration leads to an enhanced illumination rate.

5.1.4 Effect of Aequorin Variants on Bioluminescent Response

In this section, we examine how the choice of different aequorin mutants affects the peak illumination rate of the bioluminescent system. The aim is to evaluate how substituting one variant for another influences overall system performance under varying physical configurations.

To conduct this analysis, we simulated the system response for each mutant across a wide range of design conditions. The overall circuit topology remained unchanged in the mutant-based simulations. We followed the same simulation procedure used in the previous section, using mutant-specific parameter sets. For every aequorin variant, 500 independent simulations were performed, each corresponding to a randomly generated parameter set. These sets included unique combinations of the design parameters, aequorin concentration [Aq], nanobubble radius r_B, and SR volume fraction ϕ_{SR}, drawn from uniform distributions within defined bounds. Specifically, the parameters were sampled uniformly from the following ranges: $[\mathrm{Aq}] \in [300, 500]\,\mu\mathrm{M}$, $r_B \in [10, 20]\,\mu\mathrm{m}$, and $\phi_{\mathrm{SR}} \in [3, 15]\%$. These intervals were chosen to approximate operational conditions under which a device placed in the extracellular space could generate sufficient illumination for optogenetic modulation while staying within practical limits on aequorin concentration and device volume.

For each simulation, the peak photon emission rate I_{peak} was recorded as the primary performance metric. This value provides a direct measure of light output efficiency for each mutant under a given configuration.

Figure 5.2 presents the distribution of I_{peak} values across the five aequorin variants used in this study. These are the same variants for which model parameters were extracted in Section 4.3.3. Each boxplot represents 500 simulation results. The box spans the interquartile range (25^{th}–75^{th} percentile), with the median shown as a horizontal line. Whiskers extend to the most extreme values within 1.5 times the interquartile range (Tukey definition), and points lying outside this range appear as individual blue circles.

The results show clear performance differences among the variants. The wild-type aequorin produces relatively low light output, with median I_{peak} values on the order of 10^6–10^7 photons/s. All three mutant forms demonstrate enhanced emission rates. The Q159T and Q159D variants show median illumination values approximately one to two orders of magnitude higher than those of the wild type. The double mutant QD+AT yields the strongest response, with a median I_{peak} exceeding 1×10^9 photons/s and a maximum output above 4.5×10^9 photons/s in some configurations.

5.1.5 Sensitivity Analysis

The four test scenarios discussed earlier offer useful insight into how individual design parameters influence the performance of the bioluminescent system. However, to obtain a more comprehensive view of how these parameters affect the illumination rate (particu-

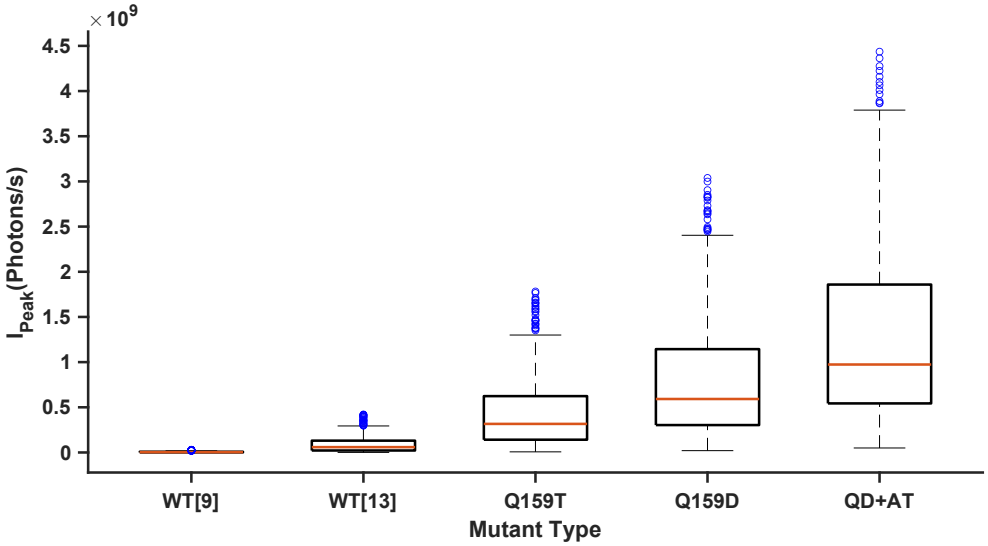

Figure 5.2: Distribution of peak illumination rates for five aequorin variants, based on 500 simulation runs per mutant. Each box summarizes the range, median, and interquartile spread of the illumination rate I_{peak} produced by the circuit model under randomized physical configurations. Data points lying outside this range are plotted individually as blue circles.

larly given the nonlinear interactions between them) sensitivity analysis is helpful. This approach quantifies the influence of each parameter on system behaviour and identifies those that have the strongest effect on model outputs.

As a first step, we derive the local elasticities of the peak illumination rate with respect to the three design parameters: the aequorin concentration [Aq], the bubble radius r_B, and the SR volume V_{SR}. These analytical expressions serve as a reference for interpreting the results of the numerical sensitivity analysis. We then conduct a simulation-based analysis by evaluating a large number of distinct parameter sets to assess the sensitivity of the system across a wide parameter space.

To derive the elasticities, let us express the peak photon emission rate, I_{peak}, as the

maximum value of $I_D(t)$ over time

$$I_{\text{peak}} \;=\; \max_t \; I_D(t). \tag{5.8}$$

Given the monotonicity of the characteristic equation (Equation 5.1), the peak emission occurs at the maximum value of $V_D(t)$. This allows a closed-form expression:

$$I_{\text{peak}} = I_{\max} \left(\frac{1 + K_R \cdot V_D^*}{1 + K_{TR} + K_R \cdot V_D^*} \right)^{n_H}, \tag{5.9}$$

where $V_D^* = \max_t V_D(t) = G(\phi) \cdot C_{\text{peak}}$, with C_{peak} denoting the peak of the calcium waveform in the reference myocyte cell, and $I_{\max}$ is given by Equation 5.2.

For conciseness, let

$$x = V_D^* = G(\phi_{SR}) \cdot C_{\text{peak}}, \tag{5.10}$$

denote the scaled peak diode voltage, and define the Hill-like function

$$F(x) = \left(\frac{1 + K_R x}{1 + K_{TR} + K_R x} \right)^{n_H}. \tag{5.11}$$

Then

$$I_{\text{peak}} = I_{\max} F(x), \tag{5.12}$$

and the partial derivatives are obtained via the product and chain rules. The derivative of

F is

$$F'(x) = F(x) \cdot \frac{n_H K_R K_{TR}}{(1 + K_R x)(1 + K_{TR} + K_R x)}. \tag{5.13}$$

The sensitivity to ϕ_{SR} reflects the nonlinear dependence of I_{peak} on ϕ_{SR}:

$$\begin{aligned} \frac{\partial I_{\text{peak}}}{\partial \phi_{SR}} &= I_{\max} F'(x) \cdot \frac{\partial x}{\partial \phi_{SR}} \\ &= I_{\max} F'(x) \cdot \left(\frac{\mathrm{V}_{\text{myocyte,ref}}}{\mathrm{V}_{\text{SR,ref}}} \cdot C_{\text{peak}} \right), \end{aligned} \tag{5.14}$$

which can equivalently be expressed as:

$$\frac{\partial I_{\text{peak}}}{\partial \phi_{SR}} = I_{\text{peak}} \cdot \frac{n_H K_R K_{TR}\, x}{\phi_{SR}\,(1 + K_R x)(1 + K_{TR} + K_R x)}, \tag{5.15}$$

since $\partial x / \partial \phi_{SR} = x / \phi_{SR}$ (see Equation 5.10).

The sensitivities to r_B and [Aq] arise from their scaling of $I_{\max}$ through the dependence expressed in Equation 5.3:

$$\begin{aligned} \frac{\partial I_{\text{peak}}}{\partial r_B} &= \frac{\partial I_{\max}}{\partial r_B} . F(x) \\ &= \frac{3\, I_{\text{peak}}}{r_B}. \end{aligned} \tag{5.16}$$

Also,

$$\begin{aligned}\frac{\partial I_{\text{peak}}}{\partial [\text{Aq}]} &= \frac{\partial I_{\max}}{\partial [\text{Aq}]}.F(x) \\ &= \frac{I_{\text{peak}}}{[\text{Aq}]}.\end{aligned} \tag{5.17}$$

For dimensionless quantification, we compute the elasticities:

$$\mathcal{E}_{\phi_{SR}} = \frac{\phi_{SR}}{I_{\text{peak}}} \frac{\partial I_{\text{peak}}}{\partial \phi_{SR}} = \frac{n_H K_{\text{R}} K_{\text{TR}}\, x}{(1 + K_{\text{R}} x)(1 + K_{\text{TR}} + K_{\text{R}} x)} \tag{5.18}$$

$$\mathcal{E}_{r_{\text{B}}} = \frac{r_{\text{B}}}{I_{\text{peak}}} \frac{\partial I_{\text{peak}}}{\partial r_{\text{B}}} = 3 \tag{5.19}$$

$$\mathcal{E}_{[\text{Aq}]} = \frac{[\text{Aq}]}{I_{\text{peak}}} \frac{\partial I_{\text{peak}}}{\partial [\text{Aq}]} = 1 \tag{5.20}$$

After deriving the analytical sensitivities, we proceed with a simulation-based sensitivity analysis. This analysis uses the same 500 randomly generated parameter sets described earlier, where each set defines a unique combination of [Aq], r_B, and ϕ_{SR}. Since the objective of this analysis is sensitivity characterization rather than formal optimization, a random sampling approach is adopted to explore the design space. This enables broad coverage of the feasible parameter domain and facilitates the identification of nonlinear

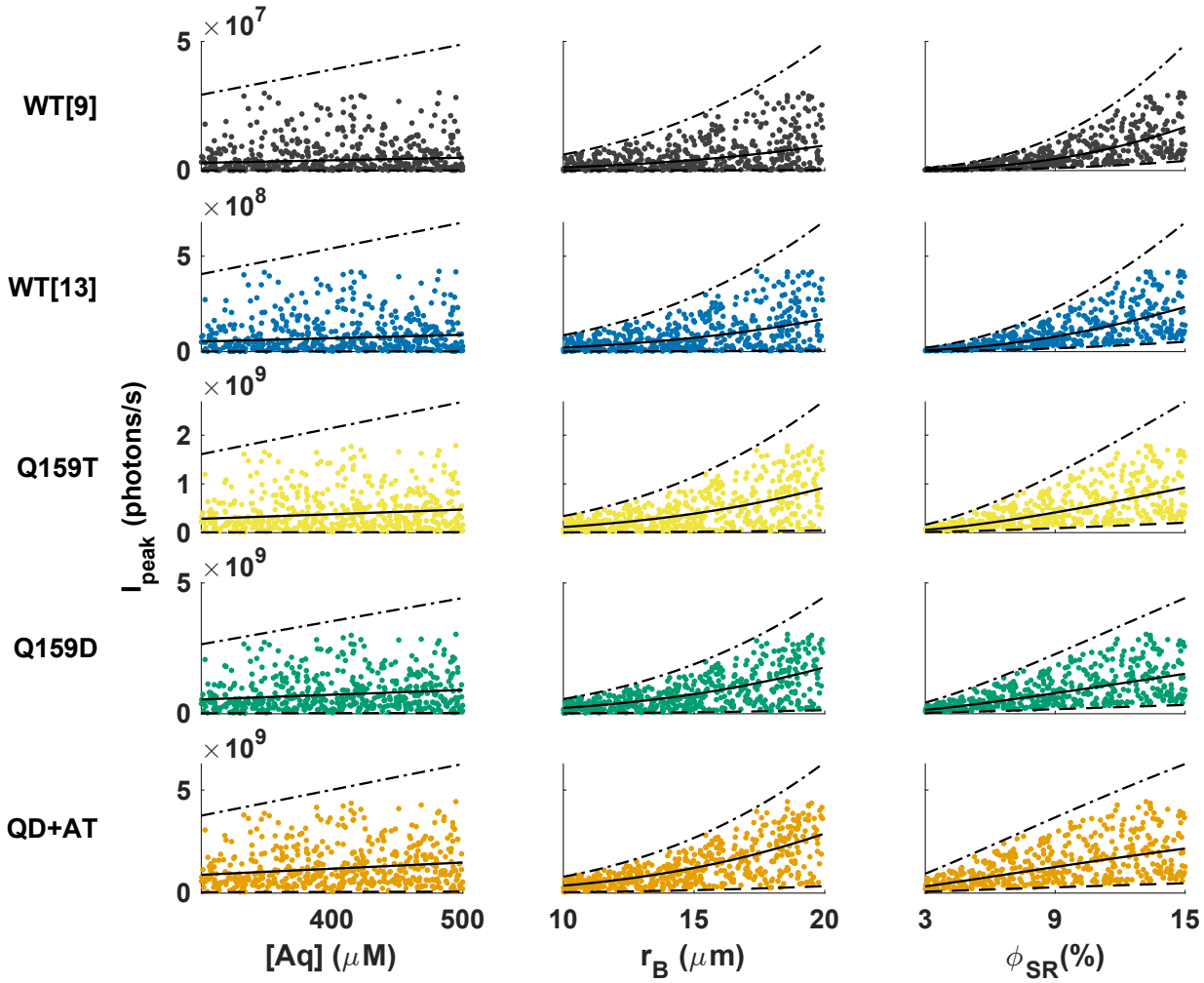

Figure 5.3: Simulation–analytical comparison of peak photon emission rate across design parameters and aequorin variants. Each row corresponds to a different mutant. Each column shows I_{peak} versus one design parameter: [Aq] (µM), r_B (µm), or ϕ_{SR} (%). Dots: simulated I_{peak} for $N = 500$ design-parameter sets per variant. The same points appear in all three panels of a row and are re-positioned by the panel's x-variable. Curves: analytic predictions from (5.9) with the two non-displayed parameters held at their empirical minimum (dashed), median (solid), or maximum (dash–dot).

interactions between parameters. While this approach does not seek an optimal configuration, the resulting trends can inform future optimization studies.

Figure 5.3 presents the results. Each row corresponds to a specific aequorin variant, and each column displays one of the design parameters along the horizontal axis. Within each row, the same 500 simulation points appear across all three panels, arranged according to the parameter plotted on the x-axis. Each panel provides a two-dimensional projection of the full three-parameter space.

The vertical spread of data points at a fixed x-value reflects the variability in I_{peak} caused by changes in the two non-displayed parameters. A wide vertical distribution indicates that the hidden parameters influence the output significantly. In contrast, a narrow spread suggests that the displayed parameter explains most of the observed variation.

Each panel also includes three overlay curves derived, from the closed-form expression for I_{peak} (see Eq. (5.9)). These curves are computed by fixing the two non-displayed parameters at their minimum, median, and maximum values. The overlays are based on the analytical assumption introduced in the sensitivity formulation, where $x = G(\phi)\, C_{\text{peak}}$, and G is a function of ϕ_{SR} alone (see Eq. (4.8)). Within this framework, the bubble radius r_B affects I_{peak} only through its contribution to I_{max}.

In all tested aequorin variants, the peak illumination rate I_{peak} increases monotonically with the SR volume fraction ϕ_{SR} over the investigated range of 3–15%. The strength of this dependence varies among variants: the WT shows the highest sensitivity to ϕ_{SR}, the single mutants Q159D and Q159T exhibit intermediate, and the double mutant QD+AT shows

the weakest overall dependence. In each case, the analytical curve corresponding to the median values of the held parameters aligns closely with the densest region of the simulated data. The curves associated with the minimum and maximum parameter values form outer bounds around the simulation results. Moreover, at low SR fractions, the spread in I_{peak} is narrow, while at intermediate values, the dispersion becomes wider. This pattern indicates that the system's sensitivity to ϕ_{SR} varies across the operational range. The sensitivity to ϕ_{SR} also varies across different mutants. This difference is particularly evident when comparing the overlay curves of the wild-type and the QD+AT mutant.

By comparison, the influence of the bubble radius r_B on I_{peak} is slightly weaker. The point clouds are more dispersed, which reflects a lower correlation between r_B and light output. According to the framework presented in this section (where $x = G(\phi_{\text{SR}})\, C_{\text{peak}}$ and G does not depend on r_B) the overlay curves in the r_B column all follow the same cubic trend across variants. Within each row, the three curves represent scaled versions of an r_B^3 relationship, with the scaling factor determined by the fixed values of [Aq], ϕ_{SR}, and the variant-specific function $F(x)$ in Equation 5.9.

The apparent increase in scatter at higher values of r_B results from the cubic scaling, which amplifies residual variations in [Aq] and ϕ_{SR}. Differences in the slopes of the scatter plots (such as the nearly flat trend for the wild-type versus the mild positive slope in Q159D) arise from vertical rescaling rather than any fundamental change in r_B dependence. This interpretation is consistent with the analytical elasticity result in Eq. (5.19), which gives a constant $\mathcal{E}_{r_B} = 3$ for all variants. The vertical spacing between overlay curves associated with minimum, median, and maximum held parameter values varies across mutants,

reflecting differences in the value of $F(x)$ evaluated under those specific conditions.

In the [Aq] column, within the simulated concentration range of 300–500 µM, the peak illumination rate I_{peak} exhibits a modest but consistent increase across all aequorin variants. The analytical overlay curves appear as straight lines passing through the origin because, when r_B and ϕ_{SR} are held constant, the model reduces to a linear form:

$$I_{\text{peak}} = (\text{constant} \times r_B^3 \times F(\phi_{SR})) \times [\text{Aq}]. \tag{5.21}$$

Consequently, the three overlay lines within each row differ only in slope, determined by the fixed values of r_B and ϕ_{SR}. The steepest line corresponds to the maximum-hold case, reflecting the combined effect of the cubic dependence on r_B and the monotonic increase of $F(\phi_{SR})$ across the tested range.

The vertical dispersion of the simulated data points arises from variability in the two non-displayed parameters, ϕ_{SR} and r_B. These dependencies dominate the spread in this projection, leading to broader clouds even though the direct sensitivity of I_{peak} to [Aq] remains relatively weak.

Moreover, to validate the analytical sensitivity expressions, we compared the elasticities obtained from simulation with those calculated analytically. For each aequorin variant, empirical elasticities were estimated through multivariate log–log regression of I_{peak} against the three design parameters using the 500 randomly sampled configurations. The corresponding analytical elasticities were computed from Equations (5.18 and 5.20), using the median operating point of each variant as a representative condition.

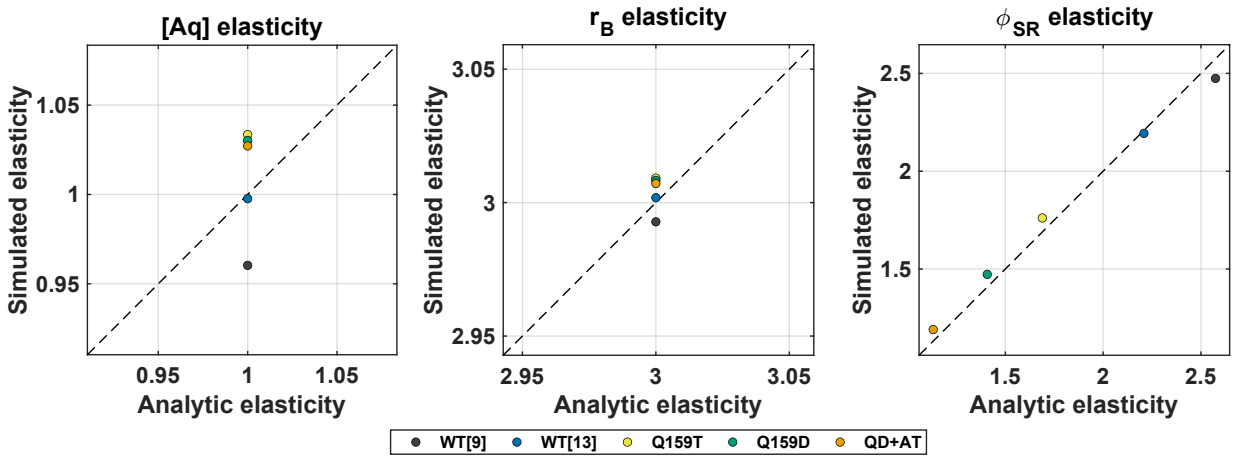

Figure 5.4: Comparison between simulated and analytic elasticities. Each panel compares simulated elasticities (y-axis), estimated from the 500 simulated triplets per mutant via a multivariate log–log regression of I_{peak} on [Aq], r_B, and ϕ_{SR}, with the corresponding analytic elasticities (x-axis) derived from the sensitivity expressions in Equations (5.18–5.20). Dots indicate individual aequorin variants; the dashed line denotes the 45° identity.

Figure 5.4 compares the empirical and analytical elasticities. In all three panels, the data points lie close to the 45° identity line, which indicates strong agreement between simulation and theory. In the [Aq] panel, all variants align with the predicted elasticity of $\mathcal{E}_{[\text{Aq}]} = 1$, consistent with a linear relationship between I_{peak} and [Aq] over the simulated range (300–500 µM). The r_B panel shows a similar pattern, with all points clustered near $\mathcal{E}_{r_B} = 3$, confirming the expected cubic dependence from volume scaling. In the ϕ_{SR} panel, the variant-specific trends are also captured accurately: the wild-type constructs display the highest $\mathcal{E}_{\phi_{\text{SR}}}$, the single mutants Q159D and Q159T fall in the intermediate range, and the double mutant QD+AT shows the lowest sensitivity to SR volume fraction, which matches the ordering observed in Figure 5.3.

The present analysis does not yield a single optimal design, as the notion of optimality

depends on application-specific requirements (e.g., maximizing emission intensity versus extending operational lifetime). Instead, the results provide insight into parameter sensitivities and trade-offs, which can inform subsequent optimization studies. A broader discussion of application-dependent design considerations and optimization directions is provided in Chapter 6.

5.2 Bioluminescent Light Transport Results and Validation

This section presents the light transport results obtained from the numerical solution of the RTE, based on the modelling framework described in Section 4.4 using COMSOL (version 6.2). In addition, we use the analytically derived ballistic (uncollided) solutions as a benchmark to validate the simulation setup. The primary objectives are: (i) to visualize and quantify the spatial distribution of the bioluminescent field within brain tissue; (ii) to validate the accuracy of the COMSOL-based RTE simulations through comparison with the analytical ballistic solutions; and (iii) to assess how source geometry, quantity, and tissue type influence the fluence rate at biologically relevant locations.

5.2.1 Notation and Conventions for Fluence Rate

All results in this section are reported in terms of the time-dependent fluence rate $\Phi(\mathbf{r}, t)$. Bold symbols such as $\mathbf{r}$ denote position vectors, and their magnitudes are written as $r =$

$\|\mathbf{r}\|$. In spherically symmetric geometries we therefore write $\Phi(r,t)$ as shorthand for $\Phi(\mathbf{r},t)$.

Depending on the context, the results are presented either (i) as spatial distributions $\Phi(\mathbf{r},t_0)$ at a fixed time t_0, or (ii) as temporal profiles $\Phi(\mathbf{r}_0,t)$ at a fixed observation point $\mathbf{r}_0$. When we report fluence rate at labeled observation points $X \in \{A,B,C,\dots\}$, the position of such a point is denoted by $\mathbf{r}_X$, and we write $\Phi(\mathbf{r}_X,t)$ or, equivalently, $\Phi(X,t)$ for its temporal profile. The 3D visualizations shown in this section correspond to spatial snapshots at specific time points, i.e. fixed-t_0 maps of $\Phi(\mathbf{r},t_0)$.

Throughout this section, we distinguish between the different components of the fluence rate using superscript notation. The ballistic contribution is denoted by $\Phi^{(0)}(\mathbf{r},t)$, the collided or scattered component by $\Phi^{(c)}(\mathbf{r},t)$, and the total fluence rate by $\Phi(\mathbf{r},t)$ without superscript:

$$\Phi(\mathbf{r},t) = \Phi^{(0)}(\mathbf{r},t) + \Phi^{(c)}(\mathbf{r},t). \tag{5.22}$$

Moreover, the absorption coefficient μ_a, the scattering coefficient μ_s, the anisotropy factor g, and the reduced scattering coefficientμ_s'follow the definitions provided in section 2.4. When referring to tissue-specific quantities, we use subscripts to indicate the medium, e.g. $\mu_{a,\mathrm{Grey}}$ for the grey-matter absorption coefficient or $\Phi_{\mathrm{Cereb}}(\mathbf{r},t)$ for the fluence rate in cerebellar tissue. Throughout this section, the parameter r_B denotes the radius of the bubble (i.e. the emitting spherical source).

Throughout the light transport results, the source illumination profiles are computed from the equivalent circuit model described in Section 4.2, using the QD+AT[4] aequorin

[4]As in the previous subsection, the QD+AT variant was selected for its higher photon yield compared

mutant. Unless otherwise specified, we set the SR volume fraction to $\phi_{\mathrm{SR}} = 0.15$ and the aequorin concentration to [Aq] = 455 µM to maximize illumination rate.

5.2.2 Single-source Configuration

To validate the simulation setup, we compare the numerical results to the analytically derived ballistic solution (see subsection 4.4.2) in the near-source regime, where scattering is limited and the ballistic term dominates the fluence rate. Small differences between the two are expected and physically meaningful, as the full RTE solution includes in-scattered[5] contributions that are absent from the purely ballistic analytical solution.

We first examined light transport from a single bioluminescent source embedded in a homogeneous brain medium. In this part, the surrounding tissue is modeled as grey matter, and the optical properties used in the simulation reflect this specific tissue type (as represented in Table 4.3). While the medium is treated as homogeneous, we consider a representative configuration in which the target neuron's membrane is located at a surface-to-surface separation of 2 µm from the source, noting that this choice is illustrative and that the same measurement can be repeated for any arbitrary source–membrane separation.

Figure 5.5(a,b) illustrates the COMSOL-based results for a source with radius r_B = 10 µm, while Figure 5.5(c,d) presents the results for r_B = 15 µm. The left panels in this

to other mutants. However, the results presented here are reproducible for any other variant by following the procedure outlined in subsection 4.3.3 and updating the source illumination profiles accordingly.

[5] As in the previous section, *in-scattered* term represents photons that are redirected by scattering events from other directions $\hat{\mathbf{\Omega}}'$ into the observation direction $\hat{\mathbf{\Omega}}$ at position $\mathbf{r}$, thereby increasing the radiance along $\hat{\mathbf{\Omega}}$.

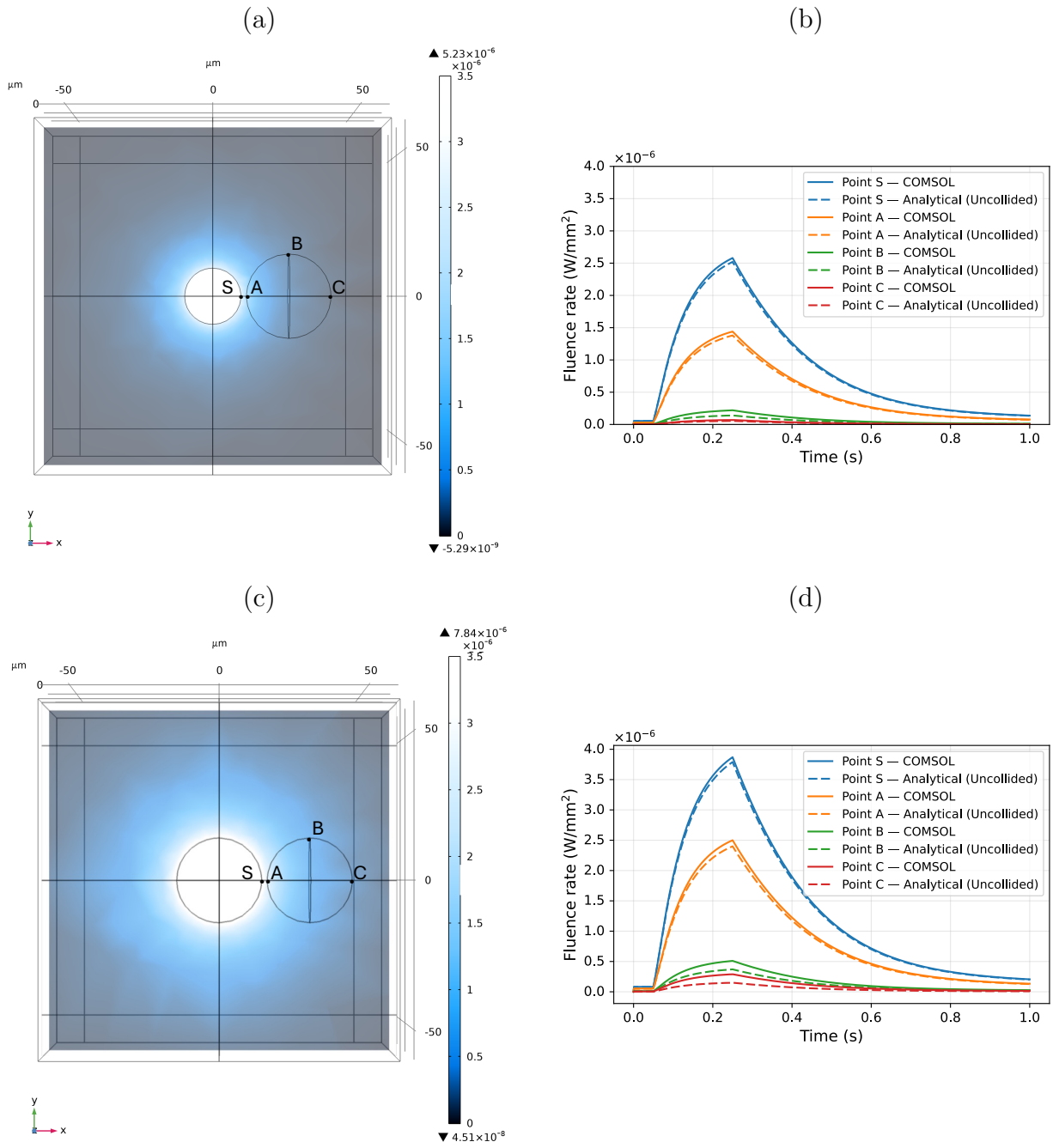

Figure 5.5: Validation of the RTE model against the analytical ballistic solution for a single spherical bioluminescent source. (Caption continues on the next page.)

Figure 5.5: (continued) (a,b) Results for a source radius $r_B = 10$ µm; (c,d) results for source radius $r_B = 15$ µm. Left panels show spatial distributions of the instantaneous fluence rate $\Phi(\mathbf{r}, t_0)$ in the $x-y$ plane through the source centre ($z = 0$), evaluated at the time of peak emission ($t_0 = 0.25$ s)). Labeled points denote sampling locations used for temporal analysis: S lies on the source surface, and A, B, and C are positioned on the membrane of the target soma at increasing distances. Right panels depict the temporal evolution of the fluence rate at these points. Solid lines indicate the full time-dependent RTE solution (COMSOL). Dashed lines show the analytical ballistic solution.

figure illustrate the spatial distribution of the fluence rate $\Phi(\mathbf{r}, t_0)$, evaluated at the peak of the source's emission profile (with $t_0 = 0.25$ s, corresponding to the peak on the right panel). As expected, with a single source in the medium, the fluence rate decreases monotonically with radial distance due to geometric spreading and attenuation from absorption and scattering in the tissue.

To quantify the temporal dynamics, we evaluated the fluence rate $\Phi(\mathbf{r}, t)$ at four representative locations: point S (on the source surface), and points A, B, and C, located on the neuronal membrane at increasing distances from the source. Figure 5.5(b,d) compares the time-dependent COMSOL RTE solutions (solid lines) with the corresponding analytical ballistic solutions (dashed lines). As expected, the absolute fluence values decrease systematically from point S to point C, consistent with increased distance from the emitter and the combined effects of geometric spreading, absorption, and scattering losses.

In all cases, the temporal profile of the fluence rate closely follows the emission dynamics of the bioluminescent source (see Figure 5.1). This behaviour arises because the spatial scale of the domain (~ 120 µm) yields photon propagation times on the order of tens to hundreds of femtoseconds. This is several orders of magnitude shorter than the sub-second

timescale of the source emission. As a result, light transport through the tissue appears effectively instantaneous, and the observed temporal evolution of $\Phi(\mathbf{r}, t)$ directly reflects the variations in the source's illumination rate.

The comparison between the COMSOL results and the analytical ballistic solution demonstrates strong agreement in the near-source regime, particularly at points S and A, where the ballistic component strongly dominates the photon population. At larger distances (points B and C), the COMSOL results remain consistently higher than the ballistic predictions. This small but consistent offset is expected and arises from photons that have undergone one or more scattering events. Contribution of these photons is absent from the analytical ballistic model but is captured by the full RTE solution. The magnitude of this difference provides a measure of the in-scattering contribution to the fluence rate.

When the source radius increases from 10 to 15 µm, the ballistic fluence within the surrounding tissue increases proportionally to the source's total radiant power. This trend is consistent with the sensitivity analysis results presented earlier: if the volumetric fraction of the luminescent component (ϕ_{sr}) is held constant, the total emitted power scales with the source volume, $P_0 \propto r_{\mathrm{b}}^3$. At the same time, the radiant flux is distributed over the surface of the spherical source, whose area scales as $A_{\mathrm{b}} = 4\pi r_{\mathrm{b}}^2$. Since the ballistic fluence rate at the source's surface is defined as the radiant power per unit area $\Phi^{(0)}(r_B, t) \sim P_0/A_{\mathrm{b}}$, it follows that:

$$\Phi^{(0)}(r_B, t) \propto \frac{r_{\mathrm{b}}^3}{r_{\mathrm{b}}^2} = r_{\mathrm{b}}. \tag{5.23}$$

Thus, increasing the source radius by a factor of 1.5 (from 10 to 15 µm) is expected to increase the ballistic fluence rate near the source surface by the same factor.

This proportional trend is also reproduced in the COMSOL numerical results: the larger source generates higher fluence magnitudes while maintaining nearly identical spatial decay characteristics. The temporal profiles remain unchanged across both cases, reflecting the fact that our modelling framework (the linear RTE) scales the fluence rate directly with the source strength. Such a linear treatment is appropriate for the present application, as the bioluminescent intensities involved are far below thresholds for nonlinear absorption. Within this regime, the assumption of linear superposition is well justified and yields accurate predictions of the light field.

The results presented in Figure 5.5 confirm that the RTE implementation accurately reproduces the expected near-source attenuation behaviour and yields fluence magnitudes consistent with the analytical ballistic solution, with deviations remaining within a few percent, depending on the distance from the source. These small discrepancies are physically interpretable as contributions from scattered light, which are absent in the ballistic model but captured by the full RTE solution. This agreement validates both the numerical setup and the use of the ballistic term as a reliable benchmark within the parameter regime relevant to bioluminescent optogenetic stimulation.

To assess bioluminescent light transport across different brain tissues and evaluate the accuracy of the numerical RTE implementation, we simulated photon propagation in four brain regions considered in this study (grey matter, cerebellum, pons, and thalamus) and

validated the results against the analytical ballistic solution.

Figure 5.6 shows the fluence rate evaluated at the peak of the source's emission profile ($t = 0.25\,\mathrm{s}$), as a function of radial distance from the surface of the source. In all cases, the geometry corresponds to the single-source configuration shown in Figure 5.5(a), with a source radius of $r_\mathrm{b} = 10$ µm. The fluence rate was computed along the line segment connecting the source centre (S) to point (C).

At the surface of the source ($r = r_B$), the difference between the analytical ballistic and COMSOL-based numerical fluence rate is minimal (below approximately 2%). Moreover, the ballistic fluence rate at the sources boundary is identical across all tissues: $\Phi(r_B, t = 0.25s) \approx 2.58 \times 10^{-6}\ \mathrm{W\,mm^{-2}}$. This result is physically expected since at the source's surface, the ballistic fluence depends only on the internal emission characteristics, (namely, the volumetric power density q and the optical properties within the source ($\mu_{a,\mathrm{in}}, \mu_{s,\mathrm{in}}$)) which are held constant across all simulations. Since the refractive indices are also matched ($n_\mathrm{in} = n_\mathrm{out} = 1.37$), the radiance is continuous across the boundary, and the immediate outward fluence is unaffected by the external tissue properties.

Differences among tissue types emerge only beyond the boundary, as photons begin propagating through the surrounding medium and are attenuated according to the tissue-specific absorption and scattering coefficients (μ_a, μ_s).

Across all tissues, the full-form RTE results obtained from COMSOL consistently exceed the analytical ballistic solution. This is physically expected, as the ballistic model accounts only for ballistic photons and neglects all in-scattered contributions. In con-

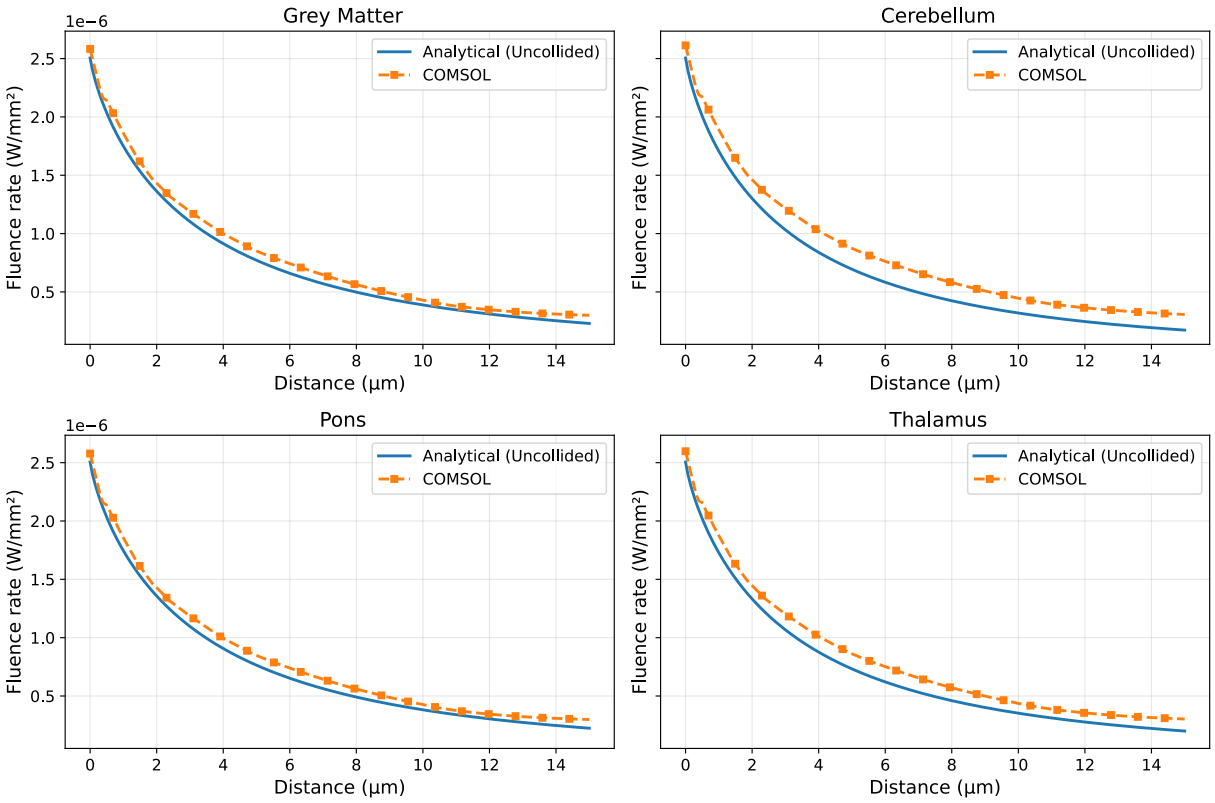

Figure 5.6: Comparison between the analytical ballistic solution and full RTE simulations for four human brain tissues. Each panel shows the fluence rate $\Phi(\mathbf{r}, t = 0.25\ \text{s})$, evaluated at the peak of the source's emission profile, as a function of radial distance from the surface of a spherical bioluminescent source ($r_\text{b} = 10\ \mu\text{m}$) embedded in: (top-left) grey matter, (top-right) cerebellum, (bottom-left) pons, and (bottom-right) thalamus. Solid blue curves represent the analytical ballistic (ballistic) solution given by Equation 4.40, while dashed orange curves show the corresponding fluence profiles obtained from full COMSOL RTE simulations.

trast, the complete RTE solution includes both ballistic and scattered photons, resulting in higher fluence rates at observation points. In this context, the analytical ballistic solution serves as a lower bound on the true fluence, while the full RTE simulation provides a more accurate depiction of light transport in scattering media.

A similar trend is observed in Figure 5.7, which compares the fluence rate across all four tissue types at two representative spatial locations: (i) the surface of the bioluminescent source and (ii) a point located 5 µm radially outward from the source surface. At both locations, fluence-rate values are evaluated at a fixed time $t_0 = 0.25$ s. The fluence rate obtained from the analytical ballistic solution, $\Phi^{(0)}(r, t_0)$ evaluated at the corresponding radial positions, is shown alongside the COMSOL RTE simulations $\Phi(\mathbf{r}, t_0)$, highlighting the consistent offset due to in-scattered contributions in the latter.

As discussed earlier and expected from the analytical formulation, the ballistic fluence rate at the surface of the source is identical for all tissue types, as reflected in the blue bars (representing the analytical solution) in the left panel of Figure 5.7. When comparing the COMSOL-based fluence at the source surface (orange-colored bars in the left panel of Figure 5.7), small but systematic differences are observed across tissues, following the order

$$\Phi_{\text{Cerebellum}}(r_B, t_0) > \Phi_{\text{Thalamus}}(r_B, t_0) > \Phi_{\text{Grey}}(r_B, t_0) > \Phi_{\text{Pons}}(r_B, t_0), \qquad t_0 = 0.25 \text{ s}.$$

This ordering is fully consistent with each tissue's reduced scattering coefficient $\mu_s' = \mu_s(1 - g)$, which quantifies the strength of angular randomization per unit length. From

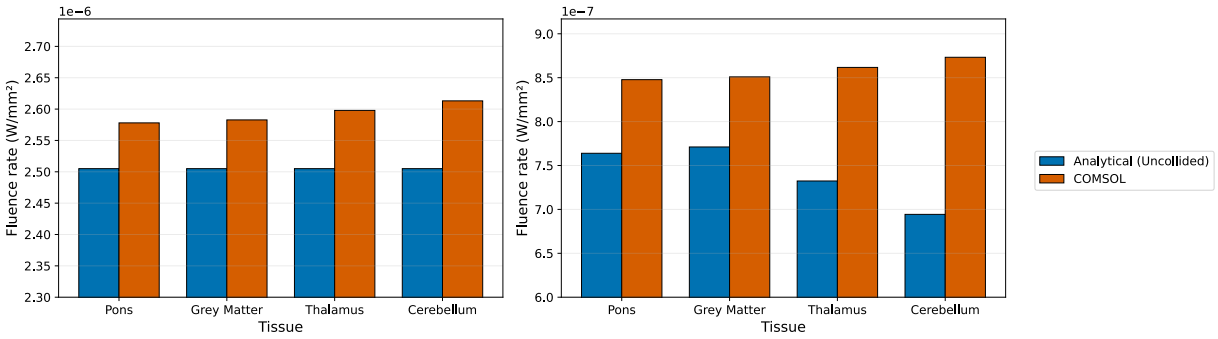

Figure 5.7: Fluence rate at two radial positions at $t = 0.25$ s for four brain tissues. Bar plots show the fluence rate on the surface of the bioluminescent source (left) and at a point 5 µm away along the radial direction (right) for grey matter, cerebellum, pons, and thalamus. For each tissue, the analytical ballistic fluence (blue bars) and the full COMSOL-based RTE fluence (orange bars) are shown at the corresponding location.

Table 4.3 we know cerebellum exhibits the largest μ_s' (≈ 4.48 mm^{-1}), followed by thalamus (≈ 2.89 mm^{-1}), grey matter (≈ 1.32 mm^{-1}), and pons (≈ 1.12 mm^{-1}).

A higher μ_s' increases the probability of very early scattering events that redirect photons while keeping them near the source, thereby slightly elevating the local fluence relative to the ballistic value. Thus, the ordering observed in the COMSOL results at the surface is physically reasonable and reflects the tissue-dependent strength of near-source scattering.

The right panel of Figure 5.7 illustrates the fluence rates measured 5 µm away from the source surface ($r = r_B + 5$ µm). At this location, three additional trends are observed. First, the ordering of the COMSOL fluence rates (orange-colored bars) remains unchanged:

$$\Phi_{\text{Cerebellum}}(r_B{+}5\ \mu\text{m}, t_0) > \Phi_{\text{Thalamus}}(r_B{+}5\ \mu\text{m}, t_0) > \Phi_{\text{Grey}}(r_B{+}5\ \mu\text{m}, t_0) > \Phi_{\text{Pons}}(r_B{+}5\ \mu\text{m}, t_0),$$

for $t_0 = 0.25$ s. This reflects the effect of scattered-photon contributions in tissues with higher reduced scattering coefficients.

Second, the ordering of the analytical ballistic fluence (blue-colored bars) is different:

$$\Phi^{(0)}_{Grey}(r_B{+}5\ \mu\text{m}, t_0) > \Phi^{(0)}_{Pons}(r_B{+}5\ \mu\text{m}, t_0) > \Phi^{(0)}_{Thalamus}(r_B{+}5\ \mu\text{m}, t_0) > \Phi^{(0)}_{Cerebellum}(r_B{+}5\ \mu\text{m}, t_0),$$

for $t = 0.25$ s. This trend is exactly what one would expect based on the total attenuation coefficients. Because the ballistic solution includes only ballistic photons, its decay is governed by the total attenuation coefficient $\mu_t = \mu_a + \mu_s$ of each tissue. Using the emission-weighted values from Table 4.3, the total attenuation coefficients are:

$$\mu_{t,\text{Grey}} = 0.07 + 10.97 = 11.04\ \text{mm}^{-1}, \tag{5.24}$$

$$\mu_{t,\text{Pons}} = 0.11 + 12.46 = 12.57\ \text{mm}^{-1}, \tag{5.25}$$

$$\mu_{t,\text{Thalamus}} = 0.18 + 19.28 = 19.46\ \text{mm}^{-1}, \tag{5.26}$$

$$\mu_{t,\text{Cerebellum}} = 0.16 + 28.02 = 28.18\ \text{mm}^{-1}. \tag{5.27}$$

Tissues with larger μ_t (specifically cerebellum ($28.18\ \text{mm}^{-1}$) and thalamus ($19.46\ \text{mm}^{-1}$)) attenuate unscattered photons more strongly over a given propagation distance. Conversely, tissues with lower μ_t (grey matter ($11.04\ \text{mm}^{-1}$) and pons ($12.57\ \text{mm}^{-1}$)) preserve a larger fraction of ballistic photons at short distances. Thus, the observed ballistic be-

haviour is consistent with the relative magnitudes of each tissue's attenuation coefficient and highlights the distinct physical regimes captured by the two solution approaches.

Finally, the relative difference between the COMSOL and ballistic fluence values at $r = r_B + 5$ µm is noticeably larger than at the source surface. This increase is expected. At $r = r_B$, photons have just exited the source and have had negligible probability of scattering, so the total fluence satisfies $\Phi(r_B, t_0) \approx \Phi^{(0)}(r_B, t_0)$. By contrast, at $r = r_B + 5$ µm, photons have already traversed a fraction of a scattering mean free path, increasing the contribution of the first-collision and multiple-scattering terms $\Phi^{(c)}(r, t_0)$. As a result, the total fluence rate

$$\Phi(r, t_0) = \Phi^{(0)}(r, t_0) + \Phi^{(c)}(r, t_0), \tag{5.28}$$

diverges from the ballistic estimate as the propagation distance increases.

Taken together, these observations reinforce that the differences between the ballistic and full RTE predictions stem from well-understood physical mechanisms, specifically, the scattering strength and attenuation characteristics of the tissue. Moreover, the consistency of these trends across all four tissue types further validates the correctness and robustness of the numerical RTE implementation.

5.2.3 Multi-source Configuration

Our simulation framework also enables the study of configurations containing multiple bioluminescent sources within the same tissue volume. In COMSOL, each mote is represented as a distinct volumetric emission domain, and the radiative transfer equation is solved with all source terms present simultaneously in the computational domain. This approach allows the resulting fluence field to reflect the combined illumination patterns produced by multiple emitters, including the effects of overlapping radiation fields and scattering-induced redistribution in the surrounding tissue. Multi-source configurations therefore provide a means to investigate how spatial arrangement and source density influence the energy fluence distribution.

To illustrate these effects, we next consider a representative geometry consisting of nine identical sources arranged in a 3×3 array placed in grey-matter brain tissue (see Figure 5.8), and evaluate the resulting fluence distribution at biologically relevant locations. Figure 5.9 summarizes the corresponding fluence patterns for this multi-mote configuration. The left panel shows the spatial distribution of the fluence rate $\Phi(\mathbf{r}, t_0)$ in the $x-y$ cross-section passing through the centres of the motes and the target soma (i.e. $z = 0$), with $t_0 = 0.25$ s. The right panel displays the time-dependent fluence rate at four representative points (S, A, B, C) located at increasing distances from the central source; the position of each point is denoted by $\mathbf{r}_X$, and we write $\Phi(X, t)$ for its temporal profile. As in the single-source case, each temporal curve follows the characteristic profile of the aequorin emission. This reflects the fact that photon propagation over distances of tens of micrometres occurs

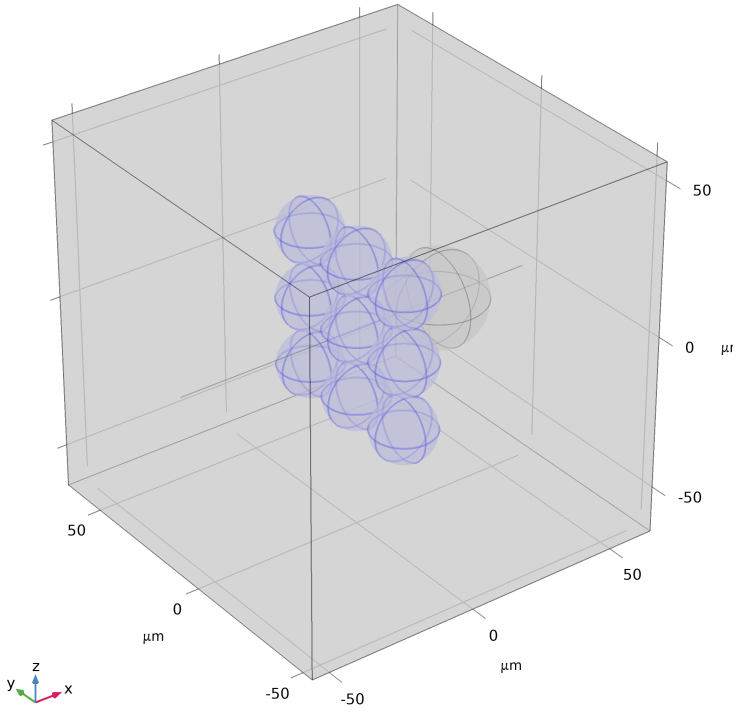

Figure 5.8: Geometry used in the multi-source configuration. The computational domain is a cubic volume of brain tissue with side length $L = 120$ µm. In this configuration, nine identical bioluminescent motes (shown as blue spheres) are arranged in a 3×3 array, each modeled as a spherical volumetric emitter with radius $r_{\mathrm{b}} = 10$ µm. Adjacent motes are separated by a 2 µm gap between their surfaces. A spherical neuronal soma (shown as a grey sphere) with radius $r_{\mathrm{tgt}} = 15$ µm is positioned in front of the central mote, with a surface-to-surface separation of 2 µm. As in the single-source case, the medium outside the sources and target is assumed to be homogeneous and is assigned the optical properties of the grey matter brain tissue.

on sub-picosecond timescales, and therefore does not introduce any noticeable delay or distortion in the temporal shape of the fluence rate.

Overall, the multi-source configuration produces a higher fluence throughout the domain, with the magnitude of the increase depending on the distances between each observation point and the surrounding motes, as well as the geometric arrangement of the array. Because the radiative transfer equation is solved with all volumetric emitters present simultaneously in the domain, the resulting fluence field reflects the superposition of contributions from each source. As a result, while the temporal shape of $\Phi(\mathbf{r}, t)$ remains consistent with the single-source case (being determined by the emission profile), the amplitude increases in a spatially dependent manner governed by the relative proximity of each source and the attenuation along its path to the observation point.

To interpret these trends, we compare the COMSOL results with the analytical ballistic solution derived in subsection 4.4.2. In the single-source configuration (see Figure 5.5(a)), the ballistic fluence rate at a radial distance $r \geq r_B$ from the mote centre is given by the spherical-source expression introduced in Equation 4.40. To explicitly distinguish between source configurations, we write this quantity as $\Phi^{(0)}_{\text{single}}(r, t)$ for the single-source case (and analogously $\Phi^{(0)}_{\text{multi}}(r, t)$ for the mote array).

For the multi-source configuration, we exploit the linearity of the ballistic transport problem and approximate the ballistic field at a point $\mathbf{r}$ by a superposition of nine identical single-source solutions. Each mote is treated as emitting into an otherwise homogeneous grey-matter background. Let $\mathbf{r}_i$ denote the centre of the i-th mote and $r_i = \|\mathbf{r} - \mathbf{r}_i\|$ the

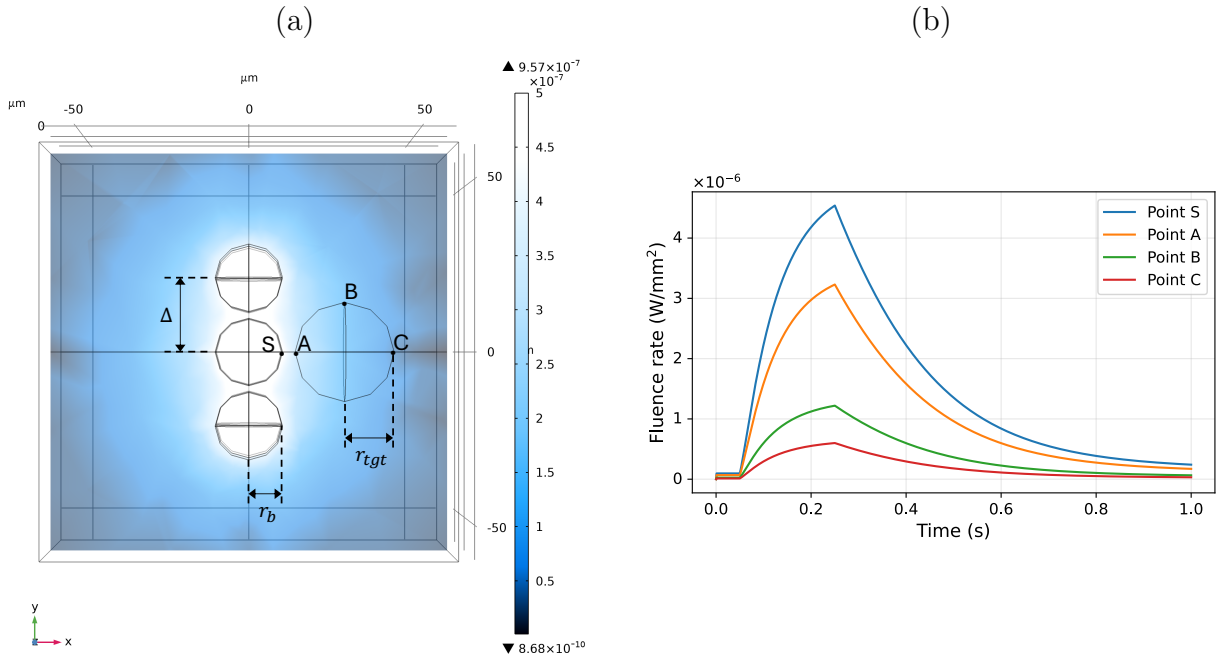

Figure 5.9: Fluence rate distribution and temporal evolution for a multi-source configuration. Nine bioluminescent motes (radius 10 µm) are arranged in a 3×3 geometry, and a neuronal soma (radius 15 µm) is placed 2 µm from the surface of the central mote. (a) Instantaneous fluence rate $\Phi(\mathbf{r}, t = 0.25 \text{ s})$ in the $x-y$ plane intersecting the centres of the emitters and the target soma ($z = 0$). Although nine motes are present in a 3×3 arrangement, only three circular source cross-sections are visible in this view because the remaining six motes lie outside the plane (at different z-positions). The full 3D arrangement is shown in Figure 5.8. The labeled points denote positions used for temporal sampling: S on the source surface, A on the soma surface, and B and C inside the soma at increasing depths. Δ shows the centre-to-centre spacing which is equal between the each source and its neighbor sources. (b) Temporal evolution of the fluence rate $\Phi(\mathbf{r}, t)$ at these locations, computed from the full time-dependent RTE solution (COMSOL).

distance from that mote to the observation point $\mathbf{r}$. The multi-source ballistic field is then written as

$$\Phi^{(0)}_{\text{multi}}(\mathbf{r}, t) = \sum_{i=1}^{N=9} \Phi^{(0)}_{\text{single}}(r_i, t), \tag{5.29}$$

i.e. as the sum of nine single-source ballistic solutions evaluated at the corresponding source–observer distances. Analytical predictions for the ballistic enhancement factor can then be obtained as $\Phi^{(0)}_{\text{multi}}(\mathbf{r}, t)/\Phi^{(0)}_{\text{single}}(\mathbf{r}, t)$.

The behaviour at point S, located on the surface of the central mote, follows the expectations from the analytical benchmark. In the single-source configuration (Figure 5.5(a)), S lies at a distance $r = r_B$ from the centre of the source, so the ballistic fluence rate at this point is given by the spherical-source expression $\Phi^{(0)}(r_B, t)$ introduced in Equation 4.40. In the multi-source configuration (Figure 5.9(a)), S receives additional contributions from the eight neighbouring motes, each of which lies at a larger centre–to–point distance than the central mote. Evaluating $\Phi^{(0)}(r, t)$ at these distances[6] and summing the nine contributions yields an analytical prediction for the ballistic enhancement factor at point S,

$$\frac{\Phi^{(0)}_{\text{multi}}(\text{S})}{\Phi^{(0)}_{\text{single}}(\text{S})} \approx 1.6. \tag{5.30}$$

Since both the single-source and multi-source ballistic fields are proportional to the same

[6]In Figure 5.9, all nine motes are in the $y-z$ plane at $x = 0$, with centre-to-centre spacing $\Delta = 2r_B + 2\ \mu\text{m} = 22\ \mu\text{m}$. The central mote is at $(x, y, z) = (0, 0, 0)$, and the others are located at $(0, \pm\Delta, 0)$, $(0, 0, \pm\Delta)$, and $(0, \pm\Delta, \pm\Delta)$. Point S is on the surface of the central mote facing the soma, at $(x, y, z) = (r_B, 0, 0) = (10, 0, 0)\ \mu\text{m}$. The centre of the central mote is therefore 10 µm from point S. Each of the four nearest neighbouring motes (those sharing a row or column with the central mote) has its centre at a distance $\sqrt{10^2 + 22^2} \approx 24.2\ \mu\text{m}$ from S, and each of the four diagonal motes has its centre at a distance $\sqrt{10^2 + 22^2 + 22^2} \approx 32.7\ \mu\text{m}$ from S.

Table 5.2: Comparison between the fluence rate resulting from single source configurations and a 3×3 array of sources based on COMSOL-based full RTE solutions and analytical ballistic approximations.

	Peak fluence rate from single source (W/mm^2)	Peak fluence rate from 3×3 array (W/mm^2)	Enhancement factors ($\Phi_{\text{multi}}/\Phi_{\text{single}}$)	
			Analytical	COMSOL
Point S	2.58×10^{-6}	4.50×10^{-6}	≈ 1.6	1.74
Point A	1.44×10^{-6}	3.23×10^{-6}	≈ 2.0	2.24
Point B	0.22×10^{-6}	1.22×10^{-6}	≈ 4.6	5.55
Point C	0.09×10^{-6}	0.60×10^{-6}	≈ 5.3	6.67

emission envelope $E(t)$, this ratio is independent of time.

Thus, even though eight additional motes are present, the ballistic fluence at S increases by only about 60%, because the central mote remains dominant and the more distant neighbours are strongly attenuated by geometry and extinction. The full COMSOL solution in Table 5.2 yields a slightly larger enhancement of 1.74, as expected once scattered photons are included; nevertheless, the analytical prediction correctly captures both the order of magnitude and the fact that S experiences the smallest relative increase among the four sampling points.

The behaviour at point A, located on the surface of the target soma facing the array (see Figure 5.9(a)), can be interpreted in the same way. In the single-source configuration, A lies at a distance of 12 µm from the centre of the central mote, and the ballistic fluence rate at this point is given by the spherical-source expression $\Phi^{(0)}(r = 12\ \mu\text{m}, t)$. In the multi-source configuration, point A receives additional contributions from the eight neighbouring

motes at different distances[7]. The corresponding analytical superposition gives

$$\frac{\Phi^{(0)}_{\text{multi}}(\text{A})}{\Phi^{(0)}_{\text{single}}(\text{A})} \approx 2.0, \tag{5.31}$$

so that the ballistic fluence rate at the soma surface roughly doubles when going from one to nine motes. This enhancement is larger than at S (≈ 1.6), because at point A the direct contribution from the central mote is reduced while the relative weight of the neighbouring motes increases. The full COMSOL RTE solution gives an enhancement of 2.24 (see Table 5.2), again slightly larger than the purely ballistic estimate but consistent with the same physical picture.

Point B lies on the upper surface of the soma. In the single-source configuration (see Figure 5.5(a)), the ballistic fluence rate at B is given by $\Phi^{(0)}(r = 30.9\ \mu\text{m}, t)$, where $r \approx 30.9$ µm is the distance from B to the central mote. Because B is located above the central line, in the multi-source configuration (Figure 5.9(a)) it is relatively far from the central mote but lies at comparable distances from several motes in the vertical column of the array. In the multi-source configuration, none of the emitters dominates as strongly as at S or A, and the contributions from several motes add more nearly on an equal footing.

[7]In Figure 5.9(a) point A lies on the soma surface facing the mote array so its coordinates are $(x, y, z) = (12, 0, 0)$ µm. The centre of the central mote is therefore 12 µm from point A. Each of the four nearest neighbouring motes (those sharing a row or column with the central mote) has its centre at a distance $\sqrt{12^2 + 22^2} \approx 25.1$ µm from A, and each of the four diagonal motes has its centre at a distance $\sqrt{12^2 + 22^2 + 22^2} \approx 33.4$ µm from A.

The analytical superposition considering all different distances[8] yields

$$\frac{\Phi^{(0)}_{\text{multi}}(\text{B})}{\Phi^{(0)}_{\text{single}}(\text{B})} \approx 4.6, \tag{5.32}$$

indicating that the ballistic fluence rate at B is enhanced by more than a factor of four when the 3×3 array is present. The full COMSOL solution gives an even larger enhancement of 5.55 (Table 5.2), reflecting the additional contribution of multiply scattered photons, but the analytical result correctly predicts that B experiences a much stronger relative increase than S or A.

Finally, point C is located on the far side of the soma (see Figure 5.9(a)). In the single-source configuration, the distance between C and the central mote is $r \approx 42$ µm, thus the ballistic fluence rate at this point is given by $\Phi^{(0)}(r = 42\ \mu\text{m}, t)$. At this distance, the ballistic contribution from the central mote alone is strongly attenuated. In the multi-source configuration, C receives eight additional terms of comparable magnitude from the rest of the array[9]. The resulting analytical superposition gives

$$\frac{\Phi^{(0)}_{\text{multi}}(\text{C})}{\Phi^{(0)}_{\text{single}}(\text{C})} \approx 5.3, \tag{5.33}$$

[8] In Figure 5.9(a), the soma centre is at $(x, y, z) = (27, 0, 0)$ µm. Point B is at the top of the soma, at $(27, 15, 0)$ µm. The central mote located at $(0, 0, 0)$, has therefore $\sqrt{27^2 + 15^2} \approx 30.9$ µm distance from point B, while the upper neighbouring mote located at $(0, 22, 0)$ is slightly closer, at $\sqrt{27^2 + 7^2} \approx 27.9$ µm. The distances from point B to the remaining seven motes lie between ≈ 36 and ≈ 51 µm.

[9] In Figure 5.9(a), the soma centre is at $(27, 0, 0)$ µm. Point C is on the far surface of the soma, at $(42, 0, 0)$ µm. The central mote at $(0, 0, 0)$ is therefore 42 µm from point C. Each of the four nearest neighbouring motes (those sharing a row or column with the central mote) has its centre at a distance $\sqrt{42^2 + 22^2} \approx 47.4$ µm from C, and each of the four diagonal motes has its centre at a distance $\sqrt{42^2 + 22^2 + 22^2} \approx 52.3$ µm from C.

so that, even when only the ballistic component is considered, the fluence on the far side of the soma is enhanced by more than a factor of five. The full COMSOL RTE solution yields an enhancement of 6.67 (Table 5.2), which is larger in magnitude but consistent with C, displaying the strongest relative increase among all points. Taken together, these comparisons demonstrate that the analytical ballistic benchmark, combined with simple superposition, provides a physically transparent framework for understanding how the spatial arrangement of bioluminescent motes shapes the local illumination landscape, while the full numerical RTE solution quantifies the additional amplification due to scattered light.

6

Conclusion and Future Work

This chapter concludes the thesis by revisiting its central aim: the design and evaluation of a wireless, ultrasound-powered, aequorin-based bioluminescent illumination mote for deep-tissue optogenetic and bio-optical applications. Building on the modelling framework developed in chapter 4, we first summarize the main contributions of this work. We then discuss the implications of these findings for optogenetics and bio-optical communication, outline the key limitations of the present study, and propose directions for future research.

6.1 Summary of Main Contributions

The work presented in this thesis makes several contributions to the design and analysis of wireless bioluminescent illumination systems for applications in optogenetics and bio-optical interfaces.

- **Wireless stimulation and system-level modelling**

  This work builds on the concept of CMOS-based neural dust [193] and addresses two of its major limitations: constraints on miniaturization and limited biocompatibility. Drawing inspiration from a previously proposed wired bioluminescent transceiver [69], it introduces a wireless and biologically compatible stimulation strategy using M13 bacteriophage–based piezoelectric nanogenerators to harvest ultrasonic energy in vivo. Unlike earlier studies, the present thesis develops and evaluates a system-level model of the bioluminescent mote, capturing the dynamic behaviour of the entire illumination process for the first time.

  To model the full process, an equivalent-circuit framework was developed that integrates piezoelectric energy conversion, calcium-induced calcium release (CICR) dynamics, and aequorin-based bioluminescence within a microscale emitting compartment. This framework establishes a quantitative input–output relationship and serves as the foundation for subsequent design optimization and parameter sensitivity analysis. It should be noted that the equivalent-circuit representation of the

piezoelectric nanogenerator is adapted from the literature, while the remaining components of the model are developed in this thesis.

- **Characterization of the bioluminescent mote behaviour**

  The equivalent circuit framework was used to characterise the illumination behaviour of the bioluminescent mote under ultrasonic stimulation. The analysis focused on how three design parameters (the aequorin concentration [Aq], the nanobubble radius r_B, and the engineered SR volume fraction ϕ_{SR}) shape calcium dynamics and photon emission. The model was also applied to several aequorin variants in order to compare their performance under identical geometric and loading conditions.

  These studies clarified how geometric parameters and biochemical properties influence peak illumination. Mutant constructs with high calcium sensitivity produce substantially higher light output than the wild type, whereas the wild type shows stronger modulation by geometric changes. Together, these results outline how biochemical choice and device geometry jointly determine the behaviour of the mote and provide guidance for selecting suitable variants for either tunability or maximal brightness.

  In practice, the modelling workflow combines multi-physics simulation and system-level analysis. The relevant parameters are first obtained by fitting to results reported in the literature. These parameters are then used in the equivalent-circuit model implemented in MATLAB, where the time-dependent behaviour of calcium dynamics and bioluminescent emission is computed.

- **Sensitivity analysis and design guidelines**

  Analytical expressions were derived to quantify the sensitivity of peak photon emission to changes in [Aq], r_B, and ϕ_{SR}. The results show a linear dependence on aequorin concentration, a cubic scaling with nanobubble radius through its volume, and a nonlinear, variant-dependent response to sarcoplasmic-reticulum volume fraction. These expressions were validated through numerical sensitivity analysis using data from 500 simulated configurations per variant, showing excellent agreement.

  Together, these results establish clear design guidelines: nanobubble size provides the strongest control over emission strength, while concentration and SR volume offer additional, biologically tunable parameters for controlling the output.

- **Light transport modelling and multi-source illumination**

  A time-dependent radiative transfer model was implemented in COMSOL to study bioluminescent light propagation through brain tissue. The numerical solutions were validated against an analytically derived ballistic (uncollided) solution for a spherical source geometry across four representative brain tissues. The comparison confirmed that the RTE implementation reproduces near-source behaviour and captures tissue-specific attenuation and scattering effects.

  The framework was then applied to both single- and multi-mote configurations in the vicinity of a neuronal soma. The results quantify how tissue type and source number influence the fluence rate at biologically relevant locations. In particular, multi-mote arrays were shown to enhance the fluence stronger at the distal side of the soma. This

demonstrates the potential of distributed emitter designs for achieving more uniform and effective neuronal illumination.

6.2 Discussion of Key Findings

This section discusses the main findings of the thesis in relation to the original research objectives. The results are organised around three themes: (i) the wireless stimulation, calcium dynamics and resulting bioluminescence of the mote, (ii) the influence of design parameters and aequorin variants on the illumination response, and (iii) the propagation of emitted light through brain tissue in both single- and multi-source configurations.

6.2.1 Wireless Stimulation and Mote Operation

The first key finding is that, short ultrasonic pulses delivered to M13-based piezoelectric nanogenerators are sufficient to drive bioluminescent emission from the mote. In particular, the results in Figure 3.7 and Figure 5.1 show that a 5 ms stimulation pulse at an acoustic intensity of 2.5 $\mathrm{mW\,cm^{-2}}$ at the location of the M13 phage nanogenerators is sufficient to initiate CICR in the engineered SR. This leads to a transient elevation in the nanobubble calcium concentration, rising to peak values in the sub-micromolar range (on the order of hundreds of nM, depending on configuration). Stimulation pulses shorter than this threshold fail to trigger CICR. This identifies a minimum effective stimulation duration and intensity required for reliable activation of the mote under the chosen parameterisation.

The resulting bioluminescent response follows the calcium transient. For representative parameter values, specifically, a nanobubble radius $r_B = 15$ µm, a sarcoplasmic reticulum volume fraction $\phi_{\mathrm{SR}} = 3\%$ (geometric dimensions matching a reference myocyte cell), and a wild-type aequorin concentration of $[\mathrm{Aq}] = 455$ µM, the system produces a transient photon emission, with peak illumination rates in the range of 10^8–10^9 photons/s and total photon outputs on the order of 10^8 photons over a one-second stimulation cycle (Figure 5.1(c),(d)).

An additional practical question is how many stimulation illumination cycles can sustain before the available bioluminescent output degrades significantly. In the absence of aequorin recombination/regeneration, the achievable number of cycles is primarily determined by the initial number of aequorin molecules contained in the nanobubble and their consumption rate per cycle. The initial number scales with the aequorin concentration and the nanobubble volume, whereas the consumption rate depends on the illumination level produced during each stimulation event. Consequently, for low-emission regimes such as the wild type, only a relatively small fraction of the available aequorin pool is consumed per cycle, so the mote could in principle operate over a comparatively large number of cycles before depletion becomes limiting factor. In contrast, for higher-output mutants such as QD+AT, the stronger photon emission is expected to consume the available aequorin pool more rapidly, thereby reducing the number of sustainable cycles. If recombination/regeneration is taken into account, however, the effective operational lifetime could be extended substantially, potentially enabling much longer repeated-use operation. Under this interpretation, the limiting factor is not the triggering mechanism itself, but rather the balance between the available aequorin reservoir, its cycle-by-cycle consumption, and

the rate at which active aequorin can be restored.

These results provide, for the first time, a quantitative estimate of the expected optical output of an aequorin-based mote, both in terms of intensity and time course.

6.2.2 Dependence on Design Parameters and aequorin Variants

A central objective of this work was to understand how the geometric and biochemical parameters of the mote influence its illumination behaviour. The time-domain simulations in Figure 5.1 illustrate the distinct roles played by the nanobubble radius r_B, the engineered SR volume fraction ϕ_{SR}, and the aequorin concentration [Aq].

Increasing the nanobubble radius r_B while holding ϕ_{SR} constant preserves the calcium transient waveform, since the relative volume available for calcium release remains unchanged. However, the larger nanobubble volume contains a greater number of aequorin molecules, thereby increasing the total emission capacity $I_{\max}$. This results in a higher peak illumination rate, as seen when comparing Scenario 1 and Scenario 2 in Table 5.1. The analytical sensitivity analysis reveals an elasticity $\mathcal{E}_{r_B} = 3$, indicating that the peak emission scales cubically, consistent with geometric volume scaling.

In contrast, increasing ϕ_{SR} at fixed bubble size directly impacts the calcium dynamics. A larger engineered SR stores more calcium and releases a higher absolute amount into the nanobubble upon stimulation, raising the peak intracellular calcium concentration. This leads to increased photon emission rates, as observed in Scenario 3 of Figure 5.1. The

dependence of the peak emission on ϕ_{SR} is captured by a Hill-like function in the diode model. As such, the corresponding elasticity $\mathcal{E}_{\phi_{\mathrm{SR}}}$ depends on both, the operating point and the choice of aequorin variant.

Finally, variations in [Aq] influence the photon emission profile without altering the underlying calcium waveform. Higher aequorin concentrations increase the number of emitter molecules available for photon generation, resulting in a proportional increase in peak emission rate. This trend is illustrated in Scenario 4 of Figure 5.1 and is captured analytically by an elasticity of $\mathcal{E}_{[\mathrm{Aq}]} = 1$.

Together, these findings establish that the three parameters act as complementary tuning knobs for system performance: r_B primarily governs geometric scaling of output, ϕ_{SR} shapes the calcium transient and system responsiveness, and [Aq] modulates the biochemical conversion of calcium binding events into light.

The results in Figure 5.2 and Figure 5.3 extend this analysis across multiple aequorin variants and 500 randomly sampled parameter sets. They show that engineered mutants significantly outperform the wild type in terms of enabling higher illumination rates. In particular, the Q159D and Q159T variants exhibit median peak emission rates one to two orders of magnitude higher than wild-type aequorin. The QD+AT double mutant delivers the highest overall performance, with median emission rates exceeding 10^9 photons/s and peak values over 4.5×10^9 photons/s within the explored parameter space. These findings identify QD+AT as a strong candidate for high-output motes, while also revealing that this variant exhibits a comparatively weaker dependence on ϕ_{SR}, consistent with its high

calcium sensitivity and early saturation.

The comparison between analytically derived elasticities and empirical elasticities obtained from multivariate log–log regression (Figure 5.4) shows strong agreement across all variants and design parameters. This consistency validates both the underlying structure of the circuit-based model and its utility as a predictive tool for design exploration. In practical terms, the sensitivity results suggest that increasing the bubble radius (while maintaining the SR volume fraction) is the most effective strategy for enhancing emission, but it comes at the cost of having a larger device footprint. Adjusting [Aq] and ϕ_{SR} offers biologically relevant tuning knobs.

6.2.3 Light Transport and Multi-Source Illumination in Brain Tissue

The final group of findings concerns the propagation of bioluminescent light through brain tissue. The time-dependent radiative transfer model implemented in COMSOL and validated against analytical ballistic solutions, provides a physically grounded framework for computing the fluence rate generated by the mote in various brain regions. This approach captures both absorption and scattering effects and enables quantitative evaluation of light delivery at biologically relevant distances and locations.

The validation of the numerical RTE framework against the analytical ballistic benchmark confirmed the correctness and physical fidelity of the simulation setup, while highlighting the fundamental distinction between uncollided and scattered light transport. For

a single spherical source, the numerical results (Figure 5.5) accurately reproduce the expected near-source behaviour, showing excellent agreement with the analytical solution at the source boundary. However, as the radial distance increases, the COMSOL-computed fluence rate consistently exceeds the ballistic prediction. This divergence is physically meaningful, as it quantifies the contribution of in-scattered photons (those that have undergone one or more scattering events) which are neglected by the ballistic solution.

A comparative analysis across different brain tissues (Figure 5.6 and Figure 5.7) revealed a complex relationship between tissue optical properties and the resulting fluence rate. While the ballistic fluence at the source surface is identical across all tissues (depending only on internal source properties) the decay behaviour diverges between the analytical and numerical models. In the ballistic solution, attenuation is governed by the total extinction coefficient, $\mu_t = \mu_a + \mu_s$; accordingly, tissues with higher μ_t, such as the cerebellum, exhibit the steepest decay in the uncollided photon flux. In contrast, the full RTE simulations show that these same tissues yield the highest total fluence rates in the near-source region. This apparent inversion arises from the role of the reduced scattering coefficient, $\mu_s' = \mu_s(1-g)$: in highly scattering media, photons are more likely to be redirected rather than absorbed, increasing the probability of energy remaining near the source through multiple scattering events. These findings underscore that relying solely on ballistic approximations can underestimate the available optical power in high-scattering brain regions.

Finally, the results quantify two physical characteristics relevant to the design and operation of bioluminescent motes. First, in terms of geometric scaling, the fluence rate evaluated on the surface of the mote increase linearly with the source radius. Second,

regarding timescale separation, the temporal evolution of the fluence rate at the target neuron follows the bioluminescent emission profile essentially instantaneously. Since photon propagation times over the simulated domain (approximately 100 µm) are on the order of femtoseconds (several orders of magnitude faster than the sub-second kinetics of the bioluminescence reaction) light transport through the tissue can be accurately treated as instantaneous relative to the source dynamics.

The multi-source simulations extend these insights to configurations involving arrays of motes. In the representative arrangement shown in Figure 5.8 and Figure 5.9, a 3×3 array of identical motes placed near a neuronal soma generates a spatially structured illumination field that is stronger than that produced by a single source, and notably more homogeneous throughout the surrounding medium. Quantitatively, the peak fluence rate at the closest point on the soma increases by a factor of approximately 2.2. The enhancement is even more pronounced at the furthest point on the opposite side of the soma, where the fluence increases by a factor of 6.6 relative to the single-mote case (Table 5.2).

These trends can be well understood through the superposition of the analytical ballistic fields from each mote, combined with scattering-mediated redistribution captured by the full RTE model. At locations near the central emitter, the direct ballistic contribution from that mote dominates the local fluence, so the relative influence of neighboring sources is limited. In contrast, at more distant points such as those on the far side of the target soma, no single source contributes overwhelmingly. Therefore, the cumulative effect of multiple emitters becomes more uniform. This results in larger relative enhancements in fluence, demonstrating the benefit of distributed emission in achieving more homogeneous

and intensified illumination.

Taken together, these findings indicate that arrays of smaller bioluminescent motes may be more effective than a single bright source for achieving spatially distributed illumination of a target neuron. In combination with the mote-level sensitivity analysis, the light transport results provide a quantitative basis for designing source geometries and array configurations that maximize fluence at specific cellular locations while remaining within realistic constraints on device size, biochemical loading, and tissue optical properties.

6.3 Implications for Optogenetics and Bio-Optical Communication

The results of this thesis have several implications for the design of next-generation optogenetic tools and for emerging concepts in bio-optical communication and brain–machine interfaces. While the analysis presented here is based on modelling rather than experimental validation, the findings provide quantitative evidence that ultrasound-powered, aequorin-based bioluminescent motes could form a building block for minimally invasive, wireless optical interfacing with neural tissue.

6.3.1 Implications for Optogenetic Stimulation

Conventional optogenetics rely on optical fibres, rigid waveguides, or electromagnetically powered micro-LED implants to deliver light to opsins. These approaches have enabled im-

portant breakthroughs, but they face persistent challenges related to tethering, mechanical mismatch with soft neural tissue, heating, and long-term biocompatibility. The wireless bioluminescent mote concept proposed in this thesis potentially offers a bio-inspired alternative to conventional metallic and semiconductor-based implants.

A related design consideration concerns the choice of an extracellular, PDMS-encapsulated mote rather than an implementation in which all functional elements are introduced directly into the target cell. Although an intracellular arrangement might appear attractive, it would likely perturb the intrinsic behaviour of the host cell by occupying intracellular volume and by introducing additional artificial components into an already crowded environment. Since cells already contain endogenous organelles and other intracellular structures, the volume available for engineered bioluminescent elements would be limited. This is particularly important because the achievable light output scales with the number of aequorin molecules that can be accommodated within the emitting medium. An intracellular implementation would therefore not only risk altering normal cell function, but would also reduce the available loading volume and, consequently, the maximum photon output. In this respect, the extracellular mote architecture considered in this thesis offers a more practical compromise between preserving cellular integrity and maintaining sufficient internal volume for light generation.

The simulations of mote-level behaviour confirm that short, clinically relevant ultrasonic pulses can trigger transient calcium elevations and initiate photon emission without requiring wired connections or local batteries. Moreover, the light-transport analysis indicates that the resulting bioluminescent field achieves fluence rates consistent with the

levels required to induce a neuronal response. Specifically, the results show that even a single mote, with a surface-to-target separation of 2 µm, can generate a fluence rate of approximately 4×10^{-6} W mm^{-2} at the membrane of the target neuron. This value lies within the comparable range for cellular activation, as optogenetic literature indicates that high-sensitivity opsins can be excited with intensities as low as 1×10^{-6} W mm^{-2} [194]. Furthermore, the deployment of multi-mote arrays was found to not only amplify the signal but also render the fluence distribution significantly more homogeneous across the target medium. Together, these results suggest that distributed ensembles of small bioluminescent motes could eventually provide an alternative to fibre-based or micro-LED-based implants in scenarios where minimal invasiveness and mechanical compliance are critical, such as chronic studies in freely moving animals.

Moreover, these quantitative design rules provide a pathway to tailor motes for targeted applications. The sensitivity analysis results offers a principled way to balance device size against required photon output. Additionally, the use of high-yield variants like QD+AT is shown to enhance peak emission by orders of magnitude over the wild type. Although the present thesis does not model specific opsin activation curves, it provides the illumination metrics needed to perform such an analysis in a systematic manner.

6.3.2 Implications for Bio-Optical Communication and Brain–Machine Interfaces

Beyond optogenetic stimulation, the proposed mote architecture fits into broader visions of bio-optical communication, in which information is encoded, transmitted, and processed using light within or between biological tissues. The modelling framework developed in this thesis links an internally generated light source, whose dynamics are governed by biochemistry and ultrasound control, to the resulting optical field in realistic brain-like media. As such, it can be viewed as a prototype for a bio-integrated optical transmitter whose output can be shaped both temporally (via ultrasound drive) and spatially (via mote design and array geometry).

In the context of brain–machine interfaces, such motes could in principle serve as local optical nodes that communicate with opsin-expressing neurons, with other photoreceptive molecular constructs, or with external photodetectors coupled through transparent windows or implanted waveguides. The ability to form arrays of motes and to predict how their combined emission patterns fill a volume of tissue is particularly relevant for network-level interfacing strategies, where multiple channels of optical input and output must coexist in a confined region. The linearity of the radiative transfer regime studied here means that more complex spatiotemporal illumination patterns could be synthesised by driving subsets of motes with different ultrasound waveforms, offering a form of spatial multiplexing that does not rely on complex optical hardware.

Furthermore, the simulations in this thesis are performed for Aequorin with native coelenterazine and the emitted light is therefore modelled as blue with a peak near 470 nm. Nevertheless, the mote architecture and equivalent-circuit framework can be readily extended to alternative Aequorin variants with different emission spectra (see subsection 2.1.2). In such cases, the predicted illumination rates can be interpreted at the variant's peak emission wavelength. On this basis, although multi-wavelength operation is not investigated in this thesis, it remains a plausible extension that could enable spectral multiplexing using heterogeneous mote arrays emitting at distinct wavelengths.

More speculatively, the results also relate to emerging ideas about intrinsic biophotons and natural light-guiding structures such as myelinated axons [38]. Although these mechanisms are not explicitly modelled in the present work, the ability to generate controlled, localized bioluminescent fields suggests a possible route towards hybrid systems in which engineered motes inject photons into endogenous optical pathways. The framework established here can be extended to explore such scenarios by substituting appropriate tissue geometries and optical parameters.

6.3.3 Methodological and Design Implications

Finally, the thesis contributes a modular modelling framework that can be reused and extended beyond the specific aequorin-based mote studied here. The equivalent-circuit representation of the biochemical and bioluminescent dynamics provides a compact, computationally efficient way to explore large parameter spaces and to compare different molec-

ular variants. The sensitivity analysis yields interpretable design metrics that translate directly into engineering trade-offs. The radiative transfer implementation, validated against analytical ballistic solutions, offers a general tool for predicting light distributions from arbitrary volumetric sources in homogeneous tissue.

Taken together, these elements form a quantitative design framework for bio-optical interfaces that is not limited to a particular molecule, tissue type, or application. They can, in principle, be adapted to other bioluminescent systems, alternative energy-harvesting schemes, or different target organs where optical access is limited. In this sense, the implications of the present work extend beyond the specific mote concept and point towards a broader class of biocompatible, wirelessly driven optical devices for neuromodulation and bio-communication.

6.4 Limitations

The conclusions drawn in this thesis are subject to several limitations arising from modelling assumptions, biological and engineering constraints, and the scope of validation. These limitations do not invalidate the main results, but they describe the conditions under which they should be interpreted and highlight directions for future work.

6.4.1 Modelling Assumptions and Biological Simplifications

The first set of limitations concerns the abstraction level of the mote and tissue models. Calcium handling, CICR, and aequorin kinetics are represented using an equivalent-circuit formulation with simplified parameter sets. This approach enables computationally efficient simulations and supports analytical sensitivity analysis, but it necessarily abstracts the full biochemical details. In particular, the present model does not include detailed representations of ion channels and ion pumps that may influence the response of the engineered SR.

Similarly, the assumed aequorin concentrations and engineered SR volume fractions are based on solubility data and reference values from myocytes. However, the feasibility of achieving comparable loading levels in neurons, or within nanoscale motes, has not been established experimentally.

Furthermore, the present model quantifies photon emission from the mote and models the subsequent propagation of the emitted light through the surrounding medium. However, the downstream optogenetic response is not modelled and therefore lies outside the scope of this work. As such, conclusions regarding the suitability of the mote for optogenetic stimulation remain qualitative at this stage.

6.4.2 Ultrasound, Energy Harvesting, and Tissue Optics

A second group of limitations arises from the treatment of ultrasound stimulation, piezoelectric energy harvesting, and light transport in tissue. The interaction between the ultrasonic field and the M13-based piezoelectric nanogenerator is modelled at a system level. Spatial variations in the ultrasound field and beamforming are not explicitly resolved.

On the optical side, the framework used for modelling light transport, the RTE, relies on a linear, scalar description of tissue optics. As such, it neglects coherence, interference, polarization, and any time-varying changes in tissue properties (for example due to blood flow). Within this framework, the radiative transfer analysis is based on several additional idealisations that should be kept in mind when interpreting the results.

First, the geometry is deliberately simplified: motes and somata are represented as spheres, and the surrounding brain tissue is treated as a homogeneous medium. This neglects microscale heterogeneity in the tissue which can locally perturb the light field.

Second, the optical properties themselves are simplified. Within each tissue type, absorption, scattering, anisotropy, and refractive index are assumed spatially uniform and are taken from reported measurements in human brain samples. These parameters are further compressed into emission-weighted averages over the aequorin half-maximum band and then used in a monochromatic model at 470 nm. This procedure underestimates the wavelength dependence within the 440 nm to 520 nm interval, sample-to-sample variability in the underlying measurements. However, the results indicate that in the near-source region, the fluence rate is primarily reduced due to the geometric spreading, with only minor

variations observed across different tissue types. This suggests that, within the spatial scales considered in this work, the impact of spectral averaging over the 440 nm to 520 nm emission band is limited, and the monochromatic approximation at 470 nm provides a reasonable representation of the light field.

A further simplification concerns the optical representation of the mote itself. In the proposed design, the bioluminescent compartment is surrounded by an approximately 1 µm-thick PDMS encapsulation layer. For tractability, this layer is not modelled explicitly in the radiative transfer simulations; instead, the mote is approximated as a single homogeneous emitting region embedded directly in tissue. This neglects the refractive-index mismatch at the nanobubble–PDMS–tissue interfaces, and thus ignores associated Fresnel reflections and refraction, as well as any residual absorption or scattering within the PDMS. These effects are expected to have only a modest influence on the overall fluence, but they may alter the detailed angular emission pattern and near-field distribution in the immediate vicinity of a PDMS-coated device.

Finally, the benchmark used to validate the numerical implementation is itself idealised: it isolates only the uncollided (ballistic) component of the solution. This analytical expression can therefore be interpreted as a lower bound on the fluence, since the full radiative transfer solution necessarily includes additional contributions from scattered photons. Taken together, these assumptions mean that the optical results should be regarded as first-order, physically informed estimates of light availability around a mote embedded in brain tissue, rather than precise predictions for any particular anatomical arrangement.

6.4.3 Engineering Constraints, Functional Interpretation, and Validation

Finally, there are limitations related to practical implementation, functional interpretation, and validation. The motes considered in this work are assumed to have well-defined sizes, internal compartmentalisation, and positions relative to a target neuron. In particular, some of the simulated configurations assume source-to-membrane separations in the order of 2 µm. Achieving such close proximity may be difficult for freely diffusing motes in the extracellular space and would likely require a dedicated delivery or membrane-targeting strategy, which is not addressed in the present work. As such, the assumed mote positions should be interpreted as an idealized configuration used to evaluate light delivery under favourable geometric conditions. Issues such as fabrication yield, variability in mote geometry, and methods for in vivo delivery and anchoring are not addressed in detail. The multi-source configurations analysed here also assume ideal placement and synchronised operation. Furthermore, aspects such as the biocompatibility of M13 nanogenerators and aequorin constructs, isolation of the engineered SR compartment, and M13-nanogenerator surface display are treated only at a conceptual level, sufficient to assess the basic feasibility of the proposed design. A full engineering exploration of these topics lies beyond the scope of the present work.

From a functional perspective, the thesis quantifies photon emission rates and fluence levels but does not implement explicit models of opsin activation or neural firing. Additionally, all results are based on simulations; there is currently no experimental validation of the

full chain from ultrasound stimulation through piezoelectric harvesting and aequorin-based bioluminescence to measured light distributions in tissue.

These limitations suggest that the present work should be regarded as a theoretical and computational feasibility study that establishes a quantitative design framework. Addressing these gaps through targeted experiments, more detailed multi-physics modelling, and robustness analysis will be essential steps in translating the proposed mote concept into a practical optogenetic or bio-optical interface.

6.5 Future Work

The results of this thesis open up several directions for further research, spanning experimental validation, model refinement, design optimisation, and broader applications in optogenetics and bio-optical communication.

6.5.1 Experimental Validation of the Mote Concept

A natural next step is to validate the core components of the proposed mote through targeted experiments. Experimental attention can be directed toward confirming the feasibility of engineering internal components of the mote that support the CICR process. Prior studies in muscle cells have demonstrated SR structures with controlled calcium handling [195], but further investigation is needed to assess whether similar behaviour can be achieved in synthetic constructs at the microscale. Furthermore, experiments on

M13 PENGs could quantify the electrical output produced under ultrasonic stimulation in biologically relevant media.

Ultimately, a proof-of-concept demonstration would aim to show ultrasound-triggered bioluminescence from an aequorin-loaded compartment coupled to an M13-based nanogenerator. Initial validation could be performed in fluid environments, followed by experiments in tissue-mimicking gel constructs that approximate the acoustic and optical properties of brain tissue. These results would help establish the practical feasibility of wireless optical actuation and support refinement of model parameters.

6.5.2 Refinement of Biophysical and Optical Models

Several extensions on the modelling side could improve the biological realism and predictive accuracy of the framework. The current equivalent-circuit description of calcium handling and bioluminescent kinetics could be expanded to include additional biophysical processes such as ion pumps and ion channel dynamics. In parallel, future work could explore alternative modelling strategies (beyond the circuit-based approach) to enhance predictive capability. Coupling the mote to a biophysical model of neuron would also enable simulation of how the emitted light interacts with opsin-expressing membranes or other light-sensitive targets.

In the optical domain, the radiative transfer simulations could be extended to more anatomically realistic tissue geometries, including spatially varying scattering and absorption properties. Incorporating the full spectral profile of aequorin emission, along with

wavelength-dependent optical coefficients, would allow finer-grained predictions of fluence. Finally, a systematic uncertainty analysis, in which both optical and biochemical parameters are varied within plausible experimental ranges, would help assess the robustness of the model's conclusions.

6.5.3 Design Optimization and Array Architectures

The sensitivity analysis presented in this work provides an initial set of design rules for tuning mote parameters. Future studies could build on this foundation by formulating explicit optimization problems; for example, maximizing fluence at a specified target region subject to constraints on mote size, emitter concentration, and total volume, or minimizing the number of motes required to achieve a given illumination profile.

At the multi-source level, a broader range of spatial configurations and stimulation strategies remains to be explored. This includes irregular mote distributions, three-dimensional lattice arrangements, and selective targeting of subsets of motes using spatially patterned ultrasound fields. Time-multiplexed or phase-shifted ultrasound waveforms could be employed to generate more complex spatiotemporal illumination profiles, and the radiative transfer framework developed here is well suited to predicting the resulting light fields.

Moreover, because nanogenerator structures exhibit geometry-dependent resonance frequencies, it is possible to implement frequency-based multiplexing schemes by assigning distinct resonance frequencies to different motes or subgroups. This would enable selective activation using frequency-tuned ultrasound pulses, providing an additional degree of

control over the spatial and temporal patterning of light delivery.

6.5.4 Integration with Optogenetic and Bio-Optical Interfaces

An important direction for future work is the integration of the mote concept with established optogenetic and bio-optical systems. By combining the fluence predictions developed here with existing models of opsin activation, it becomes possible to evaluate specific mote designs and array geometries in terms of their ability to induce excitation or inhibition for specific opsins. Genetically encoded voltage or calcium indicators can be integrated into the design, enabling the use of motes as targeted illumination sources for optical recording.

6.5.5 Towards In Vivo Implementation

Finally, translating the mote concept into an in vivo technology will require addressing several engineering and biological challenges. These include the development of manufacturable mote architectures with controlled size and internal structure, methods for targeted delivery and long-term stabilization in neural tissue, and comprehensive safety studies covering both ultrasonic stimulation and chronic exposure to the mote materials. Progress in these areas will depend on close collaboration between materials science, molecular biology, neuroscience, and biomedical engineering. The present thesis provides a quantitative foundation on which such multidisciplinary efforts can build, by clarifying the parameter regimes and performance targets that a practical implementation would need to achieve.

6.5.6 Safety, Ethical, Security, and Regulatory Considerations

An additional set of considerations that will become increasingly important as the proposed mote concept moves toward experimental and in vivo implementation concerns safety, ethics, security, and regulation. Although these aspects lie beyond the scope of the present modelling study, they are essential for any future translation of the technology.

From a safety perspective, an important outcome of the present work is that the acoustic stimulation required to trigger the mote remains below commonly accepted safe exposure ranges. This suggests that, at least at the level of the current modelling framework, ultrasound-driven activation of the engineered system can in principle be achieved without requiring excessively high acoustic pressures. In this sense, the results provide an encouraging first indication that the proposed stimulation strategy may be compatible with safe operation.

At the same time, this conclusion should be interpreted with appropriate caution. Demonstrating that activation occurs below established exposure limits does not by itself constitute a complete safety assessment. Future work should examine more specific effects associated with localized and repeated stimulation and confirm that the stimulation protocol remains safe under realistic biological conditions.

Ethical considerations will also become central once the system advances beyond theoretical modelling and is tested in animal models and, potentially, in human subjects. Such

studies will need to be conducted within established ethical frameworks for biomedical research, including institutional review, careful risk–benefit analysis, and, where applicable, informed consent. More broadly, because the proposed system is intended to modulate neural activity through wireless stimulation, its development should be accompanied by continued reflection on issues of autonomy, privacy, and responsible use.

In addition, the wireless nature of the mote introduces security-related considerations. A technology capable of externally influencing neural function should ultimately be designed with safeguards against unintended activation, electromagnetic or acoustic interference, and malicious misuse.

Finally, any progression toward practical biomedical use will need to account for the relevant regulatory pathway. Before deployment in vivo, the technique would require rigorous evaluation of safety, efficacy, and biocompatibility in accordance with applicable standards and approval processes for biomedical and implantable technologies. These regulatory considerations are especially important in view of the combined use of ultrasound, engineered biological components, and neural interfacing.

Taken together, these issues highlight that the future development of wireless bioluminescent motes is not only a problem of device performance, but also one of safe, ethical, secure, and clinically responsible implementation.

6.6 Concluding Remarks

This thesis set out to investigate whether a wireless, ultrasound-powered, aequorin-based bioluminescent mote could, in principle, serve as a building block for deep-tissue optical interfacing in neural systems. To that end, a new stimulation architecture was based on M13 bacteriophage nanogenerators and ultrasonic energy harvesting. On top of this, a modelling framework was developed to link ultrasonic excitation, piezoelectric transduction, calcium-induced bioluminescence, and light transport through brain tissue.

Within this framework, the behaviour of the mote was characterized as a function of geometric and biochemical design parameters, as well as across different aequorin variants. The analysis revealed clear scaling laws and sensitivities, and demonstrated that arrays of small motes can help toward having more uniform energy fluence at neuron-scale targets. Radiative transfer simulations (benchmarked against analytical ballistic solutions) confirmed that bioluminescent light fields can be predicted in tissue, and that both tissue-specific optical properties and array geometry affect the resulting illumination patterns.

Taken together, these results support the view that ultrasound-driven bioluminescent motes represent a plausible and potentially powerful direction for minimally invasive optogenetic and bio-optical interfaces. At the same time, they highlight the substantial experimental and engineering work that remains. The contributions of this thesis are therefore twofold: first, it offers a quantitative feasibility study of a specific bio-inspired illumination strategy; second, it establishes a modular design and modelling framework

that can be adapted to future bioluminescent systems, energy-harvesting mechanisms, and tissue environments. It is hoped that this work will serve as a useful foundation for the development of biocompatible, wirelessly driven optical tools for probing and interacting with complex biological networks.

References

[1] P. Alberts, B., Johnson, A., Lewis, J., Raff, M., Roberts, K., and Walter, "Ion Channels and the Electrical Properties of Membranes," in *Molecular biology of the cell*, 4th, New York: Garland Science, 2002, ISBN: 9780815332183.

[2] J. Rivnay, H. Wang, L. Fenno, K. Deisseroth, and G. G. Malliaras, "Next-generation probes, particles, and proteins for neural interfacing," *Science Advances*, vol. 3, no. 6, Jun. 2017, ISSN: 2375-2548. DOI: 10.1126/sciadv.1601649.

[3] C. A. Hubner, "Ion channel diseases," *Human Molecular Genetics*, vol. 11, no. 20, pp. 2435–2445, Oct. 2002, ISSN: 14602083. DOI: 10.1093/hmg/11.20.2435.

[4] K. K. Hartford Svoboda and W. R. Reenstra, "Approaches to studying cellular signaling: A primer for morphologists," *The Anatomical Record*, vol. 269, no. 2, pp. 123–139, Apr. 2002, ISSN: 0003-276X. DOI: 10.1002/ar.10074.

[5] A. D. Gitler, P. Dhillon, and J. Shorter, "Neurodegenerative disease: models, mechanisms, and a new hope," *Disease Models & Mechanisms*, vol. 10, no. 5, pp. 499–502, May 2017, ISSN: 1754-8411. DOI: 10.1242/dmm.030205.

[6] D. T. Brocker and W. M. Grill, "Principles of electrical stimulation of neural tissue," in *Handbook of Clinical Neurologybb*, Elsevier, 2013, pp. 3–18. DOI: 10.1016/B978-0-444-53497-2.00001-2.

[7] M. M. Bellet et al., "Pharmacological modulation of circadian rhythms by synthetic activators of the deacetylase SIRT1," *Proceedings of the National Academy of Sciences*, vol. 110, no. 9, pp. 3333–3338, Feb. 2013, ISSN: 0027-8424. DOI: 10.1073/pnas.1214266110.

[8] L. E. Russell et al., "All-optical interrogation of neural circuits in behaving mice," *Nature Protocols*, vol. 17, no. 7, pp. 1579–1620, Jul. 2022, ISSN: 17502799. DOI: 10.1038/s41596-022-00691-w.

[9] K. S. Chen and R. Chen, "Invasive and Noninvasive Brain Stimulation in Parkinson's Disease: Clinical Effects and Future Perspectives," *Clinical Pharmacology & Therapeutics*, vol. 106, no. 4, pp. 763–775, Oct. 2019, ISSN: 0009-9236. DOI: 10.1002/cpt.1542.

[10] L. Fenno, O. Yizhar, and K. Deisseroth, "The Development and Application of Optogenetics," *Annual Review of Neuroscience*, vol. 34, no. 1, pp. 389–412, Jul. 2011, ISSN: 0147-006X. DOI: 10.1146/annurev-neuro-061010-113817.

[11] T. D. Y. Kozai, A. S. Jaquins-Gerstl, A. L. Vazquez, A. C. Michael, and X. T. Cui, "Brain Tissue Responses to Neural Implants Impact Signal Sensitivity and Intervention Strategies," *ACS Chemical Neuroscience*, vol. 6, no. 1, pp. 48–67, Jan. 2015, ISSN: 1948-7193. DOI: 10.1021/cn500256e.

[12] G. M. Alexander et al., "Remote Control of Neuronal Activity in Transgenic Mice Expressing Evolved G Protein-Coupled Receptors," *Neuron*, vol. 63, no. 1, pp. 27–39, Jul. 2009, ISSN: 08966273. DOI: 10.1016/j.neuron.2009.06.014.

[13] Y. Pan, C. Pan, L. Mao, and P. Yu, "Neuromodulation with chemicals: Opportunities and challenges," *Fundamental Research*, vol. 5, no. 1, pp. 55–62, Apr. 2024, ISSN: 26673258. DOI: 10.1016/j.fmre.2024.04.010.

[14] W. Chen et al., "The Roles of Optogenetics and Technology in Neurobiology: A Review," *Frontiers in Aging Neuroscience*, vol. 14, Apr. 2022, ISSN: 1663-4365. DOI: 10.3389/fnagi.2022.867863.

[15] Q. Lu, Y. Sun, Z. Liang, Y. Zhang, Z. Wang, and Q. Mei, "Nano-optogenetics for Disease Therapies," *ACS Nano*, vol. 18, no. 22, pp. 14 123–14 144, Jun. 2024, ISSN: 1936-0851. DOI: 10.1021/acsnano.4c00698.

[16] G.-H. Lee et al., "Multifunctional materials for implantable and wearable photonic healthcare devices," *Nature Reviews Materials*, vol. 5, no. 2, pp. 149–165, Jan. 2020, ISSN: 2058-8437. DOI: 10.1038/s41578-019-0167-3.

[17] J. L. Sandell and T. C. Zhu, "A review of in-vivo optical properties of human tissues and its impact on pdt," *Journal of Biophotonics*, vol. 4, no. 11-12, pp. 773–787, Nov. 2011. DOI: 10.1002/jbio.201100062.

[18] K. Scholle, S. Lamrini, P. Koopmann, and P. Fuhrberg, "2 µm Laser Sources and Their Possible Applications," in *Frontiers in Guided Wave Optics and Optoelectronics*, InTech, Feb. 2010. DOI: 10.5772/39538.

[19] D. Miyamoto and M. Murayama, "The fiber-optic imaging and manipulation of neural activity during animal behavior," *Neuroscience Research*, vol. 103, pp. 1–9, Feb. 2016, ISSN: 01680102. DOI: 10.1016/j.neures.2015.09.004.

[20] K. Ung and B. R. Arenkiel, "Fiber-optic Implantation for Chronic Optogenetic Stimulation of Brain Tissue," *Journal of Visualized Experiments*, no. 68, Oct. 2012, ISSN: 1940-087X. DOI: 10.3791/50004.

[21] S. Mondello, B. Pedigo, M. Sunshine, A. Fischedick, P. Horner, and C. Moritz, "A micro-LED implant and technique for optogenetic stimulation of the rat spinal cord," *Experimental Neurology*, vol. 335, p. 113 480, Jan. 2021, ISSN: 00144886. DOI: 10.1016/j.expneurol.2020.113480.

[22] F. Wu, E. Stark, P.-C. Ku, K. D. Wise, G. Buzsáki, and E. Yoon, "Monolithically Integrated μLEDs on Silicon Neural Probes for High-Resolution Optogenetic Studies in Behaving Animals," *Neuron*, vol. 88, no. 6, pp. 1136–1148, Dec. 2015, ISSN: 08966273. DOI: 10.1016/j.neuron.2015.10.032.

[23] S. P. Lacour, G. Courtine, and J. Guck, "Materials and technologies for soft implantable neuroprostheses," *Nature Reviews Materials*, vol. 1, no. 10, p. 16 063, Sep. 2016, ISSN: 2058-8437. DOI: 10.1038/natrevmats.2016.63.

[24] E. Song, J. Li, S. M. Won, W. Bai, and J. A. Rogers, "Materials for flexible bioelectronic systems as chronic neural interfaces," *Nature Materials*, vol. 19, no. 6, pp. 590–603, Jun. 2020, ISSN: 1476-1122. DOI: 10.1038/s41563-020-0679-7.

[25] R. Qazi et al., "Wireless optofluidic brain probes for chronic neuropharmacology and photostimulation," *Nature Biomedical Engineering*, vol. 3, no. 8, pp. 655–669, Aug. 2019, ISSN: 2157-846X. DOI: 10.1038/s41551-019-0432-1.

[26] G. Assat and J.-M. Tarascon, "Fundamental understanding and practical challenges of anionic redox activity in Li-ion batteries," *Nature Energy*, vol. 3, no. 5, pp. 373–386, Apr. 2018, ISSN: 2058-7546. DOI: 10.1038/s41560-018-0097-0.

[27] G. Shin et al., "Flexible Near-Field Wireless Optoelectronics as Subdermal Implants for Broad Applications in Optogenetics," *Neuron*, vol. 93, no. 3, 509–521.e3, Feb. 2017, ISSN: 08966273. DOI: 10.1016/j.neuron.2016.12.031.

[28] L.-G. Tran, H.-K. Cha, and W.-T. Park, "RF power harvesting: a review on designing methodologies and applications," *Micro and Nano Systems Letters*, vol. 5, no. 1, p. 14, Dec. 2017, ISSN: 2213-9621. DOI: 10.1186/s40486-017-0051-0.

[29] W. T. Joines, "Frequency-Dependent Absorption of Electromagnetic Energy in Biological Tissue," *IEEE Transactions on Biomedical Engineering*, vol. BME-31, no. 1, pp. 17–20, Jan. 1984, ISSN: 0018-9294. DOI: 10.1109/TBME.1984.325365.

[30] M. Ulbrich, M. Lüken, J. Mühlsteff, and S. Leonhardt, "Wearable bioimpedance systems for homecare monitoring using BSNs," in *Wearable Sensors*, Elsevier, 2021, pp. 519–540. DOI: 10.1016/B978-0-12-819246-7.00019-X.

[31] J. Charthad et al., "A mm-Sized Wireless Implantable Device for Electrical Stimulation of Peripheral Nerves," *IEEE Transactions on Biomedical Circuits and Systems*, vol. 12, no. 2, pp. 257–270, Apr. 2018, ISSN: 1932-4545. DOI: 10.1109/TBCAS.2018.2799623.

[32] A. Goldstein and R. L. Powis, "Medical Ultrasonic Diagnostics," in *Physical Acoustics*, Elsevier, 1999, pp. 43–195. DOI: 10.1016/S0893-388X(99)80012-8.

[33] N. T. Ersaro, C. Yalcin, and R. Muller, "The future of brain–machine interfaces is optical," *Nature Electronics*, vol. 6, no. 2, pp. 96–98, Feb. 2023, ISSN: 2520-1131. DOI: 10.1038/s41928-023-00926-y.

[34] H. H. Yang and F. St-Pierre, "Genetically Encoded Voltage Indicators: Opportunities and Challenges," *The Journal of Neuroscience*, vol. 36, no. 39, pp. 9977–9989, Sep. 2016, ISSN: 0270-6474. DOI: 10.1523/JNEUROSCI.1095-16.2016.

[35] R. R. Mould et al., "Ultra weak photon emission—a brief review," *Frontiers in Physiology*, vol. 15, Feb. 2024, ISSN: 1664-042X. DOI: 10.3389/fphys.2024.1348915.

[36] A. Zangari et al., "Photons detected in the active nerve by photographic technique," *Scientific Reports*, vol. 11, no. 1, p. 3022, Feb. 2021, ISSN: 2045-2322. DOI: 10.1038/s41598-021-82622-5.

[37] S. Kumar, K. Boone, J. Tuszyński, P. Barclay, and C. Simon, "Possible existence of optical communication channels in the brain," *Scientific Reports*, vol. 6, no. 1, p. 36 508, Nov. 2016, ISSN: 2045-2322. DOI: 10.1038/srep36508.

[38] P. Zarkeshian, T. Kergan, R. Ghobadi, W. Nicola, and C. Simon, "Photons guided by axons may enable backpropagation-based learning in the brain," *Scientific Reports*, vol. 12, no. 1, p. 20 720, Dec. 2022, ISSN: 2045-2322. DOI: 10.1038/s41598-022-24871-6.

[39] P. Zarkeshian, S. Kumar, J. Tuszynski, P. Barclay, and C. Simon, "Are there optical communication channels in the brain," *Frontiers in Bioscience*, vol. 23, no. 8, p. 4652, 2018, ISSN: 10939946. DOI: 10.2741/4652.

[40] C. Moro et al., "The code of light: do neurons generate light to communicate and repair?" *Neural Regeneration Research*, vol. 17, no. 6, p. 1251, 2022, ISSN: 1673-5374. DOI: 10.4103/1673-5374.327332.

[41] O. M. Ostafiychuk, V. A. Es'kin, A. V. Kudrin, and A. A. Popova, "Electromagnetic Waves Guided by a Myelinated Axon in the Optical and Infrared Ranges," in *2019 PhotonIcs & Electromagnetics Research Symposium - Spring (PIERS-Spring)*, IEEE, Jun. 2019, pp. 1180–1184, ISBN: 978-1-7281-3403-1. DOI: 10.1109/PIERS-Spring46901.2019.9017803.

[42] M. Omidi, M. I. Zibaii, and N. Granpayeh, "Simulation of nerve fiber based on anti-resonant reflecting optical waveguide," *Scientific Reports*, vol. 12, no. 1, p. 19 356, Nov. 2022, ISSN: 2045-2322. DOI: 10.1038/s41598-022-23580-4.

[43] A. Maghoul, A. Khaleghi, and I. Balasingham, "Engineering Photonic Transmission Inside Brain Nerve Fibers," *IEEE Access*, vol. 9, pp. 35 399–35 410, 2021, ISSN: 2169-3536. DOI: 10.1109/ACCESS.2021.3062299.

[44] J. Joshi, M. Rubart, and W. Zhu, "Optogenetics: Background, Methodological Advances and Potential Applications for Cardiovascular Research and Medicine," *Frontiers in Bioengineering and Biotechnology*, vol. 7, Jan. 2020, ISSN: 2296-4185. DOI: 10.3389/fbioe.2019.00466.

[45] O. A. Shemesh et al., "Temporally precise single-cell-resolution optogenetics," *Nature Neuroscience*, vol. 20, no. 12, pp. 1796–1806, Dec. 2017, ISSN: 1097-6256. DOI: 10.1038/s41593-017-0018-8.

[46] M. T. Hill and M. C. Gather, "Advances in small lasers," *Nature Photonics*, vol. 8, no. 12, pp. 908–918, Dec. 2014, ISSN: 1749-4885. DOI: 10.1038/nphoton.2014.239.

[47] V. Heiskanen and M. R. Hamblin, "Photobiomodulation: lasers vs. light emitting diodes?" *Photochemical & Photobiological Sciences*, vol. 17, no. 8, pp. 1003–1017, Aug. 2018, ISSN: 1474-905X. DOI: 10.1039/c8pp00176f.

[48] J. Quereda, Q. Zhao, E. Diez, R. Frisenda, and A. Castellanos-Gomez, "Fiber-coupled light-emitting diodes (LEDs) as safe and convenient light sources for the characterization of optoelectronic devices," *Open Research Europe*, vol. 1, p. 98, Jul. 2022, ISSN: 2732-5121. DOI: 10.12688/openreseurope.14018.2.

[49] E. A. Ferenczi, X. Tan, and C. L.-H. Huang, "Principles of Optogenetic Methods and Their Application to Cardiac Experimental Systems," *Frontiers in Physiology*, vol. 10, Sep. 2019, ISSN: 1664-042X. DOI: 10.3389/fphys.2019.01096.

[50] H. Adesnik and L. Abdeladim, *Probing neural codes with two-photon holographic optogenetics*, Oct. 2021. DOI: 10.1038/s41593-021-00902-9.

[51] G.-H. Lee et al., "Multifunctional materials for implantable and wearable photonic healthcare devices," *Nature Reviews Materials*, vol. 5, no. 2, pp. 149–165, Jan. 2020, ISSN: 2058-8437. DOI: 10.1038/s41578-019-0167-3.

[52] Stephen Kershaw, "Two-Photon Absorption," in *Characterization Techniques and Tabulations for Organic Nonlinear Optical Materials*, 1st, New York: Routledge, May 2018, pp. 515–654, ISBN: 9781351461818. DOI: 10.1201/9781315139036.

[53] M. Rumi and J. W. Perry, "Two-photon absorption: an overview of measurements and principles," *Advances in Optics and Photonics*, vol. 2, no. 4, p. 451, Dec. 2010, ISSN: 1943-8206. DOI: 10.1364/AOP.2.000451.

[54] F. Pisanello et al., "Multipoint-Emitting Optical Fibers for Spatially Addressable In Vivo Optogenetics," *Neuron*, vol. 82, no. 6, pp. 1245–1254, Jun. 2014, ISSN: 08966273. DOI: 10.1016/j.neuron.2014.04.041.

[55] F. Pisanello et al., "Dynamic illumination of spatially restricted or large brain volumes via a single tapered optical fiber," *Nature Neuroscience*, vol. 20, no. 8, pp. 1180–1188, Aug. 2017, ISSN: 1097-6256. DOI: 10.1038/nn.4591.

[56] D. Shan et al., "Flexible biodegradable citrate-based polymeric step-index optical fiber," *Biomaterials*, vol. 143, pp. 142–148, Oct. 2017, ISSN: 01429612. DOI: 10.1016/j.biomaterials.2017.08.003.

[57] S. Nizamoglu et al., "Bioabsorbable polymer optical waveguides for deep-tissue photomedicine," *Nature Communications*, vol. 7, no. 1, p. 10 374, Jan. 2016, ISSN: 2041-1723. DOI: 10.1038/ncomms10374.

[58] M. Choi, J. W. Choi, S. Kim, S. Nizamoglu, S. K. Hahn, and S. H. Yun, "Light-guiding hydrogels for cell-based sensing and optogenetic synthesis in vivo," *Nature Photonics*, vol. 7, no. 12, pp. 987–994, Dec. 2013, ISSN: 1749-4885. DOI: 10.1038/nphoton.2013.278.

[59] J. Guo, M. Zhou, and C. Yang, "Fluorescent hydrogel waveguide for on-site detection of heavy metal ions," *Scientific Reports*, vol. 7, no. 1, p. 7902, Aug. 2017, ISSN: 2045-2322. DOI: 10.1038/s41598-017-08353-8.

[60] A. Jain, A. H. Yang, and D. Erickson, "Gel-based optical waveguides with live cell encapsulation and integrated microfluidics," *Optics Letters*, vol. 37, no. 9, p. 1472, May 2012, ISSN: 0146-9592. DOI: 10.1364/OL.37.001472.

[61] A. K. Manocchi, P. Domachuk, F. G. Omenetto, and H. Yi, "Facile fabrication of gelatin-based biopolymeric optical waveguides," *Biotechnology and Bioengineering*, vol. 103, no. 4, pp. 725–732, Jul. 2009, ISSN: 00063592. DOI: 10.1002/bit.22306.

[62] A. D. Mickle et al., "A wireless closed-loop system for optogenetic peripheral neuromodulation," *Nature*, vol. 565, no. 7739, pp. 361–365, 2019, ISSN: 14764687. DOI: 10.1038/s41586-018-0823-6.

[63] J. Ausra et al., "Wireless, battery-free, subdermally implantable platforms for transcranial and long-range optogenetics in freely moving animals," *Proceedings of the National Academy of Sciences*, vol. 118, no. 30, Jul. 2021, ISSN: 0027-8424. DOI: 10.1073/pnas.2025775118.

[64] Y. Zhang et al., "Battery-free, lightweight, injectable microsystem for in vivo wireless pharmacology and optogenetics," *Proceedings of the National Academy of Sciences*, vol. 116, no. 43, pp. 21 427–21 437, Oct. 2019, ISSN: 0027-8424. DOI: 10.1073/pnas.1909850116.

[65] Y. Yang et al., "Wireless multilateral devices for optogenetic studies of individual and social behaviors," *Nature Neuroscience*, vol. 24, no. 7, pp. 1035–1045, Jul. 2021, ISSN: 1097-6256. DOI: 10.1038/s41593-021-00849-x.

[66] V. K. Samineni et al., "Fully implantable, battery-free wireless optoelectronic devices for spinal optogenetics," *Pain*, vol. 158, no. 11, pp. 2108–2116, 2017, ISSN: 18726623. DOI: 10.1097/j.pain.0000000000000968.

[67] R. M. Neely, D. K. Piech, S. R. Santacruz, M. M. Maharbiz, and J. M. Carmena, "Recent advances in neural dust: towards a neural interface platform," *Current Opinion in Neurobiology*, vol. 50, pp. 64–71, 2018, ISSN: 18736882. DOI: 10.1016/j.conb.2017.12.010.

[68] S. A. Wirdatmadja, M. T. Barros, Y. Koucheryavy, J. M. Jornet, and S. Balasubramaniam, "Wireless Optogenetic Nanonetworks for Brain Stimulation: Device Model and Charging Protocols," *IEEE Transactions on Nanobioscience*, vol. 16, no. 8, pp. 859–872, 2017, ISSN: 15361241. DOI: 10.1109/TNB.2017.2781150.

[69] O. A. Dambri, S. Cherkaoui, and D. Makrakis, "Design and Evaluation of a Receiver for Wired Nano-Communication Networks," *IEEE Transactions on NanoBioscience*, vol. 22, no. 2, pp. 223–236, Apr. 2023, ISSN: 1536-1241. DOI: 10.1109/TNB.2022.3182587.

[70] D. Makrakis, O. A. Dambri, and A. S. Hafid, "Design of Bio-Optical Transceiver for In Vivo Biomedical Sensor Applications," *Sensors*, vol. 24, no. 8, p. 2584, Apr. 2024, ISSN: 1424-8220. DOI: 10.3390/s24082584.

[71] S. H. Haddock, M. A. Moline, and J. F. Case, "Bioluminescence in the sea," *Annual review of marine science*, vol. 2, no. 1, pp. 443–493, 2010. DOI: 10.1146/annurev-marine-120308-081028.

[72] E. A. Widder, "Bioluminescence in the ocean: Origins of biological, chemical, and ecological diversity," *Science*, vol. 328, no. 5979, pp. 704–708, 2010. DOI: 10.1126/science.1174269.

[73] O. Shimomura, *Bioluminescence*. WORLD SCIENTIFIC, Sep. 2006, vol. 106, pp. 319–321, ISBN: 978-981-256-801-4. DOI: 10.1142/6102.

[74] M. Porta-de-la Riva, L.-F. Morales-Curiel, A. Carolina Gonzalez, and M. Krieg, "Bioluminescence as a functional tool for visualizing and controlling neuronal activity in vivo," *Neurophotonics*, vol. 11, no. 02, Feb. 2024, ISSN: 2329-423X. DOI: 10.1117/1.NPh.11.2.024203.

[75] S. M. Lewis and C. K. Cratsley, "Flash Signal Evolution, Mate Choice, and Predation in Fireflies," *Annual Review of Entomology*, vol. 53, no. 1, pp. 293–321, Jan. 2008, ISSN: 0066-4170. DOI: 10.1146/annurev.ento.53.103106.093346.

[76] S. Johnsen, E. A. Widder, and C. D. Mobley, "Propagation and Perception of Bioluminescence: Factors Affecting Counterillumination as a Cryptic Strategy," *The Biological Bulletin*, vol. 207, no. 1, pp. 1–16, Aug. 2004, ISSN: 0006-3185. DOI: 10.2307/1543624.

[77] E. A. Widder, M. I. Latz, P. J. Herring, and J. F. Case, "Far Red Bioluminescence from Two Deep-Sea Fishes," *Science*, vol. 225, no. 4661, pp. 512–514, Aug. 1984, ISSN: 0036-8075. DOI: 10.1126/science.225.4661.512.

[78] A. F. Mensinger and J. F. Case, "Dinoflagellate luminescence increases susceptibility of zooplankton to teleost predation," *Marine Biology*, vol. 112, pp. 207–210, 1992.

[79] E. N. Harvey, *Bioluminescence*. Academic Press, 1952.

[80] Y. Ando et al., "Firefly bioluminescence quantum yield and colour change by pH-sensitive green emission," *Nature Photonics*, vol. 2, no. 1, pp. 44–47, Jan. 2008, ISSN: 1749-4885. DOI: 10.1038/nphoton.2007.251.

[81] L. F. Greer and A. A. Szalay, "Imaging of light emission from the expression of luciferases in living cells and organisms: a review," *Luminescence*, vol. 17, no. 1, pp. 43–74, Jan. 2002, ISSN: 1522-7235. DOI: 10.1002/bio.676.

[82] S. B. Mali, "Bioluminescence in cancer research - Applications and challenges," *Oral Oncology Reports*, vol. 9, p. 100 127, Mar. 2024, ISSN: 27729060. DOI: 10.1016/j.oor.2023.100127.

[83] D. M. Close, T. Xu, G. S. Sayler, and S. Ripp, "In Vivo Bioluminescent Imaging (BLI): Noninvasive Visualization and Interrogation of Biological Processes in Living Animals," *Sensors*, vol. 11, no. 1, pp. 180–206, Dec. 2010, ISSN: 1424-8220. DOI: 10.3390/s110100180.

[84] C. J. Kelly, N. Tumsaroj, and C. A. Lajoie, "Assessing wastewater metal toxicity with bacterial bioluminescence in a bench-scale wastewater treatment system," *Water Research*, vol. 38, no. 2, pp. 423–431, Jan. 2004, ISSN: 00431354. DOI: 10.1016/S0043-1354(03)00432-9.

[85] T. Kuchimaru et al., "A luciferin analogue generating near-infrared bioluminescence achieves highly sensitive deep-tissue imaging," *Nature Communications*, vol. 7, p. 11 856, 2016.

[86] S. Liu, H. Liu, P. Yan, L. Zhang, and Z. Cheng, "Advances in luciferase systems for in vivo imaging," *ACS Chemical Biology*, vol. 16, no. 12, pp. 2709–2718, 2021.

[87] M. P. Hall et al., "Engineered luciferase reporter from a deep sea shrimp utilizing a novel imidazopyrazinone substrate," *ACS Chemical Biology*, vol. 7, no. 11, pp. 1848–1857, 2012.

[88] N. Gaspar, G. Clavier, B. Meunier, et al., "Evaluation of nanoluc substrates for bioluminescence imaging of transferred cells in mice," *International Journal of Molecular Sciences*, vol. 22, no. 3, p. 1118, 2021.

[89] T. Kuchimaru et al., "Emerging synthetic bioluminescent reactions for non-invasive imaging of freely moving animals," *Bioconjugate Chemistry*, 2024.

[90] Y. Su, J. R. Walker, Y. Park, T. P. Smith, C. Liu, et al., "An optimized bioluminescent substrate for non-invasive imaging in the brain," *Nature Chemical Biology*, vol. 19, pp. 1010–1018, 2023.

[91] S. Schramm and D. Weiß, "Bioluminescence – The Vibrant Glow of Nature and its Chemical Mechanisms," *ChemBioChem*, vol. 25, no. 9, May 2024, ISSN: 1439-4227. DOI: 10.1002/cbic.202400106.

[92] A. Mithöfer and C. Mazars, "Aequorin-based measurements of intracellular Ca2+-signatures in plant cells," *Biological Procedures Online*, vol. 4, no. 1, pp. 105–118, Jun. 2002, ISSN: 1480-9222. DOI: 10.1251/bpo40.

[93] M. Bonora et al., "Subcellular calcium measurements in mammalian cells using jellyfish photoprotein aequorin-based probes," *Nature Protocols*, vol. 8, no. 11, pp. 2105–2118, Nov. 2013, ISSN: 1754-2189. DOI: 10.1038/nprot.2013.127.

[94] A. Bakayan et al., "Redquorinxs mutants with enhanced calcium sensitivity and bioluminescence output efficiently report cellular and neuronal network activities," *International Journal of Molecular Sciences*, vol. 21, no. 21, pp. 1–22, 2020, ISSN: 14220067. DOI: 10.3390/ijms21217846.

[95] E. Dikici et al., "Aequorin variants with improved bioluminescence properties," *Protein Engineering, Design and Selection*, vol. 22, no. 4, pp. 243–248, 2009, ISSN: 17410126. DOI: 10.1093/protein/gzn083.

[96] A. Bakayan, B. Domingo, C. F. Vaquero, N. Peyriéras, and J. Llopis, "Fluorescent Protein–photoprotein Fusions and Their Applications in Calcium Imaging," *Photochemistry and Photobiology*, vol. 93, no. 2, pp. 448–465, Mar. 2017, ISSN: 0031-8655. DOI: 10.1111/php.12682.

[97] O Shimomura, B Musicki, and Y Kishi, "Semi-synthetic aequorins with improved sensitivity to Ca2+ ions," *Biochemical Journal*, vol. 261, no. 3, pp. 913–920, Aug. 1989, ISSN: 0264-6021. DOI: 10.1042/bj2610913.

[98] A. Bakayan, C. F. Vaquero, F. Picazo, and J. Llopis, "Red fluorescent protein-aequorin fusions as improved bioluminescent Ca2+ reporters in single cells and mice," *PLoS ONE*, vol. 6, no. 5, e19520, 2011, ISSN: 19326203. DOI: 10.1371/journal.pone.0019520.

[99] A. Bakayan, B. Domingo, A. Miyawaki, and J. Llopis, "Imaging Ca2+ activity in mammalian cells and zebrafish with a novel red-emitting aequorin variant," *Pflugers Archiv European Journal of Physiology*, vol. 467, no. 9, pp. 2031–2042, 2015, ISSN: 14322013. DOI: 10.1007/s00424-014-1639-3.

[100] A. Bakayan et al., "Redquorinxs mutants with enhanced calcium sensitivity and bioluminescence output efficiently report cellular and neuronal network activities," *International Journal of Molecular Sciences*, vol. 21, no. 21, pp. 1–22, 2020, ISSN: 14220067. DOI: 10.3390/ijms21217846.

[101] E. S. Boyden, F. Zhang, E. Bamberg, G. Nagel, and K. Deisseroth, "Millisecond-timescale, genetically targeted optical control of neural activity," *Nature Neuroscience*, vol. 8, no. 9, pp. 1263–1268, 2005. DOI: 10.1038/nn1525.

[102] P. Tan, L. He, G. Han, and Y. Zhou, "Optogenetic Immunomodulation: Shedding Light on Antitumor Immunity," *Trends in Biotechnology*, vol. 35, no. 3, pp. 215–226, Mar. 2017, ISSN: 01677799. DOI: 10.1016/j.tibtech.2016.09.002.

[103] J. H. Park et al., "Optogenetic Modulation of Urinary Bladder Contraction for Lower Urinary Tract Dysfunction," *Scientific Reports*, vol. 7, no. 1, p. 40 872, Jan. 2017, ISSN: 2045-2322. DOI: 10.1038/srep40872.

[104] C. Yu, I. R. Cassar, J. Sambangi, and W. M. Grill, "Frequency-Specific Optogenetic Deep Brain Stimulation of Subthalamic Nucleus Improves Parkinsonian Motor Behaviors," *The Journal of Neuroscience*, vol. 40, no. 22, pp. 4323–4334, May 2020, ISSN: 0270-6474. DOI: 10.1523/JNEUROSCI.3071-19.2020.

[105] G. Nagel et al., "Channelrhodopsin-2, a directly light-gated cation-selective membrane channel," *Proceedings of the National Academy of Sciences*, vol. 100, no. 24, pp. 13 940–13 945, Nov. 2003, ISSN: 0027-8424. DOI: 10.1073/pnas.1936192100.

[106] D. Oesterhelt and W. Stoeckenius, "Functions of a New Photoreceptor Membrane," *Proceedings of the National Academy of Sciences*, vol. 70, no. 10, pp. 2853–2857, Oct. 1973, ISSN: 0027-8424. DOI: 10.1073/pnas.70.10.2853.

[107] J. Mattis et al., "Principles for applying optogenetic tools derived from direct comparative analysis of microbial opsins," *Nature Methods*, vol. 9, no. 2, pp. 159–172, Feb. 2012, ISSN: 1548-7091. DOI: 10.1038/nmeth.1808.

[108] G. Nagel et al., "Channelrhodopsin-1: A Light-Gated Proton Channel in Green Algae," *Science*, vol. 296, no. 5577, pp. 2395–2398, Jun. 2002, ISSN: 0036-8075. DOI: 10.1126/science.1072068.

[109] O. Volkov et al., "Structural insights into ion conduction by channelrhodopsin 2," *Science*, vol. 358, no. 6366, Nov. 2017, ISSN: 0036-8075. DOI: 10.1126/science.aan8862.

[110] C. Marian, *Retinal*, 2024. DOI: 10.1080/002689798167359.

[111] R. A. Stefanescu, R. G. Shivakeshavan, P. P. Khargonekar, and S. S. Talathi, "Computational Modeling of Channelrhodopsin-2 Photocurrent Characteristics in Relation to Neural Signaling," *Bulletin of Mathematical Biology*, vol. 75, no. 11, pp. 2208–2240, Nov. 2013, ISSN: 0092-8240. DOI: 10.1007/s11538-013-9888-4.

[112] K. Nikolic, N. Grossman, M. S. Grubb, J. Burrone, C. Toumazou, and P. Degenaar, "Photocycles of channelrhodopsin-2," *Photochemistry and Photobiology*, vol. 85, no. 1, pp. 400–411, 2009, ISSN: 00318655. DOI: 10.1111/j.1751-1097.2008.00460.x.

[113] N. Grossman, V. Simiaki, C. Martinet, C. Toumazou, S. R. Schultz, and K. Nikolic, "The spatial pattern of light determines the kinetics and modulates backpropagation of optogenetic action potentials," *Journal of Computational Neuroscience*, vol. 34, no. 3, pp. 477–488, Jun. 2013, ISSN: 0929-5313. DOI: 10.1007/s10827-012-0431-7.

[114] S. J. Rupitsch, *Piezoelectricity*. Springer Berlin Heidelberg, 2019, ch. 3, pp. 43–81, ISBN: 9783662575321. DOI: 10.1007/978-3-662-57534-5_3.

[115] A. Kelly and K. M.Knowles, *Crystallography and crystal defects*, 2nd. John Wiley & Sons, Ltd, 2012, vol. 2, p. 522, ISBN: 9780470750155. DOI: 10.1016/0047-7206(70)90050-6.

[116] F Mandl, *Statistical Physics*, 2nd. John Wiley & sons, 1988, vol. 26, pp. 52–52, ISBN: 978-0471915331. DOI: 10.1063/1.3128142.

[117] M. de Jong, W. Chen, H. Geerlings, M. Asta, and K. A. Persson, "A database to enable discovery and design of piezoelectric materials," *Scientific Data*, vol. 2, no. 1, p. 150 053, Sep. 2015, ISSN: 2052-4463. DOI: 10.1038/sdata.2015.53.

[118] L. O. Björn, "The Nature of Light and Its Interaction with Matter," in *Photobiology*, New York, NY: Springer New York, 2015, ch. 1, pp. 1–39. DOI: 10.1007/978-0-387-72655-7_1.

[119] P. N. Prasad, *Introduction to Biophotonics*. Wiley, Apr. 2003, vol. 254, pp. 1–16, ISBN: 9780471287704. DOI: 10.1002/0471465380.

[120] G. Keiser, "Basic Principles of Light," in *Biophotonics*, Springer, 2022, ch. 2, pp. 27–54. DOI: 10.1007/978-981-19-3482-7_2.

[121] L. de Broglie, "The reinterpretation of wave mechanics," *Foundations of Physics*, vol. 1, no. 1, pp. 5–15, Mar. 1970, ISSN: 0015-9018. DOI: 10.1007/BF00708650.

[122] M. Schmitt, T. Mayerhöfer, J. Popp, I. Kleppe, and K. Weisshart, "Light–Matter Interaction," in *Handbook of Biophotonics*, Wiley, Jun. 2012, ch. 3, pp. 87–261. DOI: 10.1002/9783527643981.bphot003.

[123] L. V. Wang and H. Wu, *Biomedical Optics*. Wiley, Jul. 2009, vol. 29, ISBN: 9780471743040. DOI: 10.1002/9780470177013.

[124] S. L. Jacques, "Optical properties of biological tissues: a review," *Physics in Medicine and Biology*, vol. 58, no. 11, R37–R61, Jun. 2013, ISSN: 0031-9155. DOI: 10.1088/0031-9155/58/11/R37.

[125] L. O. Björn, "Principles and Nomenclature for the Quantification of Light," in *Photobiology*, New York, NY: Springer New York, 2015, ch. 2, pp. 41–49. DOI: 10.1007/978-0-387-72655-7_2.

[126] S. E. Braslavsky, "Glossary of terms used in photochemistry, 3rd edition (IUPAC Recommendations 2006)," *Pure and Applied Chemistry*, vol. 79, no. 3, pp. 293–465, Jan. 2007, ISSN: 1365-3075. DOI: 10.1351/pac200779030293.

[127] D. P. Hampshire, "A derivation of Maxwell's equations using the Heaviside notation," *Philosophical Transactions of the Royal Society A: Mathematical, Physical and Engineering Sciences*, vol. 376, no. 2134, p. 20 170 447, Dec. 2018, ISSN: 1364-503X. DOI: 10.1098/rsta.2017.0447.

[128] A. Doicu and M. I. Mishchenko, "Overview of methods for deriving the radiative transfer theory from the maxwell equations. i: Approach based on the far-field foldy equations," *Journal of Quantitative Spectroscopy and Radiative Transfer*, vol. 220, pp. 123–139, 2018, ISSN: 0022-4073. DOI: https://doi.org/10.1016/j.jqsrt.2018.09.004.

[129] K. F. Evans, "The Spherical Harmonics Discrete Ordinate Method for Three-Dimensional Atmospheric Radiative Transfer," *Journal of the Atmospheric Sciences*, vol. 55, no. 3, pp. 429–446, Feb. 1998, ISSN: 0022-4928. DOI: 10.1175/1520-0469(1998)055<0429:TSHDOM>2.0.CO;2.

[130] C. Miclea, *Piezoelectric Nanomaterials for Biomedical Applications* (Nanomedicine and Nanotoxicology), G. Ciofani and A. Menciassi, Eds. Berlin, Heidelberg: Springer Berlin Heidelberg, 2012, pp. 29–61, ISBN: 978-3-642-28043-6. DOI: 10.1007/978-3-642-28044-3.

[131] X. Wang, J. Song, J. Liu, and Z. L. Wang, "Direct-Current Nanogenerator Driven by Ultrasonic Waves," *Science*, vol. 316, no. 5821, pp. 102–105, Apr. 2007, ISSN: 0036-8075. DOI: 10.1126/science.1139366.

[132] H. Bishara, A. Nagel, M. Levanon, and S. Berger, "Amino acids nanocrystals for piezoelectric detection of ultra-low mechanical pressure," *Materials Science and Engineering: C*, vol. 108, p. 110 468, Mar. 2020, ISSN: 09284931. DOI: 10.1016/j.msec.2019.110468.

[133] K. Ryan et al., "Nanoscale Piezoelectric Properties of Self-Assembled Fmoc–FF Peptide Fibrous Networks," *ACS Applied Materials & Interfaces*, vol. 7, no. 23, pp. 12 702–12 707, Jun. 2015, ISSN: 1944-8244. DOI: 10.1021/acsami.5b01251.

[134] S. Dishon et al., "Surface Piezoelectricity and Pyroelectricity in Centrosymmetric Materials: A Case of α-Glycine," *Materials*, vol. 13, no. 20, p. 4663, Oct. 2020, ISSN: 1996-1944. DOI: 10.3390/ma13204663.

[135] S. Guerin et al., "Control of piezoelectricity in amino acids by supramolecular packing," *Nature Materials*, vol. 17, no. 2, pp. 180–186, Feb. 2018, ISSN: 1476-1122. DOI: 10.1038/nmat5045.

[136] E. S. Ferrari, R. J. Davey, W. I. Cross, A. L. Gillon, and C. S. Towler, "Crystallization in Polymorphic Systems: The Solution-Mediated Transformation of β to α Glycine," *Crystal Growth & Design*, vol. 3, no. 1, pp. 53–60, Jan. 2003, ISSN: 1528-7483. DOI: 10.1021/cg025561b.

[137] A. Jain, P. K. J., A. K. Sharma, A. Jain, and R. P.N, "Dielectric and piezoelectric properties of PVDF/PZT composites: A review," *Polymer Engineering and Science*, vol. 55, no. 7, pp. 1589–1616, Jul. 2015, ISSN: 0032-3888. DOI: 10.1002/pen.24088.

[138] D. Kim, S. A. Han, J. H. Kim, J. Lee, S. Kim, and S. Lee, "Biomolecular Piezoelectric Materials: From Amino Acids to Living Tissues," *Advanced Materials*, vol. 32, no. 14, Apr. 2020, ISSN: 0935-9648. DOI: 10.1002/adma.201906989.

[139] S. Vasilev, P. Zelenovskiy, D. Vasileva, A. Nuraeva, V. Y. Shur, and A. L. Kholkin, "Piezoelectric properties of diphenylalanine microtubes prepared from the solution," *Journal of Physics and Chemistry of Solids*, vol. 93, pp. 68–72, Jun. 2016, ISSN: 00223697. DOI: 10.1016/j.jpcs.2016.02.002.

[140] J. Wang et al., "Piezoelectric Nanocellulose Thin Film with Large-Scale Vertical Crystal Alignment," *ACS Applied Materials and Interfaces*, vol. 12, no. 23, pp. 26 399–26 404, Jun. 2020, ISSN: 1944-8244. DOI: 10.1021/acsami.0c05680.

[141] E. Fukada, "History and recent progress in piezoelectric polymers," *IEEE Transactions on Ultrasonics, Ferroelectrics and Frequency Control*, vol. 47, no. 6, pp. 1277–1290, Nov. 2000, ISSN: 0885-3010. DOI: 10.1109/58.883516.

[142] R. Lay, G. S. Deijs, and J. Malmström, "The intrinsic piezoelectric properties of materials – a review with a focus on biological materials," *RSC Advances*, vol. 11, no. 49, pp. 30 657–30 673, 2021, ISSN: 2046-2069. DOI: 10.1039/D1RA03557F.

[143] C. Miao, L. Reid, and W. Y. Hamad, "Moisture-tunable, ionic strength-controlled piezoelectric effect in cellulose nanocrystal films," *Applied Materials Today*, vol. 24, p. 101 082, Sep. 2021, ISSN: 23529407. DOI: 10.1016/j.apmt.2021.101082.

[144] L. Zhai, H. C. Kim, J. W. Kim, and J. Kim, "Alignment Effect on the Piezoelectric Properties of Ultrathin Cellulose Nanofiber Films," *ACS Applied Bio Materials*, vol. 3, no. 7, pp. 4329–4334, Jul. 2020, ISSN: 2576-6422. DOI: 10.1021/acsabm.0c00364.

[145] J.-S. Moon et al., "M13 bacteriophage-based self-assembly structures and their functional capabilities," *Mini-Reviews in Organic Chemistry*, vol. 12, no. 3, pp. 271–281, 2015. DOI: 10.2174/1570193x1203150429105418.

[146] I. W. Park et al., "Recent developments and prospects of M13-bacteriophage based piezoelectric energy harvesting devices," *Nanomaterials*, vol. 10, no. 1, p. 93, 2020, ISSN: 20794991. DOI: 10.3390/nano10010093.

[147] J.-H. Lee, J. H. Lee, J. Xiao, M. S. Desai, X. Zhang, and S.-W. Lee, "Vertical self-assembly of polarized phage nanostructure for energy harvesting," *Nano Letters*, vol. 19, no. 4, pp. 2661–2667, 2019. DOI: 10.1021/acs.nanolett.9b00569.s001.

[148] Y. Yan et al., "Nanogenerators facilitated piezoelectric and flexoelectric characterizations for bioinspired energy harvesting materials," *Nano Energy*, vol. 81, p. 105 607, 2021. DOI: 10.1016/j.nanoen.2020.105607.

[149] B. Y. Lee et al., "Virus-based piezoelectric energy generation.," *Nature nanotechnology*, vol. 76, no. 6, pp. 351–6, 2012. DOI: 10.1038/nnano.2012.69.

[150] W. N. Zou, C. X. Tang, and E. Pan, "Symmetry types of the piezoelectric tensor and their identification," *Proceedings of the Royal Society A: Mathematical, Physical and Engineering Sciences*, vol. 469, no. 2155, p. 20 120 755, 2013, ISSN: 14712946. DOI: 10.1098/rspa.2012.0755.

[151] J. F. Nye, *Physical Properties of Crystals*. OXFORD University Press, 1985, vol. 11, p. 352, ISBN: 9780198511656. DOI: 10.1107/s0365110x58001754.

[152] R. Dorey, *Ceramic Thick Films for MEMS and Microdevices*. Elsevier, 2011, ch. 4, p. 86, ISBN: 9781437778175. DOI: 10.1016/C2009-0-20338-2.

[153] B. Y. Lee et al., "Virus-based piezoelectric energy generation," *Nature Nanotechnology*, vol. 7, no. 6, pp. 351–356, 2012, ISSN: 17483395. DOI: 10.1038/nnano.2012.69.

[154] V. A. Fonoberov and A. A. Balandin, "Low-frequency vibrational modes of viruses used for nanoelectronic self-assemblies," *physica status solidi (b)*, vol. 241, no. 12, R67–R69, Oct. 2004, ISSN: 03701972. DOI: 10.1002/pssb.200409062.

[155] S. Speziale et al., "Sound Velocity and Elasticity of Tetragonal Lysozyme Crystals by Brillouin Spectroscopy," *Biophysical Journal*, vol. 85, no. 5, pp. 3202–3213, 2003, ISSN: 00063495. DOI: 10.1016/S0006-3495(03)74738-9.

[156] O. Morag, N. Sgourakis, D. Baker, and A. Goldbourt, *Capsid model of M13 bacteriophage virus from Magic-angle spinning NMR and Rosetta modeling*, 2015. DOI: doi.org/10.2210/pdb2MJZ/pdb.

[157] M. I. Chilvers, L. J. du Toit, H. Akamatsu, and T. L. Peever, "A Real-Time, Quantitative PCR Seed Assay for Botrytis spp. that Cause Neck Rot of Onion," *Plant Disease*, vol. 91, no. 5, pp. 599–608, May 2007, ISSN: 0191-2917. DOI: 10.1094/PDIS-91-5-0599.

[158] COMSOL AB, *COMSOL Multiphysics v. 6.2*, https://www.comsol.com, COMSOL AB, Stockholm, Sweden, 2023.

[159] M. Amir Sohrabi and A. H. Muliana, "Nonlinear and time dependent behaviors of piezoelectric materials and structures," *International Journal of Mechanical Sciences*, vol. 94-95, pp. 1–9, May 2015, ISSN: 00207403. DOI: 10.1016/j.ijmecsci.2015.02.005.

[160] D. Damjanovic, "Stress and frequency dependence of the direct piezoelectric effect in ferroelectric ceramics," *Journal of Applied Physics*, vol. 82, no. 4, pp. 1788–1797, Aug. 1997, ISSN: 0021-8979. DOI: 10.1063/1.365981.

[161] J. Fritz, "Cantilever biosensors," *The Analyst*, vol. 133, no. 7, p. 855, 2008, ISSN: 0003-2654. DOI: 10.1039/b718174d.

[162] T. N. Lamichhane, N. D. Abeydeera, A.-C. E. Duc, P. R. Cunningham, and C. S. Chow, "Selection of Peptides Targeting Helix 31 of Bacterial 16S Ribosomal RNA by Screening M13 Phage-Display Libraries," *Molecules*, vol. 16, no. 2, pp. 1211–1239, Jan. 2011, ISSN: 1420-3049. DOI: 10.3390/molecules16021211.

[163] D. Rossi, E. Pierantozzi, D. O. Amadsun, S. Buonocore, E. M. Rubino, and V. Sorrentino, "The Sarcoplasmic Reticulum of Skeletal Muscle Cells: A Labyrinth of Membrane Contact Sites," *Biomolecules*, vol. 12, no. 4, p. 488, Mar. 2022, ISSN: 2218-273X. DOI: 10.3390/biom12040488.

[164] H. L. Roderick, M. J. Berridge, and M. D. Bootman, "The Endoplasmic Reticulum: A Central Player in Cell Signalling and Protein Synthesis," in *Understanding Calcium Dynamics*, Berlin, Heidelberg: Springer, Nov. 2003, ch. 2, pp. 17–35. DOI: 10.1007/978-3-540-44878-5_2.

[165] M. Periasamy and A. Kalyanasundaram, "SERCA pump isoforms: Their role in calcium transport and disease," *Muscle & Nerve*, vol. 35, no. 4, pp. 430–442, Apr. 2007, ISSN: 0148639X. DOI: 10.1002/mus.20745.

[166] P. Vangheluwe, L. Raeymaekers, L. Dode, and F. Wuytack, "Modulating sarco(endo)plasmic reticulum Ca2+ ATPase 2 (SERCA2) activity: Cell biological implications," *Cell Calcium*, vol. 38, no. 3-4, pp. 291–302, Sep. 2005, ISSN: 01434160. DOI: 10.1016/j.ceca.2005.06.033.

[167] H. Takeshima, E. Venturi, and R. Sitsapesan, "New and notable ion-channels in the sarcoplasmic/endoplasmic reticulum: Do they support the process of intracellular Ca2+ release?" *Journal of Physiology*, vol. 593, no. 15, pp. 3241–3251, 2015, ISSN: 14697793. DOI: 10.1113/jphysiol.2014.281881.

[168] H. X. Nguyen and N. Bursac, "Ion channel engineering for modulation and de novo generation of electrical excitability," *Current Opinion in Biotechnology*, vol. 58, pp. 100–107, Aug. 2019, ISSN: 09581669. DOI: 10.1016/j.copbio.2019.01.004.

[169] J. T. Lanner, D. K. Georgiou, A. D. Joshi, and S. L. Hamilton, "Ryanodine Receptors: Structure, Expression, Molecular Details, and Function in Calcium Release," *Cold Spring Harbor Perspectives in Biology*, vol. 2, no. 11, a003996–a003996, Nov. 2010, ISSN: 1943-0264. DOI: 10.1101/cshperspect.a003996.

[170] J.-A. Heuson-Stiennon, J.-C. Wanson, and P. Drochmans, "Isolation and characterization of the sarcoplasmic reticulum of skeletal muscle," *The Journal of Cell Biology*, vol. 55, no. 2, 471–488, 1972, ISSN: 0021-9525. DOI: 10.1083/jcb.55.2.471.

[171] J. M. Autry, C. B. Karim, M. Cocco, S. F. Carlson, D. D. Thomas, and S. J. Valberg, "Purification of sarcoplasmic reticulum vesicles from horse gluteal muscle," *Analytical Biochemistry*, vol. 610, p. 113 965, 2020, ISSN: 0003-2697. DOI: https://doi.org/10.1016/j.ab.2020.113965.

[172] E.-K. Dimitriadou, "Redesign of calcium-regulated protein aequorin towards the development of a novel ion bioreporter," Ph.D. dissertation, University College London, 2014.

[173] A. A. Paknahad, L. Kerr, D. A. Wong, M. C. Kolios, and S. S. H. Tsai, "Biomedical nanobubbles and opportunities for microfluidics," *RSC Advances*, vol. 11, no. 52, pp. 32 750–32 774, 2021, ISSN: 2046-2069. DOI: 10.1039/D1RA04890B.

[174] M. Wdowiak, J. Paczesny, and S. Raza, "Enhancing the Stability of Bacteriophages Using Physical, Chemical, and Nano-Based Approaches: A Review," *Pharmaceutics*, vol. 14, no. 9, p. 1936, Sep. 2022, ISSN: 1999-4923. DOI: 10.3390/pharmaceutics14091936.

[175] Y. Yang and L. Tang, "Equivalent circuit modeling of piezoelectric energy harvesters," *Journal of Intelligent Material Systems and Structures*, vol. 20, no. 18, pp. 2223–2235, 2009, ISSN: 1045389X. DOI: 10.1177/1045389X09351757.

[176] J. T. Koivumäki, T. Korhonen, and P. Tavi, "Impact of sarcoplasmic reticulum calcium release on calcium dynamics and action potential morphology in human atrial myocytes: A computational study," *PLoS Computational Biology*, vol. 7, no. 1, e1001067, 2011, ISSN: 15537358. DOI: 10.1371/journal.pcbi.1001067.

[177] S. N. Hatem et al., "Different compartments of sarcoplasmic reticulum participate in the excitation-contraction coupling process in human atrial myocytes," *Circulation Research*, vol. 80, no. 3, pp. 345–353, 1997, ISSN: 00097330. DOI: 10.1161/01.RES.80.3.345.

[178] H. Motulsky and A. Christopoulos, *Fitting Models to Biological Data Using Linear and Nonlinear Regression: A practical guide to curve fitting*. Oxford University Press, May 2004, ISBN: 9780195171792. DOI: 10.1093/oso/9780195171792.001.0001.

[179] D. G. Allen, J. R. Blinks, and F. G. Prendergast, "Aequorin Luminescence: Relation of Light Emission to Calcium Concentration—A Calcium-Independent Component," *Science*, vol. 195, no. 4282, pp. 996–998, Mar. 1977, ISSN: 0036-8075. DOI: 10.1126/science.841325.

[180] J. D. Rogers, A. J. Radosevich, Ji Yi, and V. Backman, "Modeling Light Scattering in Tissue as Continuous Random Media Using a Versatile Refractive Index Correlation Function," *IEEE Journal of Selected Topics in Quantum Electronics*, vol. 20, no. 2, pp. 173–186, Mar. 2014, ISSN: 1077-260X. DOI: 10.1109/JSTQE.2013.2280999.

[181] *Heat transfer module user's guide*, COMSOL Multiphysics v6.3, See "Radiation in Absorbing-Scattering Media (rasm)" section. Accessed 2025-1-15, COMSOL AB, Stockholm, Sweden, 2024.

[182] A. K. Dunn, "Optical properties of neural tissue," in *Optical Imaging of Neocortical Dynamics*, ser. Neuromethods, B. Weber and F. Helmchen, Eds., vol. 85, Springer Science+Business Media New York, 2014, pp. 33–51. DOI: 10.1007/978-1-62703-785-3_3.

[183] S. L. Jacques, "Optical properties of biological tissues: A review," *Physics in Medicine and Biology*, vol. 58, no. 11, R37–R61, May 2013, Topical Review, ISSN: 0031-9155. DOI: 10.1088/0031-9155/58/11/R37.

[184] M. Schürmann, J. Scholze, P. Müller, J. Guck, and C. J. Chan, "Cell nuclei have lower refractive index and mass density than cytoplasm," *Journal of Biophotonics*, vol. 9, no. 10, pp. 1068–1076, 2016. DOI: 10.1002/jbio.201500273.

[185] Z. A. Steelman, W. J. Eldridge, J. B. Weintraub, and A. Wax, "Is the nuclear refractive index lower than cytoplasm? validation of phase measurements and implications for light scattering technologies," *Journal of Biophotonics*, vol. 10, no. 12, pp. 1714–1722, Dec. 2017. DOI: 10.1002/jbio.201600314.

[186] A. N. Yaroslavsky, P. C. Schulze, I. V. Yaroslavsky, R. Schober, F. Ulrich, and H. J. Schwarzmaier, "Optical properties of selected native and coagulated human brain tissues in vitro in the visible and near infrared spectral range," *Physics in Medicine and Biology*, vol. 47, no. 12, pp. 2059–2073, 2002, ISSN: 00319155. DOI: 10.1088/0031-9155/47/12/305.

[187] J. Sun, S. J. Lee, L. Wu, M. Sarntinoranont, and H. Xie, "Refractive index measurement of acute rat brain tissue slices using optical coherence tomography," *Optics Express*, vol. 20, no. 2, p. 1084, Jan. 2012, ISSN: 1094-4087. DOI: 10.1364/OE.20.001084.

[188] D. Watson, N. Hagen, J. Diver, P. Marchand, and M. Chachisvilis, "Elastic Light Scattering from Single Cells: Orientational Dynamics in Optical Trap," *Biophysical Journal*, vol. 87, no. 2, pp. 1298–1306, Aug. 2004, ISSN: 00063495. DOI: 10.1529/biophysj.104.042135.

[189] A. K. Dunn, "Optical Properties of Neural Tissue," in 2014, pp. 33–51. DOI: 10.1007/978-1-62703-785-3{_}3.

[190] G. E. Thomas and K. Stamnes, *Radiative Transfer in the Atmosphere and Ocean*. Cambridge, UK: Cambridge University Press, 1999, ISBN: 9780521455076. DOI: 10.1017/9781316148549.

[191] J. J. Duderstadt and W. R. Martin, *Transport Theory*. New York: John Wiley & Sons, 1979, vol. 3, pp. 147–166, ISBN: 9780471224127. DOI: 10.1080/00411457308205277.

[192] M. KGaA, *Specification Sheet of Aequorin from jellyfish (Aequorea sp.) Type III, solid*, 2024. DOI: 10.1016/s0040-4039(00)91607-1.

[193] D. Seo, J. M. Carmena, M. Rabaey, E. Alon, and M. M. Maharbiz, "Neural Dust: An Ultrasonic, Low Power Solution for Chronic Brain-Machine Interfaces," *The Future of the Brain*, no. 4, pp. 243–252, 2013. DOI: 10.2307/j.ctt9qh0x7.26. arXiv: 1307.2196.

[194] S. Leemann, S. Kleinlogel, and F. Schneider-Warme, "Optogenetic interrogation of cell signalling: Human neuropsin (hopn5) represents a potent tool for controlling the gq pathway with light," *Pflügers Archiv - European Journal of Physiology*, vol. 474, no. 10, pp. 1217–1219, 2022. DOI: 10.1007/s00424-022-02765-w.

[195] T. Asano, H. Igarashi, T. Ishizuka, and H. Yawo, "Organelle Optogenetics: Direct Manipulation of Intracellular Ca2+ Dynamics by Light," *Frontiers in Neuroscience*, vol. 12, Aug. 2018, ISSN: 1662-453X. DOI: 10.3389/fnins.2018.00561.